GEMS & GEMOLOGY

WINTER 2022
VOLUME LVIII

THE QUARTERLY JOURNAL OF THE GEMOLOGICAL INSTITUTE OF AMERICA

Low-Temperature Heat Treatment of Burmese Ruby

Identifying Copper-Diffused Red Feldspar

Characteristics of Porcelain-Treated Turquoise

Gem Artist Chi Huynh

GEMS & GEMOLOGY

Winter 2022
VOLUME 58, No. 4


p. 401


p. 440


p. 461

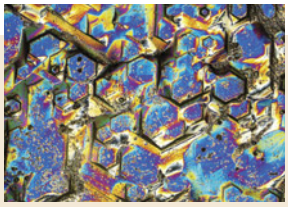
p. 493


p. 495

p. 524

Editorial

Feature Articles

Field Reports

Regular Features

GEMS & GEMOLOGY

gia.edu/gems-gemology

Customer Service
(760) 603-4200
gandg@gia.edu

Subscriptions
Copies of the current issue may be purchased for $29.95 plus shipping. Subscriptions are $79.99 for one year (4 issues) in the U.S. and $99.99 elsewhere. Canadian subscribers should add GST. Discounts are available for renewals, group subscriptions, GIA alumni, and current GIA students. To purchase print subscriptions, visit store.gia.edu or contact Customer Service. For institutional rates, contact Customer Service.

Database Coverage
Gems & Gemology's impact factor is 2.045, according to the 2021 Journal Citation Reports by Clarivate Analytics (issued June 2022). *G&G* is abstracted in Thomson Reuters products (Current Contents: Physical, Chemical & Earth Sciences and Science Citation Index—Expanded, including the Web of Knowledge) and other databases. For a complete list of sources abstracting *G&G*, go to gia.edu/gems-gemology, and click on "Publication Information."

Manuscript Submissions
Gems & Gemology, a peer-reviewed journal, welcomes the submission of articles on all aspects of the field. Please see the Author Guidelines at gia.edu/gems-gemology or contact the Managing Editor. Letters on articles published in *G&G* are also welcome. Please note that Field Reports, Lab Notes, Gem News International, Micro-World, Colored Stones Unearthed, Diamond Reflections, and Charts are not peer-reviewed sections but do undergo technical and editorial review.

Gems & Gemology is published quarterly by the Gemological Institute of America, a nonprofit educational organization for the gem and jewelry industry.

Postmaster: Return undeliverable copies of *Gems & Gemology* to GIA, The Robert Mouawad Campus, 5345 Armada Drive, Carlsbad, CA 92008.

Our Canadian goods and service registration number is 126142892RT.

About the Cover

This issue profiles Chi Huynh, the creative force behind Galatea: Jewelry by Artist. The ring on the cover combines two of Huynh's innovations, the Galatea Pearl and the Diamond in a Pearl. Galatea Pearls are gem bead cultured pearls carved to reveal the beauty of the gem inside. This yellow gold "Sutol Ring" features a 0.08 ct diamond set inside a 10.5 mm Galatea Pearl cultured with a synthetic turquoise bead. Courtesy of Chi Huynh.

Printing is by L+L Printers, Carlsbad, CA.

GIA World Headquarters The Robert Mouawad Campus 5345 Armada Drive Carlsbad, CA 92008 USA

ISSN 0016-626X

FSC www.fsc.org MIX Paper from responsible sources FSC® C006300

Low-Temperature Heating of Mogok Ruby, Copper-Diffused Feldspar, Porcelain-Treated Turquoise, and the Work of Gem Artist Chi Huynh

Welcome to the Winter 2022 edition of *Gems & Gemology*! This issue concludes our volume year with studies on identifying treatments in various colored gemstones and a field report on the inspiring work of an award-winning gem artist.

In our lead article, E. Billie Hughes and Wim Vertriest examine the difficulty of detecting low-temperature heat treatment in ruby. Using careful microscopic examination, they observed that many types of solid inclusions in Mogok ruby samples, including calcite, mica, spinel, and zircon, were sensitive to heat treatment at lower temperatures between 600° and 1100°C. Additionally, Raman analysis of calcite and spinel inclusions provided complementary evidence of low-temperature heat treatment.

"Many types of solid inclusions in Mogok ruby samples...were sensitive to heat treatment at lower temperatures between 600° and 1100°C."

Next, Qingchao Zhou and colleagues present their findings on identifying copper diffusion treatment in red andesine feldspar, which has been in question for more than a decade. Conducting experiments on both colorless labradorite and light yellow andesine feldspar to modify their color, the authors studied the samples' fluorescence characteristics and verified that strong fluorescence provided key evidence of treatment.

A team led by Liying Huang contributes our third article, which distinguishes a newer treatment technique used to mimic the color and luster of high-quality untreated turquoise. Known in the Chinese trade as "porcelain-treated" turquoise, this material can be identified by its surface features in combination with low specific gravity, strong luster, and trace element chemistry.

In our final feature article of this issue, Tao Hsu and coauthors profile the groundbreaking work and artistry of Chi Huynh, the designer behind Galatea: Jewelry by Artist. During a visit to the Galatea store and workshop, Huynh shared several of his innovative designs and patents, along with stories of inspiration as an artist and pioneer in the jewelry industry.

G&G's regular columns continue to offer exciting gemological findings from all over the world. Highlights from *Lab Notes* include an extraordinarily large cat's-eye emerald reportedly from Brazil, details of pearl submissions to GIA labs worldwide, and the largest extraterrestrial peridot examined at GIA to date. Observations of fascinating gemstone inclusions are captured in the *Micro-World* section, sharing a glance at spiral-like "horsetail" inclusions in demantoid, a bluish green omphacite crystal in a Fancy brown-pink diamond, aegirine crystals in two rare samples of poudretteite from Mogok, and more. *Colored Stones Unearthed* returns in this issue, focusing on gem minerals that form in magmatic environments. Finally, in *Gem News International*, catch up on the latest information from around the globe, including the observation of an extremely rare hellandite inclusion in a ruby from Mogok and coverage of the 2022 Geological Society of America annual meeting.

We hope you enjoy the latest issue of *Gems & Gemology*!

Duncan Pay | Editor-in-Chief | dpay@gia.edu

A Canary in the Ruby Mine: Low-Temperature Heat Treatment Experiments on Burmese Ruby

E. Billie Hughes and Wim Vertriest

Detection of heat treatment below 1200°C in ruby and sapphire can present challenges to gemologists, as alterations to the material are often subtle. In this study, the authors heated Burmese ruby samples from Mogok, Myanmar, at temperatures ranging from 600° to 1500°C. The samples were documented using macrophotography, photomicrography of inclusions, ultraviolet fluorescence imaging, and spectroscopic analysis (Raman, ultraviolet/visible/near-infrared, and infrared) to record any changes, with a focus on features that could help detect heat treatment.

A wide variety of solid inclusions, including calcite, mica, spinel, and zircon, were found in Mogok ruby. Many of those were found to be sensitive to heat treatment with regard to morphology and phase transition; their reactions varied depending on a number of factors such as size, distance from the surface, and species. Microscopic examination provided useful visual indications of heat treatment, even at lower temperatures. Raman analysis of calcite and spinel inclusions also proved valuable in providing complementary evidence of low-temperature heat treatment.

Due to the value and rarity of fine gems, early pioneers developed techniques to treat lower-quality material, including fracture filling and heat treatment. With ruby and sapphire, records of heat treatment go back more than a thousand years (Al-Beruni, 1989).

Heat-treatment temperatures were pushed higher as furnace technology improved with the advent of electricity, reaching temperatures of 1500°–1800°C (corundum melts at 2040°C). Thankfully, this type of treatment tends to be easy to spot because the high temperatures produce significant alterations (Hughes et al., 2017). Although technological advances have allowed for a wider range of treatments, many consumers still appreciate the natural beauty of gems, and there is a premium on untreated ruby and sapphire of high quality.

Because of this market premium, some treaters have returned to heating ruby at lower temperatures, hoping to evade detection. In other cases, extremely high heat is not required to create the desired change. Whatever the reason, identification of low-temperature-treated ruby is often challenging for laboratory gemologists. Thus, this study aims to find useful indicators that corundum has been heat treated at lower temperatures.

BACKGROUND

This project focuses specifically on marble-related ruby, for which Mogok (figure 1) is the most important source in terms of value. Most research on low-temperature treatment has been focused on East African amphibole-related ruby and so-called metamorphic sapphire from extensive secondary deposits in Madagascar and Sri Lanka (Pardieu et al., 2015; Sripoonjan et al., 2016; Hughes and Perkins, 2019).

We define high-temperature treatment as that which involves the dissolution of secondary-phase microcrystals. In corundum, the most common of these microcrystals is rutile silk, which tends to dissolve with heat at temperatures of approximately 1200°–1350°C. Thus, treatment in this temperature range is considered the boundary between "low" and "high" heat in corundum (Hughes et al., 2017).

Rutile silk in ruby and sapphire comes from a variety of sources. As a result, its altered appearance has become a key indicator of heat treatment. But because rutile tends to be affected by heat only at

See end of article for About the Authors and Acknowledgments.
Gems & Gemology, Vol. 58, No. 4, pp. 400–423,
http://dx.doi.org/10.5741/GEMS.58.4.400

Figure 1. A faceted heated ruby from Mogok, Myanmar, weighing more than 3 ct, stands out against a backdrop of untreated ruby rough from the same origin. The striking appearance of Mogok ruby is highly sought after. Photo by Wimon Manorotkul; faceted ruby courtesy of Kiarttichatra Intarungsee.

1200°C or above, it is not a reliable indicator of lower-temperature heat treatment. Thus, we wanted to determine whether other types of solid inclusions are more sensitive to heat at lower temperatures.

Mica and amphibole crystals, for example, are commonly seen in Mozambique ruby but do not always react to heat in the same way. Mica crystals have been reported to be the more sensitive of the two, frequently displaying visual alteration after treatment at low temperatures, while amphibole crystals are less likely to display damage when heated to the same temperatures (Pardieu et al., 2015).

In a previous era, coal miners learned to be cautious of the air quality while mining. Dangerous gases such as carbon monoxide could build up in a mine, causing illness or even death. To prevent this, miners began bringing canaries down into the mine. These birds are highly sensitive to poisonous gases, so if one died it was a signal to evacuate. From this came the expression "canary in a coal mine," referring to an early warning of potential trouble.

Our experiments aimed to detect something similar: an "early" warning at lower temperatures that could signal heat treatment in corundum. What crystal inclusions might act as the metaphorical canary in our ruby mine?

MATERIALS AND METHODS

Samples. A total of 46 samples from Mogok were selected for study. For this project, the authors did not analyze rubies from the Mong Hsu area, which is the second major ruby mining area in Myanmar (Peretti et al., 1995). While Mong Hsu also produces ruby of commercial importance, its appearance and internal features make it distinct from the Mogok material. Mong Hsu stones tend to have fewer crystal inclusions, making the Mogok material better suited for these experiments. Research on low-temperature heat treatment of Mong Hsu ruby would be a fascinating avenue for further study but was beyond the scope of this project.

Samples 1–44 were selected from a larger parcel of rubies reportedly from Myanmar that was purchased from a Burmese trader in Bangkok. Examination of the parcel showed that all had characteristics (inclusion scene, fluorescence, and trace element composition) consistent with those of untreated ruby from Mogok. The samples were chosen for their interesting solid inclusions as well as their color range from pink to red.

In addition, samples 45 and 46 were selected from GIA's reference collection. Both rubies were collected directly by GIA gemologists from mine rejects in the village of Baw-Lon-Gyi in Mogok. Sample 46 was chosen because it had areas free of inclusions that made it suitable for high-quality ultraviolet/visible/near-infrared (UV-Vis-NIR) spectroscopy. Samples 1–45 were polished into unoriented wafers measuring approximately 1.4–3.2 mm in thickness, with diameters ranging from 2.2 to 5.7 mm. Due to the nature of the rough ruby crystals, most of these wafers were oriented approximately perpendicular to the *c*-axis, resulting in a color dominated by the more purplish o-ray component. Sample 46 was polished into a wafer with surfaces oriented perpendicular to the *c*-axis with a tolerance of less than 2°, ideal for spectroscopy.

Of the 46 samples, 15 were chosen for heating experiments (samples 4, 8, 10, 11, 12, 17, 18, 22, 25, 30, 37, 39, 40, 45, and 46). These were selected to represent the diversity of mineral inclusions observed in ruby from Mogok. The 31 samples that were not heated were analyzed to identify and document their inclusions.

Photography and Photomicrography. Photos were taken with a Canon EOS 6D camera with a 65 mm lens mounted to a copy stand. The samples were placed on a light box illuminated by an XD-300 xenon white light source.

Samples were observed before and after each round of heat treatment using an Olympus SZX16 microscope with an SDF PLAPO 0.8× objective lens. Photomicrographs were taken with the same microscope, connected to a Canon EOS 6D camera using a Spot Imaging DE25TMT microscope adapter. Illumination was provided by a modified Motic darkfield base, supplemented by fiber-optic illuminators.

Raman Spectroscopy. To identify mineral inclusions, Raman spectra were obtained using a Renishaw inVia Raman system fitted with a 514 nm argon-ion laser attached to a Leica DM2700M microscope. Spectra were collected in the range of 200–1200 cm^{-1}. The grating was 1800 l/mm with a spectral resolution of 1 cm^{-1}. Exposure time was 10 s at 100% light power using a 6 mW laser. Accumulations were set at a minimum of three until the spectra's signal-to-noise ratio was greater than 10 and the major identifying peaks could be visually resolved from the background noise. Calibration was performed using the 520.5 cm^{-1} line of a silicon wafer. In all cases, entries from the RRUFF database (Lafuente et al., 2015) were used as references when identifying inclusions. Spectral comparisons were performed with Renishaw Wire (version 3.4) software. This analysis was conducted on most solid crystals and repeated on selected crystals after each heating step. All spectra were collected at room temperature.

UV-Vis-NIR Spectroscopy. For samples 4, 8, 10, 11, 12, 17, 18, 22, 25, 30, 37, 39, and 40, UV-Vis-NIR spectroscopy was conducted with a Magilabs GemmoSphere UV-Vis-NIR spectrometer before and after each stage of heating. The wavelength range was 365–1000 nm, with a resolution of 1.3 nm and an integration time of 40 ms.

With samples 45 and 46, UV-Vis-NIR spectra were collected with a Hitachi U-2910 spectrophotometer using a wavelength resolution of 1.5 nm. The spectra obtained were corrected by calculating the reflection loss from the refractive index data, and the data was converted to show their absorption coefficients (α, cm^{-1}) using $\alpha = 2.303A/d$, where A is absorbance and d is the path length in centimeters. The ruby samples were mounted in wax-coated aluminum plates with a 1 mm hole to ensure consistent measurements throughout the experiment.

Infrared Spectroscopy. Fourier-transform infrared (FTIR) spectroscopy was performed using a Bruker Tensor 27 spectrometer before and after each stage of heating on the 15 heated samples. Each specimen was placed on a Pike DRIFTS attachment and scanned 16 times at a resolution of 4 cm^{-1}.

Trace Element Analysis. Trace element chemical analyses were performed on all samples using laser ablation–inductively coupled plasma–mass spectrometry (LA-ICP-MS) technology with a Thermo Fisher Scientific iCAP Q ICP-MS coupled with a Q-switched Nd:YAG laser ablation device (Electro Scientific Industries Inc. New Wave NWR213) operating at a wavelength of 213 nm. The laser ablated spots were 55 µm in diameter, created using a laser fluence of approximately 10 J/cm^2 with a repetition rate of 10 Hz and a dwell time of 40 s. The forward power was set at 1350 W, and the typical nebulizer gas flow was at approximately 0.80 L/min. A special set of corundum reference standards was used for quantitative analysis of beryllium, magnesium, titanium, vanadium, chromium, iron, and gallium (Stone-Sundberg et al., 2017, 2021), whereas NIST Standard Reference Materials 610 and 612 glasses were used for other elements. All elemental measurements were normalized on aluminum as the internal elemental standard.

Ultraviolet (UV) Fluorescence Imaging. The 15 heated samples were observed in both long-wave and short-wave UV radiation using two different methods. One method was with a standard UV light box. We used an Ultraviolet Products UVLS-26 EL Series UV lamp using a 6-watt bulb, with a long-wave light source at 365 nm and a short-wave light source at 254 nm. We also placed each specimen in a Magilabs custom-designed deep-UV fluorescence system, consisting of a fluorescence microscope equipped with a

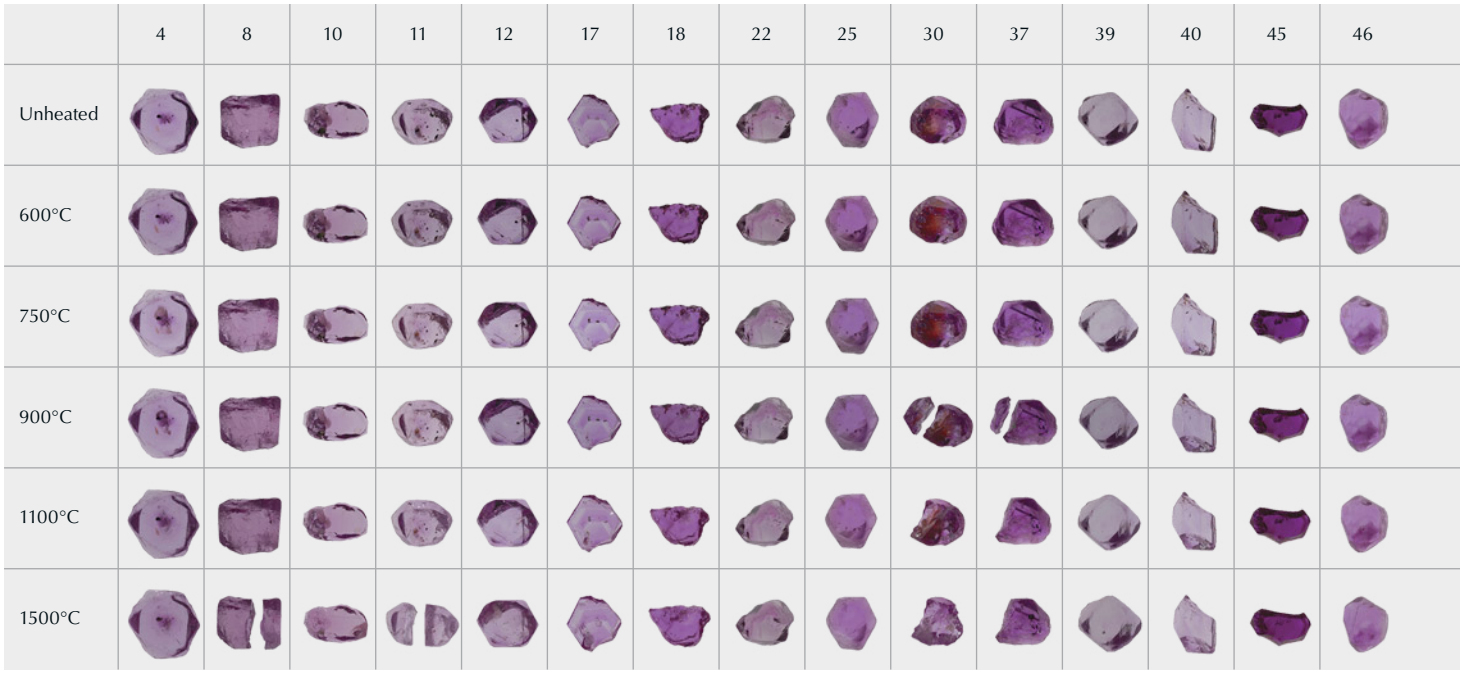

Figure 2. The 15 ruby samples from the experiments, before heat treatment and after each stage of heating. While the overall bodycolors did not show significant changes, there were changes to clarity as the inclusions altered. Sample 30 in particular showed a dramatic change in color due to the alteration of iron staining in a large fissure. Four samples (8, 11, 30, and 37) broke apart during heat treatment. We continued to heat the larger of the two pieces in subsequent rounds. Photos by Sora-at Manorotkul.

high-intensity pulsed xenon flash lamp with an interference bandpass filter at 228 nm.

Fluorescence photography was taken with the samples placed in the Magilabs system attached to a Wild M400 Photomakroskop with an attached Canon EOS 6D camera. For long-wave images, we used an external Convoy S2+ 4-watt UV flashlight. For short-wave images, we used the built-in illumination from the Magilabs system at 228 nm.

HEATING EXPERIMENT

Sample Selection. As previously mentioned, 15 of the 46 samples examined were selected for heat treatment experiments. Thirteen of the samples (numbers 4, 8, 10, 11, 12, 17, 18, 22, 25, 30, 37, 39, and 40) were chosen for their diverse inclusion scenes featuring a wide variety of solid inclusions. Two additional samples (numbers 45 and 46) were selected with a focus on spectroscopy. These had areas that were free of inclusions. Sample 45 was on the lighter end of the color range and 46 on the darker end, giving us examples of how different shades might react to heat treatment.

Heat Treatment. For the first four rounds of heat treatment, the 15 samples chosen were placed on a piece of synthetic corundum felt and heated in a Vulcan 3-550 oven in air, which is an oxidizing atmosphere. They were heated to 600°, 750°, 900°, and 1100°C and kept at their maximum temperature for four hours. After each heating round, the samples were cooled down to room temperature and data was collected on each sample.

The specimens were also heated for a final round by John Emmett (Crystal Chemistry, Brush Prairie, Washington) and Eric Braunwart (Columbia Gem House, Vancouver, Washington). Treatment conditions were 1500°C in a flowing oxygen atmosphere for five hours in a Thermal Technology Inc. 3060 furnace. This round took the stones into the realm of high-temperature heat treatment.

RESULTS AND DISCUSSION

Appearance. All 15 heated ruby samples were examined and photographed before and after heat treatment under controlled lighting conditions. Across the various rounds of heating, the 15 selected samples did not display significant alteration in bodycolor, but we did notice many inclusion changes. One of the most notable was to sample 30, which contained a large fissure with orange iron staining.

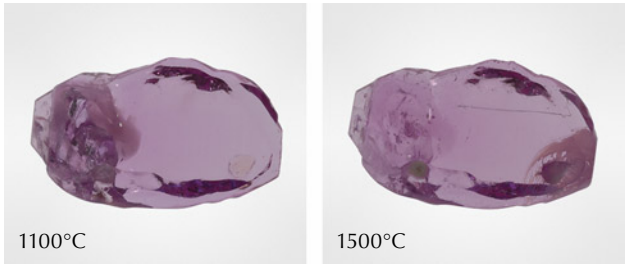

Figure 3. When heated to 1500°C, a cluster of inclusions on the left side of sample 10 became less obvious. On the right side, the alteration of a sphene crystal created clarity issues. Photos by Sora-at Manorotkul.

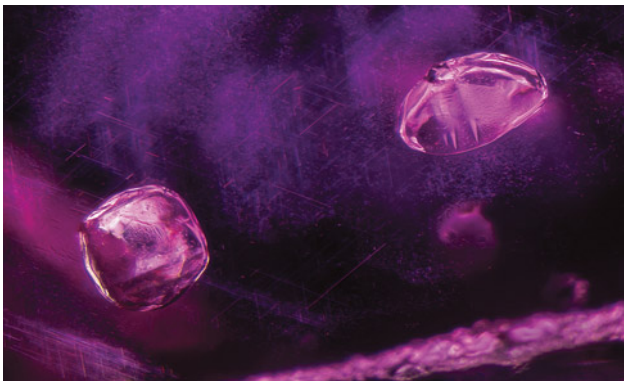

Figure 5. In sample 6, a pair of calcite crystals stands out above a cloud of undissolved rutile silk needles. Note the twinning planes in both crystals, a common feature for calcite. Photomicrograph by E. Billie Hughes; field of view 2 mm.

After the first round of heating, the stain deepened in color; this change was eye visible (see figure 2).

Another dramatic change was that some rubies broke apart during heat treatment. Samples 30 and 37 split after heating to 900°C, while samples 8 and 11 split after heating to 1500°C. Following this 1500°C heating round, another small corner of sample 30 broke off, but we were unable to recover the fragment. For the rubies that broke apart, we continued to heat the larger of the two pieces.

In many cases, the treatment affected clarity. Figure 3 compares sample 10 after heating to 1100°C and 1500°C. The left side of the specimen shows a darker fissure beginning to heal as well as a cloud of rutile silk that is less visible, improving the clarity of that side of the stone. But on the right side, a sphene crystal melted and lowered the clarity in that section.

In Brief

- Microscopic observation of inclusions in Mogok ruby can provide evidence of low-temperature heat treatment. The appearance of calcite, mica, spinel, and zircon crystals can be particularly useful.
- Raman analysis of calcite and spinel inclusions can provide strong evidence of heat treatment, even at lower temperatures.
- Chalky short-wave UV fluorescence reactions provide strong evidence of higher-temperature heat treatment.

INTERNAL FEATURES

Solid Inclusions. A variety of mineral inclusions were identified in the 46 samples using Raman spectroscopy. The most common solid mineral inclusion observed was calcite (figures 4–5). Mica (figure 6), zircon (figure 7), and spinel (figure 8) were also frequently observed. Rutile and sphene (titanite) were occasionally seen. Apatite, CO_2-rich fluid inclusions,

Figure 4. A: In sample 5, transmitted light reveals a variety of transparent rounded crystals of relatively high relief compared to the surrounding corundum. They appear to be nearly colorless. B: The same crystals in darkfield illumination. C: Between crossed polarizers, the same crystals display interference colors, suggesting that they are doubly refractive. Micro-Raman analysis identified these as calcite. Photomicrographs by E. Billie Hughes; field of view 2 mm.

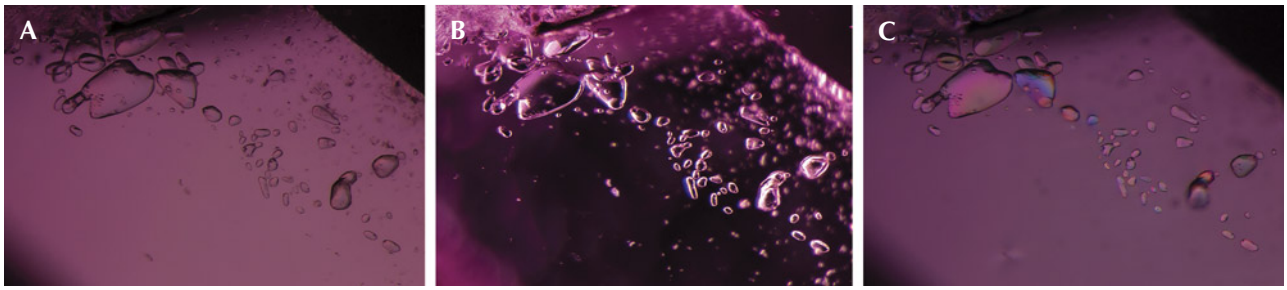

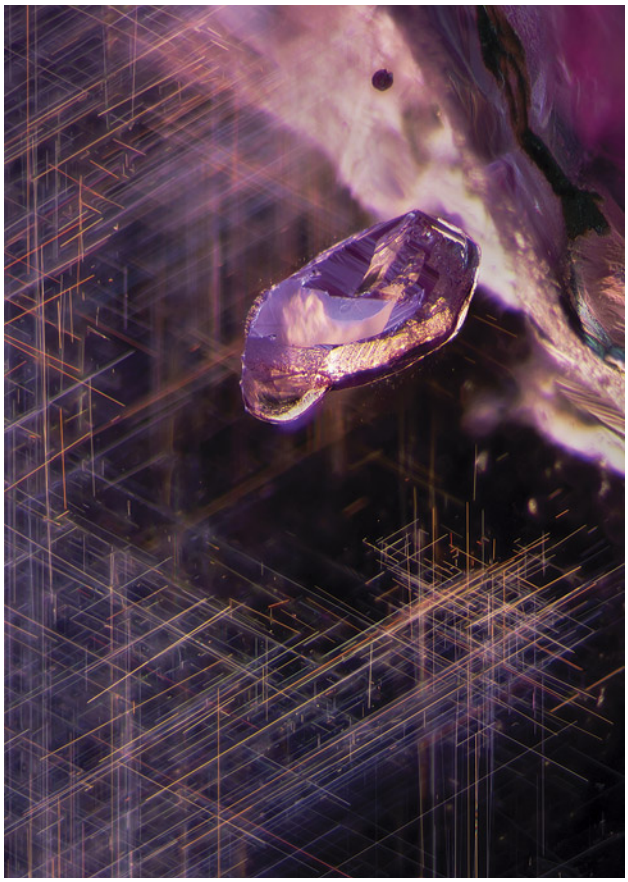

Figure 6. A mica crystal in sample 28, surrounded by a cloud of undissolved rutile silk. While this type of silk is a hallmark of untreated Burmese ruby, it can also be seen in stones heated at relatively low temperatures. Photomicrograph by E. Billie Hughes; field of view 3 mm.

diaspore, feldspar, garnet, iron sulfide, and scapolite were detected infrequently in our ruby samples.

Inclusion Documentation. Each specimen was examined and photographed in the microscope before and after every stage of treatment. The changes to solid inclusions tended to follow a pattern as the samples were heated to increasing temperatures. Notable changes included the following:

1. *Alterations to fissure stains:* Epigenetic iron staining in fissures in corundum is known to be impacted by heating to temperatures as low as 350°C (Koivula, 2013). In our experiments, the staining stood out in one ruby in particular: sample 30. Even after our first round at 600°C, this staining displayed a dramatic change in appearance, becoming a brighter, deeper reddish orange. This is visible in the background of figure 9.
2. *Formation and subsequent healing of fissures:* One of the first changes noted was that shiny, smooth fissures began to develop around some solid minerals, often at temperatures as low as 600°–750°C. When heated to temperatures of 900°C and higher, these fissures tended to heal, often starting at the outside edges (figures 10–12). This healing often took the form of elongated channels. As the samples were heated further, these channels "necked down" and separated into shorter, more bubble-like shapes (Roedder, 1984). These partially healed

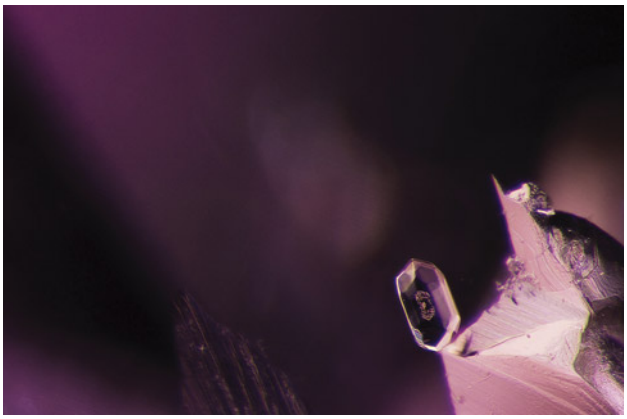

Figure 7. A zircon crystal in an untreated Burmese ruby, sample 41. Zircon was a frequent inclusion in the Burmese ruby samples. Photomicrograph by E. Billie Hughes; field of view 2 mm.

Figure 8. Spinel crystals, such as this one in sample 15, were seen frequently in the Burmese ruby samples. Photomicrograph by E. Billie Hughes; field of view 3 mm.

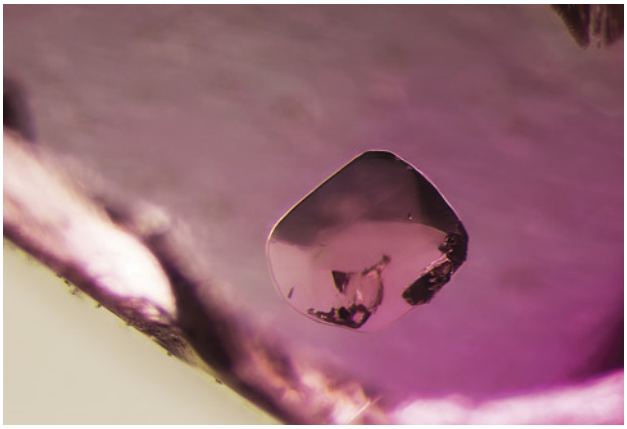

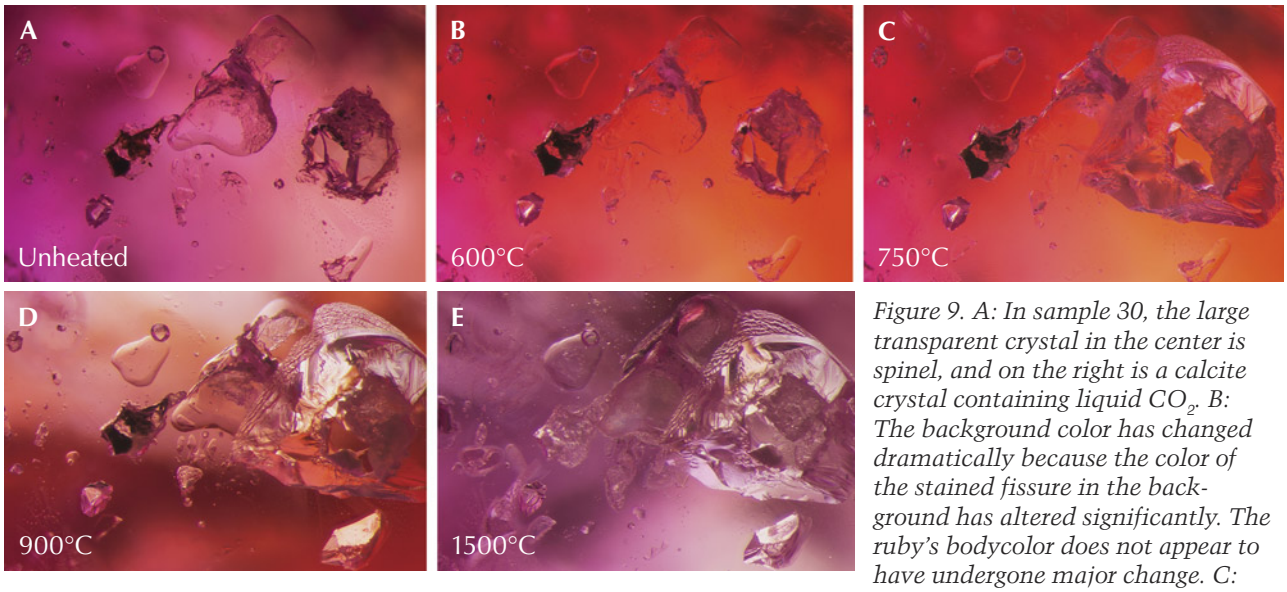

Figure 9. A: In sample 30, the large transparent crystal in the center is spinel, and on the right is a calcite crystal containing liquid CO_2. B: The background color has changed dramatically because the color of the stained fissure in the background has altered significantly. The ruby's bodycolor does not appear to have undergone major change. C: The crystal to the right has exploded, leaving a small surface-reaching hole. On the top left, a glassy discoid can be seen around a small crystal. D: The staining in the background has again changed color. E: Much alteration is visible, with partially healed fissures in several spots. Photomicrographs by E. Billie Hughes; field of view 2 mm.

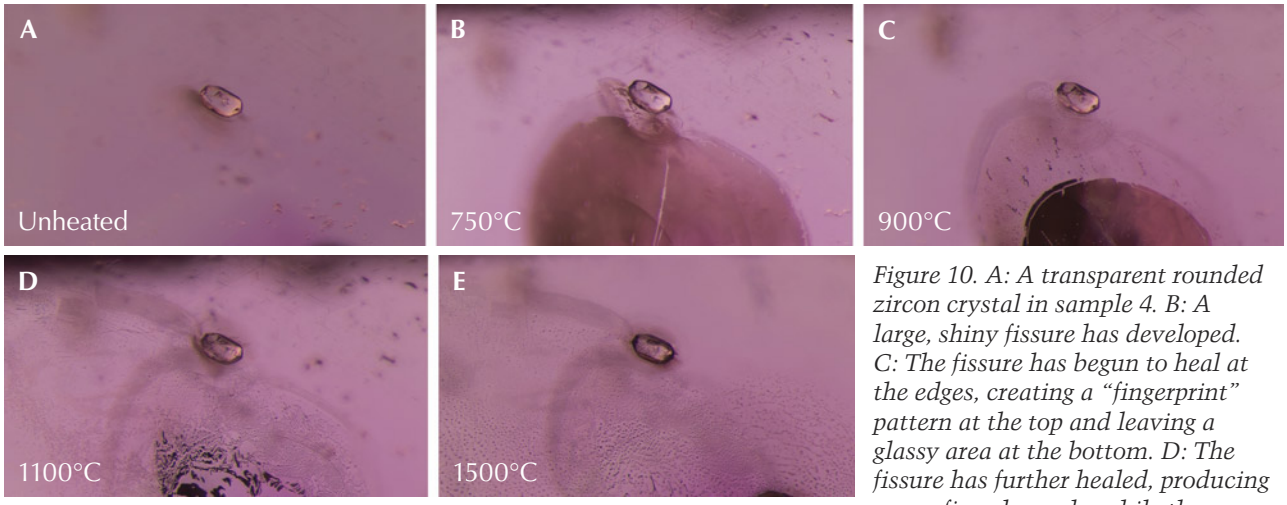

Figure 10. A: A transparent rounded zircon crystal in sample 4. B: A large, shiny fissure has developed. C: The fissure has begun to heal at the edges, creating a "fingerprint" pattern at the top and leaving a glassy area at the bottom. D: The fissure has further healed, producing many fine channels, while the glassy area has largely disappeared; the texture of the surface of the zircon crystal itself has also altered and become less smooth. E: The fingerprint has expanded, and many of the elongated channels have "necked down" to form smaller bubble-like features. Photomicrographs by E. Billie Hughes; field of view 1.5 mm.

fissures form what gemologists often refer to as "fingerprints."

3. *Alterations in the appearance of solid mineral inclusions:* The solid inclusions themselves also tended to follow a pattern in response to increasing temperatures. In addition to developing fissures, many crystals began to display changes in opacity and texture as they were heated to progressively higher temperatures. Their tendency was to become less transparent, often developing a white interior. In many cases they also developed a more textured exterior, sometimes becoming so "frosted" that they appeared opaque. The mica crystals in sample 40 showed some of the most dramatic changes in texture (see figure 13). Heating to 900°C caused linear features to become much less visible. After heating to 1500°C, the crystal was barely recognizable, with a frosty appearance resembling a fresh dusting of snow.

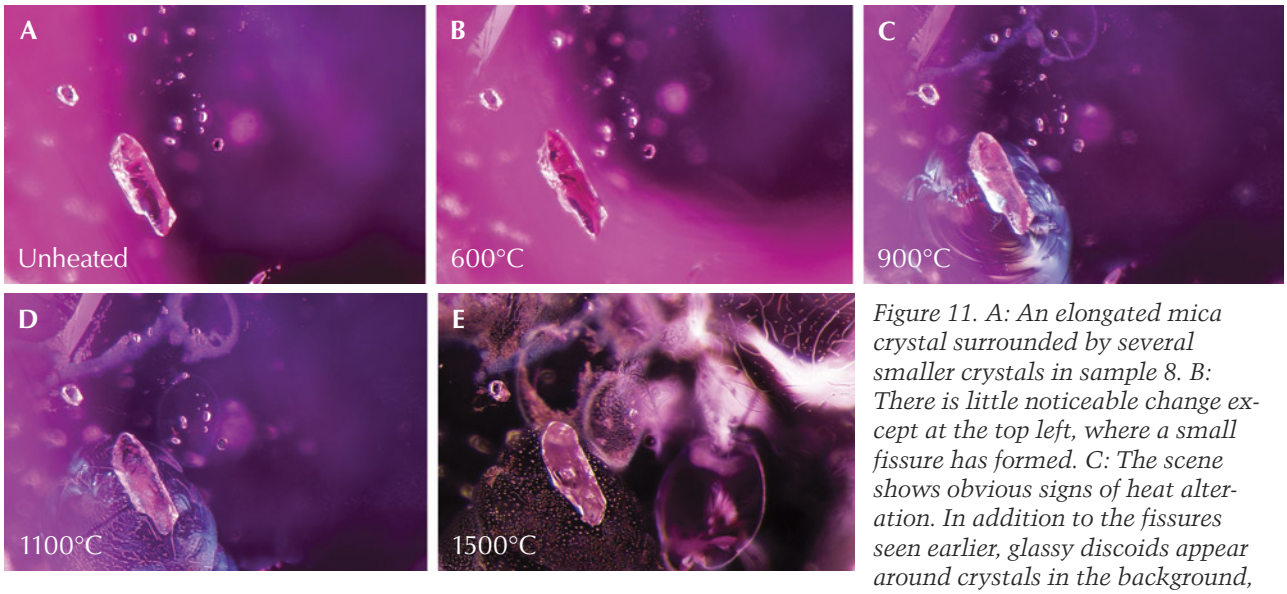

Figure 11. A: An elongated mica crystal surrounded by several smaller crystals in sample 8. B: There is little noticeable change except at the top left, where a small fissure has formed. C: The scene shows obvious signs of heat alteration. In addition to the fissures seen earlier, glassy discoids appear around crystals in the background, and a shiny fissure is conspicuous around the biotite crystal in the foreground. D: Some fissures have begun to heal; the glassy fissure around the biotite crystal has developed elongated channels, and the partially healed edges of the glassy discoid at the top of the frame have started to neck down and become wider. E: The scene has changed dramatically; glassy discoids and partially healed fissures with a melted appearance are visible across the field of view, and the biotite crystal has developed an immobile gas bubble in its center. Images A and B were captured with darkfield illumination; diffused fiber-optic illumination has been added in C–E to reveal the fissures more clearly. Photomicrographs by E. Billie Hughes; field of view 1.5 mm.

One of the calcite crystals shown in figure 14 went from transparent to displaying a translucent white filling after it was heated to 750°C. Following the next round at 900°C, the white area expanded to

Figure 12. A: A calcite crystal from sample 40, shown in its untreated state. B: A glassy fissure has developed around the crystal. C: The edges of the fissure have begun to heal and assume a cloudy appearance. D: Further healing in the fissure. E: Almost all of the glassy areas have disappeared as the fissure has healed. Meanwhile, the calcite crystal has become more opaque. F: Darkfield illumination shows detailed channels in the fingerprint around the calcite, which is becoming whiter and more opaque. Photomicrographs by E. Billie Hughes; field of view 2.2 mm.

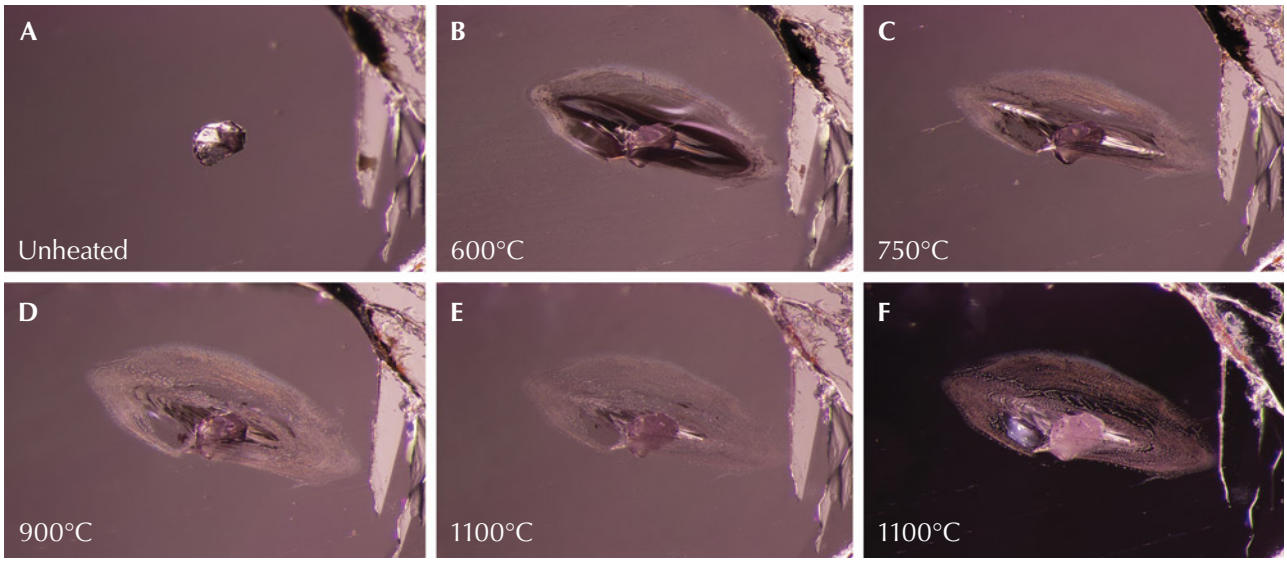

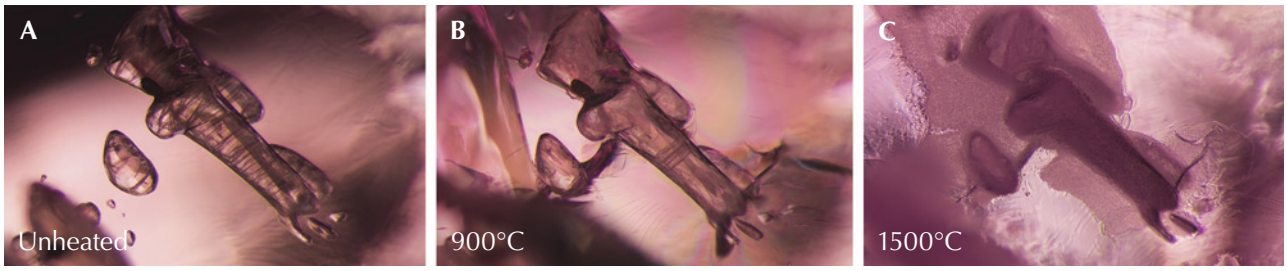

Figure 13. A: These mica crystals in sample 40 show a series of striations. B: Fissures have developed around the mica crystals, and the striations have become much less prominent. C: Significant changes are observed, with the entire area on and around the crystals assuming a frosty white appearance. Photomicrographs by E. Billie Hughes; field of view 3 mm.

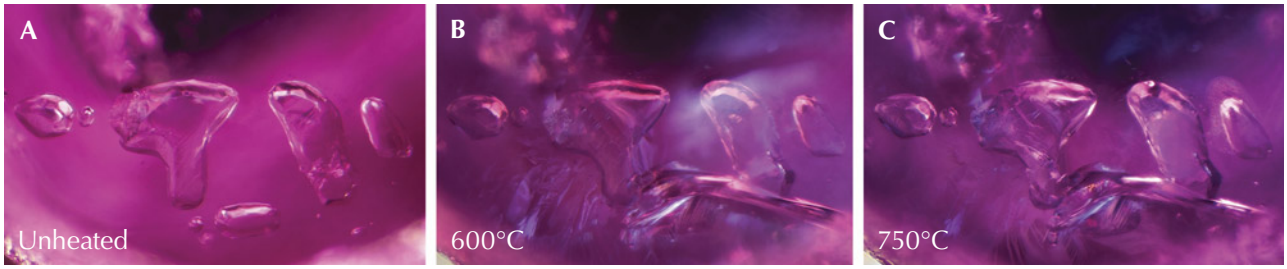

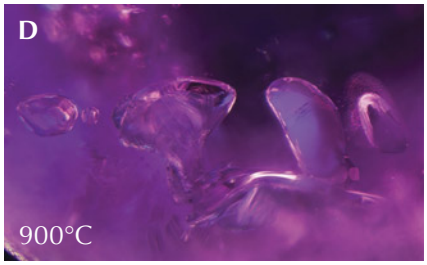

Figure 14. A: A group of transparent calcite crystals in sample 8. B: A large glassy fissure has formed around the cluster. C: The crystal second from the right has changed in texture and become slightly opaque; the one on the far right has also developed a fissure that has begun to heal. D: Note the significant changes to the crystal second from the right, which has taken on a whitish appearance and become opaque. Photomicrographs by E. Billie Hughes; field of view 2 mm.

the point where the whole crystal was opaque. These observations were not limited to calcite inclusions but were seen across a variety of solid inclusions. Similar patterns were noted with mica (figure 15), spinel (figures 16 and 17), sphene (figure 18), iron sulfide (figure 19), diaspore (figure 20), primary rutile (figure 21), scapolite (figure 22), feldspar (figure 23), and apatite (figures 24–26).

Solid Inclusions Most Sensitive to Heat. Some of the solid inclusions stood out as particularly sensitive to heat at lower temperatures. In certain samples, some calcite crystals began to show a reaction even after the first round of heating to 600°C. This can be seen in sample 8 (figure 14) and sample 40 (figure 12). Zircon (figure 10), mica (figures 11, 13, and 15), and spinel (figures 16 and 17) crystals began to display changes after heating to 750°C.

Fortunately for gemologists, these highly sensitive solid inclusions were also the most common inclusions in the rubies studied, providing a useful visual aid when trying to detect low-temperature heat treatment.

Scapolite, which we found in fewer samples, also began to show changes at the slightly higher temperature of 900°C (see figure 22). This makes it another helpful sign of heat, but one that we expect to see less frequently.

Solid Inclusions Less Sensitive to Heat. Other solid inclusions had to be heated to higher temperatures before they displayed clear visual changes. Crystals of sphene (figure 18), primary rutile (figures 20 and 21), and feldspar (figure 23) in our specimens did not show changes until they were heated to 1100°C. Some apatite crystals also began to display alteration at this temperature, but one apatite in sample 46 did not display clear changes until the last round of heating to 1500°C (figure 26).

Impact on Rutile Silk. One of the hallmarks of ruby from Mogok is the presence of rutile silk, often in

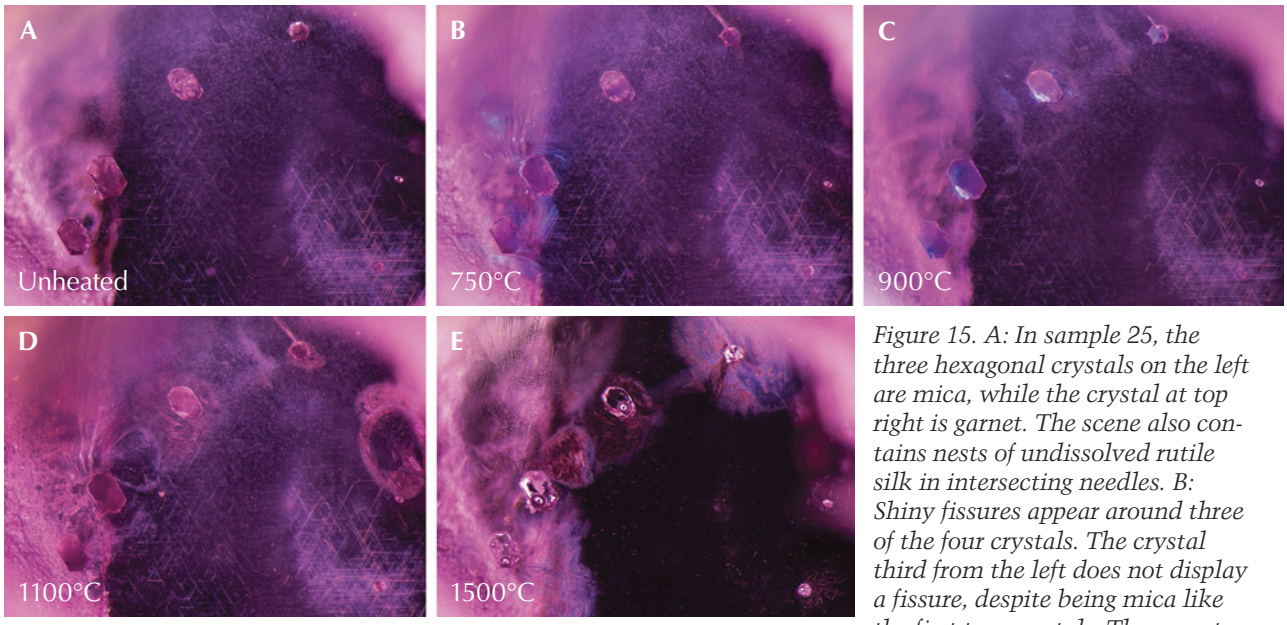

Figure 15. A: In sample 25, the three hexagonal crystals on the left are mica, while the crystal at top right is garnet. The scene also contains nests of undissolved rutile silk in intersecting needles. B: Shiny fissures appear around three of the four crystals. The crystal third from the left does not display a fissure, despite being mica like the first two crystals. The garnet does display a fissure, however. C: All four crystals have altered, and the fissures have begun to heal at the edges. D: More changes can be noted as existing fissures have expanded and healed further. New fingerprints have developed to the right of the garnet crystal. Through four rounds of heat, the rutile silk in the background remains unaltered. E: Fissures now show significant alteration, with cloudy areas and drippy channels. The three mica crystals on the left have become more transparent and contain several immobile gas bubbles. In the background, the rutile silk needles have altered significantly, partially dissolving into shorter, broken needles and dotted particles. The previously "silky" area appears more transparent. Photomicrographs by E. Billie Hughes; field of view 3 mm.

dense nests of unbroken needles (see figure 6). In fact, the point at which rutile silk begins to dissolve is often cited as the boundary between "low-temperature" and "high-temperature" heat. Rutile generally begins to dissolve at around 1200°–1350°C (Hughes et al., 2017).

This was supported by the results of the experiment. In all the samples we heated, the rutile silk showed no noticeable change after heating up to 1100°C. Even as other features began to change, the rutile silk needles remained intact. After heating to 1500°C, the rutile silk dissolved from needles into small dotted particles. In some instances, it dissolved to such an extent that it was no longer visible. This dissolution is particularly clear in figure 15, where the silk that was still intact across the stone at 1100°C has largely dissolved after heating to 1500°C, leaving behind just a few short dotted needles and particles.

Figure 16. A: This transparent spinel crystal in sample 39 retains the same appearance through subsequent rounds of heating to 600°, 750°, and 900°C. B: The spinel crystal has begun to change in appearance and started to develop elongated lines. C: The crystal has taken on a frosty, whitish appearance. Photomicrographs by E. Billie Hughes; field of view 1.5 mm.

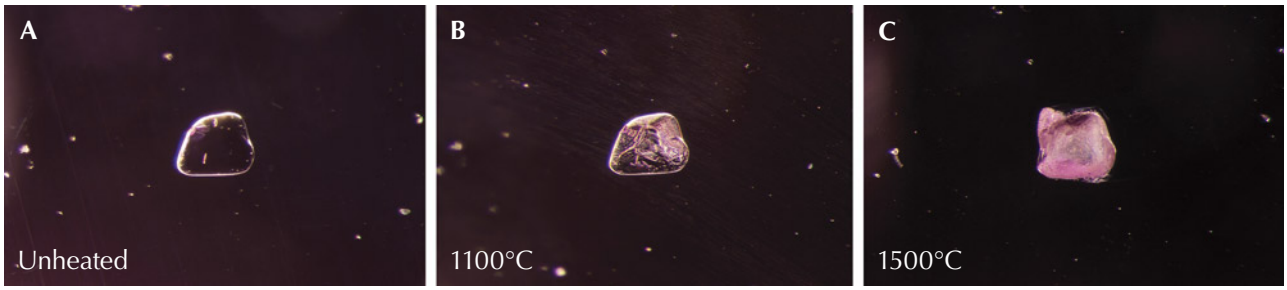

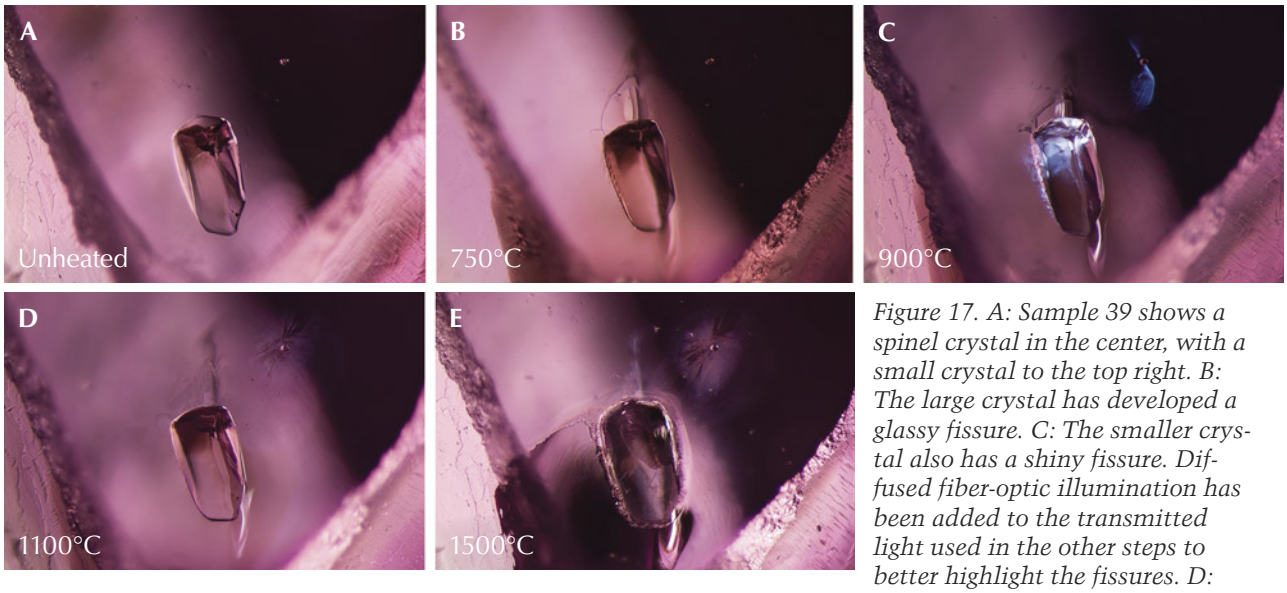

Figure 17. A: Sample 39 shows a spinel crystal in the center, with a small crystal to the top right. B: The large crystal has developed a glassy fissure. C: The smaller crystal also has a shiny fissure. Diffused fiber-optic illumination has been added to the transmitted light used in the other steps to better highlight the fissures. D: The fissures begin to heal, creating fingerprints around the crystals. E: The fissures have expanded and appear cloudier. The larger crystal's surface has altered, while the smaller crystal displays a more rounded, bubble-like appearance. Photomicrographs by E. Billie Hughes; field of view 3 mm.

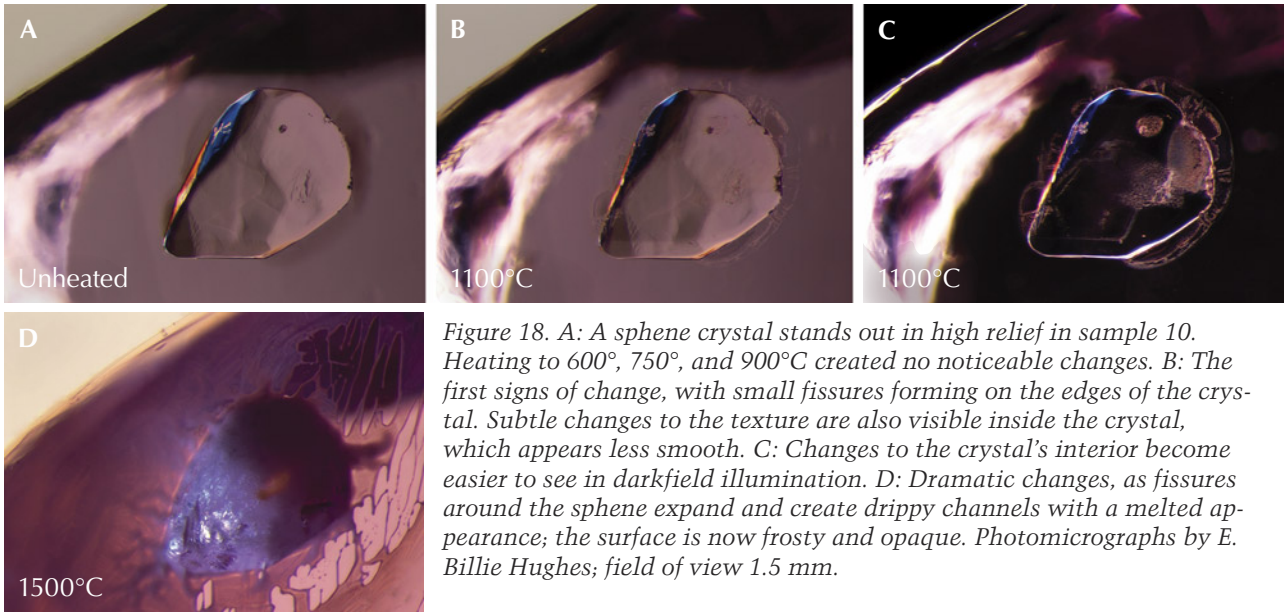

Figure 18. A: A sphene crystal stands out in high relief in sample 10. Heating to 600°, 750°, and 900°C created no noticeable changes. B: The first signs of change, with small fissures forming on the edges of the crystal. Subtle changes to the texture are also visible inside the crystal, which appears less smooth. C: Changes to the crystal's interior become easier to see in darkfield illumination. D: Dramatic changes, as fissures around the sphene expand and create drippy channels with a melted appearance; the surface is now frosty and opaque. Photomicrographs by E. Billie Hughes; field of view 1.5 mm.

Immobile Bubbles. Another notable change to solid inclusions was the development of immobile bubbles, which only appeared after heating to 1500°C. These features are particularly clear in the mica crystals in figures 11 and 15 and the scapolite in figure 22.

When these inclusions reach higher temperatures, they start to break down. Hydrous minerals and carbonates will release volatiles such as water and carbon dioxide when they break down into other minerals. This results in the separating of a vapor phase and a remaining solid phase. In the case of cal-

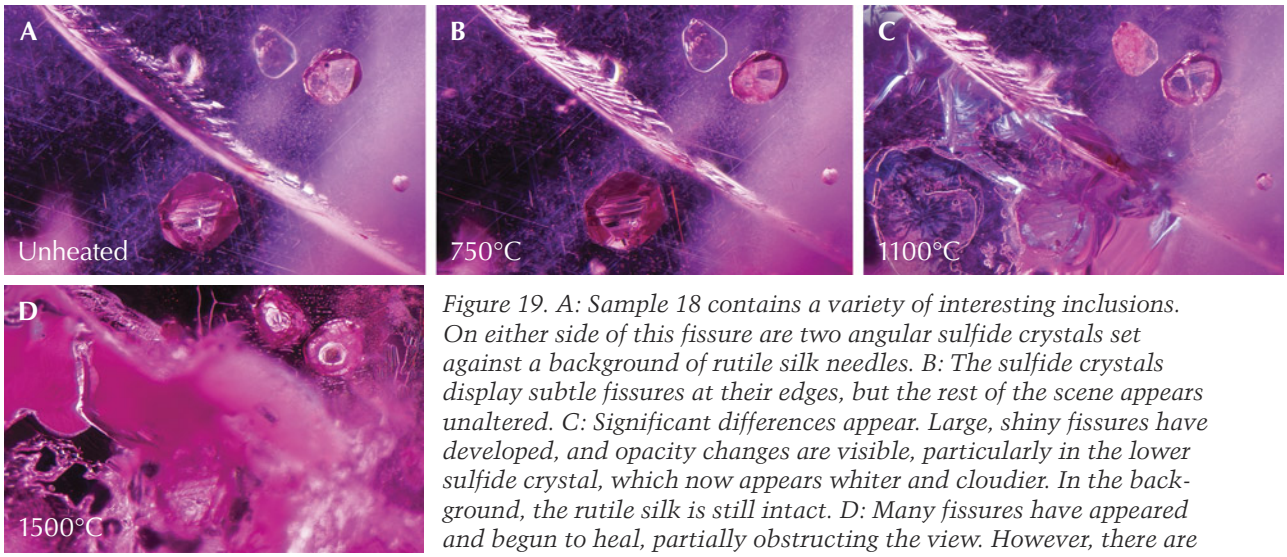

Figure 19. A: Sample 18 contains a variety of interesting inclusions. On either side of this fissure are two angular sulfide crystals set against a background of rutile silk needles. B: The sulfide crystals display subtle fissures at their edges, but the rest of the scene appears unaltered. C: Significant differences appear. Large, shiny fissures have developed, and opacity changes are visible, particularly in the lower sulfide crystal, which now appears whiter and cloudier. In the background, the rutile silk is still intact. D: Many fissures have appeared and begun to heal, partially obstructing the view. However, there are notable changes. The sulfide crystal at the top right has developed an immobile gas bubble. In the background, the rutile silk needles have dissolved. Photomicrographs by E. Billie Hughes; field of view 2 mm.

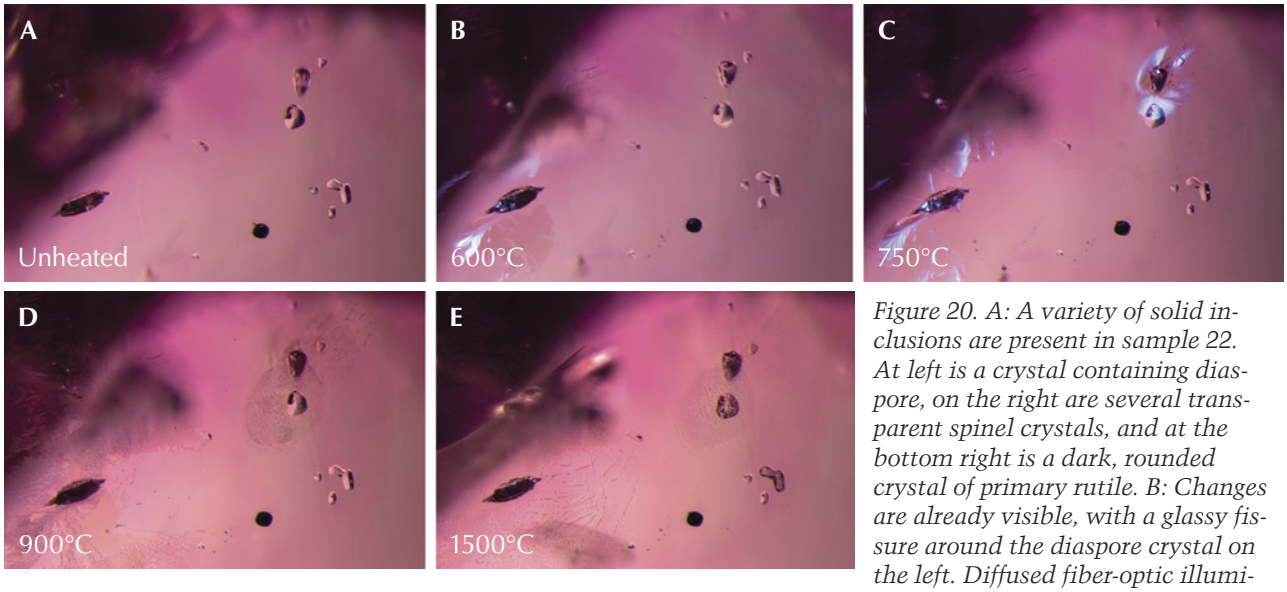

Figure 20. A: A variety of solid inclusions are present in sample 22. At left is a crystal containing diaspore, on the right are several transparent spinel crystals, and at the bottom right is a dark, rounded crystal of primary rutile. B: Changes are already visible, with a glassy fissure around the diaspore crystal on the left. Diffused fiber-optic illumination has been added to the transmitted light used for the other images in this set to accentuate the fissure. C: A fissure has also developed around the top of the spinel crystal. Again, diffused fiber-optic illumination has been added. D: The fissures that developed in previous stages have begun to heal and form fingerprints. E: These fissures heal further and melted-looking channels appear. Photomicrographs by E. Billie Hughes; field of view 2 mm.

cite, the breakdown product consists of the mineral lime (CaO) and the gas carbon dioxide. Depending on the complexity of the mineral, the solid phase after breakdown can consist of various components, or it might start to melt (congruently or incongruently) at higher temperatures. Upon quenching, these phases do not have time to crystallize as a single entity. The newly formed phases are preserved, with the solids in a glassy state. Since this glassy material occupies less volume than the previous crystal, the result is

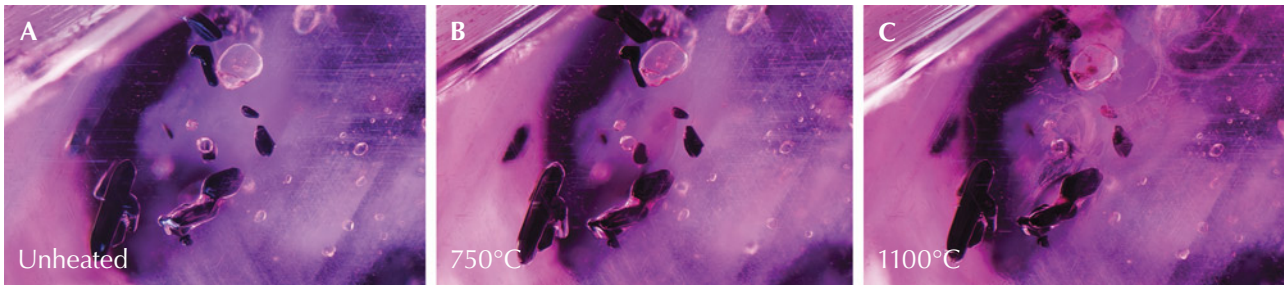

Figure 21. A: Sample 37 shows dark crystals of primary rutile, along with clouds of exsolved rutile silk. B: Small fissures have begun to form around some of the primary rutile crystals. C: The fissures have expanded and begun to heal, though the primary rutile crystals appear unaltered and the rutile silk needles in the background are intact. Photomicrographs by E. Billie Hughes; field of view 2 mm.

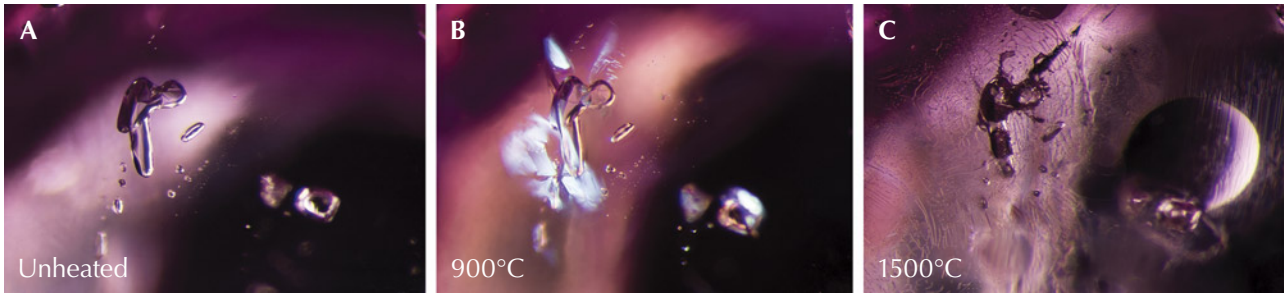

Figure 22. A: This scapolite crystal in sample 12 displays a distinctive shape, similar to a lowercase "r." B: The scapolite begins showing signs of alteration. Diffused fiber-optic illumination was added to the darkfield illumination used for the previous image to highlight the shiny fissures that developed around the scapolite. C: Major changes are evident, as many fissures have formed and then healed with elongated channels that have a drippy appearance. The scapolite crystal has developed opaque areas and immobile gas bubbles. Photomicrographs by E. Billie Hughes; field of view 2 mm.

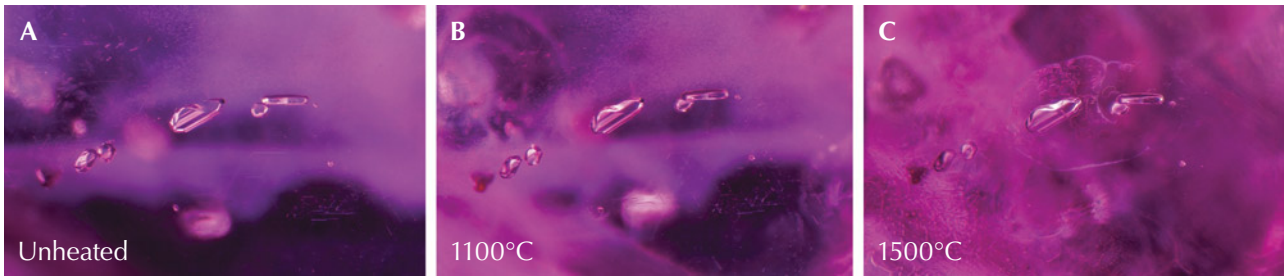

Figure 23. A: A cluster of feldspar crystals in sample 37 that show no alteration through several rounds of heating. B: The feldspar crystals are intact and appear unaffected by heat. However, discoid fissures appear in the background at the top left and bottom right. C: Many more fissures have developed, including some around the feldspar crystals in the center. Photomicrographs by E. Billie Hughes; field of view 1.7 mm.

an inclusion with a combination of solids (crystalline or glassy) and a vapor phase, seen as an immobile bubble (Roedder, 1984).

Raman Spectroscopy and Heat Treatment. Raman spectroscopy detects a shift in phonons of scattered light when it interacts with a material (the "Raman shift"); this shift is characteristic for each mineral. Every peak in the spectrum corresponds to a specific vibration between molecules within the mineral. While each mineral has a characteristic spectrum defined by its crystal structure, many other variables can influence the vibrations and thus the final spectrum.

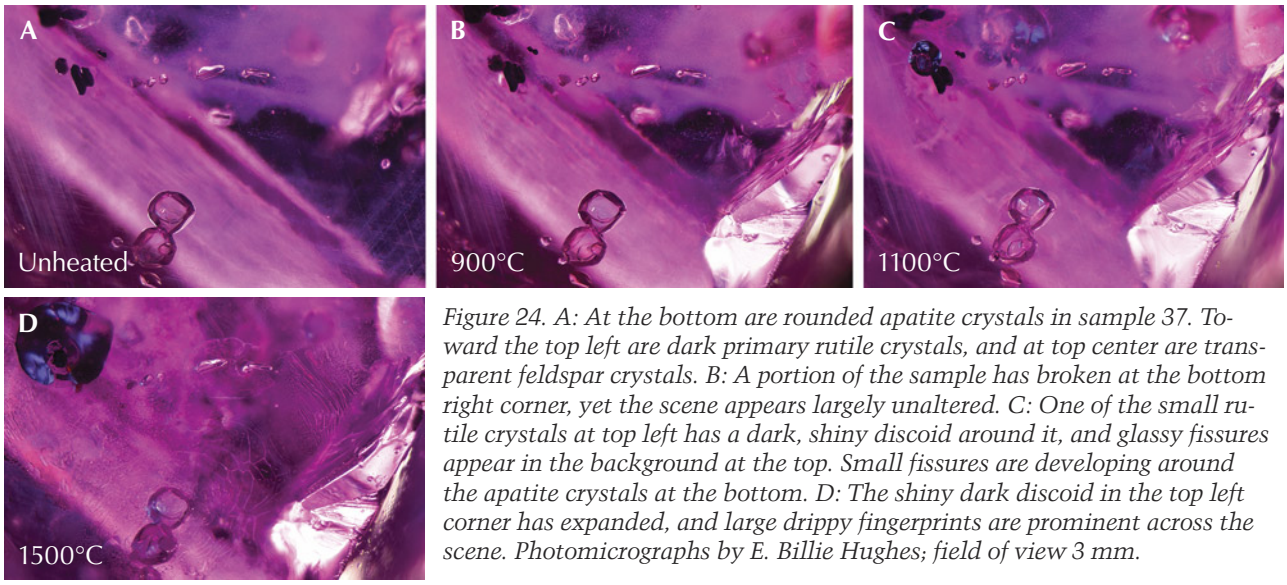

Figure 24. A: At the bottom are rounded apatite crystals in sample 37. Toward the top left are dark primary rutile crystals, and at top center are transparent feldspar crystals. B: A portion of the sample has broken at the bottom right corner, yet the scene appears largely unaltered. C: One of the small rutile crystals at top left has a dark, shiny discoid around it, and glassy fissures appear in the background at the top. Small fissures are developing around the apatite crystals at the bottom. D: The shiny dark discoid in the top left corner has expanded, and large drippy fingerprints are prominent across the scene. Photomicrographs by E. Billie Hughes; field of view 3 mm.

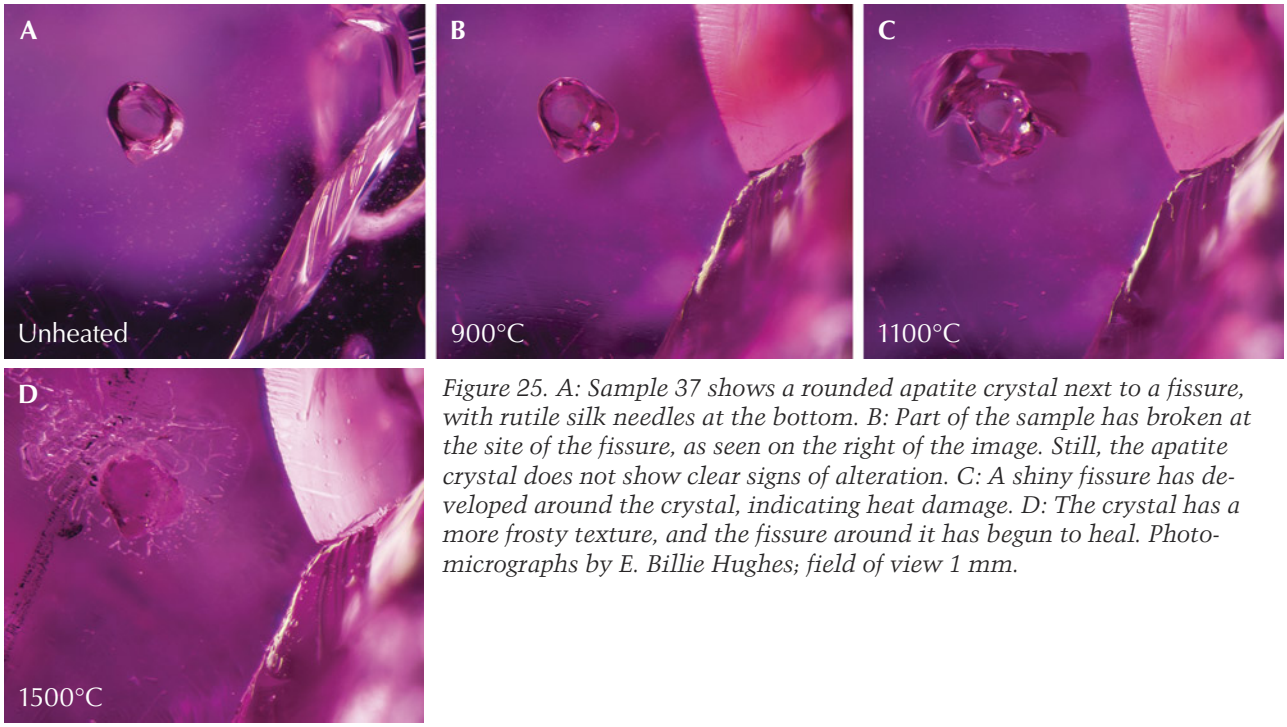

Figure 25. A: Sample 37 shows a rounded apatite crystal next to a fissure, with rutile silk needles at the bottom. B: Part of the sample has broken at the site of the fissure, as seen on the right of the image. Still, the apatite crystal does not show clear signs of alteration. C: A shiny fissure has developed around the crystal, indicating heat damage. D: The crystal has a more frosty texture, and the fissure around it has begun to heal. Photomicrographs by E. Billie Hughes; field of view 1 mm.

Variations in the crystal structure can cause subtle shifts in the spectrum. This includes substitution of certain elements, lattice damage due to radioactivity, and compressed structures due to pressure.

The exact position of the peaks is variable and determined by the conditions under which the analysis is done, as well as the exact composition of the mineral (Gillet et al., 1993). We believe that while the mineral is at room temperature, the pressure on the inclusion is significantly higher since it is still completely encased in its ruby host. This means that the pressure in the inclusion is the same as when it was trapped by the growing ruby deep in the earth.

Another challenge faced in this study comes from the nature of the host material. While confocal Raman spectroscopy allows one to focus on a specific point within the gem, the laser light still has to travel through the corundum host. Ruby absorbs much of the 514 nm wavelength and emits

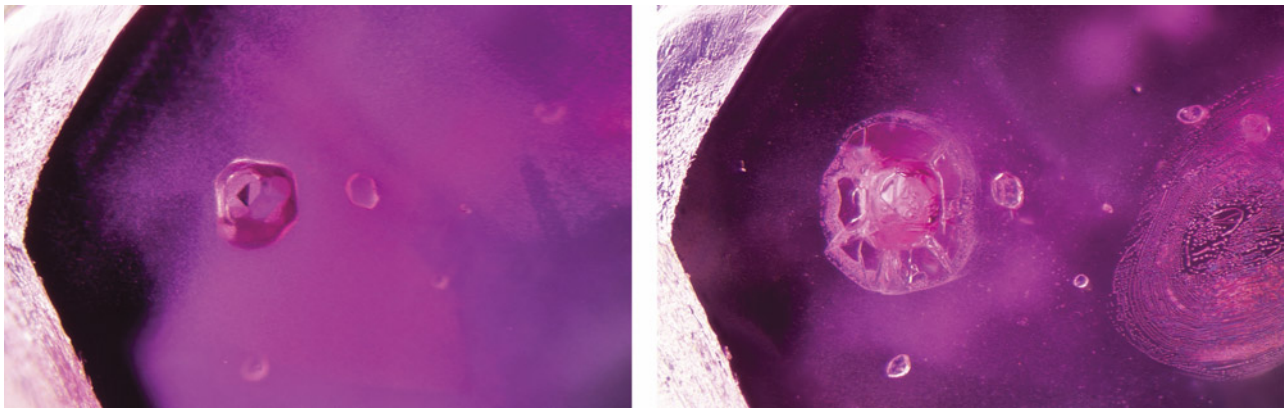

Figure 26. Left: Sample 46 contains a rounded apatite crystal (the larger crystal on the left with the dark triangle) and a small transparent zircon crystal immediately to its right. Remarkably, the apatite crystal remains unchanged until the last round of heating. Right: After heating to 1500°C, the apatite crystal has developed a partially healed fracture around it and become more whitish and opaque. The zircon crystal to the right of it has developed a mottled appearance with a few spots in its interior. On the far right, a partially healed fissure has developed. Photomicrographs by E. Billie Hughes; field of view 1.5 mm.

light (fluorescence) as a result. This will always overlay the Raman spectrum and may overpower it to such a degree that the weaker Raman inclusion spectrum drowns in the noise of the ruby's fluorescence. Despite the high background noise introduced by fluorescence, major peaks of corundum can still be observed. This is characterized by a major peak at 415 cm^{-1} and smaller peaks at 640, 375, 750, and 575 cm^{-1} (in decreasing order of relative intensity).

We explored the use of Raman spectroscopy to observe structural changes in solid inclusions in Burmese ruby. It is intuitively understood that heat treatment destroys inclusions, but at lower temperatures it can also anneal any crystal damage in the inclusions, especially in inclusions that tend to contain radioactive elements, which has been observed in Madagascar sapphires (Saeseaw et al., 2020). In our experiments, we focused on the Raman spectra of the calcite, spinel, and apatite inclusions.

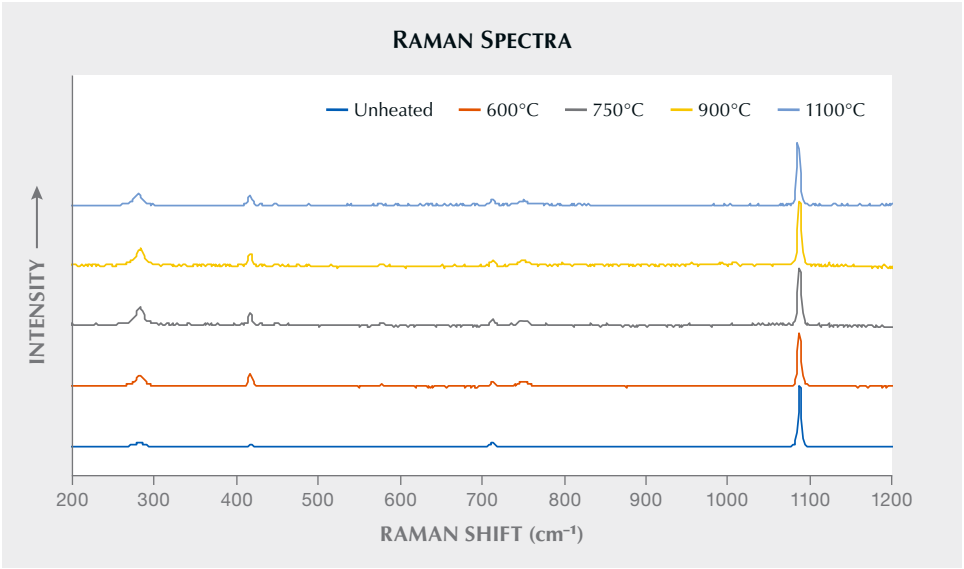

Figure 27. Raman spectra of calcite (the crystal on the far left in sample 8; see figure 14). The main feature of the spectra, the peak at 1080 cm^{-1}, remained consistent after each round of heating. Spectra are offset vertically for clarity.

Calcite. The Raman spectra of carbonate minerals are characterized by a strong peak in the range of 1080–1095 cm^{-1} and minor peaks around 155, 280, and 715 cm^{-1} (Krishnamurti, 1957). For calcite crystals, one interesting case study is that of sample 8 (figure 14), which shows four large carbonate crystals lined up. These calcite crystals exhibit two different behaviors in their Raman spectra during successive rounds of heat treatment.

Three of the crystals displayed minimal changes, where the peak shape remained similar. These are the same crystals that exhibited no significant visual changes during low-temperature treatment. Figure 27 shows the Raman spectra of the crystal on the far left, which remained similar throughout the heating process.

In contrast, one crystal from this series (the third from the left) looked very similar to the others in its unheated state but reacted strongly to heating. During the first two heating steps (600°C and 750°C), its appearance and Raman spectrum barely changed. At 900°C and above, the Raman spectra show a significant widening of the main carbonate peak as well as a slight shift to higher wavenumbers (see figure 28). Visually, the crystal started to turn white and opaque. The peak between 1080 and 1090 cm^{-1} corresponds to the symmetric stretching of C-O bonds of carbonate (CO_3); such a reduction in the sharpness and intensity of this peak means that the carbonate is decomposed. Additional peaks appearing around 360 cm^{-1} match with lime (CaO). At higher temperatures, calcite breaks down into lime and CO_2, which is probably what we observed here. The Raman spectra did not reveal the presence of CO_2, most likely due to its low concentration. It might also have escaped via (hairline) fractures that developed during treatment.

We observed the same reaction in the calcite inclusion in sample 30, but here the breakdown did not start until 1100°C. Thermal decomposition of calcite under atmospheric pressure typically takes place in the range of 750°C (Harker and Tuttle, 1955). These observations of unaltered calcite at temperatures above the reported decomposition temperature show that there are other factors playing a role. Probably the most prominent variable is the pressure under which the inclusion is encased in the host mineral.

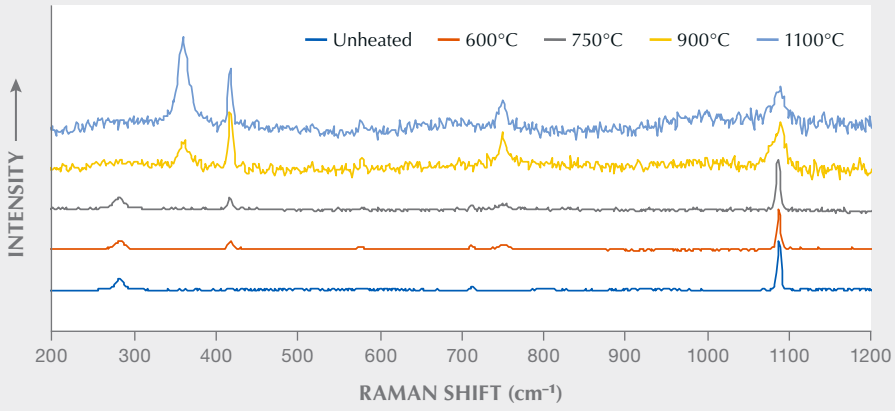

	Position of carbonate peak	Full width at half maximum (FWHM) of carbonate peak
Unheated	1087.12	6.48
600°C	1086.89	6.53
750°C	1086.57	6.32
900°C	1088.15	20.08
1100°C	1090.13	14.88

Figure 28. Raman spectra of calcite (the crystal third from the left in sample 8, see figure 14). After heating to 900°C, the spectrum showed significant changes. Note how the peak at 1080 cm^{-1} widens and becomes less sharp, which corresponds to the changes observed in the crystal as it becomes white and opaque. This corresponds to calcite being transformed into lime. Spectra are offset vertically for clarity.

The observation of how both the appearance and spectra of the same types of mineral inclusions can vary, despite having been heated to the same temperature, is one of the more thought-provoking results of these experiments. In some cases, as seen with calcite, even the same types of mineral inclusions in the same sample can react differently. This highlights the variety of factors that can influence the behavior of crystals during heat treatment, which are discussed later in this article. Because of the numerous factors that can have an impact, it is difficult to pinpoint just one reason for the inclusions' differing responses to heat.

Spinel. Another common inclusion in Burmese ruby is spinel. In the last two decades, several heat treatment studies have been performed on gem spinel, often focused on nondestructive analytical detection techniques (Saeseaw et al., 2009; Widmer et al., 2014). Most of the work has concentrated on the photoluminescence of spinel, where changes in the emission spectrum are reliable indicators of heat treatment. Unfortunately, this technique cannot be used for spinel inclusions in ruby, since the photoluminescence spectrum would be dominated by that of the chromium-rich host corundum, so instead we focused on the Raman spectrum.

The Raman spectrum of spinel is dominated by a single sharp peak in the range of 405–420 cm^{-1}, with additional peaks around 670 and 770 cm^{-1}. We did not observe any changes in the spectra of the spinel inclusions after the first heating step (at 600°C), but after heating to 750°C, the peak widened significantly (see figure 29). This effect became more pronounced at higher temperatures. The position of the peak also shifted to slightly higher wavenumbers. Our observations match those observed in gem spinel crystals.

These changes correspond to an increased disorder in the spinel crystal lattice starting at temperatures around 600°–700°C (Yamanaka and Takéuchi, 1983; Wang et al., 2019). This characteristic can be a relevant criterion for treatment detection. Visual observation of the spinel crystal revealed little change during heating, but changes in the Raman spectrum after treatment above 700°C can be strong indicators of low-temperature treatment.

Apatite. The spectrum of apatite is dominated by the phosphate peak around 965 cm^{-1}. This peak remained stable throughout the entire heating experiment, even during high-temperature treatment at 1500°C (see figure 30). Both the peak position and full width at half maximum (FWHM) of the main apatite peak remain constant, although a slight widening of the peak is observed during treatment at the highest temperature.

The thermal stability of apatite depends on its exact composition, especially the anion group that is part of the mineral. In geological conditions these are typically F^-, Cl^-, OH^-, and, in rarer cases, CO_3^{2-}. While there is no exact analysis of the apatite species in Burmese ruby, there are strong indications that they are chlorine-rich (Bieri et al., 2010). This apatite variety does not decompose at higher temperatures and has a melting temperature above 1500°C (Tõnsuaadu et al., 2011). As a result, it remains unaffected by treatment at low temperature and into the high-temperature ranges as well.

Factors That Affect How Inclusions React to Heat. Our observations revealed that even inclusions of the same type did not always react to heat treatment the same way at the same temperature. For example, in sample 25 (figure 15), two of the three mica crystals developed fissures after heating to 750°C, yet a third mica crystal showed no signs of heat alteration. Meanwhile, a garnet crystal in the same sample also developed a fissure during the same round of heating.

While one might expect inclusions of the same type of material to react similarly to heat at the same temperature, in reality the issue is more complex. A perfect example is the series of four calcite crystals in sample 8 (figure 14), all of which looked similar in their unheated states but reacted differently during the experiment. Several factors can affect how inclusions react to heat, including the following (J. Koivula, pers. comm., 2021; J. Emmett, pers. comm., 2021):

- *Type and chemical composition:* The identity of each inclusion can affect how it reacts to heat. Every solid mineral has its own unique coefficient of thermal expansion, which is the tendency of matter to increase in volume in response to an increase in temperature. If the inclusion expands more rapidly than the host, the added pressure can produce stress fractures. This can happen both naturally and as a result of artificial heat treatment (Wang et al., 2006). The identity of the crystal also determines its chemical stability at higher temperatures.

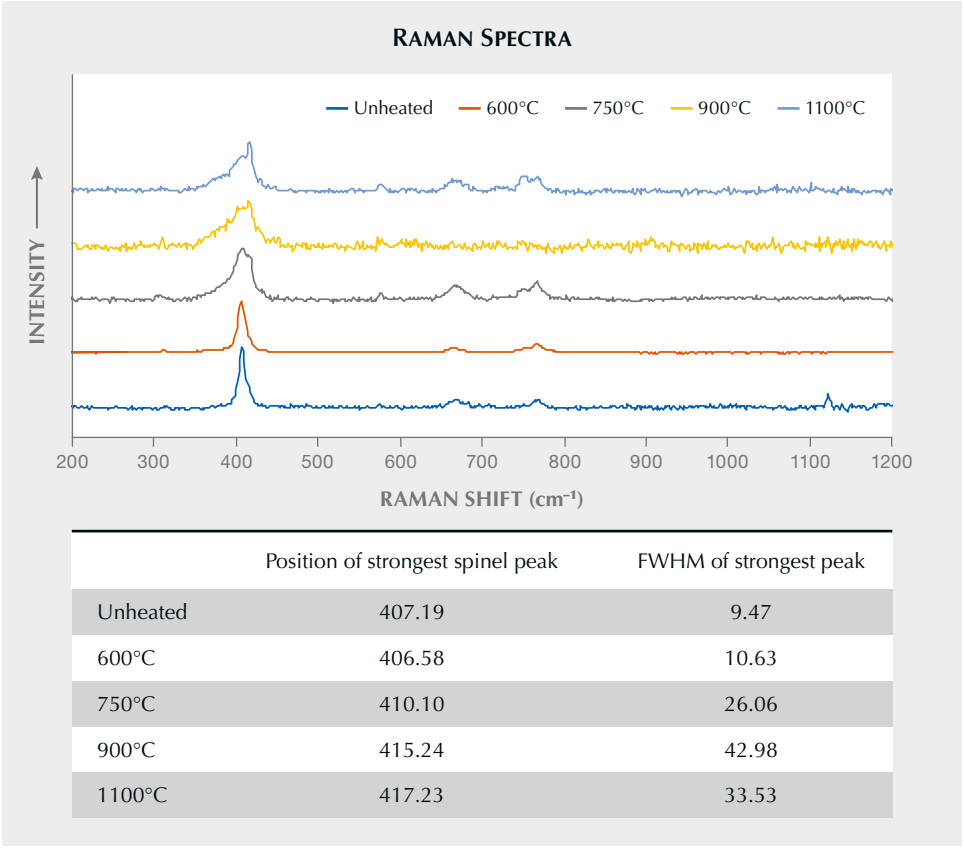

	Position of strongest spinel peak	FWHM of strongest peak
Unheated	407.19	9.47
600°C	406.58	10.63
750°C	410.10	26.06
900°C	415.24	42.98
1100°C	417.23	33.53

Figure 29. Raman spectra of the spinel crystal in sample 30 (see figure 9). After the first round of heating to 600°C, the spectrum remained consistent, but notable changes occurred after heating to 750°C. The peak between 405 and 420 cm^{-1} widened and shifted to a slightly higher wavenumber, a trend that continued with heating to higher temperatures. Spectra are offset vertically for clarity.

- *Size:* The expansion of a larger inclusion as it is heated tends to create more dramatic changes.
- *Relative orientation and shape:* The orientation and/or shape of an inclusion may have an impact because all host crystals have their own directions of weakness.
- *Inclusions within inclusions:* Included solids may contain their own inclusions of various types.

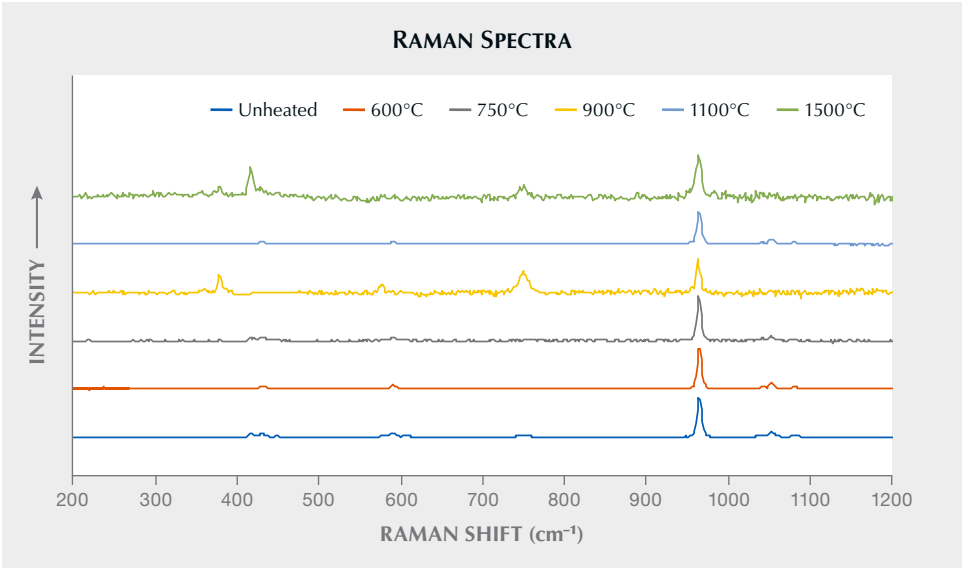

Figure 30. Raman spectra of an apatite inclusion in sample 46 (see figure 24). The spectra remained fairly consistent after each round of heating, with just a slight widening of the peak around 965 cm^{-1} after heating to 1500°C. Some spectra show the host corundum, with peaks at around 380, 420, and 750 cm^{-1}. Spectra are offset vertically for clarity.

- *Location:* Proximity to the surface or to other inclusions may affect how an inclusion reacts.
- *Trapping pressure and temperature:* The pressure and temperature under which an inclusion was trapped within its host can have an impact.
- *Melting point:* Solid minerals with lower melting points are in general more sensitive to heat treatment than those with higher melting points.

UV-Vis-NIR Spectroscopy. UV-Vis-NIR spectroscopy showed a typical spectrum for Burmese ruby (figure 31). The color is determined nearly exclusively by the Cr^{3+} chromophore, which is characterized by two strong absorption bands at around 400 and 560 nm.

One sample (sample 46) was analyzed after each round of low-temperature treatment as well as after high-temperature treatment. This ruby was selected because it had an area relatively free of inclusions that made it ideal for spectroscopy. Changes in the absorption spectrum were minimal during the low-temperature treatment at 1100°C. After high-temperature treatment (1500°C), the shoulder at around 330 nm started to become stronger (see figure 31).

This 330 nm band is typically linked to iron (Dubinsky et al., 2020). Formation of the chromophore composed of Fe^{3+}-Fe^{3+} pairs is unlikely due to the low concentration of iron in this material. Even at a low iron concentration, it is possible that trapped holes associated with iron are formed, which can add significant yellow color to the stone. However, these iron features should also create sharp bands at 378 and 450 nm, which are absent here. As such, the origin of the 330 nm band cannot be explained by these known iron-related chromophores.

We did observe silk dissolution during treatment at high temperatures, but the low iron concentrations and relatively high magnesium content prevent any Fe^{2+}-Ti^{4+} intervalence charge transfer from forming and creating blue color in the stone.

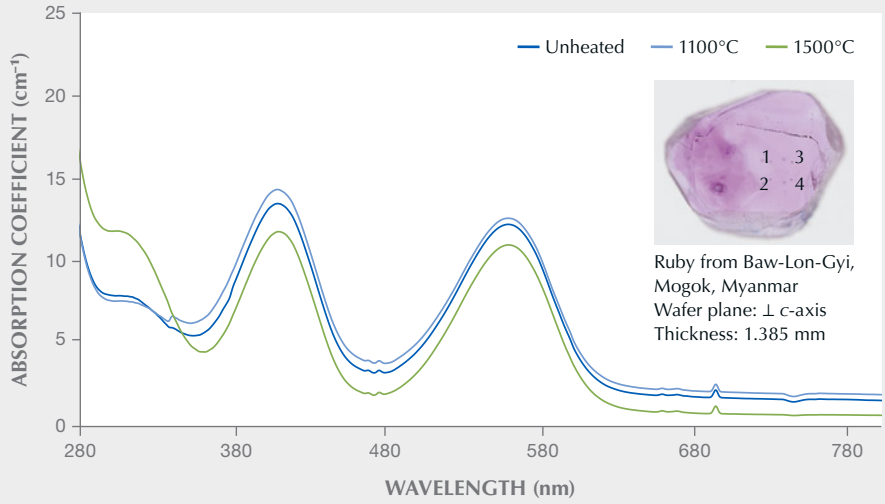

	^{24}Mg	^{47}Ti	^{51}V	^{53}Cr	^{57}Fe	^{69}Ga
Sample 46 Spot 1	17	21	53	525	9	10
Sample 46 Spot 2	16	16	51	443	7	10
Sample 46 Spot 3	18	19	51	283	8	10
Sample 46 Spot 4	19	20	50	336	7	10
Detection limit (ppma)	0.46	0.51	0.04	0.44	4.72	0.02

Figure 31. UV-Vis-NIR spectra of sample 46, with two strong absorption bands at around 400 and 560 nm. The table shows the trace element concentrations (in ppma) measured with LA-ICP-MS. The four spots cover the area where the absorption spectra were collected. Photo by S. Engniwat.

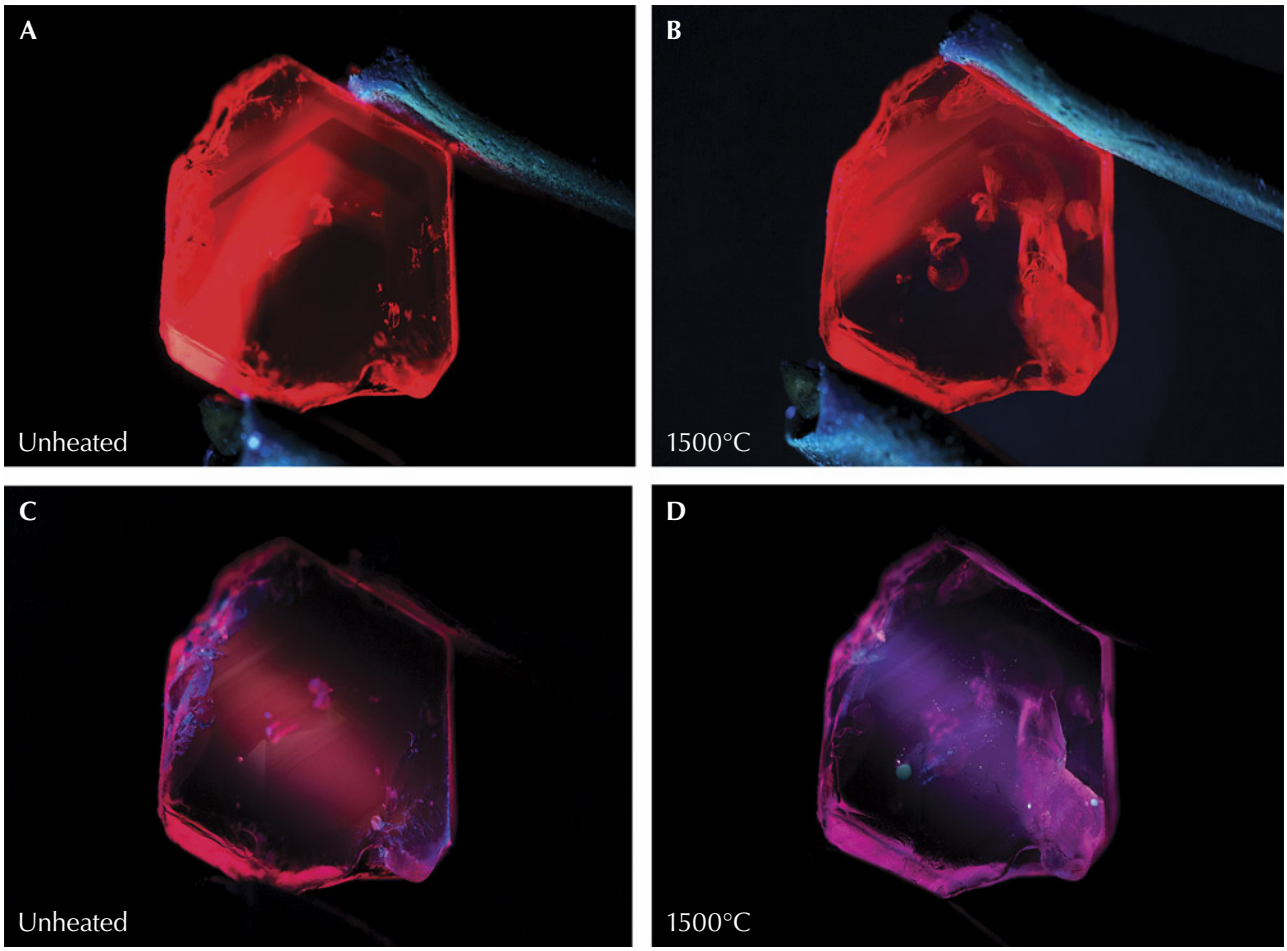

Figure 32. A: Sample 17 displays a strong red fluorescence in long-wave UV illumination prior to heating. B: After heating to 1500°C, the sample continues to display strong red fluorescence in long-wave UV. The area on the right with more visible red fluorescence is due to light striking inclusions that have altered, rather than a change in the stone's bodycolor. C: The ruby displays a medium red fluorescence in short-wave UV prior to heating. D: The sample develops a medium chalky fluorescence reaction in short-wave illumination after heating to 1500°C. Photos by E. Billie Hughes.

While we did notice these subtle changes in the UV-Vis-NIR spectrum, there was no visible change in bodycolor.

Infrared Spectroscopy. FTIR spectra of all 15 heated samples were obtained before and after each round of heating. No significant changes were noted after any round of treatment. While some corundum displays the 3309 series of peaks at 3309, 3232, and/or 3185 cm^{-1} after heat treatment, these were not detected in the ruby samples used in our experiments. This is a vivid reminder for gemologists of the importance of observing all evidence. While the presence of the 3232 cm^{-1} peak within the 3309 series may be an indication of heat, the lack thereof does not constitute proof of an untreated stone.

Ultraviolet Fluorescence Imaging. *Long-Wave Fluorescence.* The long-wave UV fluorescence reactions of all 15 specimens subjected to heat treatment were observed before and after each round of heating. Before heating, they displayed very strong red fluorescence in long-wave UV. No changes in this long-wave fluorescence were observed after any of the heating rounds. While some samples appeared slightly different at first glance, this was due to changes in the inclusions, which in some instances created larger fissures that reflected more light, rather than a change in the bodycolor. One example of this can be seen in figure 32, where sample 17 was photographed before and after heating to 1500°C. The sample displays strong red fluorescence in both images. But in the second image, the right side of the

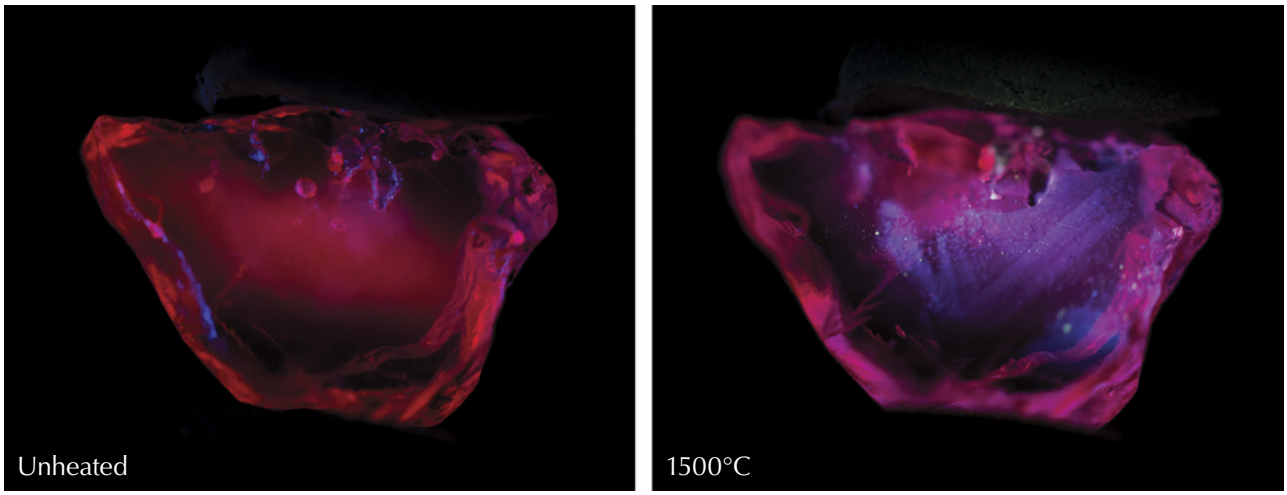

Figure 33. Left: Sample 18 displays a strong red fluorescence in short-wave UV before heat treatment. It retains this appearance after heating to 600°, 750°, 900°, and 1100°C. Right: After heating to 1500°C, it displays a zoned chalky fluorescence in short-wave UV. Photos by E. Billie Hughes.

specimen shows more bright red areas where light is reflecting off fissures that developed with heat treatment.

Short-Wave Fluorescence. We also observed the short-wave UV fluorescence reactions of all 15 specimens before and after each round of heating. Before heating and in subsequent rounds, they displayed a strong pinkish red fluorescence. After the initial rounds of heating to lower temperatures, we observed no significant change in their reactions to short-wave UV. Once the rubies were heated to 1500°C, significant changes were observed. At this point, the samples all developed a strong zoned, chalky pinkish red fluorescence. In some specimens, the reaction was clearly more pinkish red than be-

Figure 34. Left: Sample 12 displays strong red fluorescence in short-wave UV before heating and with each subsequent round until the highest temperature round. Right: At a relatively high temperature of 1500°C, it develops a medium chalky fluorescence. The bright round chalky features here are molten material that has hardened on the surface. Photos by E. Billie Hughes.

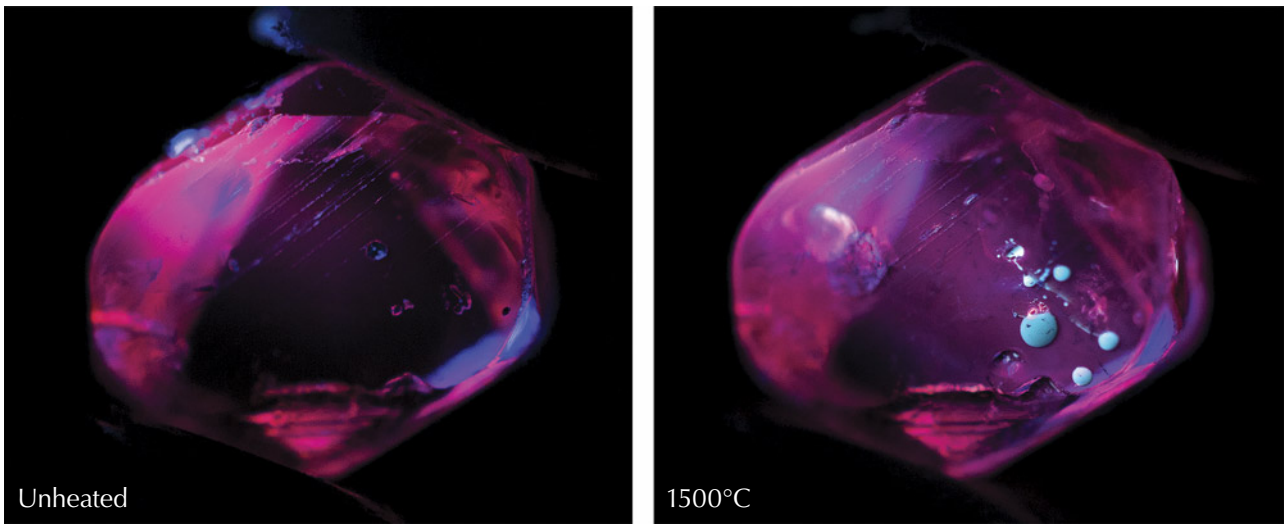

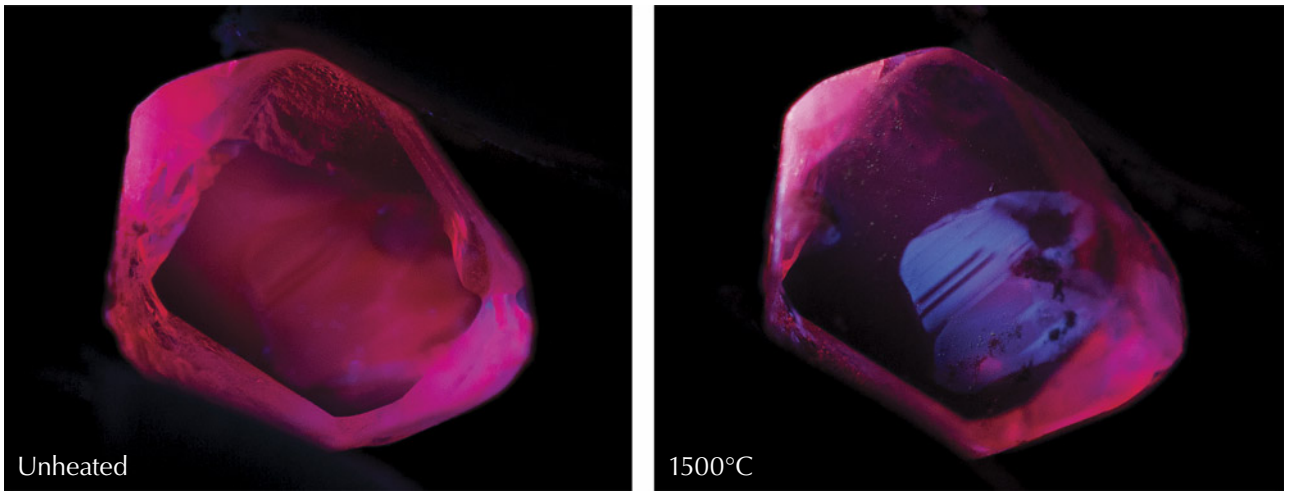

Figure 35. Left: Sample 46 displays a strong red short-wave fluorescence in its unheated state. Like the other samples tested, it did not display any change in appearance in short-wave UV illumination until after the last round of heating. Right: After heating to 1500°C, the ruby displays a clear, zoned chalky appearance in short-wave UV. Photos by E. Billie Hughes.

fore heating, as seen in figures 32 and 33. With some samples, the chalkiness was spread across the ruby, while in others the chalky areas were more prominently zoned. Sample 18 (figure 33) showed chalky areas following a clear, angular zone pattern.

Brighter chalky areas concentrated in rounded spots were also seen (see figure 34). Closer observation revealed that these are from molten material that attached and cooled on the surface, rather than from features inside the samples. Treaters will usually repolish or even acid-clean a stone after it has been heated to remove this type of foreign substance, although remnants may be visible upon close microscopic examination. In sample 46 (figure 35), the chalky area seen in short-wave UV after heat treatment is sharply delineated from the rest of the stone.

When corundum is heated and rutile dissolves, this releases Ti^{4+}. Areas with a high concentration of rutile microcrystals and rutile silk can then have a high concentration of Ti^{4+}, which creates zoned areas with chalky fluorescence (Hughes et al., 2017). Sample 18 (figure 33) offers a clear example of the chalkiness associated with a zoned cloud of partially dissolved silk.

A crystal must always be charge-balanced. When a rutile needle begins to dissolve into corundum during heat treatment, Ti^{4+} is forced into solid solution, and this upsets the charge balance. The dissolution of rutile into corundum is much like a "cylinder" that expands in diameter with time over the course of heating. At the outer edge of this cylinder, the Ti^{4+} concentration is essentially zero, while the concentration of TiO_2 is highest at the center. At some point between these extremes, the concentration of Ti^{4+} that dissolves into the corundum becomes greater than those of potential acceptors such as Fe^{2+} and Mg^{2+}, which are the easiest means of achieving charge balance. At that point, Ti^{4+} begins to be charge-compensated by aluminum vacancies rather than by Mg^{2+} and Fe^{2+}. One aluminum vacancy has a relative charge of –3 compared to the neutral lattice, so one vacancy charge compensates three Ti^{4+}. It is the various combinations of aluminum vacancies and Ti^{4+} ions that fluoresce chalky white under short-wave UV light (J. Emmett, pers. comm., 2022).

In this experiment, chalky fluorescence was observed in all samples after heat treatment. This suggests a relatively higher concentration of Ti^{4+} and lower concentrations of iron and magnesium in the rubies. In corundum containing high concentrations of iron and magnesium, the fluorescence appears weaker or inert (Hughes et al., 2017).

CONCLUSIONS

The presence of low-temperature-heated ruby on the market can present a challenge for gemologists trying to detect treatment. While features such as the appearance of rutile can provide a well-known and

helpful indicator for heat treatment at higher temperatures, these tend not to change noticeably at lower temperatures. Observation of short-wave UV fluorescence reactions yielded similar results. When heated to 1500°C, the samples developed a distinctive chalky appearance that could help separate them from unheated material. However, heating to lower temperatures did not produce this telltale sign, nor did the UV-Vis-NIR spectra of the samples yield diagnostic evidence of heat treatment. Therefore, gemologists must rely on other observations to detect low-temperature heat treatment.

Fortunately, in our experiments with heat treatment of Burmese ruby, we observed many types of solid inclusions—including calcite, mica, spinel, and zircon—that are sensitive to heat at lower temperatures between 600° and 1100°C. Careful microscopic observation of these crystals can act as our proverbial canary in the coal mine, providing evidence of heat treatment before other inclusions such as rutile silk show signs of alteration.

Nevertheless, several of these crystals showed no noticeable changes after treatment at lower temperatures. As such, the absence of visual features associated with heat treatment does not mean that stones were *not* treated at lower temperatures. Micro-Raman analysis of inclusions, particularly spinel inclusions, can support the detection of low-temperature heat treatment, even when visual observations provide no evidence of treatment, reinforcing its utility in the gemological laboratory.

It is inevitable that the boundaries of treatment procedures will continue to be pushed. Detection criteria will require constant updates, based on new research and experiments, to stay in touch with current developments.

ABOUT THE AUTHORS

E. Billie Hughes is a gemologist and co-founder of Lotus Gemology in Bangkok. Wim Vertriest is manager of field gemology at GIA in Bangkok.

ACKNOWLEDGMENTS

The authors would like to express their gratitude to those who have helped support this project. We thank the Accredited Gemologists Association (United States) for providing a research grant that helped to support and fund this project. We also thank Richard W. Hughes and Wimon Manorotkul (Lotus Gemology, Bangkok), John L. Emmett (Crystal Chemistry, Brush Prairie, Washington), John I. Koivula (GIA, Carlsbad, California), Vincent Pardieu (Bahrain), and Çigdem Lüle (Kybele LLC, Arlington Heights, Illinois) for their advice and assistance. Charuwan Khowpong, Polthep Sukpanish, and Titapa Tanawansombat (GIA, Bangkok) assisted with data collection. Eric Braunwart (Columbia Gem House, Vancouver, Washington) assisted with heating. The authors would also like to thank the peer reviewers for their thoughtful and constructive comments.

REFERENCES

Al-Beruni M.A. (1989) *The Book Most Comprehensive in Knowledge on Precious Stones: Al-Beruni's Book on Mineralogy [Kitab al-jamahir fi marifat al-jawahir]*. Trans. by H.M. Said, One Hundred Great Books of Islamic Civilization, Natural Sciences No. 66. Pakistan Hijra Council, Islamabad.

Bieri W., Grobety B., Peretti A., Hametner K., Günther D. (2010) Chemical composition of apatite inclusions in corundum and spinel determined by LA-ICP-MS and its potential for authentication and provenance determination. *Geochimica et Cosmochimica Acta*, Vol. 74, No. 12, p. A89.

Dubinsky E.V., Stone-Sundberg J., Emmett J.L. (2020) A quantitative description of the causes of color in corundum. *G&G*, Vol. 56, No. 1, pp. 2–28, http://dx.doi.org/10.5741/GEMS.56.1.2

Gillet P., Biellmann C., Reynard B., McMillan P. (1993) Raman spectroscopic studies of carbonates part I: High-pressure and high-temperature behaviour of calcite, magnesite, dolomite and aragonite. *Physics and Chemistry of Minerals*, Vol. 20, No. 1, pp. 1–18, http://dx.doi.org/10.1007/BF00202245

Harker R.I., Tuttle O.F. (1955) Studies in the system $CaO–MgO–CO_2$; Part 1, The thermal dissociation of calcite, dolomite and magnesite. *American Journal of Science*, Vol. 253, No. 4, pp. 209–224, http://dx.doi.org/10.2475/ajs.253.4.209

Hughes E.B., Perkins R. (2019) Madagascar sapphire: Low-temperature heat treatment experiments. *G&G*, Vol. 55, No. 2, pp. 184–197, http://dx.doi.org/10.5741/GEMS.55.2.184

Hughes R.W., Manorotkul W., Hughes E.B. (2017) *Ruby & Sapphire: A Gemologist's Guide*. RWH Publishing/Lotus Publishing, Bangkok.

Koivula J.I. (2013) Useful visual clue indicating corundum heat treatment. *G&G*, Vol. 49, No. 3, pp. 160–161, http://dx.doi.org/10.5741/GEMS.49.3.160

Krishnamurti D. (1957) The Raman spectrum of calcite and its in-

terpretation. *Proceedings of the Indian Academy of Sciences - Section A*, Vol. 46, No. 3, pp. 183–202, http://dx.doi.org/10.1007/BF03045968
Lafuente B., Downs R.T., Yang H., Stone N. (2015) The power of databases: The RRUFF project. In T. Armbruster and R.M. Danisi, Eds., *Highlights in Mineralogical Crystallography*, De Gruyter, Berlin, pp. 1–30, https://rruff.info/about/downloads/HMC1-30.pdf
Pardieu V., Saeseaw S., Detroyat S., Raynaud V., Sangsawong S., Bhusrisom T., Engniwat S., Muyal J. (2015) "Low temperature" heat treatment of Mozambique ruby: Results report. *GIA News from Research*, https://www.gia.edu/doc/Moz_Ruby_LowHT_US.pdf, April 16, 34 pp.
Peretti A., Schmetzer K., Bernhardt H.-J., Mouawad F. (1995) Rubies from Mong Hsu. *G&G*, Vol. 31, No. 1, pp. 2–26, http://dx.doi.org/10.5741/GEMS.31.1.2
Roedder E. (1984) *Fluid Inclusions*. Reviews in Mineralogy: Vol. 12. Mineralogical Society of America, Washington, D.C.
Saeseaw S., Wang W., Scarratt K., Emmett J.L., Douthit T.R. (2009) Distinguishing heated spinels from unheated natural spinels and from synthetic spinels: A short review of ongoing research. *GIA Research News*, https://www.gia.edu/doc/distinguishing-heated-spinels-from-unheated-natural-spinels.pdf, 13 pp.
Saeseaw S., Khowpong C., Vertriest W. (2020) Low-temperature heat treatment of pink sapphires from Ilakaka, Madagascar. *G&G*, Vol. 56, No. 4, pp. 448–457, http://dx.doi.org/10.5741/GEMS.56.4.448
Sripoonjan T., Wanthanachaisaeng B., Leelawatanasuk T. (2016) Phase transformation of epigenetic iron staining: Indication of low-temperature heat treatment in Mozambique ruby. *Journal of Gemmology*, Vol. 35, No. 2, pp. 156–161.
Stone-Sundberg J., Thomas T., Sun Z., Guan Y., Cole Z., Equall R., Emmett J.L. (2017) Accurate reporting of key trace elements in ruby and sapphire using matrix-matched standards. *G&G*, Vol. 53, No. 4, pp. 438–451, http://dx.doi.org/10.5741/GEMS.53.4.438
Stone-Sundberg J.L., Guan Y., Sun Z., Ardon T. (2021) Accurate trace element reporting in corundum: Development of secondary ion mass spectrometry relative sensitivity factors. *Geostandards and Geoanalytical Research*, Vol. 45, No. 1, pp. 207–221, http://dx.doi.org/10.1111/ggr.12360
Tõnsuaadu K., Gross K.A., Plūduma L., Veiderma M. (2011) A review on the thermal stability of calcium apatites. *Journal of Thermal Analysis and Calorimetry*, Vol. 110, No. 2, pp. 647–659, http://dx.doi.org/10.1007/s10973-011-1877-y
Wang C.-S., Shen A.H., Liu Y.-G., Zhang Q. (2019) Raman spectra study of heating treatment and order-disorder transition of Cr^{3+}-doped $MgAl_2O_4$ spinel. *Spectroscopy and Spectral Analysis*, Vol. 39, No. 1, pp. 109–113.
Wang W., Scarratt K., Emmett J.L., Breeding C.M., Douthit T.R. (2006) The effects of heat treatment on zircon inclusions in Madagascar sapphires. *G&G*, Vol. 42, No. 2, pp. 134–150, http://dx.doi.org/10.5741/GEMS.42.2.134
Widmer R., Malsy A.-K., Armbruster T. (2014) Effects of heat treatment on red gemstone spinel: Single-crystal X-ray, Raman, and photoluminescence study. *Physics and Chemistry of Minerals*, Vol. 42, No. 4, pp. 251–260, http://dx.doi.org/10.1007/s00269-014-0716-7
Yamanaka T., Takéuchi Y. (1983) Order-disorder transition in $MgAl_2O_4$ spinel at high temperatures up to 1700°C. *Zeitschrift für Kristallographie – Crystalline Materials*, Vol. 165, No. 1-4, pp. 65–78, http://dx.doi.org/10.1524/zkri.1983.165.14.65

Fluorescence Characteristics of Two Copper-Diffused Plagioclase Feldspars: Labradorite and Andesine

Qingchao Zhou, Chengsi Wang, and Andy H. Shen

Natural-color labradorite sunstone from Oregon has been available for more than a century. In the first decade of the 2000s, a type of "red andesine feldspar" was unveiled at the Tucson gem shows, and its origin remains an open question. There is still no convenient method that can quickly and reliably determine whether a red andesine feldspar has been treated. For this study, both colorless labradorite and light yellow andesine feldspars were copper diffusion treated to modify their color to mimic natural labradorite sunstone. Systematic studies of the fluorescence characteristics of both untreated and treated labradorite and andesine feldspars as well as natural gem-quality sunstone from Oregon and Ethiopia were conducted. Under 320 nm excitation, strong fluorescence emission near 394 nm and weak fluorescence emission near 554 nm were observed in the spectra of copper-diffused red labradorite and andesine feldspar. For comparison, natural red and green labradorite sunstone material from Oregon and Ethiopia were tested, and these exhibited substantially weaker fluorescence emission around 394 nm, similar to the untreated nearly colorless labradorite and light yellow andesine feldspar samples. This fluorescence characteristic, due to the presence of Cu^{+} ions in the plagioclase crystal structure, can potentially help to identify copper diffusion treatment.

Feldspar, with orthoclase ($KAlSi_3O_8$), albite ($NaAlSi_3O_8$), and anorthite ($CaAl_2Si_2O_8$) as end members, is one of the most important rock-forming minerals in the earth's crust, and those of high quality can be used as gemstones. The main feldspar gems on the market include moonstone, sunstone, amazonite, and iridescent rainbow labradorite. Among them, sunstone exhibits a strong golden and red metallic luster due to microscopic metallic inclusions. But there is a special kind of labradorite sunstone—$Ab_{50–30}An_{50–70}$, where Ab is albite and An is anorthite—that not only shows "schiller" (aventurescence) but also presents brilliant red and green bodycolors. Currently, the reported localities of this kind of natural labradorite sunstone are the U.S. state of Oregon and the Afar region of Ethiopia (Johnston et al., 1991; Kiefert et al., 2019; Sun et al., 2020). This material is highly valued and favored by many gem carvers and collectors for its unique optical properties.

See end of article for About the Authors and Acknowledgments.
Gems & Gemology, Vol. 58, No. 4, pp. 424–437,
http://dx.doi.org/10.5741/GEMS.58.4.424

Research on the color origin of labradorite sunstone has been ongoing since its discovery. In the beginning, researchers identified copper as the color-causing element in red labradorite sunstone. Quantitative analysis of labradorite sunstone with different colors verified this, but classical crystal field theory (absorption bands of Cu^{2+} or Cu^{+} ions) cannot provide a reasonable explanation. Previous studies compared the absorption spectra of red labradorite sunstone with that of "ruby glass" containing copper nanoparticles and found that the absorption peaks of these two different materials are very similar (Hofmeister and Rossman, 1985; Rossman, 2011). This result suggests that the presence of copper nanoparticles contributes to the color in labradorite sunstone. Nishida and Kimata (2002) analyzed copper microinclusions in natural labradorite sunstone by combining chemical composition results with characteristic X-ray imaging by element. They summarized that the transparent red color of the Oregon sunstone is due to the distribution of mixtures of both native copper and cuprites in oval-shaped thin films, while the transparent green color is due to the distribution of similar mixtures in short micro-

columns. However, due to technical limitations, the existence of copper nanoparticles in natural sunstone had not been directly verified. In Wang et al. (2019), authors CW and AHS from the present study directly observed the microscopic morphology of copper nanoparticles in natural sunstone by means of focused ion beam and transmission electron microscopy (FIB-TEM).

Because of the high price and market potential of natural sunstone, a new variety of red and green andesine feldspar ($Ab_{70–50}An_{30–50}$) was unveiled during the 2006 Tucson gem shows (Rossman, 2011). The gem sellers claimed that this red andesine feldspar came from a new locality in China, which attracted the attention of major gem research institutions around the world. Since then, the mining of natural red and green andesine in Tibet has been a subject of controversy (Hughes, 2011a; Schorr et al., 2012). The similar appearances of the red andesine feldspar and natural Oregon labradorite sunstone have led many gemologists to examine whether the Tibetan red andesine feldspar material is natural and untreated using two approaches: analytical technology (Rossman, 2011; Peretti et al., 2011a,b) and on-site inspection (Abduriyim et al., 2008, 2009a,b; Abduriyim and Laurs, 2010; Hughes, 2010, 2011b; Wang et al., 2011). The identification of copper diffusion treatment might be possible using a combination of several advanced techniques, such as elemental fingerprints and isotope ratio determination of copper and argon, but most of these are expensive, destructive, and not widely available.

In Brief

- High-quality natural-color labradorite sunstone is highly valued in the commercial market. But the question of whether red andesine feldspar in the market is treated by copper diffusion remains controversial, and techniques for identifying this treatment are urgently needed.
- The fluorescence spectra differences shown by labradorite and andesine feldspar before and after copper diffusion experiments reveal that strong fluorescence around 394 nm under 320 nm excitation is potentially key evidence in identifying this treatment.
- The natural red and green labradorite sunstone samples from Oregon and Ethiopia analyzed in this study exhibited weak fluorescence under 320 nm excitation, similar to the untreated nearly colorless labradorite and light yellow andesine feldspar samples.

The treatment methods used in the marketplace to modify colorless plagioclase feldspar to red and green color are not completely understood. Many researchers have tried to generate red and green colors using copper diffusion experiments, typically by placing colorless or light yellow feldspar in a zirconia powder containing a small amount of copper and then performing a high-temperature diffusion treatment (Emmett and Douthit, 2009; Thirangoon, 2009; Wang, 2012; Cao, 2013). By adjusting the diffusion temperature, different shades of red colors can be obtained. Specifically, Emmett and Douthit (2009) treated nearly colorless labradorite feldspar at 1000°, 1100°, and 1170°C for 160 hours. Cao (2013) treated light yellow andesine feldspar at 1100°, 1150°, and 1200°C for 24, 48, and 72 hours, respectively. Except for some microscopic characteristics caused by heat treatment such as black particles, lath-like hollow channels, and pipe-like growth tubes, no direct identification evidence of treatment was reported in these diffusion experiments.

Nevertheless, we still believe that copper diffusion experiments offer the best means of revealing whether red andesine feldspar has been treated by copper diffusion. This research systematically reports on copper diffusion experiments and the fluorescence characteristics excited by the 305–335 nm ultraviolet light, which is seldom used in gem identification.

MATERIALS AND METHODS

Samples. A total of 29 natural nearly colorless or light yellow labradorite and andesine feldspar samples and red labradorite sunstones were used in this study. The near-colorless and light yellow stones were used for copper diffusion experiments, and all samples were analyzed for composition and studied spectroscopically. These samples (figure 1 and table 1) were categorized into four groups, A through D. Group A contained eight nearly colorless labradorite feldspar samples from Oregon, all purchased by one of the authors (AHS) from an Oregon miner at the Tucson Gem and Mineral Show (TGMS). Group B contained four light yellow andesine feldspar samples from Inner Mongolia, China, purchased by one of the authors (QZ) from a miner there. Group C consisted of 13 natural red or green labradorite sunstone samples from different mines in Oregon, on loan from GIA: five from Ponderosa, five from Dust Devil, and three from Sunstone Butte. Group D comprised four natural red labradorite sunstone samples from Ethiopia, on loan

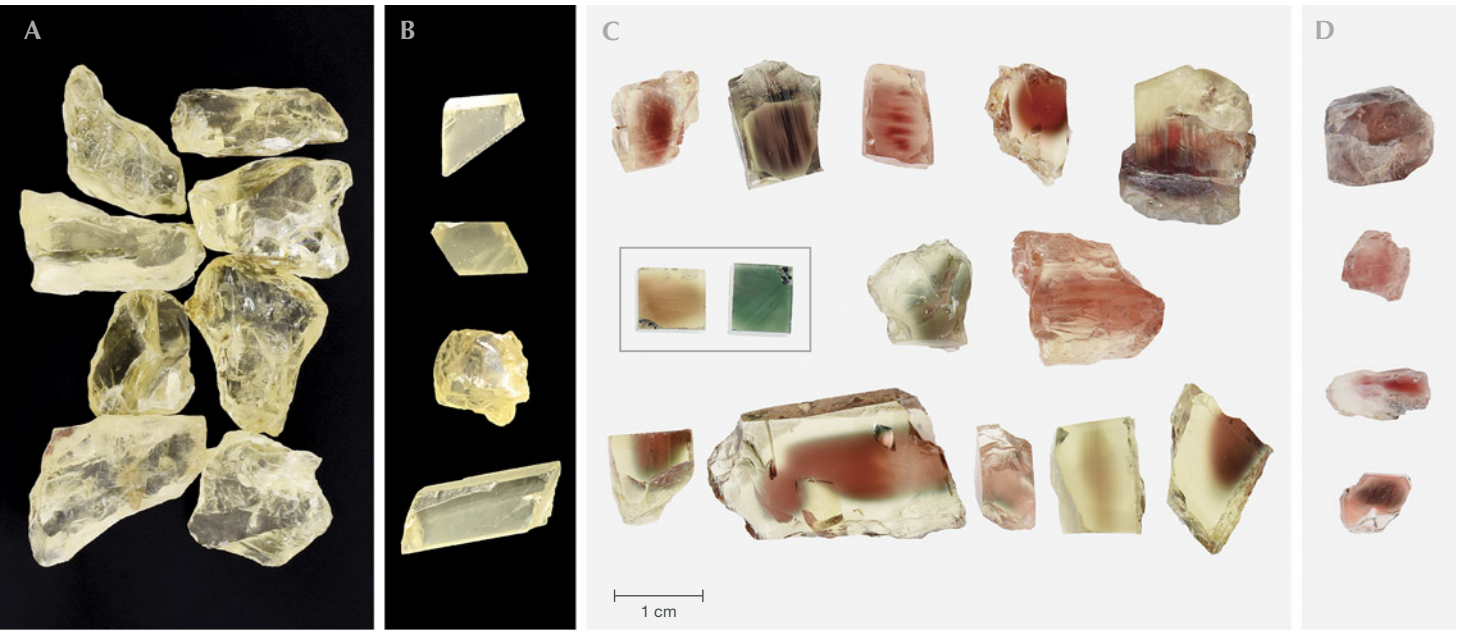

Figure 1. The 29 natural labradorite sunstone and plagioclase feldspar specimens used in this study. Groups A and C are from Oregon, United States; group B is from Inner Mongolia, China; and group D is from Afar, Ethiopia. In Group C, the top five stones are from the Ponderosa mine, the middle three samples (first one imaged in two orientations) are from the Sunstone Butte mine, and the bottom five samples are from the Dust Devil mine. Photos by Qingchao Zhou.

from Gübelin Gem Lab. Samples in groups A and B were copper diffusion treated in our laboratory, and the fluorescence and composition characteristics of the samples in groups C and D were compared to the samples in groups A and B.

Copper Diffusion Treatment. The nearly colorless and light yellow labradorite and andesine feldspar samples were precleaned with aqua regia, buried in a diffusant, and placed in a tube furnace for heating in an air atmosphere. In the corundum crucible, the diffusant used was a mixture of CuO powder (0.05 g) and ZrO_2 powder (5.00 g), with both powders having a purity of 99.9%. The heating and cooling rates were set to 5°C/min, with a soak temperature of 1170°C and a soak time of 72 hours. After the tube furnace was cooled to room temperature, the diffusion-treated feldspar samples were removed, and all samples were repolished to remove damage and surface contamination.

Characterization Techniques. Images of all the samples were captured in a light box (D55 light source)

TABLE 1. Natural labradorite sunstone and plagioclase feldspar samples used in this study.

Group	Locality	Number of samples	Weight (ct)	Description	Purpose
A	Oregon, United States	8	1.73–4.15	Rough, nearly colorless	Diffusion in the authors' lab
B	Inner Mongolia, China	4	0.46–1.78	Rough, light yellow	Diffusion in the authors' lab
C	Oregon, United States	13	2.77–19.13	Rough, red and green	For comparison
D	Afar, Ethiopia	4	0.53–5.54	Rough, red	For comparison

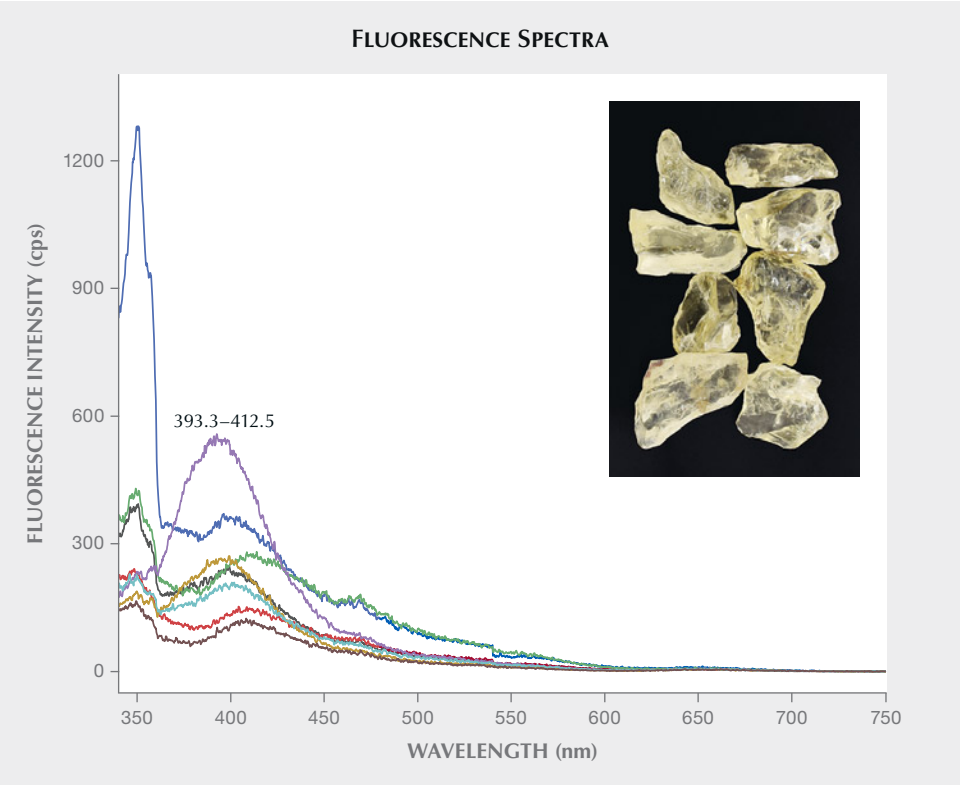

Figure 2. Untreated natural labradorite feldspar rough samples from group A and their corresponding fluorescence spectra. Note that the excitation wavelength is 320 nm. Inset photo by Qingchao Zhou.

under identical conditions to compare color changes. Fluorescence spectra were collected using a Jasco FP-8500 spectrofluorometer with a xenon lamp light source. 3D fluorescence spectral data was collected with a 2000 nm/min scan speed. The excitation wavelengths varied from 200 to 500 nm, with a step size of 5 nm and an excitation bandwidth of 5 nm. The emission spectra were collected with a starting wavelength 10 nm longer than the excitation wavelength and up to 750 nm, with the bandwidth set to 2.5 nm and a data interval of 1 nm. The photomultiplier tube (PMT) voltage was fixed at 600 V for all samples to compare the fluorescence intensity. The 2D emission spectra (340–750 nm) were measured with an excitation wavelength of 320 nm at a response time of 0.5 seconds, a scan speed of 1000 nm/min, and a starting wavelength 20 nm longer than the excitation wavelength. For all samples, the parameter settings of the instrument remained unchanged. Rhodamine B was used as a calibrator of fluorescence intensity and dissolved in ethanol to form a solution of 5 µg/mL. Under the same fluorescence test conditions, the emission wavelength of the Rhodamine B solution was 565 nm and the fluorescence emission intensity was 4500 cps.

Trace element analyses were conducted by laser ablation–inductively coupled plasma–mass spectrometry (LA-ICP-MS). Detailed operating conditions for the laser ablation system and the ICP-MS instrument and data reduction were the same as those described by Liu et al. (2008). Laser sampling was performed using a GeoLas 2005 system (laser wavelength of 193 nm, energy density of 14 J/cm^2, helium carrier gas, ablation spot size of 44 µm, repetition rate of 8 Hz, and laser pulse of 480). An Agilent 7500a ICP-MS instrument (radio-frequency power of 1350 W and dwell time of 6 ms) was used to acquire each individual data set. Element concentrations were calibrated against multiple reference glasses (BCR-2G, BIR-1G, and BHVO-2G) without applying internal standardization. The values of element concentrations used for the U.S. Geological Survey reference glasses are from the GeoReM database (http://georem.mpch-mainz.gwdg.de). Offline selection and integration of background and analyte signals as well as time-drift corrections and quantitative calibrations were performed by ICPMSDataCal. Two spots were measured for each sample, and the spots were selected in the colored area for the colored samples.

RESULTS AND DISCUSSION

Appearance, Fluorescence Spectra, and Copper Concentration of Nearly Colorless Labradorite Feldspar. According to the LA-ICP-MS data in table 2, the un-

TABLE 2. Generalized trace element profiles of all feldspar samples in this study in parts per million weight (ppmw) and mol.% end members.

	Key trace element concentrations (ppmw)					mol.% end members[a]		
	Li	Mg	Cu	Ga	Sr	Ab	An	Or
Ponderosa mine: Natural Oregon labradorite sunstone (red)								
Range	6.1–22.0	838.8–1144.5	25.5–182.6	12.4–13.3	404.2–437.1	32.02–33.89	65.79–67.58	0.31–0.40
Average	15.4	1036.2	128.6	12.9	415.3	32.80	66.87	0.33
Dust Devil mine: Natural Oregon labradorite sunstone (red)								
Range	0.5–27.4	846.0–1017.7	0.1–85.1	15.8–17.0	522.0–641.6	34.46–36.90	62.26–64.84	0.70–0.84
Average	15.1	906.9	54.5	16.3	562.3	35.53	63.71	0.76
Sunstone Butte mine: Natural Oregon labradorite sunstone (red and green)								
Range	0.3–20.6	720.3–844.8	0.4–57.1	14.3–16.9	515.5–653.6	33.79–35.92	63.32–64.42	0.69–2.31
Average	7.1	797.0	19.7	15.1	574.2	34.87	63.88	1.26
Natural Ethiopian labradorite sunstone (red)								
Range	2.0–3.9	329.1–543.5	0.7–18.3	17.1–20.2	258.3–729.4	35.61–36.68	62.05–63.96	0.42–1.26
Average	3.1	420.1	7.3	18.8	396.7	36.24	63.13	0.63
Natural Oregon labradorite (nearly colorless)								
Range	3.1–17.7	827.9–930.8	0.1–18.6	15.5–17.4	524.8–542.1	35.08–37.19	62.01–64.19	0.73–0.80
Average	8.0	889.8	7.8	16.6	534.4	36.28	62.95	0.77
Oregon labradorite after copper diffusion treatment (red)								
Range	14.6–61.4	818.9–912.3	217.7–1086.0	14.2–16.5	510.6–608.5	33.46–35.56	63.65–65.83	0.69–0.79
Average	35.2	865.3	668.5	15.6	568.4	34.65	64.60	0.75
Natural Inner Mongolian andesine (light yellow)								
Range	76.6–123.4	454.7–583.6	0.3–1.1	15.0–16.8	1041.3–1060.1	52.16–53.07	43.70–44.68	3.17–3.22
Average	101.6	496.1	0.7	16.1	1053.6	52.61	44.19	3.20
Inner Mongolian andesine after copper diffusion treatment (red)								
Range	9.0–9.4	475.2–497.6	599.8–789.5	15.9–17.8	1060.0–1074.9	51.66–52.03	44.77–45.15	3.20–3.21
Average	9.3	486.2	694.7	16.5	1064.7	51.91	44.89	3.20

[a]*Abbreviations: Ab = albite, An = anorthite, Or = orthoclase*
Detection limits: 4.25–10.98 ppmw Na, 68.82–285.67 ppmw Ca, 5.85–15.78 ppmw K, 0.78–3.25 ppmw Mg, 0.33–1.49 ppmw Li, 0.63–2.47 ppmw Cu, 0.09–0.53 ppmw Ga, and 0.03–0.12 ppmw Sr

Figure 3. The copper-diffused labradorite feldspar samples used in this study (1.73–4.15 ct). Note that the surfaces were repolished after copper diffusion treatment. Photo by Chengsi Wang.

treated feldspar crystals from Oregon are classified as labradorite, and the average mass concentration of copper is 0.1–18.6 ppmw. The labradorite feldspar crystals were transparent and nearly colorless (figure 2 inset) before the high-temperature copper diffusion treatment. The Oregon labradorite feldspar rough samples used ranged in weight from 1.73 to 4.15 ct. Figure 2 shows the fluorescence spectra of the untreated labradorite feldspar samples, which exhibit weak fluorescence emission peaks centered in the wavelength range from 400 to 420 nm under 320 nm excitation. The intensity of the fluorescence emission peak is 100–600 cps. It must be mentioned that there is another set of fluorescence emission peaks at ~350 nm. These weak fluorescence emissions may be related to the presence of copper or other trace elements contained in the feldspar crystals, but this has not been verified.

Changes in Labradorite Feldspar Appearance, Fluorescence Spectra, and Copper Concentration After Copper Diffusion Treatment. Figure 3 shows the eight labradorite feldspar samples after copper diffusion treatment. To better show the color changes, the surfaces of all samples were repolished after treatment. It can be clearly seen from the figure that a wide variety of phenomena were produced, consistent with those reported by others (Emmett and Douthit, 2009). In some cases, it appears the copper diffuses by bulk (or lattice) diffusion and the red color distribution is uniform; in others, pipe or short circuit diffusion is predominant and the red areas in the samples are intermittently distributed. In addition, the areas that were in contact with the diffusant and have not been repolished show obvious damage and darkening.

From the 3D fluorescence pattern of a red labradorite feldspar diffused in the authors' laboratory

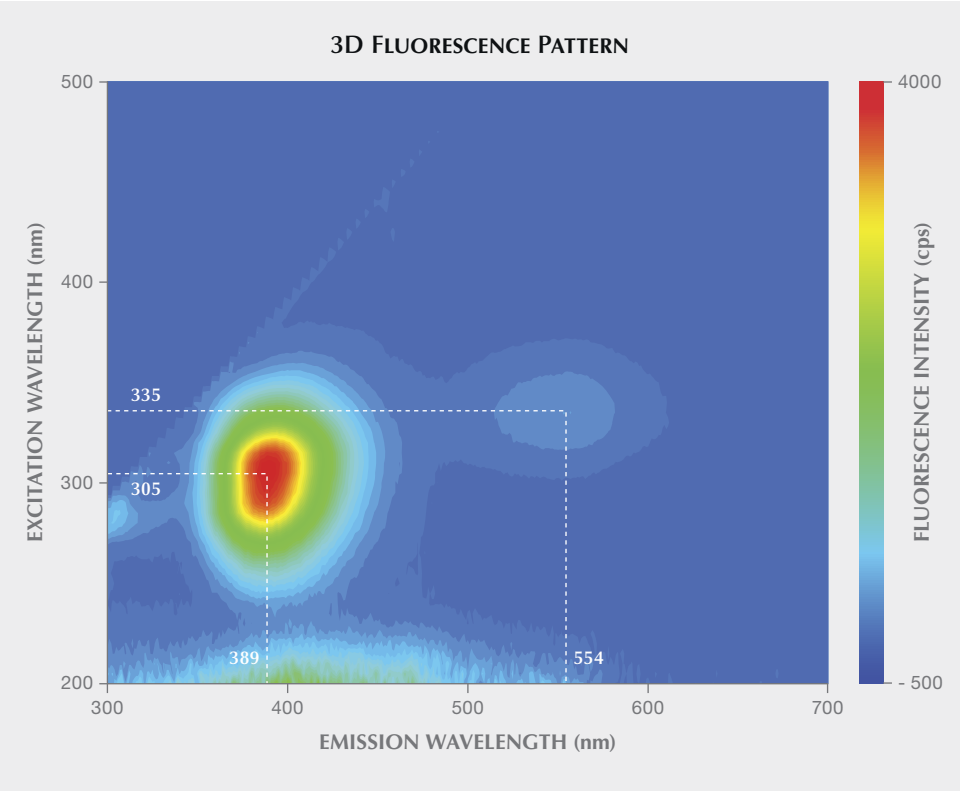

Figure 4. The 3D fluorescence pattern of a red labradorite feldspar diffused in the authors' laboratory shows two emission maxima at 389 and 554 nm and their corresponding optimal excitation wavelengths at 305 and 335 nm.

(figure 4), we found that the fluorescence emission consisted of two emission peaks at 389 and 554 nm, with their corresponding optimal excitation wavelengths at 305 and 335 nm. After identifying the main emission peaks, a specific excitation wavelength of 320 nm was chosen to balance the intensity of these two emission peaks. We chose the excitation wavelength of 320 nm so that the fluorescence emissions at both 389 nm and 554 nm could be excited well.

The fluorescence spectra in figure 5 show that all the diffused red labradorite samples exhibit two typical fluorescence emission peaks under the 320 nm excitation. Instead, the fluorescence emissions at ~350 nm in untreated labradorite samples disappeared. The wavelength of the first emission peak is 390.7–396.3 nm with an intensity of 3550–4992 cps, while the wavelength of the second emission peak is ~554 nm with an intensity of 232–620 cps. The spectral parameters are summarized in table 3. The different fluorescence characteristics of the labradorite feldspar samples under 320 nm UV light before and after copper diffusion treatment are shown in the figure 5 inset. The untreated sample shows no obvious fluorescence, but the treated one exhibits intense purple-red fluorescence. Based on the fluorescence spectra or fluorescence characteristics, it is potentially possible to determine whether a labradorite feldspar has undergone copper diffusion treatment. Although we are not aware of any copper-diffused red labradorite feldspar currently on the market, it is indeed feasible to prepare red labradorite with this treatment.

According to the LA-ICP-MS data in table 2, the copper concentration of these labradorite feldspar samples increased from 0.1–18.6 ppmw to 217.7–1086.0 ppmw with treatment. Therefore, we speculate that these two fluorescence emission peaks are related to copper. Based on previous studies of copper, CuO, Cu_2O, and $CuZr_2(PO_4)_3$ (Boutinaud et al., 1992, 1995; Lutz et al., 1997; Puppalwar et al., 2011), we attribute the strong fluorescence emission peak near 394 nm to Cu^+ ions, and the fluorescence emission peak near 554 nm to the Cu^+-Cu^+ dimers (Zhou et al., 2022a,b,c). The dimers form when the Na^+ sites in labradorite are simultaneously occupied by two Cu^+ ions with a rather short Cu-Cu distance of 2.40 Å—i.e., below the interatomic distance in copper metal (2.56 Å). In other words, the typical fluorescence spectra or characteristics that are used to identify our diffusion-treated red labradorite feldspar can be explained by the residual Cu^+ ions within the feldspar.

Appearance, Fluorescence Spectra, and Copper Concentration of Light Yellow Andesine Feldspar. According to the LA-ICP-MS data in table 2, the untreated

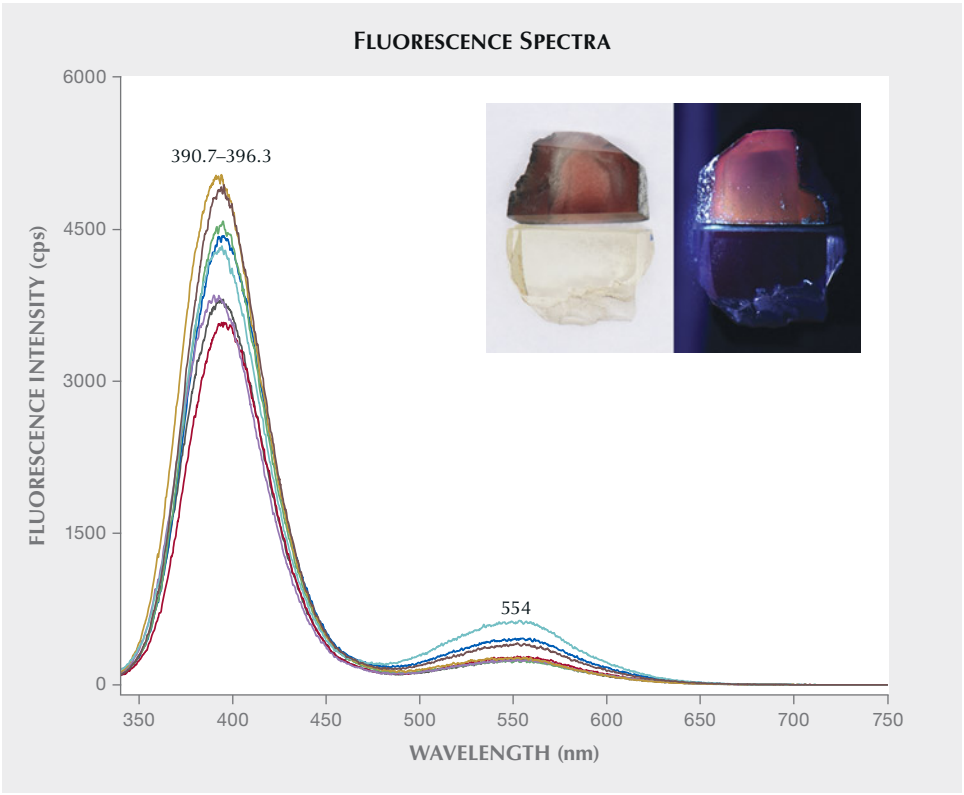

Figure 5. Fluorescence spectra of the eight diffusion-treated red labradorite feldspar specimens from group A. Note that the excitation wavelength is 320 nm. The inset photos show the appearance of a labradorite feldspar before and after copper diffusion experiment under D55 light and 320 nm UV light. Photos by Qingchao Zhou.

feldspar crystals from Inner Mongolia are classified as andesine, and the average mass concentration of element copper is 0.3–1.1 ppmw. The andesine feldspar crystals are transparent and light yellow (figure 6 inset) before the high-temperature copper diffusion treatment. The weights of the Inner Mongolian andesine feldspar rough samples ranged from 0.46 to 1.78 ct. Figure 6 shows the fluorescence spectra of the untreated andesine feldspar samples, which exhibit weak fluorescence emission in the 400–410 nm wavelength

TABLE 3. Summary of fluorescence parameters of all samples in this study.

Locality	Wavelength (Cu^+) (nm)	Intensity (Cu^+) (cps)	Wavelength (Cu^+-Cu^+ dimer) (nm)	Intensity (Cu^+-Cu^+ dimer) (cps)
Ponderosa, Oregon	388.2–389.0	433–877	~554	19–21
Dust Devil, Oregon	392.1–393.5	292–568	Not obvious	—
Sunstone Butte, Oregon	394.2–405.2	207–360	Not obvious	—
Afar region, Ethiopia	402.1–413.0	74–367	Not obvious	—
Labradorite samples diffused in the authors' lab	390.7–396.3	3550–4992	~554	232–620
Andesine samples diffused in the authors' lab	397.4–398.6	3942–6486	~554	243–495

range under 320 nm excitation. The intensity of the fluorescence emission peak is 190–550 cps. It must be mentioned that there is another set of fluorescence emission peaks at ~350 nm. These weak fluorescence emissions may also be related to the presence of copper or other trace elements contained in the feldspar crystals, but this has not been verified.

Changes in Andesine Feldspar Appearance, Fluorescence Spectra, and Copper Concentration After Copper Diffusion. The insets in figures 6 and 7 show the appearance of four andesine feldspar samples before and after copper diffusion treatment, respectively. The color of these samples changed from light yellow to light red. The fluorescence spectra in figure 7 clearly show that all of the copper-diffused red andesine feldspar samples also exhibit two typical fluorescence emission peaks under 320 nm excitation. Instead, the fluorescence emissions at ~350 nm in untreated andesine samples disappeared. The wavelength of the first emission peak is 397.4–398.6 nm with an intensity of 3942–6486 cps, while the wavelength of the second emission peak is ~554 nm with an intensity of 243–495 cps. These spectral parameters are summarized in table 3. According to the LA-ICP-MS data in table 2, the copper concentration of these andesine feldspar samples increased from 0.3–1.1 ppmw to 599.8–789.5 ppmw following copper diffusion treatment. The related changes in copper concentration and fluorescence of group B andesine feldspar subjected to copper diffusion are essentially the same as those of group A labradorite feldspar. We found that the strong fluorescence emission of diffusion-treated red labradorite and andesine feldspar is potentially a key indicator of treatment, since the strong fluorescence is difficult to attenuate through post-annealing treatment.

Appearance, Fluorescence Spectra, and Copper Concentration of Natural Labradorite Sunstone from Oregon and Ethiopia. To determine whether the fluorescence characteristics observed in our copper-diffused red feldspar samples matched those of natural red labradorite sunstone from different localities, we systematically characterized untreated red labradorite sunstone from three different mines in Oregon and also from Ethiopia. To our knowledge, the typical fluorescence spectra or characteristics of copper-diffused red feldspar under 305–335 nm UV

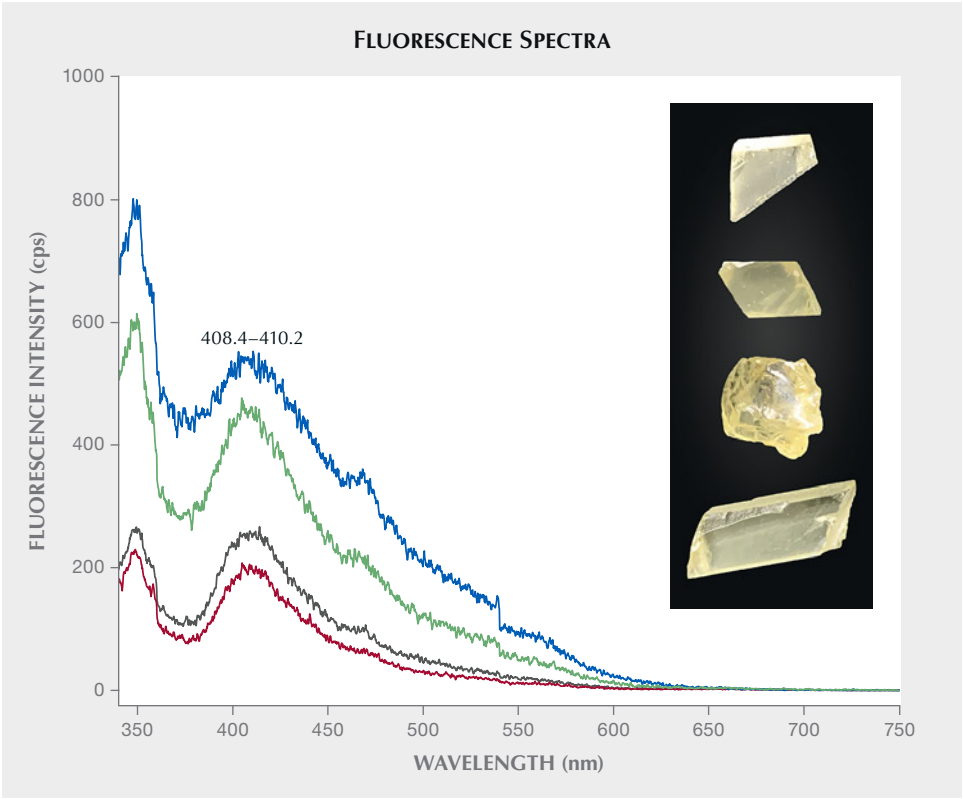

Figure 6. Untreated natural andesine feldspar rough samples from group B and their corresponding fluorescence spectra. Note that the excitation wavelength is 320 nm. Inset photo by Qingchao Zhou.

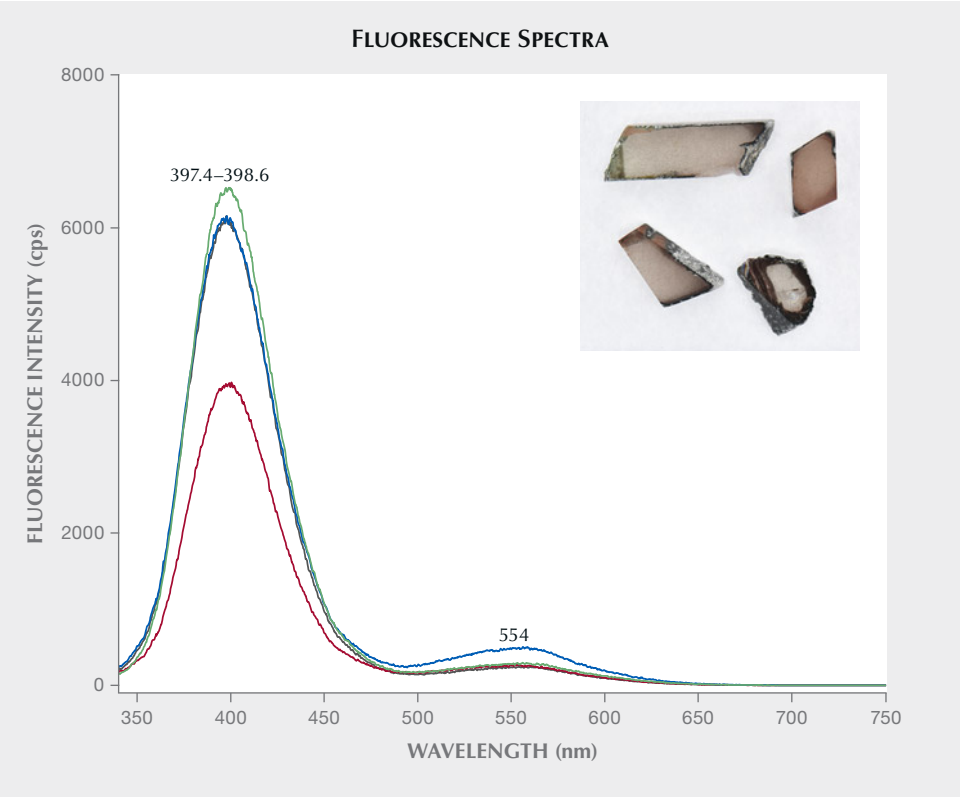

Figure 7. Fluorescence spectra of copper-diffused red andesine feldspar samples from group B. Note that the excitation wavelength is 320 nm. The inset photo shows the appearance of the andesine feldspar samples after the copper diffusion experiment under D55 light. Photo by Qingchao Zhou.

light excitation have not been previously published or reported.

Figure 8 shows the appearance of the selected 17 natural labradorite sunstones from different localities, arranged by decreasing fluorescence intensity from left to right in each row. The natural labradorite sunstones show various shades of red, and a small number of samples appear green (AD741) or display red-green dichroism (AD777). The color distribution of these natural labradorite sunstones analyzed is mostly uneven, but all of them exhibit good transparency.

All the natural labradorite sunstones exhibit considerably weaker fluorescence emission than the copper-diffused red labradorite feldspar samples (figure 9). The emission wavelength of the labradorite sunstones from Ponderosa is 388.2–389 nm, and that of the labradorite sunstones from Dust Devil is 392.1–393.5 nm. The range of peak intensity values at 554 nm of the labradorite sunstones from Ponderosa is only 433–877 cps, and that for the labradorite sunstones from Dust Devil is only 292–568 cps. In terms of the fluorescence spectra, the natural labradorite sunstones from the Sunstone Butte mine in Oregon and the Afar region of Ethiopia are somewhat like those of the nearly colorless labradorite feldspar samples in figure 2. The emission wavelength fluctuates in a relatively wide range (394.2–413.0 nm), and the peak intensity is also very weak (74–367 cps). These spectral parameters are also summarized in table 3. For the natural labradorite sunstones from the Sunstone Butte mine with dichroism (AD777), the fluorescence emission spectra of both the red and green orientations were tested, and the results were basically the same. The inert fluorescence of sample AD777 under 320 nm UV light is shown in the inset of figure 9. The natural labradorite sunstone samples in figure 8 are arranged by the decreasing peak intensity in each row, but no direct correlation was found between fluorescence emission intensity and the color appearance of natural labradorite sunstone.

The fact that natural labradorite sunstone occurs in Oregon is recognized by gemological research institutions around the world. By comparing the fluorescence spectra of the copper-diffused labradorite feldspar samples with the natural labradorite sunstone, we have observed that strong fluorescence is potentially key evidence for copper diffusion treatment in labradorite, since none of the natural labradorite sunstones tested exhibited fluorescence of the same strength.

According to the LA-ICP-MS data in table 2, the copper concentration of natural labradorite sunstones

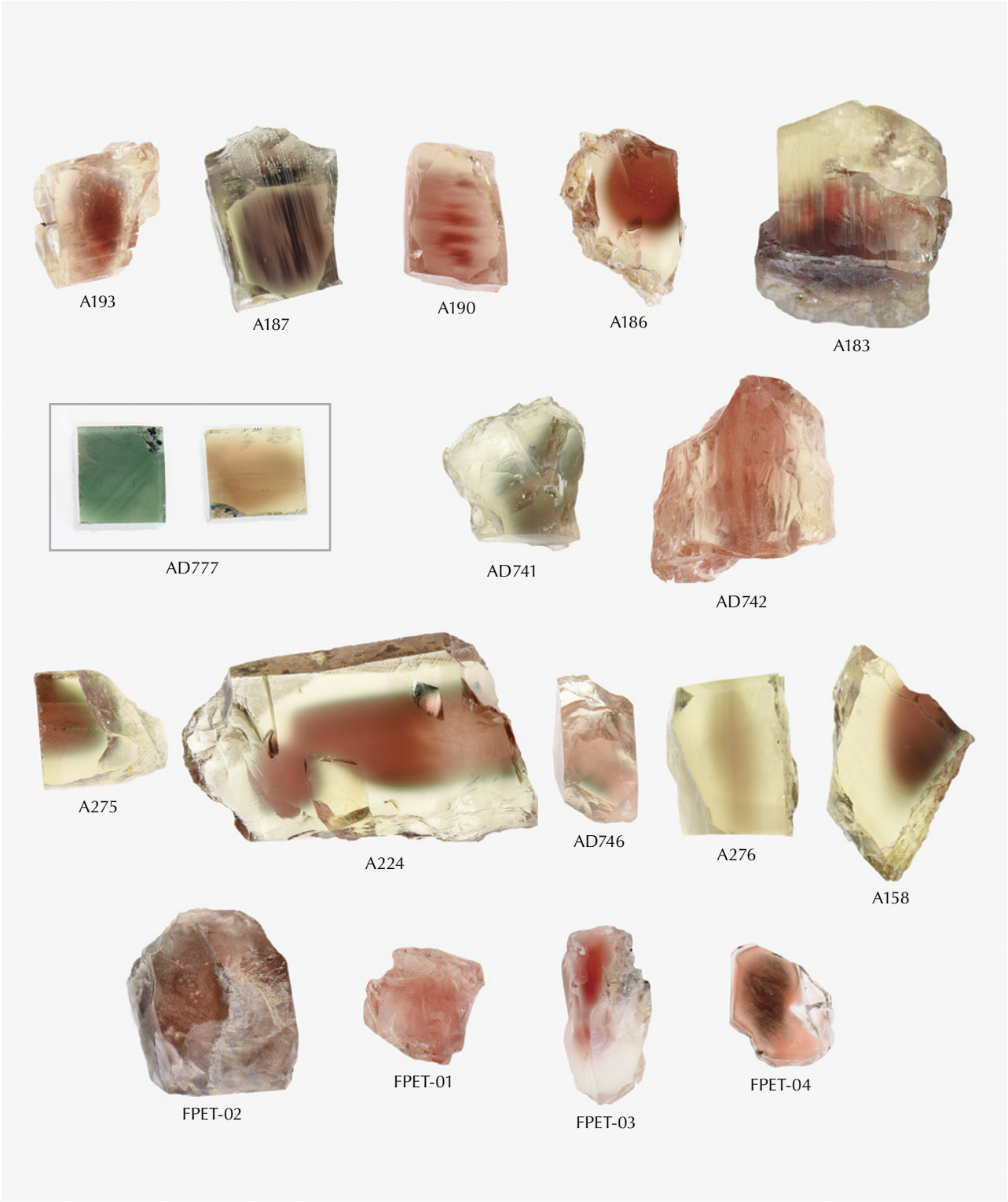

Figure 8. Natural labradorite sunstones from different localities in Oregon and Ethiopia (1.73–4.15 ct). Row 1 (top): Ponderosa mine, Oregon. Row 2: Sunstone Butte mine, Oregon. Row 3: Dust Devil mine, Oregon. Row 4 (bottom): Ethiopia. The corresponding GIA or Gübelin Gem Lab sample number is marked in the figure. Two polarization directions were imaged for AD777. Photo by Qingchao Zhou.

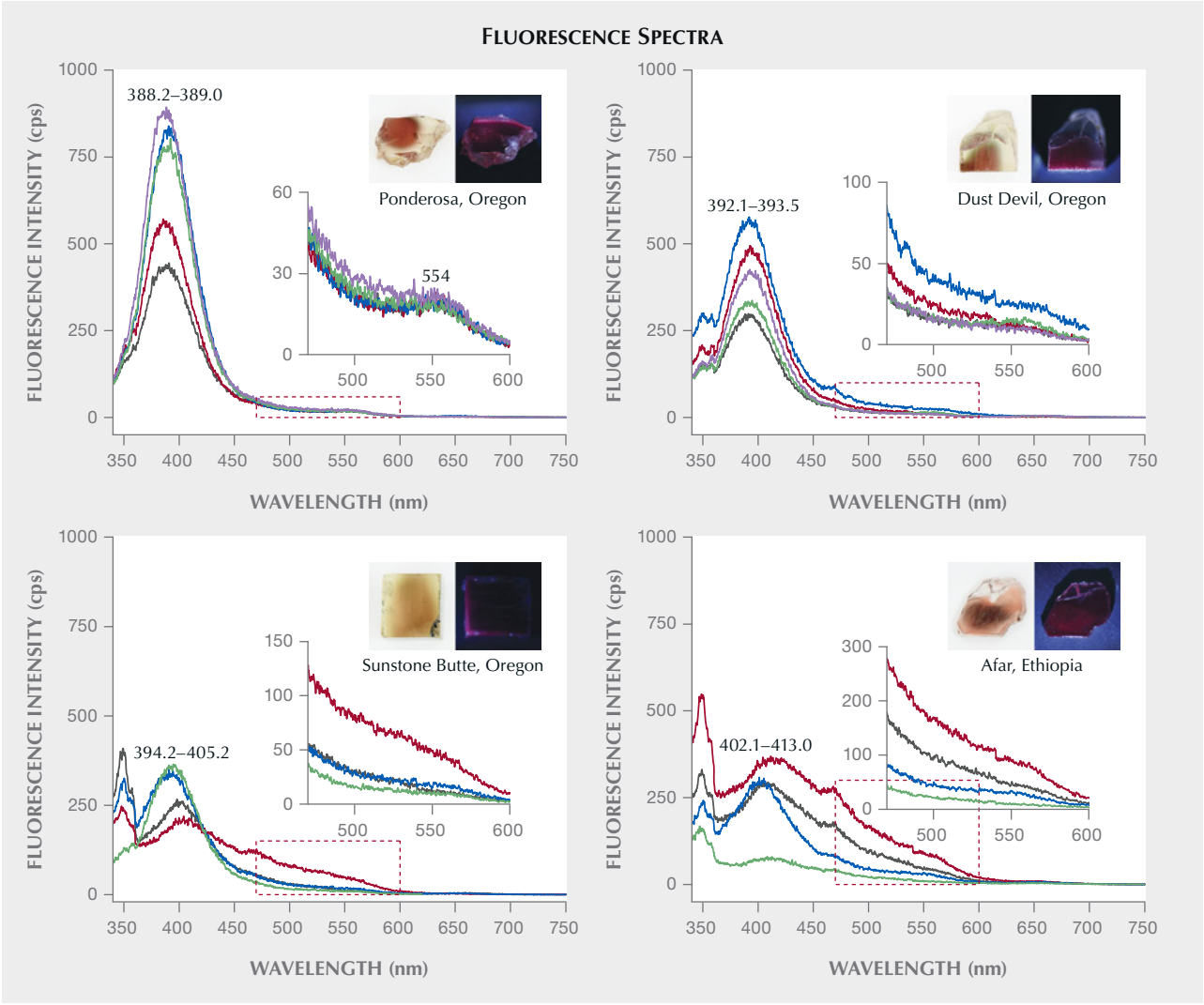

Figure 9. Fluorescence spectra of natural labradorite sunstones from Oregon (Ponderosa, Dust Devil, and Sunstone Butte mines) and the Afar region of Ethiopia. Note that the excitation wavelength is 320 nm. The appearance of typical natural labradorite sunstones (A186, AD777, A275, FPET-04) under D55 light and 320 nm UV light are shown in the upper right insets for each set of spectra. Inset photos by Chengsi Wang. The weaker emission can be seen in the center-inset enlargement plots.

from different localities is 0.1–182.6 ppmw, which is lower than that of the copper-diffused red labradorite feldspar samples (217.7–1086.0 ppmw). The comparative analysis of the natural labradorite sunstones reveals that the fluorescence intensity apparently has no direct correlation with the copper concentration measured by LA-ICP-MS, because the valence state of copper was not considered. Therefore, we infer that the weak fluorescence is due to the fact that copper in natural labradorite sunstone is mainly present in the metallic zero-valent form (Cu^0), since copper microinclusions (such as copper flakes) have been observed in many natural labradorite sunstones.

Table 3 summarizes the fluorescence emission wavelengths and peak intensities of the samples tested, including the natural labradorite sunstones from different localities and the copper-diffused red labradorite and andesine feldspars we experimentally produced.

Figure 10 presents a plot of fluorescence intensity vs. major peak wavelength of Cu^+ using the data summarized in table 3, which displays an obvious separation between the natural labradorite sunstones before and after copper diffusion treatment. The discrimination between natural labradorite sunstone (weak fluorescence) and copper-diffused labradorite feldspar (strong fluorescence) is very high. Moreover,

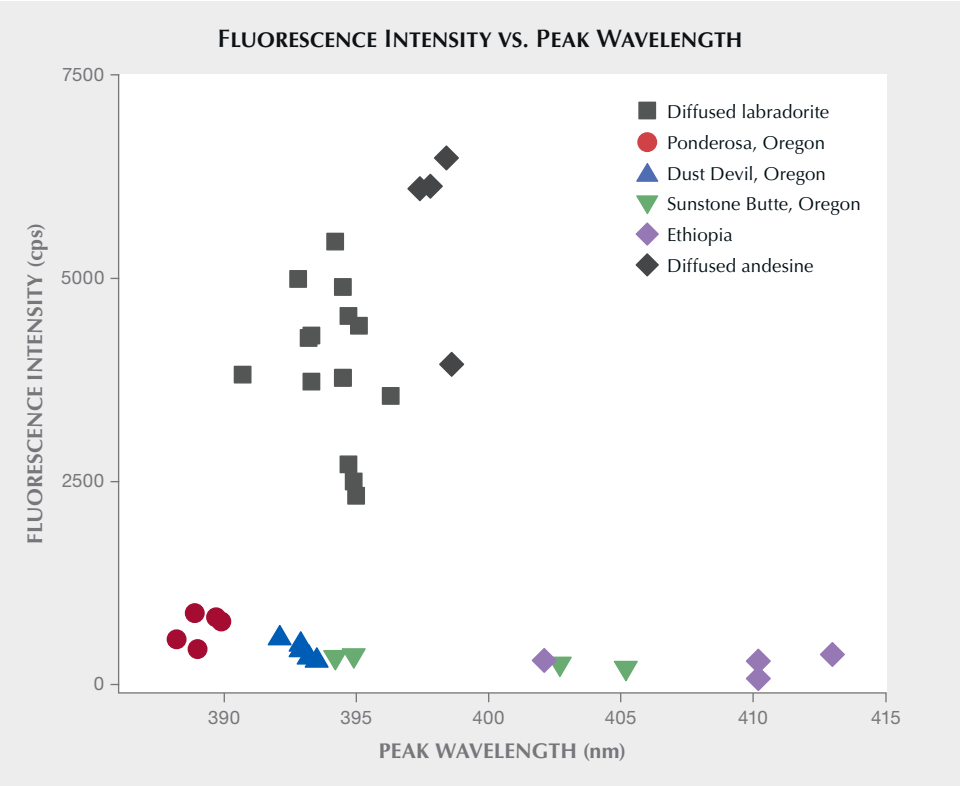

Figure 10. The plot of fluorescence intensity vs. peak wavelength shows an obvious separation between the copper-diffused red labradorite feldspar samples and natural labradorite sunstone. The fluorescence spectral parameters of all samples are listed in table 3.

the corresponding coordinates of all the copper-diffused red andesine feldspars are distributed in the area of strong fluorescence. Although the number of natural labradorite sunstones we analyzed is limited, they represent most of the localities worldwide, and we introduced red labradorite and andesine feldspar samples diffused in our laboratory as the control group. Therefore, we believe that the proposed identification method using fluorescence spectroscopy holds promise for copper diffusion treatment of labradorite.

CONCLUSIONS

In this study, we applied a copper diffusion treatment to nearly colorless or light yellow labradorite and andesine feldspars in order to modify their colors to mimic natural red/green labradorite colors. We found that the typical fluorescence emissions at 390–398 nm and at approximately 554 nm were stronger in the treated material. By comparing the fluorescence spectra of the labradorite and andesine feldspars before and after copper diffusion, the presence of strong fluorescence (320 nm excitation) was verified as key evidence of treatment in this study. Moreover, the natural labradorite sunstones from Oregon and Ethiopia analyzed exhibit weak fluorescence (320 nm excitation), similar to the untreated nearly colorless labradorite.

As a non-destructive testing method, fluorescence spectroscopy can be quickly applied to the questionable stones to identify very high emission counts and to decide if detecting high copper levels with LA-ICP-MS is warranted. Admittedly, more stones need to be tested to further validate the reliability and accuracy of this method. We still believe this new identification method will help to verify the authenticity of material from Tibet or other regions as new localities of natural sunstone, increasing confidence for consumers in purchasing these gems.

ABOUT THE AUTHORS

Dr. Zhou (zhouqc229@163.com) is a lecturer at the School of Jewelry, West Yunnan University of Applied Sciences in Tengchong. Dr. Wang (chance_w@foxmail.com) is a postdoctoral researcher, and Dr. Shen (shenxt@cug.edu.cn, corresponding author) is a distinguished professor, at the Gemmological Institute, China University of Geosciences in Wuhan.

ACKNOWLEDGMENTS

This work was supported by the Special Basic Cooperative Research Programs of Yunnan Provincial Undergraduate Universities' Association (grant no. 202101BA070001-028).

REFERENCES

Abduriyim A. (2008) Gem News International: Visit to andesine mines in Tibet and Inner Mongolia. *G&G*, Vol. 44, No. 4, pp. 369–371.

——— (2009a) A mine trip to Tibet and Inner Mongolia: Gemological study of andesine feldspar. *GIA News from Research*, Sept. 10, https://www.researchgate.net/publication/237365635_A_Mine_Trip_to_Tibet_and_Inner_Mongolia_Gemological_Study_of_Andesine_Feldspar

——— (2009b) The characteristics of red andesine from the Himalaya Highland, Tibet. *Journal of Gemmology*, Vol. 31, No. 5-8, pp. 283–298.

Abduriyim A., Laurs B.M. (2010) Andesine in Tibet: A second field study. *InColor*, No. 15, Fall–Winter, pp. 62–63.

Boutinaud P., Parent C., Le Flem G., Pedrini C., Moine B. (1992) Spectroscopic investigation of the copper (I)-rich phosphate $CuZr_2(PO_4)_3$. *Journal of Physics: Condensed Matter*. Vol. 4, No. 11, pp. 3031–3042, http://dx.doi.org/10.1088/0953-8984/4/11/026

Boutinaud P., Garcia D., Parent C., Faucher M., Le Flem G. (1995) Energy levels of Cu^+ in the oxide insulators $CuLaO_2$ and $CuZr_2(PO_4)_3$. *Journal of Physics and Chemistry of Solids*, Vol. 56, No. 9, pp. 1147–1154, http://dx.doi.org/10.1016/0022-3697(95)00044-5

Cao X. (2013) Exploration on copper diffusion treatment of colorless labradorite. Master's thesis, China University of Geosciences [in Chinese].

Emmett J., Douthit T. (2009) Copper diffusion in plagioclase. *GIA News from Research*, Aug. 21, https://www.gia.edu/doc/Cu-diffusion-Emmett.pdf.

Hofmeister A.M., Rossman G.R. (1985) Exsolution of metallic copper from Lake County labradorite. *Geology*, Vol. 13, No. 9, pp. 644–647, http://dx.doi.org/10.1130/0091-7613(1985)13%3C644:EOMCFL%3E2.0.CO;2

Hughes R.W. (2010) In search of the lost andesine mines: Part I: Hunting Barack Osama in Tibet. http://www.lotusgemology.com/index.php/library/articles/153-hunting-barack-osama-in-tibet-in-search-of-the-lost-andesine-mines

——— (2011a) Andesine: Timeline of a controversy. https://www.lotusgemology.com/images/pdf/hughes-2011-andesine-timeline-of-a-controversy.pdf

——— (2011b) Faith: In search of the lost andesine mines. *The Guide*, Vol. 30, No. 6, pp. 1, 4–9, 13.

Johnston C.L., Gunter M.E., Knowles C.R. (1991) Sunstone labradorite from the Ponderosa mine, Oregon. *G&G*, Vol. 27, No. 4, pp. 220–233, http://dx.doi.org/10.5741/GEMS.27.4.220

Kiefert L., Wang C., Sintayehu T., Link K. (2019) Sunstone labradorite-bytownite from Ethiopia. *Journal of Gemmology*, Vol. 36, No. 8, pp. 694–696.

Liu Y., Hu Z., Gao S., Günther D., Xu J., Gao C., Chen H. (2008) *In situ* analysis of major and trace elements of anhydrous minerals by LA-ICP-MS without applying an internal standard. *Chemical Geology*, Vol. 257, No. 1-2, pp. 34–43, http://dx.doi.org/10.1016/j.chemgeo.2008.08.004

Lutz T., Estournes C., Merle J.C., Guille J.L. (1997) Optical properties of copper-doped silica gels. *Journal of Alloys and Compounds*, Vol. 262-263, pp. 438–442, http://dx.doi.org/10.1016/S0925-8388(97)00350-2

Nishida N., Kimata M. (2002) Identification of microinclusions in the nanometer dimension by electron microprobe analysis. *Japanese Magazine of Mineralogical and Petrological Sciences*, Vol. 31, pp. 268–274 [in Japanese], http://dx.doi.org/10.2465/gkk.31.268

Peretti A., Villa I., Bieri W., Hametner K., Dorta L., Fontaine G., Meier M., Günther D. (2011a) Distinguishing natural Tibetan copper-bearing andesine from its diffusion-treated counterparts using advanced analytical methods. *Contributions to Gemmology*, No. 10, pp. 1–105.

Peretti A., Bieri W., Hametner K., Günther D., Hughes R.W., Abduriyim A. (2011b) Fluid inclusions confirm authenticity of Tibetan andesine. *InColor*, No. 17, pp. 50–55.

Puppalwar S.P., Dhoble S.J., Kumar A. (2011) Improvement of photoluminescence of Cu^+ ion in Li_2SO_4. *Luminescence*, Vol. 26, No. 6, pp. 456–461, http://dx.doi.org/10.1002/bio.1252

Rossman G.R. (2011) The Chinese red feldspar controversy: Chronology of research through July 2009. *G&G*, Vol. 47, No. 1, pp. 16–30, http://dx.doi.org/10.5741/GEMS.47.1.16

Schorr D., Hughes R.W., Abduriyim A., Rossman G., Peretti A., McClure S., Emmett J.L. (2012) Andesine & labradorite from Tibet, Inner Mongolia, Mexico & Oregon: A panel discussion. https://www.lotusgemology.com/images/pdf/andesine-questions.pdf

Sun Z., Renfro N.D., Palke A.C., Breitzmann H., Muyal J., Hand D., Hain M., McClure S.F., Katsurada Y., Miura M., Rossman G.R. (2020) Gem News International: Sunstone plagioclase feldspar from Ethiopia. *G&G*, Vol. 56, No. 1, pp. 184–188.

Thirangoon K. (2009) Effects of heating and copper diffusion on feldspar: An ongoing research. *GIA News from Research*, May 29, https://www.gia.edu/ongoing-research/effects-of-heating-and-copper-diffusion-on-feldspar

Wang C., Shen A.H., Palke A.C., Heaney P.J. (2019) Color origin of the Oregon sunstone. In *Proceedings of the 36th International Gemmological Conference IGC*, Nantes, France, August 27–31, pp. 71–74.

Wang L. (2012) Study on the feldspar from Guyang County, Inner Mongolia, Master's thesis, China University of Geosciences [in Chinese].

Wang W., Lan Y., Lu T., Jiang W., Chen C., Li Q., Chen Z., Xie J. (2011) Documental report of geological field investigation on "red feldspar" in Tibet, China. *Journal of Gems and Gemmology*, Vol. 13, No. 1, pp. 1–5 [in Chinese].

Zhou Q., Wang C., Shen A.H. (2022a) Copper nanoparticles embedded in natural plagioclase mineral crystals: In situ formation and third-order nonlinearity. *The Journal of Physical Chemistry C*, Vol. 126, No. 1, pp. 387–395, http://dx.doi.org/10.1021/acs.jpcc.1c09145

——— (2022b) Application of high-temperature copper diffusion in surface recoloring of faceted labradorites. *Minerals*, Vol. 12, No. 8, article no. 920, http://dx.doi.org/10.3390/min12080920

——— (2022c) High-temperature diffusion of Cu^{2+} ions into natural plagioclase crystals: The role of Li_2O. *The Journal of Physical Chemistry C*, Vol. 126, No. 29, pp. 12244–12250, http://dx.doi.org/10.1021/acs.jpcc.2c03088

Composition and Spectral Characteristics of Porcelain-Treated Turquoise

Liying Huang, Quanli Chen, Yan Li, Zuowei Yin, Fengshun Xu, Xinxin Gao, and Yang Du

To meet the ever-increasing demand for high-quality natural turquoise, a novel treatment technique utilizing an inorganic additive appeared in the Chinese market around 2019. Turquoise with this treatment bears a strong resemblance to high-quality natural turquoise, with a fine structure and high surface luster, and is known in the Chinese trade as "porcelain-treated" turquoise. This material was characterized by routine gemological methods, environmental scanning electron microscopy, and spectroscopic methods including infrared, ultraviolet/visible, energy-dispersive X-ray fluorescence, and laser Raman spectroscopy. The infrared and ultraviolet/visible reflectance spectra of porcelain-treated turquoise are difficult to distinguish from untreated turquoise. However, porcelain-treated turquoise can be effectively identified by its surface features in combination with low specific gravity, strong luster, high silica concentration (>8.29 wt.%), high atomic ratio of iron to aluminum (>0.22), and low atomic percentage of phosphorus (<37.5%).

Turquoise is hydrous copper aluminum phosphate with a general chemical formula of $CuAl_6(PO_4)_4(OH)_8 \cdot 4H_2O$. It is widely distributed across localities such as China, Egypt (Mansour, 2014), Chile (Evans and Southward, 1914), the United States (Harbottle and Weigand, 1992; Hedquist 2016), Iran (Beale, 1973; Ovissi et al., 2017), and Mexico (Zalinski, 1907; Weigand et al., 1977). The main Chinese sources are Hubei Province (Chen et al., 2012), Shanxi Province (Luo et al., 2017), the Xinjiang Uyghur Autonomous Region (Liu et al., 2018), Anhui Province (Chen and Qi, 2007), and Henan Province (Zhou and Jiang, 2005). Zhushan County in Hubei is the world's largest commercial source, and material from there usually develops dark iron veins because of its association with phosphate, iron, and copper ores (Tu, 1997).

Turquoise with various colors, fine texture, and moderate hardness has generally been used as carving material. The earliest turquoise artifacts in China were found at the Jiahu site in Wuyang County, Henan Province, and were dated back to 7000–5800 BCE (Yang et al., 2017). Porcelain is a world-renowned Chinese invention that originated from pottery around the middle of the Shang Dynasty in the sixteenth century BCE (Song, 2008). The term "porcelain" is used in China to describe the finest luster of turquoise, and high-quality material with such luster is referred to as "natural porcelain" turquoise (box A). This term was adopted because of the resemblance to the soft, bright, and long-lasting luster of porcelain. The luster of turquoise depends on the structure (density) of the material and the quality of polish.

In Brief

- A novel "porcelain" treatment technique for turquoise produces a color and luster extremely similar to that of high-quality untreated turquoise.
- Treatment with silicate filling may be used on porous or "loose" turquoise.
- Porcelain-treated turquoise can be identified by its surface features and a combination of characteristics such as low specific gravity, strong luster, and high silica content (>8.29 wt.%).

See end of article for About the Authors and Acknowledgments.
Gems & Gemology, Vol. 58, No. 4, pp. 438–457,
http://dx.doi.org/10.5741/GEMS.58.4.438

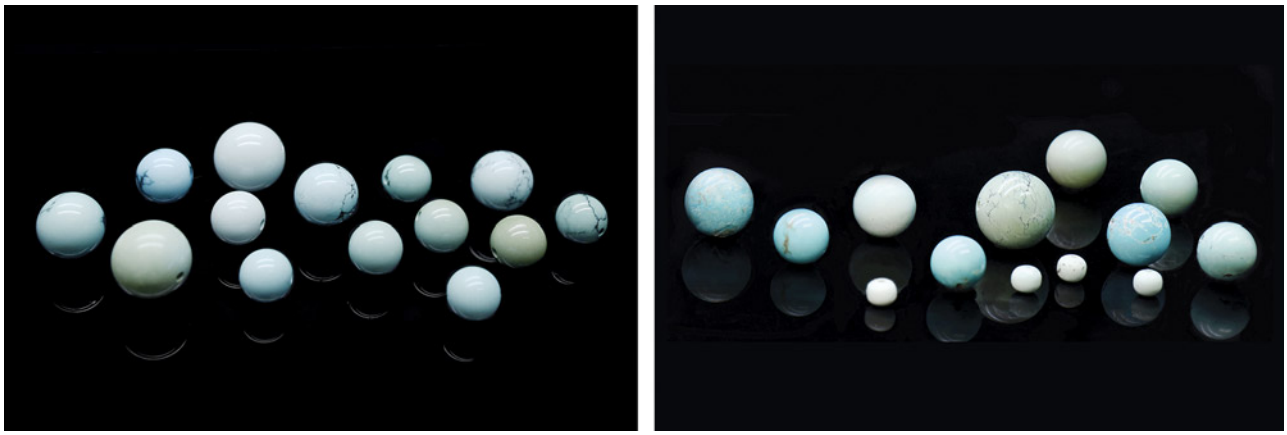

Figure 1. The appearance of natural high-quality turquoise and porcelain-treated turquoise. Left: Natural high-quality turquoise with various colors (the rightmost bead has a diameter of 10.0 mm). Right: Porcelain-treated turquoise with appearance and colors similar to those of natural high-quality turquoise (the smallest bead measures 6.0 × 5.0 mm). Photos by Liying Huang.

In the current Chinese market, natural turquoise is broadly divided into three categories according to density: porcelain, medium-quality, and porous (box A). Porcelain turquoise is sought after for its high luster, uniform color, compact texture, and high hardness. Sky blue porcelain turquoise is regarded as the finest quality. Porous turquoise of low hardness and very light color is regarded as the lowest in quality.

Turquoise is typically a polycrystalline aggregate. Its various colors are attributed to the differences in the type and content of its constituent elements (Luan et al., 2004). Water content and porosity can also affect the color (Foord and Taggart, 1998; Chen, 2009; Liu, 2019). As weathering increases, both crystalline and structural water in turquoise are lost, resulting in a reduction in the structural integrity and a lightening of its color (Chen, 2009). If the space between grain boundaries is small, turquoise usually has low porosity, high density, high hardness, bright color, and strong surface luster. Conversely, if the space between microcrystals is large, the porosity will be high with low hardness (Chen, 2009), which will result in light-colored turquoise with low surface luster. These pores can be filled, to a certain extent, by wax/resin/polymer injection or immersion treatment methods to enhance luster and color. Pore filling not only facilitates turquoise processing but also increases stability and durability (Koivula et al., 1992; McClure et al., 2010; Ou et al., 2016).

In recent decades, the supply of high-quality turquoise has steadily fallen in the Chinese market (Chen, 2009), causing higher prices. Most low- and medium-quality natural turquoise has a light or uneven color, low luster, porous texture, and a tendency to crack (Chen et al., 2010a). These problems make it difficult to meet the ever-increasing consumer demand. Therefore, imitations and "optimized" (treated) products have been on the rise in the world market. Some merchants use other natural gemstone materials to imitate the color of turquoise by dyeing (Xie et al., 2010; Zhu et al., 2016; Schwarzinger and Schwarzinger, 2017), and there are a few synthetic versions available (Choudhary, 2010; Pristacz et al., 2013). However, these are not accepted in the Chinese market.

To enhance the color, texture, and density of low- and medium-quality turquoise, the main method is to inject an organic binder under atmospheric or higher pressures (Koivula et al., 1992; McClure et al., 2010). This process maximizes yield while improving durability. This treatment can be detected by infrared absorption spectroscopy, in which absorption bands are produced by the typical $\nu_s(CH_2)$ symmetrical stretching vibration, $\nu_{as}(CH_2)$ asymmetric stretching vibration, and $\nu(C=C)$ stretching vibration of organic polymers (Xu and Di, 2018).

Surprisingly, a novel technique utilizing an inorganic additive was introduced to the Chinese market in 2019. This method uses an inorganic binder to effectively improve the luster and color of low- and medium-quality material so that it resembles high-quality turquoise (figure 1). The study of this "porcelain-treated" turquoise is relatively new, and there are few reports on the process itself. Only Deng et al. (2019) have studied a specific porcelain treatment and the silicate solution used, in which the molar ratio of the sodium silicate to potassium silicate was 3.5:1.0. Meanwhile, many merchants treat turquoise to raise its price but do not disclose the details of the process. At present, the identification of porcelain-treated

BOX A: CATEGORIES OF TURQUOISE IN THE CHINESE MARKET

Figure A-1. A variety of high-quality "natural porcelain" turquoise products from Hubei Province. A: Sky blue, 56.7 × 35.2 × 24.6 mm, 56.20 g. B: Greenish blue, 32.6 × 25.7 × 10.6 mm, 12.25 g. C: Bluish green, 36.2 × 28.0 × 13.0 mm, 13.92 g. D: Yellowish green, 15.5 × 16.3 × 19.2 mm, 6.5 g. E: Sky blue, 15.9 mm diameter, 5.63 g. F: Greenish blue, 64.7 × 37.5 × 19.2 mm, 48.75 g. Photos by Ren Fei, Jin Yu Turquoise Company.

The turquoise used for "porcelain" treatment is mostly porous, with a loose texture. Silicate filling is used to enhance its color and luster, imitating the appearance of high-quality untreated turquoise. Following this process, the material is called "porcelain-treated" turquoise. The related terms are defined as follows.

"Natural porcelain" turquoise (specific gravity ≥2.70): High-quality turquoise with high density, high hardness (5.5–6.0), bright color, and high surface luster. This material is particularly sought after because its luster resembles porcelain after polishing (figures A-1 and A-2, A and B).

turquoise is challenging, and some labs may mistakenly identify it as untreated. Our investigation found that more than 10% of the turquoise in the Chinese jewelry market is treated with a silicate inorganic binder. Most porcelain-treated turquoise is sold as untreated, which is detrimental to the market.

MATERIALS AND METHODS

Samples. A total of 14 untreated and 26 porcelain-treated samples were examined in this study (table 1). All the samples from Zhushan County were obtained through the long-term cooperation between our research group and miners from the local market. Samples from the Guangzhou jewelry market had no

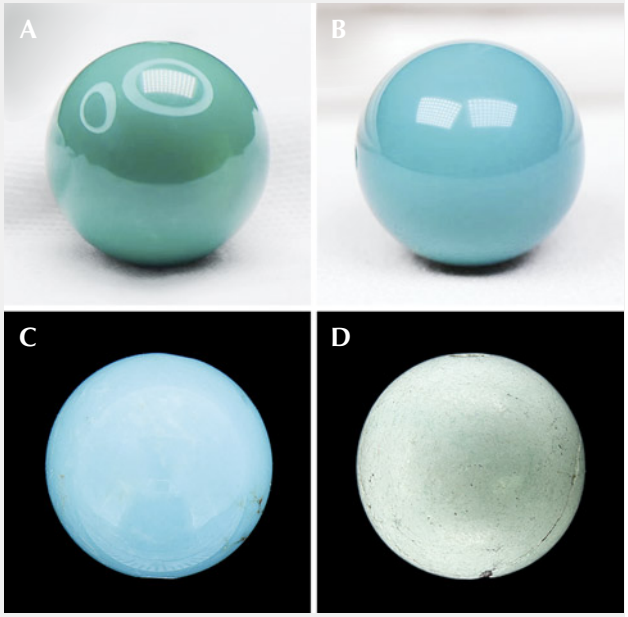

Figure A-2. The appearance of different qualities of natural turquoise. A: Greenish blue "porcelain" turquoise, 14.5 mm diameter, 4.86 g. B: Greenish blue "porcelain" turquoise, 14.5 mm diameter, 4.80 g. C: Medium-quality material, 12.0 mm diameter, 3.80 g. D: Porous material prior to treatment, 10.0 mm diameter, 1.5 g. Photos by Ren Fei, Jin Yu Turquoise Company.

Medium-quality turquoise (SG 2.50–2.70): Density, hardness (4.5–5.5), and color are between "natural porcelain" and porous turquoise, with medium surface luster (between waxy and earthy) (figure A-2, C).

Porous turquoise (SG <2.50): Also known as loose turquoise, with light blue to bluish white color and low surface luster, usually soft or even friable (hardness <4.5). Treatment methods such as the Zachery process (Fritsch et al., 1999), wax injection (Chen, 2009), and dyeing are often used to enhance its appearance (figure A-2, D).

origin record. All 40 specimens were polished (figure 2). To study the internal color distribution and the compositional and structural changes of the porcelain-treated turquoise, five of the samples after treatment were cut in half and polished (figure 3). The specimens were divided into two groups: P (porcelain-treated) and N (natural-color untreated).

The porcelain-treated specimens in this study were sky blue, whitish blue, bluish green, yellowish green, greenish blue, brownish blue, and brownish green. Some displayed an uneven color distribution, and many (such as P4, P5, P8, and N1) had irregular white patches on the surface. All the porcelain-treated samples had a waxy luster (table 1, where H refers to half beads of porcelain-treated turquoise; see also figure 2).

Standard Gemological Testing. Specific gravity (SG) of all specimens was recorded using a hydrostatic balance. Microscopic observations were carried out with a Leica M205A stereo microscope. Both tests were conducted at the Gemmological Institute, China University of Geosciences in Wuhan (GIC).

Infrared Spectroscopy. Infrared spectroscopy analysis was carried out using a Bruker Vertex 80 Fourier-transform infrared spectrometer at GIC. A small amount of sample and KBr powder (weight ratio of 1:150) were mixed, ground, and pressed to make a KBr tablet for transmission spectroscopy. The following conditions were used to test the tablet: 220 V scanning voltage, 6 mm raster, 10 kHz scanning rate, 32 scans, 400–4000 cm^{-1} range, and 4 cm^{-1} resolution. Baseline corrections were made using Bruker's OPUS spectroscopy software.

Ultraviolet/Visible (UV-Vis) Spectroscopy. A UV-Vis spectrophotometer (PerkinElmer Lambda 650 S) was used to test the samples' color characteristics at GIC. The test conditions were as follows: surface reflection method, 1 nm resolution, 100 ms collection time, a deuterium lamp excitation source at a color temperature of 2850 K, and a wavelength range of 250–800 nm.

Energy-Dispersive X-Ray Fluorescence (EDXRF) Spectroscopy. Chemical composition was determined by energy-dispersive X-ray fluorescence using a ThermoFisher ARL Quant'x EDXRF analyzer equipped with a rhodium-palladium X-ray tube and a Peltier-cooled detector at GIC. The analyses were performed using a voltage of 0 to 50 kV, a current of 1.98 mA, and a spot size of 1.5 mm^2. Testing was carried out based on the turquoise working curve established by Liu and Yang (2018). The details of the turquoise working procedures were established as follows: Liu and Yang (2018) conducted laser ablation–inductively coupled plasma–mass spectrometry

TABLE 1. Characteristics of turquoise samples from this study.

Group	Sample	Color	Shape	Luster	SG	Weight (g)	Market Source
Porcelain-treated	P1	Whitish blue	Drilled bead	Waxy	1.95	0.190	Zhushan
	P2	Sky blue	Drilled bead	Waxy	2.35	1.662	Guangzhou
	P3	Whitish blue	Drilled bead	Waxy	2.14	3.094	Guangzhou
	P4	Sky blue	Drilled barrel	Waxy	2.39	4.006	Guangzhou
	P5	Sky blue	Drilled bead	Waxy	2.44	5.249	Guangzhou
	P6	Greenish blue	Drilled bead	Waxy	2.33	2.190	Zhushan
	P7	Bluish green	Drilled bead	Waxy	2.47	2.538	Zhushan
	P8	Sky blue	Drilled bead	Waxy	2.63	2.922	Zhushan
	P9	Whitish blue	Drilled bead	Waxy	1.92	2.074	Guangzhou
	P10	Green-blue	Drilled bead	Waxy	1.93	2.129	Zhushan
	P11	Whitish blue	Drilled bead	Waxy	1.92	0.175	Zhushan
	P12	Whitish blue	Drilled bead	Waxy	1.89	0.203	Zhushan
	P13	Brownish blue	Drilled bead	Waxy	2.38	2.075	Guangzhou
	P14	Sky blue	Drilled bead	Waxy	2.41	2.051	Guangzhou
	P15	Sky blue	Drilled bead	Waxy	2.56	1.957	Guangzhou
	P16	Whitish blue	Drilled bead	Waxy	1.94	1.085	Zhushan
	P17	Whitish blue	Drilled bead	Waxy	2.13	1.000	Zhushan
	P18	Yellowish green	Drilled bead	Waxy	2.55	4.485	Guangzhou
	P19	Sky blue	Drilled bead	Waxy	2.45	1.385	Guangzhou
	P20	Whitish blue	Drilled bead	Waxy	2.13	2.191	Guangzhou
	P21	Brownish green	Drilled bead	Waxy	2.36	5.296	Guangzhou
	H1	Whitish blue	Half bead	Waxy	2.15	0.059	Zhushan
	H2	Sky blue	Half bead	Waxy	2.33	1.100	Guangzhou
	H3	Whitish blue	Half bead	Waxy	2.38	0.344	Zhushan
	H4	Yellowish green	Half bead	Waxy	2.39	1.236	Guangzhou
	H5	Sky blue	Half bead	Waxy	2.41	1.792	Zhushan
Untreated	N1	Whitish blue	Block	Waxy	2.48	3.355	Guangzhou
	N2	Yellowish green	Block	Waxy	2.66	1.002	Zhushan
	N3	Whitish blue	Drilled barrel	Waxy	2.35	1.239	Zhushan
	N4	Sky blue	Block	Weak porcelain	2.68	3.518	Zhushan
	N5	Greenish blue	Drilled barrel	Weak porcelain	2.69	6.647	Zhushan
	N6	Whitish blue	Drilled bead	Earthy	2.50	1.683	Zhushan
	N7	Sky blue	Block	Waxy	2.64	3.029	Zhushan
	N8	Greenish blue	Block	Waxy	2.65	0.713	Zhushan
	N9	Greenish blue	Block	Waxy	2.58	2.128	Zhushan
	N10	Sky blue	Drilled bead	Waxy	2.61	1.301	Zhushan
	N11	Whitish blue	Drilled bead	Waxy	2.56	1.373	Zhushan
	N12	Whitish blue	Block	Earthy	2.58	0.830	Zhushan
	N13	Whitish blue	Drilled barrel	Earthy	2.60	0.880	Zhushan
	N14	Whitish blue	Block	Earthy	2.49	0.581	Zhushan

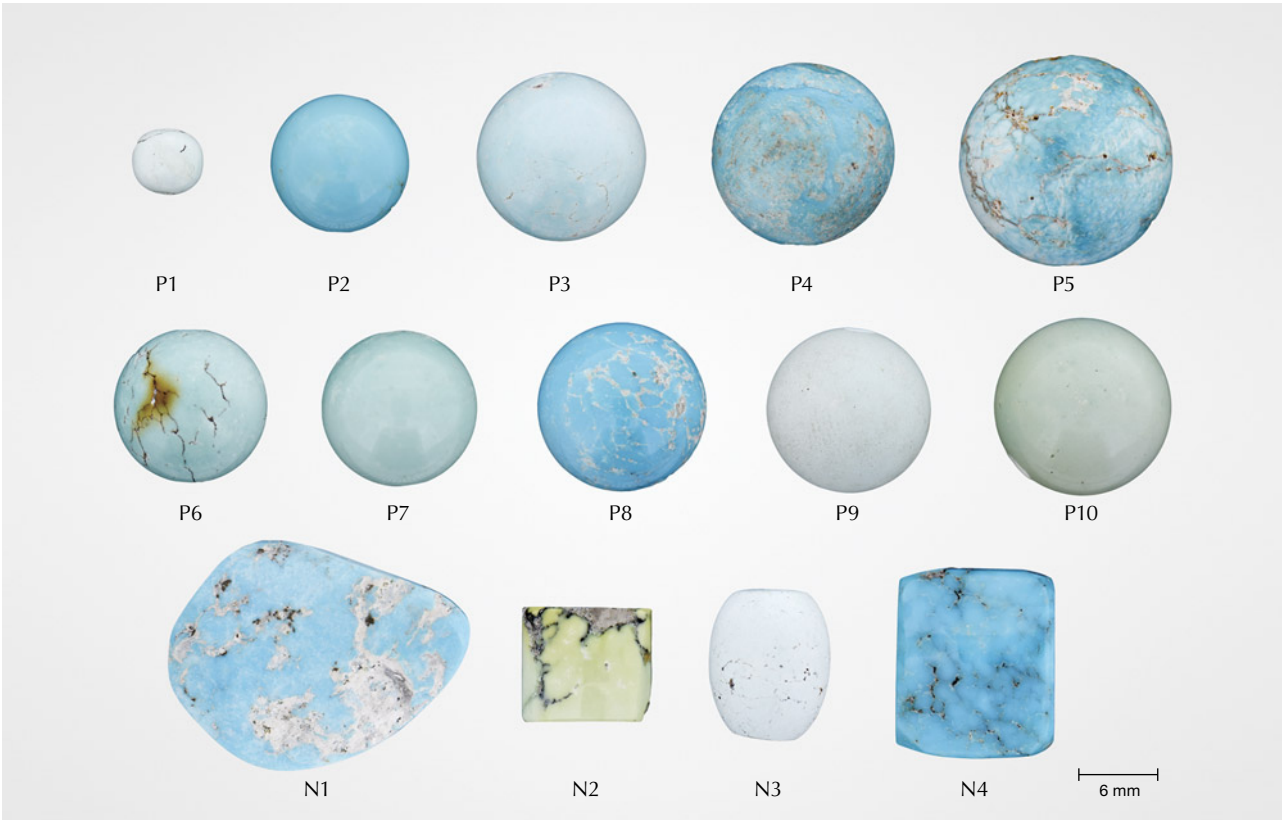

Figure 2. Ten of the porcelain-treated turquoise samples (P1–P10) and four of the untreated specimens (N1–N4) characterized in this study. Photos by Liying Huang.

(LA-ICP-MS) testing on a different set of 26 pieces of untreated turquoise from Zhushan, nine uniform color test positions were selected for each sample, and the average value was taken as the standard value of each sample. Twenty-one of 26 turquoise samples with a composition gradient were selected as reference standards, and the working curve of analytical elements was established. Ten elements (aluminum, silicon, phosphorus, potassium, calcium, copper, iron, vanadium, chromium, and zinc) were selected for examination.

Raman Spectroscopy. A Raman spectrometer (Bruker Senterra R200L) was used to explore the abnormally high SiO_2 content in the porcelain-treated turquoise at GIC. The laser wavelength was 532 nm, the laser power was 20 mW, and the acquisition time was 30 s. The laser spot size was 50 µm, the resolution was 9–15 cm^{-1}, and the test range was 34–1500 cm^{-1}.

Environmental Scanning Electron Microscope (ESEM). A Quanta 200 environmental scanning electron microscope was used to observe the structural

Figure 3. Porcelain-treated turquoise samples in group P that were cut in half for internal studies (red points indicate EDXRF testing locations). Photos by Liying Huang.

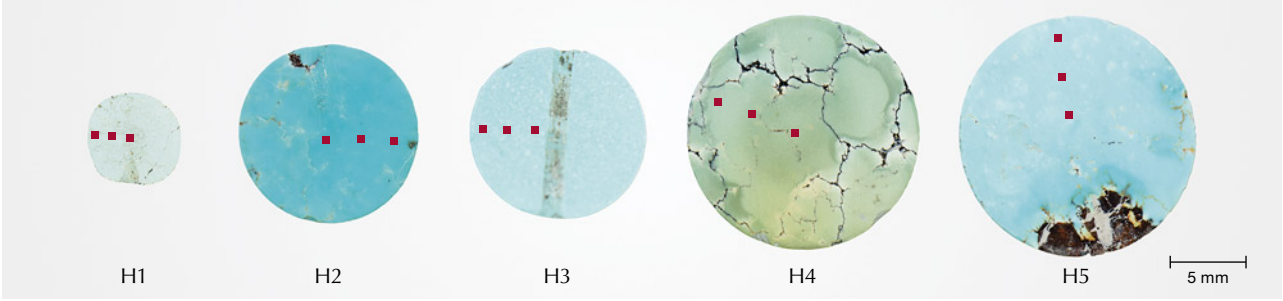

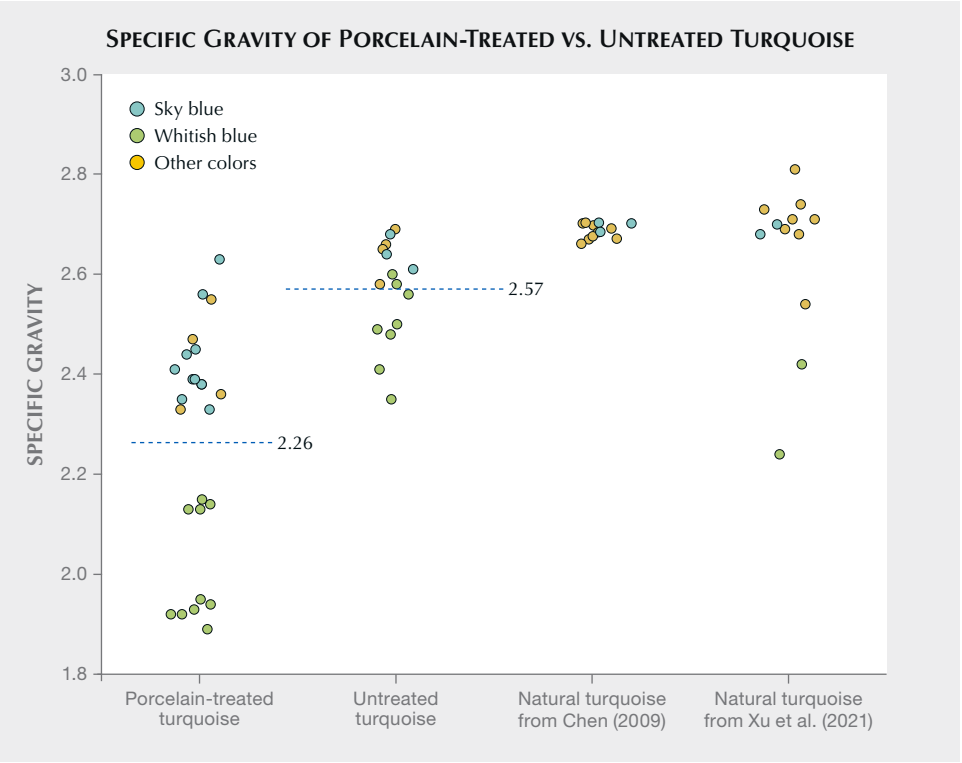

Figure 4. SG values of the samples from the present study and from Chen (2009) and Xu et al. (2021), two studies that examined many different qualities of untreated turquoise found in China. Dashed lines represent the average SG value of porcelain-treated turquoise (2.26) and untreated turquoise (2.57) in our study.

characteristics of the porcelain-treated specimens at the State Key Laboratory of Geological Process and Mineral Resources, China University of Geosciences in Wuhan (CUG). The test conditions were as follows: room temperature of 15° to 20°C, a relative humidity of <80%, an acceleration voltage of 20 kV, and a magnification of 7× to 10^6×. Secondary electron images were collected. Three porcelain-treated samples (P4, H2, and H3) and one untreated turquoise sample (N14) were selected to obtain cross sections of polished areas coated with 10–20 nm of gold using SEM.

RESULTS AND DISCUSSION

Gemological Properties. All the porcelain-treated and untreated turquoise samples were tested for their standard gemological properties.

Specific Gravity. Turquoise is a polycrystalline aggregate, and its surface pores easily absorb water. Therefore, specific gravity (table 1) should be recorded within 2 seconds after immersion (He et al., 2018). The SG of the untreated samples ranged from 2.35 to 2.69, with an average of 2.57. There was a limited number of untreated turquoise samples in the test set, and previous studies have shown that the SG of untreated turquoise with a poor texture is typically less than 2.50, while turquoise with a high-quality texture generally has an SG greater than 2.70 (Chen, 2009; Xu et al., 2021).

The SG of the porcelain-treated specimens ranged from 1.89 to 2.56, with an average of 2.26 (figure 4). The porcelain-treated whitish blue samples' SG range was 1.89–2.38 (average of 2.05), while the untreated whitish blue samples' range was 2.35–2.61 (average of 2.51). The porcelain-treated sky blue samples' SG range was 2.33–2.63 (average of 2.44), while the untreated sky blue samples' range was 2.62–2.68 (average of 2.65). Untreated sample data from Chen (2009) and Xu et al. (2021) are also in this range. As can be seen, the average SG of porcelain-treated turquoise (both whitish blue and sky blue) was lower than the average SG of untreated turquoise.

The luster and hardness of untreated turquoise are related to its density (Wang, 1986; Foord and Taggart, 1998). The denser the structure and the higher the hardness, the stronger the luster. Untreated porcelain turquoise shows a strong waxy to glassy luster after polishing, while porous material has an earthy to weak waxy luster. The porcelain-treated specimens in this study generally had a higher luster (waxy to weak porcelain). Their density was similar to that of low-quality turquoise typically chosen for treatment. Hence, the combined characteristics of low density and strong surface luster can be used to identify porcelain-treated material.

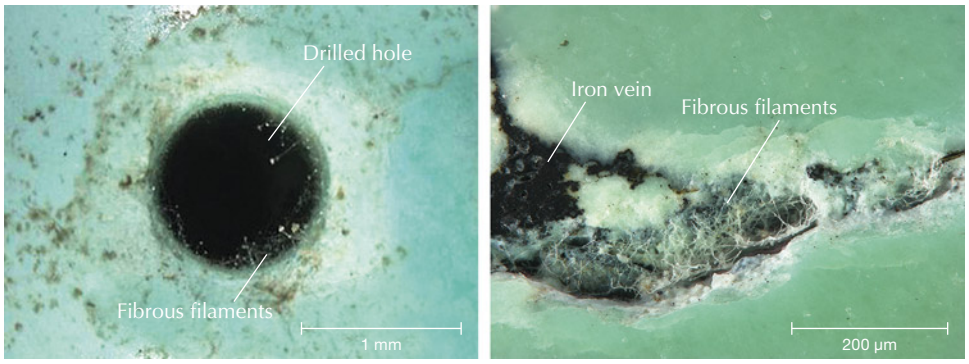

Figure 5. Surface characteristics of porcelain-treated samples P1 and P10. Left: Fibrous filaments at the edge of a drilled hole on P1. Right: Fibrous filaments near the depression of an iron vein on P10. Photomicrographs by Liying Huang.

Morphological Characteristics. Most of the porcelain-treated specimens purchased at the Zhushan market were whitish blue. They had waxy luster and a uniform color distribution, such as sample P1 in figure 2. The porcelain-treated turquoise specimens purchased in the Guangzhou market had various colors, including sky blue, whitish blue, and yellowish green. Some of the samples from both markets had high color saturation and waxy luster, such as samples P2–P10 in table 1.

Microscopic examination of porcelain-treated specimens P1, P5, and P10 showed obvious granular transparent crystals and fibrous filaments at pore channels and near the depressions of iron lines (figure 5). Specimen P1 originally had a waxy luster, but one week in an ambient environment (humidity above 50%) dulled its luster (figure 6, left) and left a blue spot on the surface (figure 6, right). Specimen H4 had a nonuniform color distribution with deep color along the edge and a bleached appearance along the iron vein. We attributed this uneven distribution to immersion in the filling material during treatment (figure 7, left). A round, transparent blob of melt with a greasy luster appeared on the surface of specimen P10 (figure 7, right).

Magnification and SG testing revealed that the stability of porcelain-treated turquoise is related to the density of the rough material before enhancement. Higher density produces a more stable color and luster. Because turquoise with high density is less porous, the filling material does not easily come out of the pores and the treatment is relatively stable.

Chemical Composition Analysis. All the porcelain-treated samples (P1–P21 and H1–H5) and ten of the untreated specimens with good luster (N1–N5 and N7–N11) were measured for major elements with EDXRF. All the porcelain-treated turquoise and some untreated samples (N1–N4) were also analyzed by Raman spectroscopy. Two or three different locations with uniform color were selected for each specimen, and each test location was tested twice with the av-

Figure 6. Surface characteristics of porcelain-treated turquoise sample P1. Left: After one week in a humid atmosphere, the surface changed from waxy in luster and uniform in color to an earthy luster with brown spots. Right: A blue spot also appeared on the surface of sample P1 after one week in an unstable ambient atmosphere. Photos by Liying Huang.

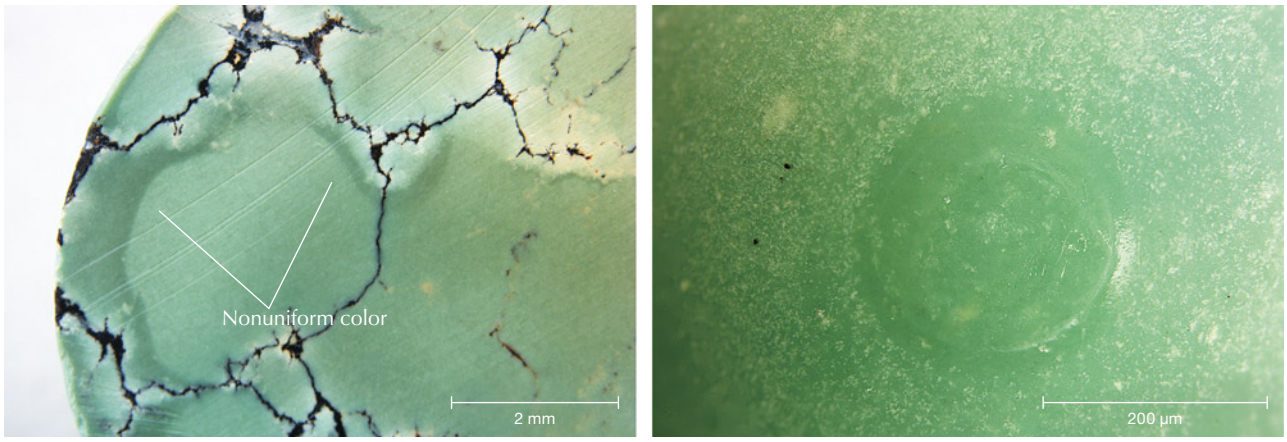

Figure 7. Surface characteristics of porcelain-treated turquoise samples H4 and P10, respectively. Left: H4 had a nonuniform color distribution, with deep color along the edge and a bleached look along an iron vein. Right: A round, transparent spot of melt with a greasy appearance on the surface of sample P10. Photos by Liying Huang.

erage value reported with detection limits in table 2. The main chemical compositions of the porcelain-treated and untreated turquoise were similar, composed mainly of CuO, Al_2O_3, and P_2O_5, with traces of FeO_T (including Fe_2O_3 and FeO), ZnO, SiO_2, K_2O, and CaO. Turquoise's ideal chemical formula is $CuAl_6(PO_4)_4(OH)_8 \cdot 4H_2O$, in which iron can replace some of the aluminum and zinc can replace copper (Zhang et al., 1984; Foord and Taggart, 1998; Chen, 2009; Liu, 2019). The ideal formula in weight percentage of oxides was 37.60% Al_2O_3, 34.90% P_2O_5, 9.78% CuO, and 17.72% H_2O. The original EDXRF test results do not include water (the total oxide content is approximately 100%), so we accounted for water by multiplying by 0.8228 (100% minus the 17.72% attributable to water). The results of these calculations are presented in table 2 (note the approximately 82% total for all of the measured samples) and plotted in figure 8. Figure 8 plots the differences between the major elements of porcelain-treated and

TABLE 2. Element concentrations (in wt.%) in porcelain-treated and untreated turquoise, measured by EDXRF.

Oxide	Porcelain-treated min–max (avg.)	Untreated min–max (avg.)	Untreated sample N2 min–max (avg.)	Ideal turquoise	Average detection limit (wt.%)
Al_2O_3	14.75–28.49 (23.78)	22.65–32.62 (29.51)	30.72–31.16 (30.93)	37.60	0.16
P_2O_5	22.03–34.18 (29.81)	31.44–38.22 (35.73)	35.82–36.17 (36.04)	34.90	0.12
CuO	7.16–11.37 (9.19)	0.82–11.38 (7.06)	0.82–0.88 (0.85)	9.78	0.0038
FeO_T	1.12–16.95 (4.14)	0.29–14.42 (4.00)	0.94–0.95 (0.95)	—	0.0042
ZnO	0.00–1.29 (0.17)	0.11–10.28 (2.47)	9.78–10.28 (10.02)	—	0.014
SiO_2	8.30–29.45 (14.15)	1.11–8.01 (2.57)	2.50–2.84 (2.71)	—	0.33
K_2O	0.03–0.94 (0.14)	0.06–0.26 (0.11)	0.06–0.08 (0.07)	—	0.0061
CaO	0.02–0.64 (0.19)	0.05–0.93 (0.18)	0.05–0.08 (0.06)	—	0.0047
H_2O	na[a]	na	na	17.72	—
Total[b]	81.57	81.63	81.63	100	—

[a]*na = not analyzed*
[b]*The given totals were added up from the average wt.% of the porcelain-treated and untreated turquoise, which did not include the content of H_2O.*

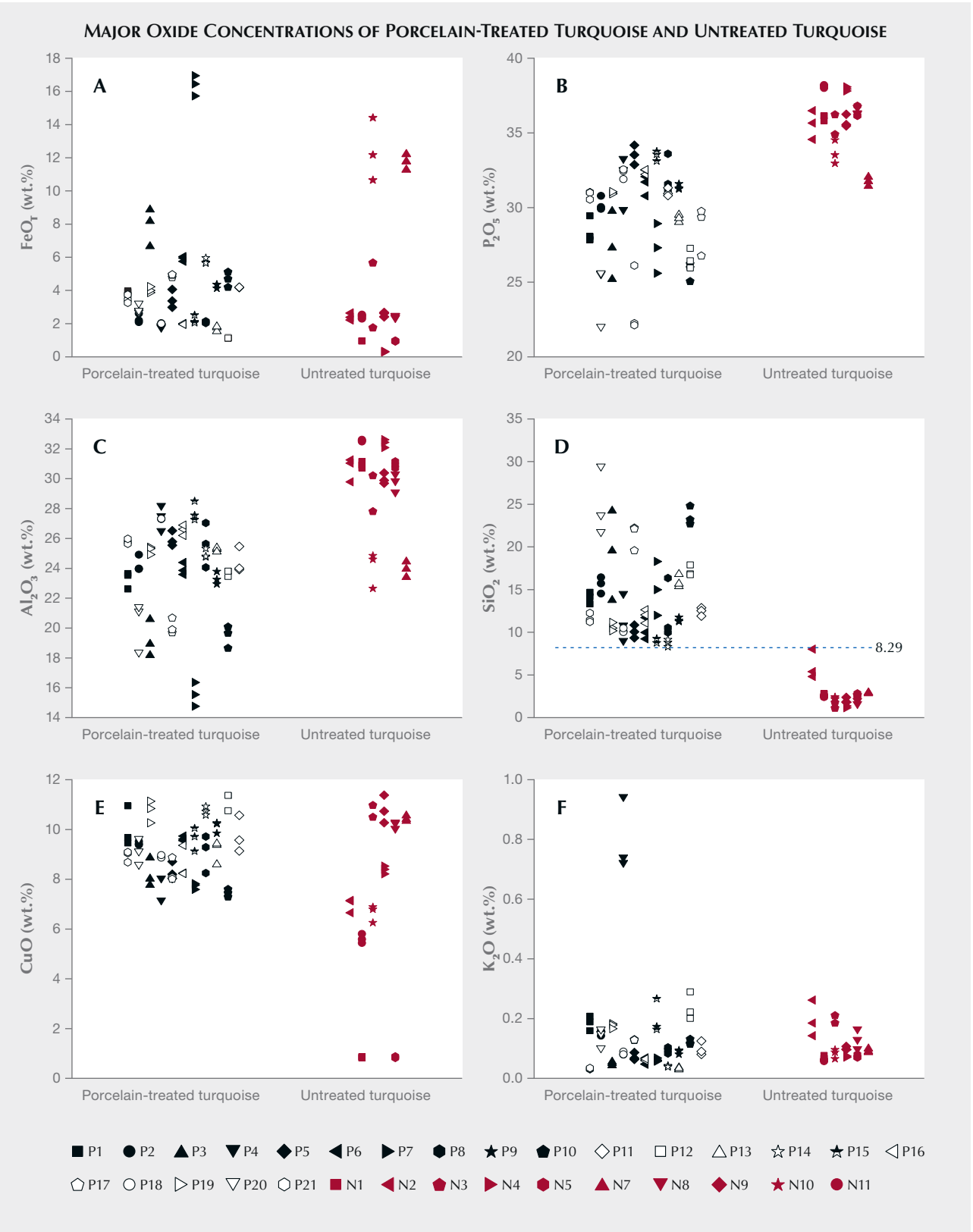

Figure 8. A–F: Major oxide concentrations corrected for water of porcelain-treated turquoise (black) and untreated turquoise (red). The different shapes represent different specimens (P1–P21, N1–N5, and N7–N11), while the blue line in the SiO_2 plot is the minimum value of the SiO_2 content of porcelain-treated turquoise.

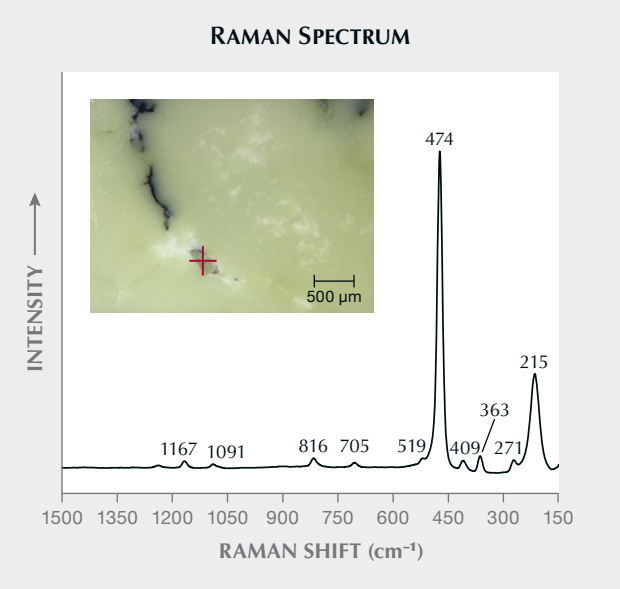

Figure 9. The Raman spectrum of quartz in untreated turquoise specimen N2.

natural turquoise. Among them, sample N2 had a ZnO to CuO weight percentage ratio greater than 1.0, making it a copper-zinc turquoise (Foord and Taggart, 1998).

The silica concentrations of all of the porcelain-treated samples were above 8.29 wt.%, generally higher than that of untreated turquoise. The silica contents of all the untreated samples tested in this study were all lower than 8.29 wt.% (the silica content of most untreated turquoise is <3 wt.%) (figure 8). Occasionally, the silica content of untreated turquoise can be high due to the existence of associated minerals, such as quartz and some clay minerals. In those cases, the elevated silica content was caused by associated minerals, according to the Raman spectroscopy results (figure 9). It was inferred that the binder used in the porcelain treatment contained silicon.

The weight percentages of aluminum + iron, copper + zinc, and phosphorus were converted into atomic percentages and plotted as the vertices of a ternary diagram (figure 10). It can be seen that untreated and porcelain-treated turquoise occupy two different areas, with some overlap. The atomic percentage of phosphorus in untreated turquoise is generally greater than 37.5%, significantly higher on average than in porcelain-treated turquoise. Data of untreated turquoise from Xu et al. (2021) are in agreement with our findings (blue points in figure 10). Therefore, the relationships between aluminum + iron, copper + zinc, and phosphorus are a useful

Figure 10. Left: Ternary diagram showing the composition of untreated (including data from Xu et al., 2021) and porcelain-treated turquoise in terms of copper + zinc, aluminum + iron, and phosphorus. Right: A partial enlargement of the ternary diagram. The atomic percentage of phosphorus in untreated turquoise is generally greater than 37.5%, significantly higher on average than in porcelain-treated turquoise.

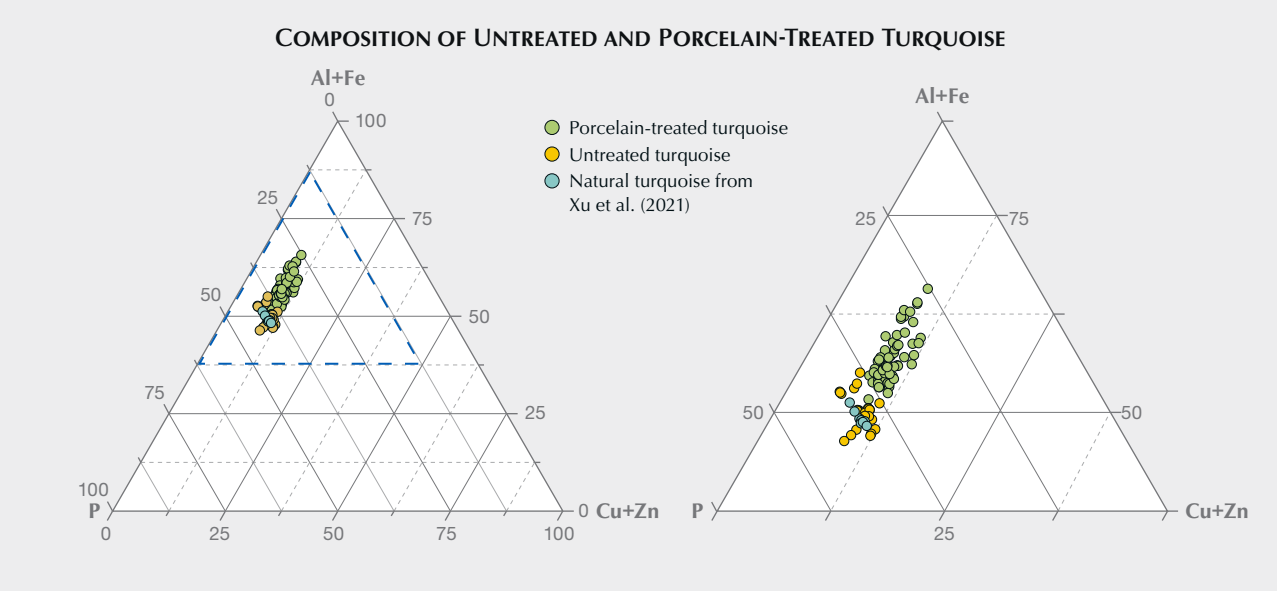

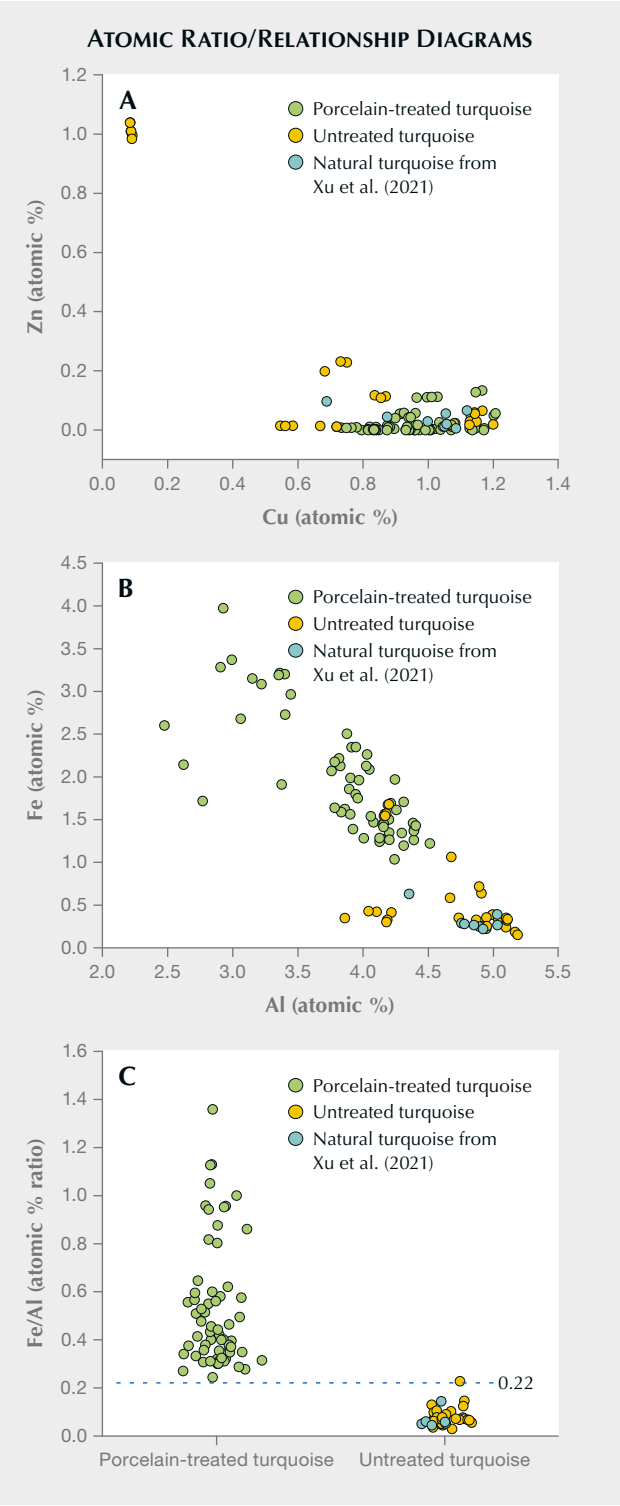

Figure 11. Diagrams showing the relationship between copper vs. zinc (A) and aluminum vs. iron (B) in atomic percentage. C: Atomic ratio of iron and aluminum scatter diagram, in which the dashed line is the boundary value of Fe/Al ratio between porcelain-treated and natural turquoise (0.22). The Fe/Al ratio of porcelain-treated turquoise is higher.

means of separation. In addition, two-dimensional separation plots were generated between zinc and copper and between iron and aluminum (figure 11, A and B). It is impossible to distinguish porcelain-treated turquoise through the content relationship of zinc and copper. Figure 11 (B and C) shows some separation between untreated and porcelain-treated turquoise. Because the Fe/Al ratio of porcelain-treated turquoise (>0.22) is higher than that of untreated turquoise, it can potentially be distinguished by its iron/aluminum ratio.

Among the tested samples, the silica content of untreated specimen N2 was as high as 8 wt.%. Microscopic observation found a light-colored mineral with a transparent glassy luster, which was identified as quartz by Raman analysis (figure 9). The Raman shifts of 1091 and 816 cm^{-1} were caused by asymmetric and symmetrical stretching vibrations of Si-O-Si, and the peak values were low. The bending vibration Raman shift of Si-O-Si was 474 cm^{-1}, and its peak was the highest. All the characteristic scattering peaks were sharp, and the full width at half maximum was small, indicating high crystallinity (Krishnan, 1945; Krishnamurti, 1958). Comparing the Raman spectra of untreated and porcelain-treated turquoise, there is little difference in spectral peaks from previous studies (Čejka et al., 2015; Štubňa and Andrášiová, 2021) (figure 12). In the 2800–3000 cm^{-1} range, some porcelain-treated material exhibited a weak peak, while untreated turquoise did not. The peak at the position of 2800–3000 cm^{-1} may be attributed to the asymmetrical stretching vibration and stretching vibration of CH_2 (Chen et al., 2010b). This peak often occurs in turquoise treated with an organic binder. This peak from porcelain-treated turquoise at the position of 2800–3000 cm^{-1} (figure 12) is weak due to low spectral resolution, so the material cannot be identified as porcelain-treated from this peak. Since the EDXRF test found a high concentration of silicon in the porcelain-treated turquoise, it was inferred that the fillings are inorganic (containing silicate).

To explore whether the high silica content is caused by the porcelain treatment, three test positions of equal distance from the edge to the center of the split samples in group P (figure 3) were measured with EDXRF. Each different test location was tested twice and averaged. The silica content near the edge was higher than that at the center, indicating that the high silica content of the porcelain-treated turquoise was due to the enhancement process (figure 13) and the observed variations from sample to sample were caused by the silicon-containing filling.

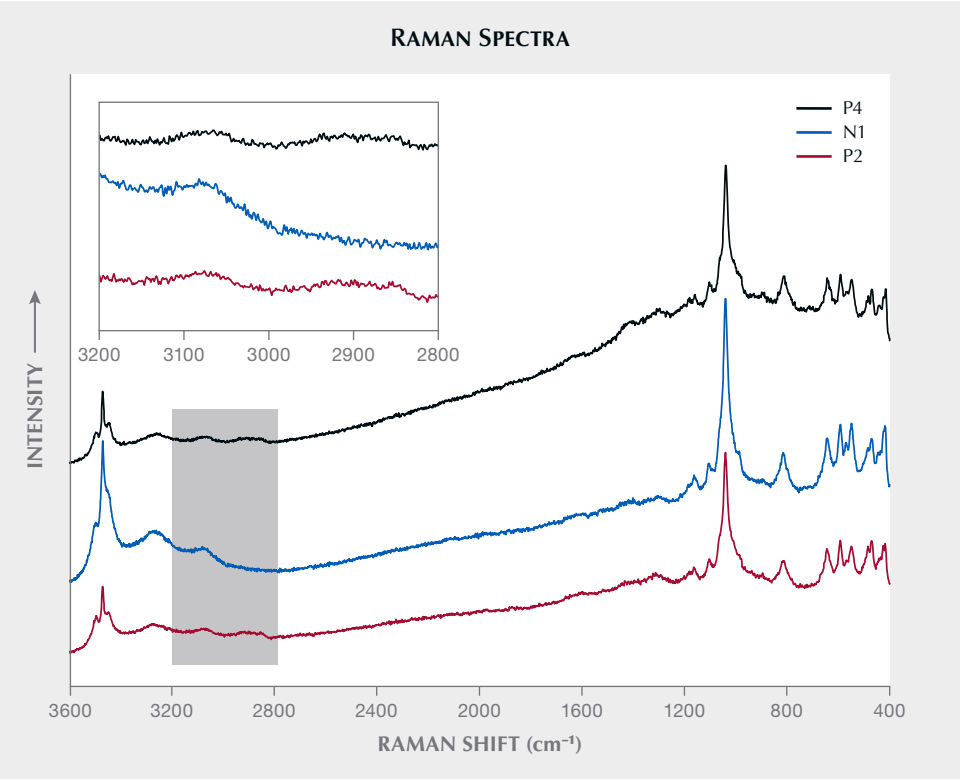

Figure 12. Raman spectroscopy of untreated (N1) and porcelain-treated (P2, P4) turquoise. The Raman spectrum characteristics of the treated and untreated turquoise are consistent. Inset: The close-up of the 2800–3200 cm^{-1} range shows that porcelain-treated (P2, P4) turquoise has a broad and weak absorption band around 2850–2950 cm^{-1}, while untreated turquoise does not. Spectra are offset vertically for clarity.

Infrared Spectroscopy Features. All the porcelain-treated and untreated turquoise specimens were measured with infrared spectroscopy. The obtained infrared absorption spectra were divided into two regions: 4000–1300 cm^{-1} (region I) and 1300–400 cm^{-1} (region II). In the ideal turquoise structure, group theory analysis shows that there are two PO_4^{3-} units in nonequivalent positions, two H_2O units in nonequivalent positions, and four OH units in nonequivalent positions. Different units have different vibration characteristics. The vibration modes and frequencies of OH, H_2O, and PO_4^{3-} units determine the infrared absorption spectra of turquoise (Lind et al., 1983; Fritsch and Stockton, 1987; Chen, 2009; Čejka et al., 2015).

Figure 13. Distribution of silica in three different locations in the porcelain-treated specimens (H1–H5) based on EDXRF results. From the edge position to the center position, the samples show different degrees of silica concentration decrease.

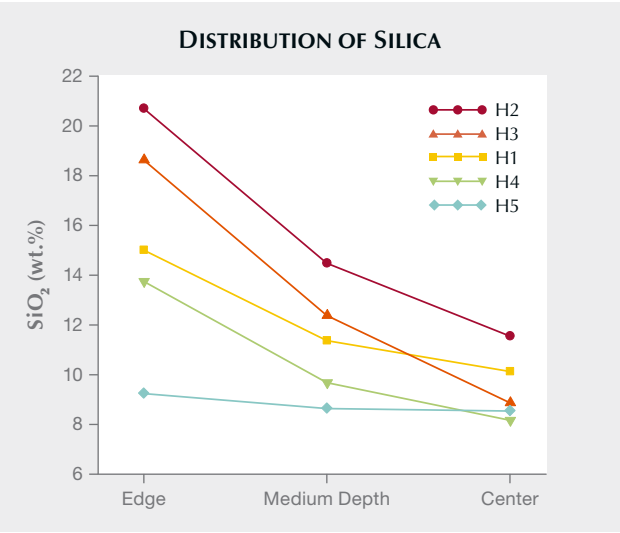

Untreated Turquoise. The absorption characteristics of untreated turquoise in region I were consistent with previous research (Chen et al., 2007). The absorption near 3500–3400 cm^{-1} corresponds to the ν(OH) stretching vibration, the absorption near 3300–3000 cm^{-1} is a δ(H_2O) stretching vibration, and the peak near 1640 cm^{-1} is the δ(H_2O) bending vibration (figure 14, left).

Untreated turquoise showed four vibration mode frequencies of PO_4^{3-} in region II. The 1200–1000 cm^{-1} asymmetric stretching vibration absorption peak was $\nu_3(PO_4^{3-})$, the four-fold set of peaks with strong absorbance. There was a $\nu_1(PO_4^{3-})$ symmetrical stretching vibration frequency near 900 cm^{-1}, with weak absorption. A δ(OH) out-of-plane bending vibration frequency was located near 840 and 786 cm^{-1}. The

bending vibration frequency of $\nu_4(PO_4^{3-})$ was near 646, 595, 549, and 476 cm^{-1}, and a symmetrical bending vibration frequency of $\nu_2(PO_4^{3-})$ was near 470–410 cm^{-1} with weak absorption. Its main peak was near 1100 cm^{-1} (figure 14, left).

Porcelain-Treated Turquoise. The porcelain-treated turquoise in region I showed an absorption peak caused by the stretching vibration of ν(OH) near 3511 and 3465 cm^{-1}, an absorption peak caused by the stretching vibration of $\nu(H_2O)$ near 3300 and 3087 cm^{-1}, and an absorption peak caused by the bending vibration of $\delta(H_2O)$ near 1640 cm^{-1} (figure 14, right). Those absorption peaks were basically the same as those of untreated turquoise (Farmer, 1974).

The infrared absorption spectroscopy characteristics of porcelain-treated turquoise in region II showed that 1160, 1108, 1060, and 1020 cm^{-1} were the asymmetric stretching vibration absorption peaks of $\nu_3(PO_4^{3-})$ (figure 14, right). The symmetrical stretching vibration frequency of $\nu_1(PO_4^{3-})$ was near 900 cm^{-1}, the out-of-plane bending vibration frequency of δ(OH) was located at 840 and 786 cm^{-1}, and the bending vibration frequency of $\nu_4(PO_4^{3-})$ was near 649, 609, 580, and 476 cm^{-1}. The symmetrical bending vibration frequency of $\nu_2(PO_4^{3-})$ was located near 470–410 cm^{-1}; its absorption was weak, and some samples did not show this peak. The main peak of most samples was 1108 cm^{-1}, consistent with that of the untreated specimens.

According to Farmer (1974), the absorption peak caused by the ν(Si-O-Si) stretching vibration was near 1100–1000 cm^{-1} with strong absorption. The ν(Si-O-Si) asymmetric stretching vibration frequency was near 1089 cm^{-1} with strong absorption. The ν(Si-O-Si) symmetric telescopic vibration frequency splits at 800 and 781 cm^{-1}, and the asymmetric and symmetrical variable angle vibrations were located at 696 and 464 cm^{-1}, respectively. The asymmetric stretching vibration of phosphate $\nu_3(PO_4^{3-})$ was located at the strong absorption of 1100–1050 cm^{-1}, and the symmetrical stretching vibration of $\nu_1(PO_4^{3-})$ was located at 970 cm^{-1}, which is very weak. A weak bending vibration of $\nu_4(PO_4^{3-})$ was located at the absorption wavelength of 630–540 cm^{-1}, and a weak symmetrical bending vibration of $\nu_2(PO_4^{3-})$ was located at the absorption wavelength of 470–410 cm^{-1} (Farmer, 1974).

The absorption peak of the ν(Si-O-Si) asymmetric stretching vibration was similar to that of the $\nu_3(PO_4^{3-})$ asymmetric stretching vibration, the absorption peak of the ν(Si-O-Si) symmetrical stretching vibration was similar to that of the δ(OH) out-of-plane bending vibration, and the ν(Si-O-Si) symmetrical stretching vibration absorption peak was close to that of the $\nu_4(PO_4^{3-})$ bending vibration

Figure 14. Left: Infrared absorption spectra of untreated turquoise (N2–N5). Right: Porcelain-treated specimens (P1–P5). The FTIR characteristics of the two groups are consistent. Spectra are offset vertically for clarity.

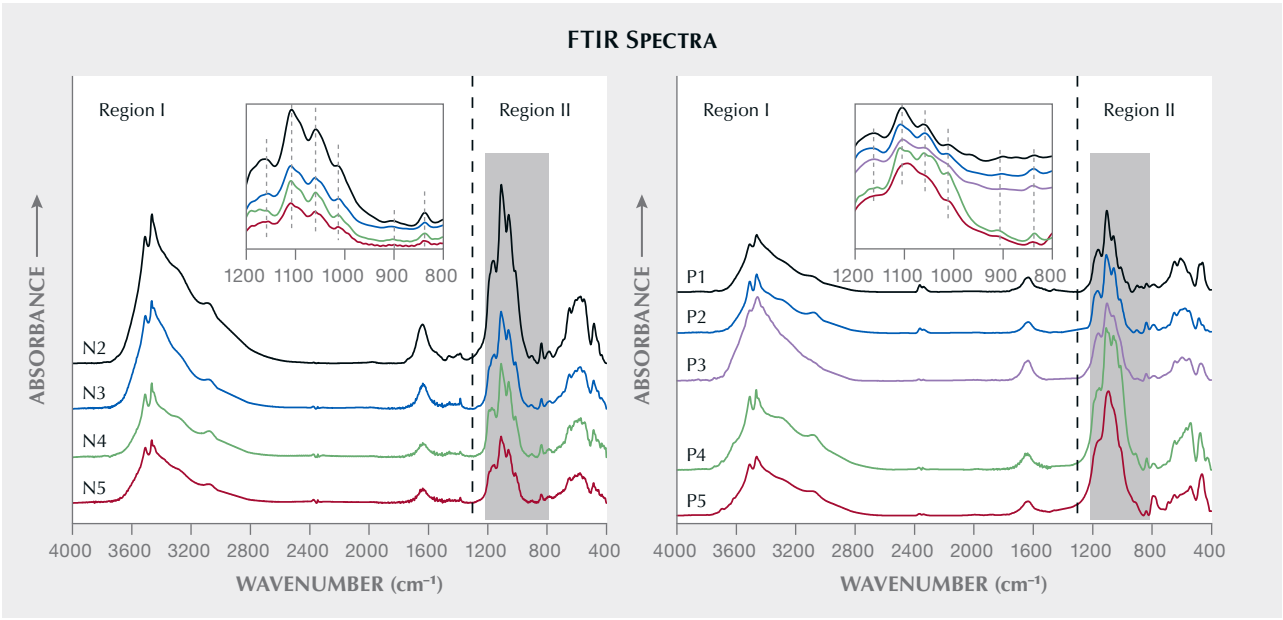

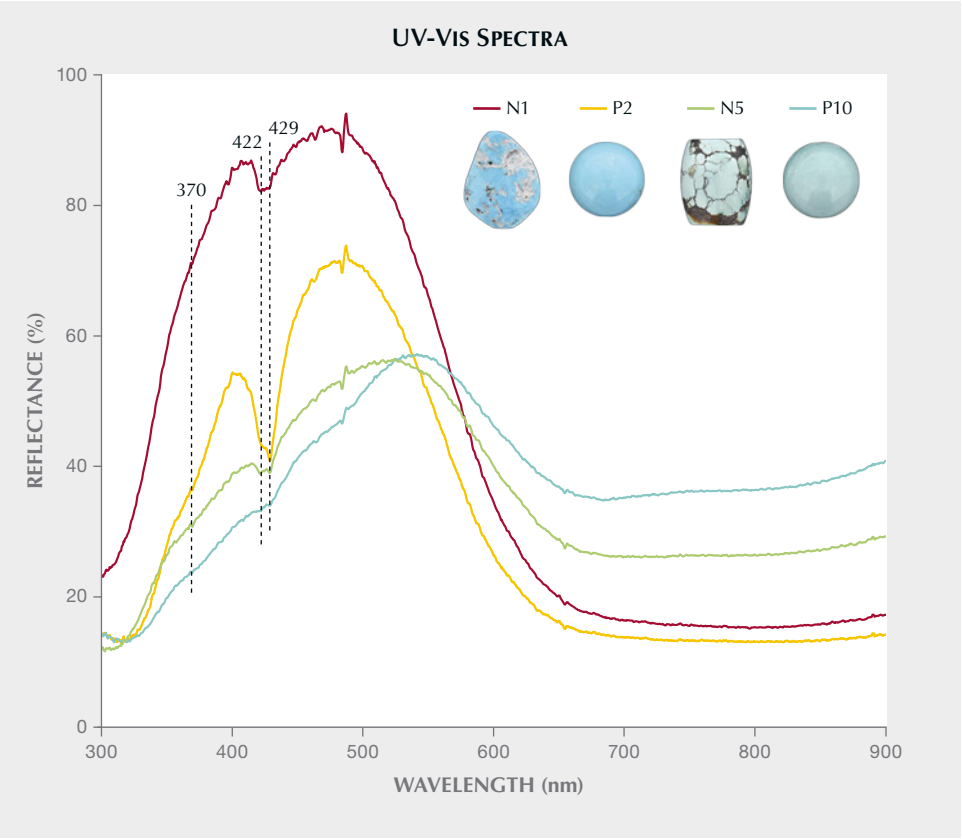

Figure 15. UV-Vis reflectance spectra of untreated (N1 and N5) and porcelain-treated (P2 and P10) turquoise samples. Their UV-Vis characteristics are essentially identical when comparing similar colors between treated and untreated.

absorption peak. It was difficult to distinguish the presence of Si-O-Si without careful comparison.

We detected no peaks of organic matter in the infrared spectrum, and the infrared absorption peak of Si-O was very similar to that of PO_4^{3-}.

UV-Vis Reflectance Spectrum Features. All the porcelain-treated and untreated specimens were measured with UV-Vis spectroscopy. In turquoise, copper is in a distorted octahedral coordination with six oxygens in an edge-sharing arrangement with pairs of alumina octahedra, and iron presumably replaces aluminum (Zhang et al., 1984; Foord and Taggart, 1998; Chen, 2009; Liu, 2019). The broad and strong absorption band near 620–750 nm is produced by the *d-d* electron transition of Cu^{2+}. The *d-d* electron transition of Fe^{3+} produces an absorption band near the violet region at 425 nm, while the weak absorption band in the ultraviolet region at 370 nm is caused by the Fe^{3+} electron transition and charge transferring from O^{2-} to Fe^{3+} (Foord and Taggart, 1998; Chen, 2009). The UV-Vis reflectance spectra of porcelain-treated turquoise (figure 15) show a broad absorption band in the yellow to red region (620–750 nm) and two absorption peaks in the purple region (~422 and 429 nm), which are almost identical to the UV-Vis absorption spectra of untreated turquoise. N5 and P10 are greener than N1 and P2 and have more iron, so their absorptions are stronger at 422 and 429 nm.

Basis for Identifying Porcelain-Treated Turquoise Using Nondestructive Methods. Both untreated and porcelain-treated turquoise can be identified through nondestructive testing, focusing on the appearance and composition characteristics of porcelain-treated turquoise (see the flowchart in figure 16):

1. the combination of strong surface luster and low density
2. fibrous filaments and potentially an area with greasy luster on the surface
3. high atomic ratio of iron to aluminum (>0.22) and low atomic percentage of phosphorus (<37.5%)
4. high silica content (>8.29 wt.%) in at least five test sites.

The silicon content at multiple test locations (without evidence of minerals that would account for it) is the decisive basis for identification of porcelain treatment, while the surface features and atomic

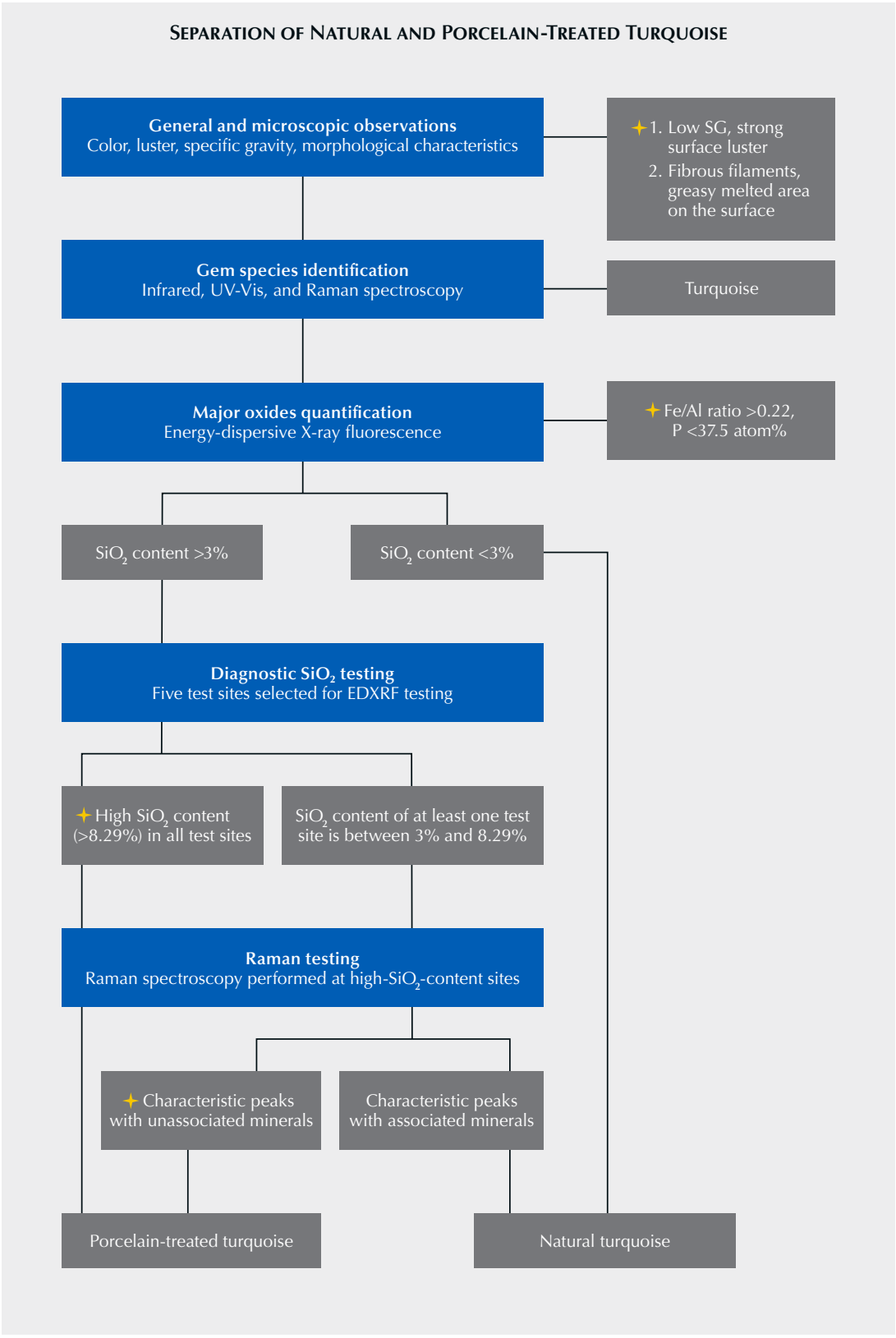

Figure 16. Identification flowchart for porcelain-treated turquoise. The blue boxes represent laboratory testing, while the gray boxes represent test results. The yellow stars indicate key distinguishing features.

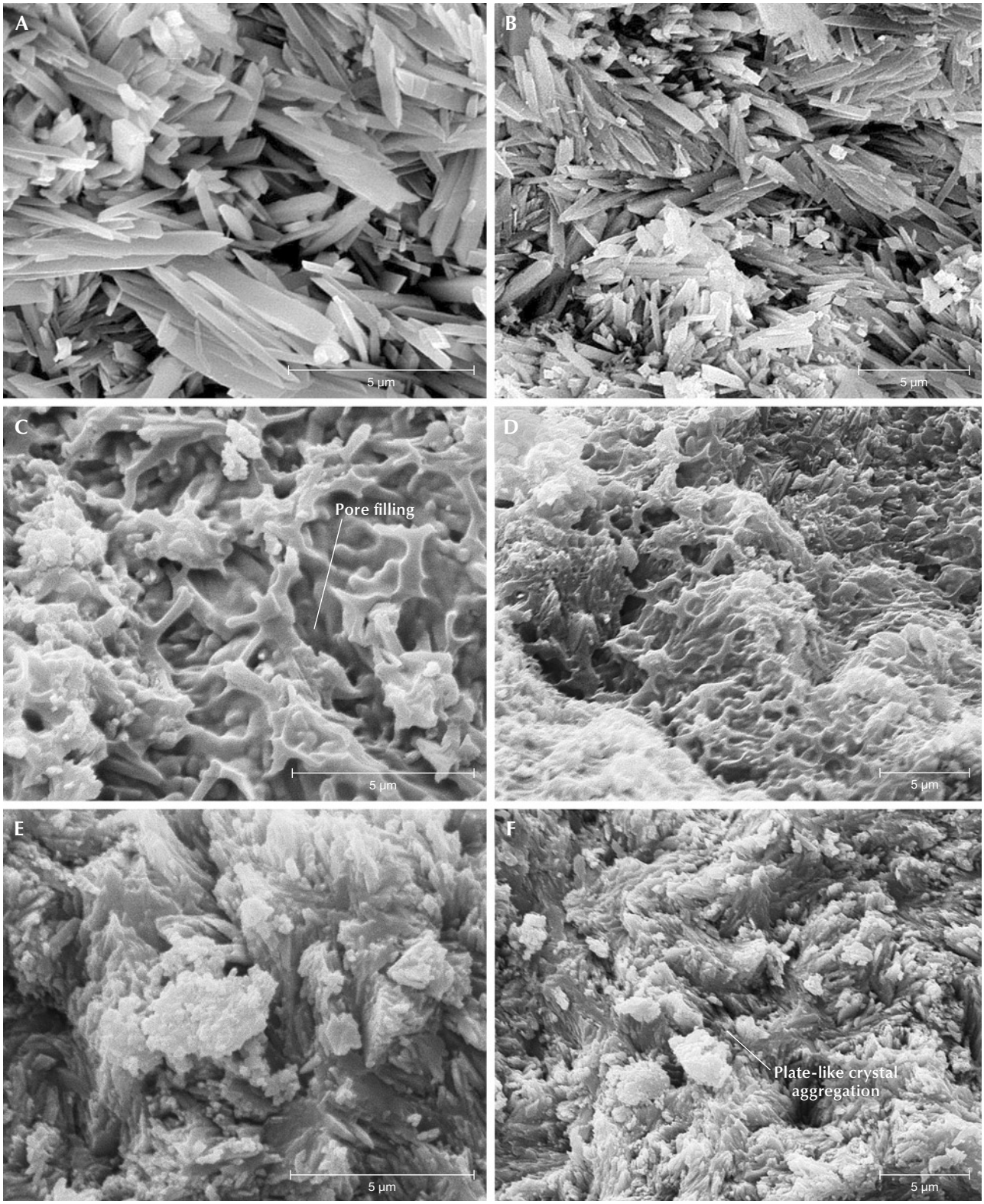

Figure 17. Morphological characteristics of untreated and porcelain-treated turquoise. The structure of untreated turquoise (N14) is shown via SEM imaging with 10,000× magnification (A) and 6,000× magnification (B). C and D: Microcrystal boundaries of porcelain-treated turquoise (H3) are blurred and pores are filled by colloidal material. E and F: The microcrystals inside sample H3 are columnar and plate-shaped.

content are the auxiliary basis. In the identification process, however, it is still necessary to comprehensively consider all four factors.

ESEM. Three porcelain-treated specimens with different densities (P4, H2, and H3) and one untreated specimen (N14) were examined with ESEM. Turquoise is triclinic and has a mostly cryptocrystalline structure with very large pores (Cid-Dresdner, 1965; Foord and Taggart, 1998; Chen, 2009; Abdu et al., 2011). Fine crystals can be observed under an electron microscope, mostly in the form of thin columns, plates, and scales. Figure 17 (A and B) shows the structure of untreated turquoise under 10,000× and 6,000× magnification, respectively. In specimens with different densities, there are also differences in the arrangements of microcrystals; turquoise with high density has a compact arrangement and small pores, whereas turquoise with low density has a loose, disorderly arrangement and large pores (Cid-Dresdner, 1965).

Three porcelain-treated specimens (P4, H2, and H3) were selected for SEM examination, and their structural characteristics were compared with those of untreated turquoise. For observation of each split specimen, three test positions were selected from edge to center. SEM images of porcelain-treated turquoise near the edge of the test sites are shown in figure 17 (C and D). Microcrystals within porcelain-treated turquoise lack the typical columnar and platelike crystals of untreated turquoise aggregates. These microcrystals within porcelain-treated turquoise are approximately lath-shaped with a disorderly distribution, and they have rounded microcrystalline edges and blurred boundaries. Also, gel-like colloids (e.g., figure 17C) distributed between the pores of microcrystals and the crystal surface can be seen (the pores between crystals are no longer visible). As shown in figure 17 (E and F), the test location near the center was less affected by the porcelain treatment and the crystals are columnar and plate-shaped, with observable edges and pores.

The surface characteristics produced by porcelain treatment are obvious, while the effect within the stone is less evident, similar to the EDXRF results. SEM imaging shows that the morphology near the center of porcelain-treated turquoise is similar to that of untreated turquoise, with complete crystal shapes, obvious pores, and a disorderly arrangement of microcrystals. SEM is a useful technique to distinguish untreated from porcelain-treated turquoise through identification of microcrystal morphologies and colloid distributions. However, it is not suitable for routine gem identification because of its destructiveness.

CONCLUSIONS

Porcelain-treated turquoise can be reliably separated from natural turquoise if a certain combination of characteristics are present: low specific gravity, strong surface luster, surface features (including fibrous filaments, greasy melted areas, and color distribution), high silica content (>8.29 wt.%), a high atomic ratio of iron to aluminum (>0.22), a low atomic percentage of phosphorus (<37.5%), and evidence of colloid-filled pores with SEM examination. High silica content is the most diagnostic feature of porcelain treatment, while low SG combined with strong luster and high atomic ratio of iron to aluminum are auxiliary identification criteria. However, it is necessary to comprehensively evaluate all four factors to make a final determination. The infrared and UV-Vis absorption spectra characteristics are basically the same for untreated and porcelain-treated turquoise and therefore not useful for separation. SEM observation of surface micromorphology provides distinct evidence of porcelain treatment but requires coating with carbon or gold, making it unsuitable for routine identification.

ABOUT THE AUTHORS

Ms. Huang holds a bachelor's degree in gemology from the Gemmological Institute, China University of Geosciences (CUG) in Wuhan. Associate Professor Chen (corresponding author, chenquanli_0302@163.com), Professor Li (yanli@cug.edu.cn), and Professor Yin teach at the Gemmological Institute, CUG, where Mr. Gao and Mr. Du are master's students and Mr. Xu is a graduate student. Associate Professor Chen is teaching for two years (until May 2024) at the School of Jewelry, West Yunnan University of Applied Sciences.

ACKNOWLEDGMENTS

This work has been funded by Hubei Gem & Jewelry Engineering Technology Center (No. CIGTXM-03-202201). The project was also supported by the "CUG Scholar" Scientific Research Funds at China University of Geosciences (Wuhan) (No.2022185), NSFC funding (No. 41874105), Fundamental Research Funds for National University, CUG (No. CUGDCJJ202221), Philosophy and Social Science Foundation of Hubei Province (No. 21G007). The publication of this article in 2022 marks the 30th anniversary of the Gemmological Institute and the 70th anniversary of the China University of Geosciences in Wuhan.

REFERENCES

Abdu Y.A., Hull S.K., Fayek M., Hawthorne F.C. (2011) The turquoise-chalcosiderite Cu(Al, Fe^{3+})$_6$(PO$_4$)$_4$(OH)$_8$·4H$_2$O solid-solution series: A Mossbauer spectroscopy, XRD, EMPA, and FTIR study. *American Mineralogist*, Vol. 96, No. 10, pp. 1433–1442, http://dx.doi.org/10.2138/am.2011.3658

Beale T.W. (1973) Early trade in highland Iran: A view from a source area. *World Archaeology*, Vol. 5, No. 2, pp. 133–148, http://dx.doi.org/10.1080/00438243. 1973. 9979561

Čejka J., Sejkora J., Macek I., Malíková R., Wang L., Scholz R., Frost R.L. (2015) Raman and infrared spectroscopic study of turquoise minerals. *Spectrochimica Acta Part A: Molecular and Biomolecular Spectroscopy*, Vol. 149, pp. 173–182, http://dx.doi.org/10.1016/j.saa.2015.04.029

Chen Q.L. (2009) Study on recycling technology and mechanism of turquoise. PhD thesis, China University of Geosciences [in Chinese].

Chen Q.L., Qi L.J. (2007) Study on the vibrational spectra characters of water in turquoise from Ma'anshan. *Journal of Mineralogy and Petrology*, Vol. 27, No. 1, pp. 30–35, http://dx.doi.org/10.3969/j.issn.1001-6872.2007.01.006 [in Chinese].

Chen Q.L., Yuan X.Q., Chen J.Z., Zhou J.H. (2010a) Structural characteristics of turquoise filled with aluminum phosphate adhesive. *Earth Science-Journal of China University of Geosciences*, Vol. 35, No. 6, pp. 1023–1028, http://dx.doi.org/10.3799/dqkx.2010.115 [in Chinese].

Chen Q.L., Yuan X.Q., Chen J.Z., Qi L.J. (2010b) Study on the treatment of turquoise using Raman spectroscopy. *Spectroscopy and Spectral Analysis*, Vol. 30, No. 7, pp. 1789–1792 [in Chinese].

Chen Q.L., Yin Z.W., Qi L.J., Xiong Y. (2012) Turquoise from Zhushan County, Hubei Province, China. *G&G*, Vol. 48, No. 3, pp. 198–204, http://dx.doi.org/10.5741/GEMS.48.3.198

Choudhary G. (2010) A new type of composite turquoise. *G&G*, Vol. 46, No. 2, pp. 106–113, http://dx.doi.org/10.5741/GEMS.46.2.106

Cid-Dresdner H. (1965) Determination and refinement of the crystal structure of turquois, CuAl$_6$(PO$_4$)$_4$(OH)$_8$·4H$_2$O. *Zeitschrift für Kristallographie - Crystalline Materials*, Vol. 121, No. 1-6, pp. 113–87, http://dx.doi.org/10.1524/zkri.1965.121.16.87

Deng Q., Hu J.M., Wang X., Cao Y., Yang W. (2019) Study on identification of turquoise treated with "porcelain." *China International Jewelry Academic Exchange Conference Proceedings*, http://dx.doi.org/10.26914/c.cnkihy.2019.013579 [in Chinese].

Evans O.H., Southward J. (1914) A further note on the occurrence of turquoise at Indio Muerto, northern Chile. *Man*, Vol. 14, pp. 37–39, http://dx.doi.org/10.2307/2788948

Farmer V.C. (1974) *The Infrared Spectra of Minerals*. Mineralogical Society Monograph 4, London.

Foord E.E., Taggart J.E. (1998) A reexamination of the turquoise group: The mineral aheylite, planerite (redefined), turquoise and coeruleolactite. *Mineralogical Magazine*, Vol. 62, No. 1, pp. 93–111, http://dx.doi.org/10.1180/002646198547495

Fritsch E., Stockton C.M. (1987) Infrared spectroscopy in gem identification. *G&G*, Vol. 23, No. 1, pp. 18–26, http://dx.doi.org/10.5741/GEMS.23.1.18

Fritsch E., McClure S.F., Ostrooumov M., Andres Y., Moses T.M., Koivula J.I., Kammerling R.C. (1999) The identification of Zachery-treated turquoise. *G&G*, Vol. 31, No. 1, pp. 4–16, http://dx.doi.org/10.5741/GEMS.35.1.4

Harbottle G., Weigand P. (1992) Turquoise in Pre-Columbian America. *Scientific American*, Vol. 266, No. 2, pp. 78–85, http://www.jstor.org/stable/24938943.

He C., Cao F.F., Di J.R., Yang M.X., Lu R., Liu L. (2018) Interpretation of national standard "turquoise classification." *Journal of Gems and Gemmology*, Vol. 20, No. 6, pp. 7–17, http://dx.doi.org/10.15964/j.cnki.027jgg.2018.06.002 [in Chinese].

Hedquist S. (2016) Ritual practice and exchange in the late prehispanic Western Pueblo Region: Insights from the distribution and deposition of turquoise at Homol'ovi I. *KIVA*, Vol. 82, No. 3, pp. 209–231, http://dx.doi.org/10.1080/00231940.2016.1214056

Koivula J.I., Kammerling R.C., Fritsch E. (1992) Gem News: Modern-day turquoise oiling. *G&G*, Vol. 28, No. 2, p. 137.

Krishnamurti D. (1958) The Raman spectrum of quartz and its interpretation. *Proceedings of the Indian Academy of Sciences-Section A*, Vol. 47, No. 5, pp. 276–291, http://dx.doi.org/10.1007/BF03052811

Krishnan R. (1945) Raman spectrum of quartz. *Nature*, Vol. 155, p. 452, http://dx.doi.org/10.1038/155452a0

Lind T., Schmetzer K., Bank H. (1983) The identification of turquoise by infrared spectroscopy and X-ray powder diffraction. *G&G*, Vol. 19, No. 3, pp. 164–168, http://dx.doi.org/10.5741/GEMS.19.3.164

Liu L. (2019) Study on origin, factors and grading of the color of turquoise from China. Master's thesis, China University of Geosciences (Wuhan) [in Chinese].

Liu L., Yang M.X. (2018) Study on EDXRF method of turquoise composition. *Spectroscopy and Spectral Analysis*, Vol. 38, No. 6, pp. 1910–1916 [in Chinese].

Liu X.F., Lin C.L., Li D.D., Zhu L., Song S., Liu Y., Shen C.H. (2018) Study on mineralogy and spectroscopy of turquoises from Hami, Xinjiang. *Spectroscopy and Spectral Analysis*, Vol. 38, No. 4, pp. 1231–1239 [in Chinese].

Luan L.J., Han Z.X., Wang C.Y., Zhang Y.W. (2004) Elementary research on color-forming mechanism of turquoise. *Northwestern Geology*, Vol. 37, No. 3, pp. 77–82, http://dx.chinadoi.cn/10.3969/j.issn.1009-6248.2004.03.013 [in Chinese].

Luo Y.F., Yu X.Y., Zhou Y.G., Yang X.G. (2017) A study of texture and structure of turquoise from Luonan, Shaanxi Province. *Acta Petrologica et Mineralogica*, Vol. 36, No. 1, pp. 115–123, http://dx.doi.org/10.3969/j.issn.1000-6524.2017.01.012 [in Chinese].

Mansour A.M.A. (2014) *Turquoise in Ancient Egypt: Concept and Role*. British Archaeological Reports, Oxford, UK, http://dx.doi.org/10.30861/9781407312347

McClure S.F., Kane R.E., Sturman N. (2010) Gemstone enhancement and its detection in the 2000s. *G&G*, Vol. 46, No. 3, pp. 218–240, http://dx.doi.org/10.5741/GEMS.46.3.218

Ou W.C., Yue S.W., Gao K. (2016) Identification of turquoise and treated turquoise. *Journal of Gems and Gemmology*, Vol. 18, No. 1, pp. 6–14, http://dx.doi.org/10.3969/j.issn.1008-214X.2016.01.003 [in Chinese].

Ovissi M., Yazdi M., Ghorbani M. (2017) Turquoise; a gemstone that relates geology to archaeology and anthropology. *The First Symposium of Turquoise: Industry and Culture* [in Persian].

Pristacz H., Wildner M., Hammer V.M.F., Libowitzky E. (2013) Investigations of a synthetic turquoise. *Conference on Raman and Luminescence Spectroscopy in the Earth Sciences*, pp. 81–82, http://dx.doi.org/10.1007/978-3-540-72816-022301

Schwarzinger B., Schwarzinger C. (2017) Investigation of turquoise imitations and treatment with analytical pyrolysis and infrared spectroscopy. *Journal of Analytical and Applied Pyrolysis*, Vol. 125, pp. 24–31, http://dx.doi.org/10.1016/j.jaap.2017.05.002

Song J.W. (2008) On the influence and development of Chinese ancient porcelain to the world. *Journal of Taiyuan Urban Vocational College*, No. 11, pp. 141–142, http://dx.doi.org/10.3969/j.issn.1673-0046.2008.11.084 [in Chinese].

Štubňa J., Andrášiová A. (2021) Turquoise from Armenia. *Journal of Gemmology*, Vol. 37, No. 5, pp. 454–456.

Tu H.K. (1997) Metallogenic characteristics of turquoise in the eastern Qinling Mountains. *Nonmetallic Geology*, No. 3, pp. 24–25 [in Chinese].

Wang F. (1986) A gemological study of turquoise in China. *G&G*, Vol. 22, No. 1, pp. 35–37, http://dx.doi.org/10.5741/GEMS.22.1.35
Weigand P.C., Harbottle G., Sayre E.V. (1977) Turquoise sources and source analysis: Mesoamerica and the southwestern USA. In T.K. Earle and J.E. Ericson, Eds., *Exchange Systems in Prehistory*. Academic Press, New York, pp. 15–34, http://dx.doi.org/10.1016/B978-0-12-227650-7.50008-0
Xie H., Pei J.C., Xu Y. (2021) Gaspeite: A new gem material like turquoise. *Journal of Gems and Gemmology*, Vol. 12, No. 3, pp. 41–43, http://dx.doi.org/10.3969/j.issn.1008-214X.2010.03.009 [in Chinese].
Xu F.S., Chen Q.L., Ding W., Wang H.T. (2021) Study on fluorescence spectrometry of natural and organic filling treated turquoise. *Spectroscopy and Spectral Analysis*, Vol. 41, No. 9, pp. 2918–2923 [in Chinese].
Xu Y.F., Di J.R. (2018) Gemological identification of natural turquoise and treatment turquoise in Hubei. *Acta Petrologica et Mineralogica*, Vol. 37, No. 4, pp. 646–654, http://dx.doi.org/10.3969/j.issn.1000-6524.2018.04.010 [in Chinese].
Yang Y.Z., Zhang J.Z., Lan W.L., Cheng Z.J., Yuan Z.J., Zhu Z.F. (2017) 2013 excavation bulletin of Jiahu site, Wuyang County, Henan Province. *Archaeology*, No. 12, pp. 3–20 [in Chinese].
Zalinski E.R. (1907) Turquoise in the Burro Mountains, New Mexico. *Economic Geology*, Vol. 2, No. 5, pp. 464–492, http://dx.doi.org/10.2113/gsecongeo.2.5.464
Zhang H.F., Lin C.Y., Ma Z.W., Yang Z.G., Zhang E.L. (1984) Magnetic properties, characteristic spectra and colors of turquoise. *Geochemistry*, Vol. 3, pp. 322–332, http://dx.doi.org/10.1007/BF03179305
Zhou S.Q., Jiang F.J. (2005) The research of the turquoise in Xichuan of Henan. *Journal of Nanyang Teachers' College*, Vol. 4, No. 3, pp. 63–65, http://dx.doi.org/10.3969/j.issn.16716132.2005.03.019 [in Chinese].
Zhu H.W., Cheng Y.F., Shan G.Q. (2016) Identification of turquoise imitation. *Superhard Material Engineering*, Vol. 28, No. 6, pp. 58–60, https://doi.org/10.3969/j.issn.1673-1433.2016.06.021 [in Chinese].

Never Stop Innovating: Gem Artist Chi Huynh

Tao Hsu, Artitaya Homkrajae, and Kevin Schumacher

Figure 1. A look inside Adamas Jewelers in San Dimas, California, operated by Chi Huynh and his brother Kiet. The store carries Galatea's jewelry and is decorated with Huynh's wood carvings and paintings, including the boat-style showcases inspired by the family's journey from Vietnam. Photo by Tao Hsu.

An elegant jewelry design enhances the beauty of a gemstone, transforming it into a wearable work of art. The designer behind Galatea: Jewelry by Artist seeks to bring the world's beauty to life through art, innovation, science, and technology. Named for the ancient Greek myth of a beautiful statue that comes to life, Galatea was established in 1994 by Chi Huynh (figures 1 and 2). The story of Galatea reflects Huynh's vision of expressing his creative ideas and innovation through jewelry. Using near field communication technology, jewelry from his Momento collection can store precious memories that are easily accessed with a smartphone. The Blossom collection uses ambient temperature changes to mimic the blooming of a flower. These and other groundbreaking works have earned Huynh numerous accolades in the industry. In early 2022, the authors had the opportunity to visit the store and workshop he co-owns and operates with his brother Kiet in San Dimas, California. During the visit, Huynh shared his experiences, inspirations, and passion for jewelry-making innovations.

Figure 2. Chi Huynh, founder and owner of Galatea: Jewelry by Artist. Photo by Kevin Schumacher.

See end of article for About the Authors.
Gems & Gemology, Vol. 58, No. 4, pp. 458–473,
http://dx.doi.org/10.5741/GEMS.58.4.458

Figure 3. Chi Huynh as an infant with his parents and siblings in South Vietnam. Courtesy of Chi Huynh.

ENTERING THE JEWELRY BUSINESS

Chi Huynh, the youngest of eight (figure 3), was born in South Vietnam, where his father was a well-respected jeweler. As a child, he learned about jewelry making from his father and was tasked with making simple wedding bands until they were perfectly round. Huynh came to understand his father's lesson: "If you want to be a good jeweler, it takes skill and repetition."

In 1980, when Huynh was 12 years old, his family fled in a small boat after the fall of South Vietnam. A violent storm left the boat drifting on the ocean for more than two weeks. After being robbed by pirates and nearly dying of hunger and thirst, they were rescued by a Thai fisherman, first reaching a refugee camp in Thailand and then Los Angeles (figure 4). Through this life-altering journey and near-death experience, Huynh realized the gift of life and vowed to bring beauty into the world. Today, he considers himself an artist who creates jewelry out of a sense of curiosity, inspired by the natural beauty of the universe.

Arriving in the United States without knowing any English, Huynh used drawing as a tool to express himself and interact with others. At a young age, he recognized visual arts as a universal language and means of communication. He explored different forms of art, including painting, sculpting, music, and poetry, seizing every opportunity to read and learn.

Huynh's father eventually started a new jewelry business. But following his father's path as a jeweler did not appeal to Huynh, who desired a more creative outlet. Nevertheless, in the early 1990s, he joined his father and brother at the JCK Show in Las Vegas to learn more about the industry. He noticed that most exhibitors carried similar jewelry styles, few of which intrigued him. This motivated him to create something different, and out of this Galatea was born in 1994. Inspired by the Greek myth, Galatea represents Huynh's vision of creating jewelry that comes to life.

Lacking the funds to start a large-scale business, Huynh initially used his sculpting and carving talents to hand-carve wax models for other manufacturers. He loved the challenge and became a well-known carver in the industry. But when that challenge waned, he decided to make his own jewelry. To him, making jewelry meant more than just design sketches—it meant bringing new concepts to the industry.

MAJOR GEM AND JEWELRY INNOVATIONS

The authors were intrigued not only by Huynh's beautiful jewelry collections on display at the Galatea workshop, but also by more than a dozen patents granted for his products. Asked what inspires his ideas, Huynh said, "Jewelry is like a painting. It enters the eyes, enters the mind, and then touches the heart. Therefore, it starts from what it means to you. Creativity is a process of expressing oneself or losing oneself in a process of living. If you want to truly see the world, you need to learn to see with the eyes of a child. See it without label and see it as what

Figure 4. Refugee documentation from 1980 for Chi Huynh at age 12 (right) and his brother Kiet. Courtesy of Chi Huynh.

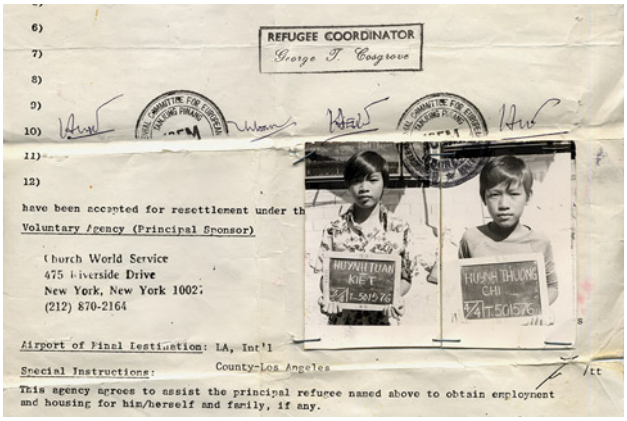

Figure 5. The Diamond in a Pearl collection, Huynh's first, is designed to illustrate a pearl's formation and symbolizes how true love can survive hardship. This jewelry set, named "Rhythm of Life," features a combination of pearl carving and Diamond in a Pearl techniques. The pendant contains a 12 mm carved Tahitian pearl, and each earring contains a 10 mm carved Tahitian pearl. The whole set is mounted with 14K white gold. Courtesy of Chi Huynh.

it is, so you can truly see it for itself through your own vision."

Huynh has brought groundbreaking jewelry design concepts to the industry by expressing himself and applying various innovations. The following sections highlight some of Huynh's products, which often combine several of his techniques into one piece of jewelry.

Diamond in a Pearl. The Diamond in a Pearl collection (figure 5) was Galatea's first, created in 1999 as an expression of Huynh's love for his wife. When a mollusk is irritated by a foreign object, such as a grain of sand, it secretes nacre, or mother-of-pearl, to surround the irritant, resulting in a beautiful pearl. In this design, the diamond represents the grain of sand, signifying pain or hardship in life, and the pearl surrounding it represents love that relieves the pain. This collection symbolizes how true love can endure and thrive to become something beautiful.

This design required extensive experimentation to find a way to avoid damaging the pearl while drilling a large hole to hold the precious metal mounting and the diamond. Huynh discovered he could achieve this goal with machinery and tools not commonly used by jewelers.

Carved Pearls. One of the most important considerations for pearl consumers is a smooth surface free of blemishes (Liddicoat, 1967). This is true for both natural and cultured pearls. While many believe that a pearl is carved to remove surface imperfections, that is not the case for Galatea. Huynh believes that no carving process can turn a low-quality pearl into a high-quality one. Instead, a carved pearl must start as a good-quality pearl. The carving gives the piece originality and individuality. (Due to the rarity of natural pearls, Huynh carves only cultured pearls of good quality.) The carved pearl technique was patented in 2006 (Huynh, 2006).

Huynh primarily uses Tahitian pearls for carving, as well as some South Sea and freshwater pearls, from round to baroque shapes (figures 6–8). Huynh considers baroque pearls especially pleasurable to work with, since their sizes and shapes allow more usable space for the carver's imagination and combination with other techniques such as "druzy in a gem" (Huynh, 2018a, 2018b) (figure 7). Akoya pearls are not ideal given their small size and thin nacre, which is insufficient for all of the carving details.

Pearls with a nacre thickness of 1.0 to 1.5 mm are suitable for carving. With his pearl culturing and harvesting experience, Huynh has discovered that even if the bead nuclei were placed at the same time and the pearls were harvested together, the nacre thickness would vary considerably between the pearls. To choose pearls for carving, he drills a tiny hole to check the nacre condition and determine whether standard gemstone carving tools can be applied. Carving patterns are designed based on the theme of the jewelry and the pearl's nacre thickness and surface appearance (figure 8). If carved pearls are to be combined in a bracelet or necklace, Huynh chooses pearls that will achieve a harmonious look (figure 9).

Figure 6. Tahitian, golden South Sea, and freshwater carved pearl necklaces from the Galatea collection. Photo by Artitaya Homkrajae.

Carved pearls are incorporated in many other Galatea collections (figure 10). This design concept becomes even more intriguing when paired with gems and precious metals (figure 11). Carved pearls have unlimited uses, as they are created for wearers who don't simply follow trends.

Figure 7. Because non-bead cultured freshwater pearls are composed mostly of nacre, the carving can be extended deep into the pearl's body, allowing for more creativity. This "Pearl Garden" pendant was constructed using a 22 × 15 mm carved baroque freshwater pearl with lab-grown diamond and natural ruby, emerald, and garnet druzy placed within (Huynh, 2006). Courtesy of Chi Huynh.

Figure 8. The "Lightness of Being" pendant symbolizes freedom and was inspired by Huynh's favorite bird. The main 15 × 11 mm Tahitian pearl body was hand-carved to imitate the body of a peacock, and the pearl's color matches its feathers. Courtesy of Chi Huynh.

Figure 9. Each pearl in this suite was carved with a different pattern. The harmonious appearance of a jewelry piece or suite is an important consideration when combining carved pearls. Courtesy of Chi Huynh.

Galatea Pearls (Gem Bead Cultured Pearls). Galatea Pearls combine Huynh's imaginative carving talent with the beauty of gemstones and pearls together. This idea was born when a pearl was accidentally damaged during the carving process, exposing a shell bead at the surface. Consequently, Huynh thought it would be interesting to experiment with using gemstones instead of mussel shells to trigger the growth of nacre, with the intent of revealing the gem's beauty inside the carved pearl.

Carrying out this idea was no easy task. The pearl culturing process begins with the insertion of a suitable bead nucleus into a host mollusk. A biologically incompatible bead often results in bead ejection by the mollusk, difficult incision healing caused by too much gravitational force from the bead, or improper nacre

Figure 10. Carved pearls can be mounted with a variety of colored gemstones such as the "Lily" jewelry set shown here. The set is made of 11 mm hand-carved freshwater pearls and emerald mounted with 14K yellow gold. Courtesy of Chi Huynh.

Figure 11. In this "Mother's Love" pendant, a large pearl was carved to resemble a bird's nest and decorated with small gemstone druzy, a round pearl, and a bird made of gold. Photo by Kevin Schumacher.

deposition. Moreover, a bead nucleus must possess a thermal expansion coefficient equivalent to that of the pearl's nacre, so that they expand to the same degree from the heat generated during drilling and carving. Otherwise, the pearl can crack or break apart.

Culturing pearls with gem materials that have different properties from the nacre posed an enormous challenge. However, Huynh remained determined, speaking with experienced pearl farmers and continuing to experiment with a variety of gem materials. The process required great patience over the course of thousands of implantations, and each batch of experiments took 18 months to two years to yield results.

Huynh's experimentation revealed that black-lipped *Pinctada margaritifera*, the mollusk species that produces Tahitian pearls, yielded the highest-quality Galatea Pearls. This mollusk is large enough to accommodate beads about 8 mm in diameter while allowing enough nacre thickness to grow over the bead (figure 12). After years of effort, gem bead cultured pearls were successfully produced and patented internationally in 2004 and domestically in

Figure 12. A Galatea Pearl begins with a gem bead nucleus implanted in the gonad area of the mollusk, a procedure similar to that using a traditional shell bead nucleus. This series of photos shows the progression from inserting a synthetic turquoise bead (left) to a finished Tahitian bead cultured pearl with the synthetic turquoise as a nucleus (bottom right). Courtesy of Chi Huynh.

Figure 13. The Galatea Pearl uses synthetic turquoise or other gem material as a bead nucleus to produce a bead cultured Tahitian pearl. Later the pearl is hand carved to display the beautiful blue color of the turquoise, highlighting the contrast against the dark nacre. The pearls in this necklace are about 10.5 mm in diameter. Photo by Kevin Schumacher.

2006 as Galatea Pearls (Huynh, 2004, 2006; figure 13). When harvested, the gem beads are entirely covered by dark nacre produced by the mollusk and will reveal a dramatic contrast after carving.

Beads used in Galatea Pearls include synthetic turquoise (made specifically for this process), red coral, and opal, as well as natural topaz, citrine, amethyst, amber, and other gems (figure 14). The technique can also be applied to the *Pinctada maxima* mollusk that produces South Sea pearl because the species and culturing technique are closely related to those of Tahitian pearls. The success of "Edison" pearls—near-round to round Chinese freshwater bead cultured pearls typically 10–14 mm in diameter, in orange, pink, and purple hues (Zhou et al., 2021)—offers an opportunity to apply the technique to freshwater cultured pearls as well. Galatea Pearls are also featured in other collections, such as Diamond in a Galatea Pearl (figure 15).

Two-Way Shape-Memory Jewelry. Shape-memory jewelry takes advantage of nitinol, a self-expanding titanium and nickel alloy commonly used in heart stents. During cardiac surgery, a stent is inserted to

Figure 14. These Galatea Pearls were created with synthetic opal (left) and natural amber (right). The gem bead cultured Tahitian pearls were entirely covered by nacre when harvested and later carved by hand to display the gem bead underneath the surface. The pendant on the left features a 16 mm Tahitian pearl and a ruby, while the pearls in the jewelry set on the right are 10–11 mm in diameter. Courtesy of Chi Huynh.

Figure 15. Galatea Pearls are combined with other techniques to create unique looks. This Galatea pearl pendant (11.5 mm in diameter) and pair of earrings (10.0 mm in diameter) were carved to resemble sakura flowers, and each was set with a diamond. Courtesy of Chi Huynh.

expand an artery or blood vessel and improve circulation (Ohkata, 2011). In medical use, the nitinol functions in one direction only, to expand in response to human body temperature. But this alloy can be "trained" to move two ways by bending the wire to the shape desired and then returning to its original shape. The repetition of this process allows the movement to be imprinted in the metal; the more training, the better the memory. The "memory" of the trained wire can be erased by heating it to about 750°F (400°C). The wires can then be used as is or embedded into other precious metals to make it move (figure 16). The Blossom collection features this innovation, patented in 2019 (Huynh, 2019), using trained nitinol wires coupled with small pearls as the petals of a flower surrounding a larger center pearl. The wire petals respond to heat to transform their shape. The flower gradually blossoms in warm temperatures and closes when it is cool, just as a living flower reacts to warm sunlight and cool nights (figures 16 and 17; see video at www.gia.edu/gems-gemology/winter-2022-gem-artist-chi-huynh). Using a blow-dryer and a glass of cold water, Huynh demonstrated the Blossom ring's function. The motion of the ring was carefully orchestrated and meticulously trained to bend to certain angles based on the size variation and arrangement of the smaller pearls and the placement of the ring on a finger. The use of nitinol wires makes each piece in the Blossom collection come to life.

Figure 16. Shape-memory jewelry in the Blossom collection uses nitinol, a self-expanding titanium and nickel alloy that can transform in response to heat. This ring's four flower petals are embedded with nitinol wires trained to gradually open and close based on temperature. Courtesy of Chi Huynh.

Nitinol wires are durable, so it is not easy to break or distort them. But in the event they are accidentally distorted, applying heat using a cup of hot water or a blow-dryer will restore the wires to their original form.

Momento Jewelry. A pocket watch inherited from Huynh's father inspired the Momento collection. For Huynh, the watch was not only a valuable accessory but also held memories of his father. Huynh pondered the idea of creating jewelry that could store

Figure 17. This ring from the Blossom collection features nitinol wires paired with small pearls placed around a larger center pearl to resemble a flower. The flower slowly opens in response to increased temperature (left) and closes when it cools (right). The Tahitian pearl is 10.5 mm in diameter, while the freshwater pearls range from 1.5 to 3.0 mm in diameter and the diamonds have a total weight of 0.30 ct. Courtesy of Chi Huynh.

memories to pass on to loved ones. He considered embedding a tiny computer chip into jewelry to store memories but realized that battery power would complicate construction and sustainability.

While collaborating on a wireless technology project with friends, Huynh became aware of near field communication (NFC) microchips, which use short-range electromagnetic radio technology. This technology allows two NFC-compatible devices to communicate or transfer data when they are physically touching or within approximately four centimeters of each other (Ortiz, 2008). An NFC microchip is able to store and transfer data but is a very small passive object that does not require a battery or an internal power source. An embedded NFC device is powered by an electromagnetic field between its antenna and another NFC antenna in the metal case of a digital device such as a mobile phone or tablet (Homkrajae, 2020; Lathiya and Wang, 2020) (figure 18). Similar in concept to the electric current created when a magnet passes through a metal coil, the electricity generated is just enough to power the device.

Figure 18. Huynh experimented with different NFC chips and various methods that allow two NFC devices to communicate. Photo by Kevin Schumacher.

The main challenge in creating the Momento collection was the NFC device's inability to operate when placed in a jewelry piece. The jewelry is a metal housing that acts as a Faraday cage, not allowing electricity to flow into the NFC device. But after extensive testing, Huynh overcame this obstacle and patented the product in 2014 (Huynh, 2018c) (figure 19). The product features a housing that hosts a "double-decker" structure. The gemstone is located in the upper deck and functions as the cover of the NFC

Figure 19. Detail of the construction of a Momento pendant. Patented by Galatea, nos. US9824310B2 and WO2017180099A1. Courtesy of Chi Huynh.

Figure 20. White freshwater pearl "carnations" accented with rubies and set in 14K white gold with teardrop-shaped Momento pearls, each holding a tiny NFC chip ready to store a variety of digital assets and precious memories. Courtesy of Chi Huynh.

chip, the antenna, and the surrounding bezel forming the lower deck. The bezel is highly electrically conductive and permits near field communication with the NFC chip.

This NFC application has been used in nearly all Galatea designs, including carved pearls, Galatea Pearls, and shape-memory jewelry, adding an element of meaning to the finished pieces (figure 20). The Momento collection uses a Galatea mobile application to transmit data between the jewelry and the user's mobile phone or tablet. The NFC chip can store a variety of digital assets, including images, audiobooks, songs, videos, health records, and more (figure 21). Special precautions are required when a Momento piece needs repair, as the NFC assembly can tolerate heat only up to 175°F (80°C), though only temperatures above 700°F (370°C) will destroy the chip.

Huynh sees each piece in the Momento collection as a digital keepsake and time capsule that can live on for generations. He continues to research new possibilities for NFC chips, including higher storage capacity.

Figure 21. A mobile application is used to transmit data between the NFC chip inside the jewelry and a mobile device. Courtesy of Chi Huynh.

Figure 22. This ring features a 14K gold setting and a white DavinChi Cut topaz. Courtesy of Chi Huynh.

DavinChi Cut. In addition to carving cultured pearls, Huynh excels in the art of gemstone cutting. The DavinChi collection was born out of Huynh's curiosity about color and light as he considered the different colors that appear on the bottom surface of a DVD. He began to study the physics of light and learned how light travels and reacts with different media. The result was a special patented cut designed to make a gem refract its surroundings such as other gems, light, and images (Huynh, 2011). This creates the illusion of a gem changing colors when viewed from different angles. The name "DavinChi" was inspired by a statement in Leonardo da Vinci's notebooks: "Be a mirror, absorb everything around you and still remain the same."

At first glance, a DavinChi Cut gem appears to be upside-down (figure 22). Yet the stone is carefully designed. Each facet angle is precisely calculated to establish the right focal point to ensure that an object behind the stone is refracted by every facet. This is clearly visible when one draws a letter on a piece of paper and places the DavinChi Cut stone on top of the letter. The letter is refracted by every facet on the gem (figure 23). Faceting a DavinChi Cut stone requires great lapidary skill.

Although the DavinChi Cut works with most types of gemstones, the cut stone must not cancel the colors of the smaller gems placed behind it.

Figure 23. These illustrations demonstrate the design and function of a DavinChi Cut stone. Each facet is positioned at a precisely calculated angle so that an object placed behind the stone is refracted by all of the facets.

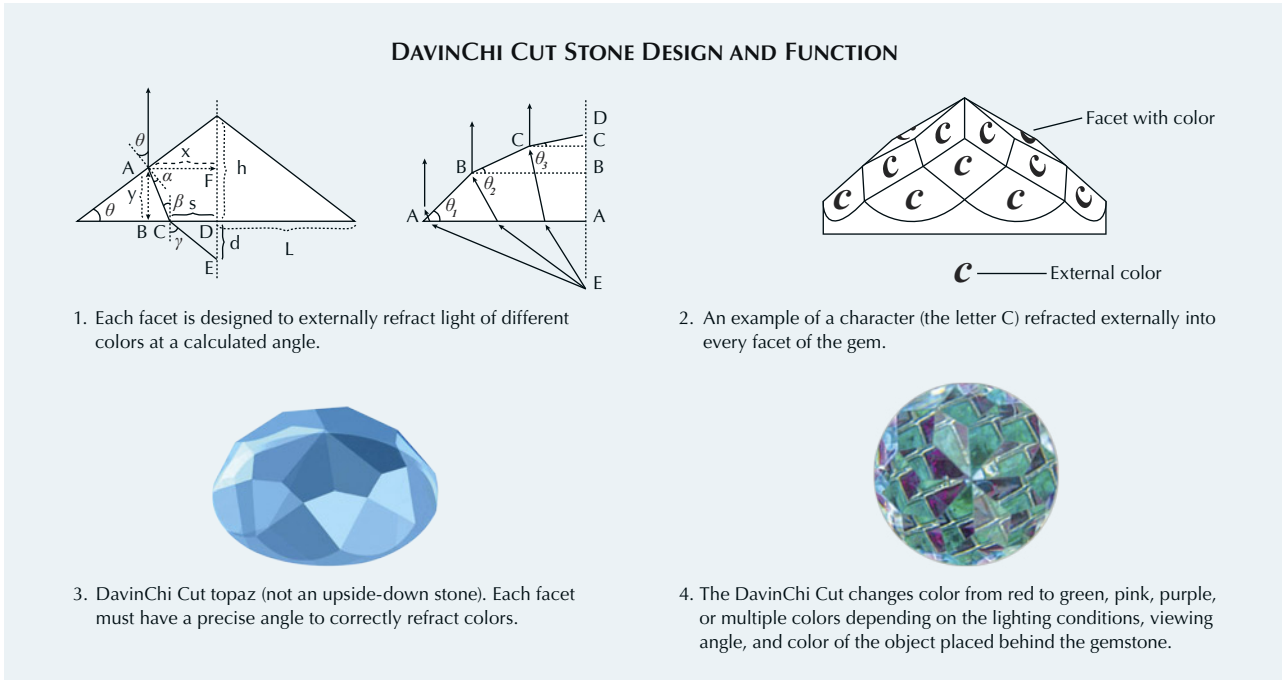

Figure 24. The top view of a DavinChi Cut pendant. Courtesy of Chi Huynh.

Therefore, light-colored or colorless stones work best for the DavinChi Cut. The distance between the DavinChi Cut stone and the smaller gems is also important. The viewer must look at the whole construction from above to see the illusion of color change (figure 24).

ALL-AROUND ARTIST

Before he started making jewelry, Huynh was a woodcarver and painter, and today many of these works decorate his store and studio (figure 25). He also enjoys writing poetry and making music. "The Secret of Life Is in the Seed," which received a 2018 JCK Jewelers' Choice Award, unites several of Huynh's artistic talents (figure 26). The center of the piece features a beautiful drop-shaped Tahitian pearl as the fruit. The pearl was partially carved open and mounted with red tourmalines, representing the seeds. Above the fruit is a small branch with green leaves and a pinkish red flower. Both were hand-painted with lacquer rather than enameled. Below the seed is a drop-shaped citrine representing the morning dew. Curiosity about his surroundings motivates and inspires Huynh to keep inventing new concepts and creating other artistic forms of expression.

Figure 25. Huynh painted the "Invisible String of Unity" in 1997 to illustrate the universal connection between people and nature. Courtesy of Chi Huynh.

Figure 26. "The Secret of Life Is in the Seed" blends Huynh's jewelry design and painting talents. Winner of a 2018 JCK Jewelers' Choice Award, the piece features a large Tahitian drop pearl resembling a fruit, tourmalines as the seeds, a citrine to represent a dewdrop, and leaves and a flower painted by hand with lacquer rather than enameled. Courtesy of Chi Huynh.

THE FUTURE OF GALATEA

Experimentation continues on the Momento collection and other shape-memory jewelry. In 2022, the authors saw newly developed men's jewelry collections incorporating Huynh's supreme carving skills (figure 27) and NFC chips, as well as other small gadgets used in jewelry pieces such as magnet-linked and stationed-pearl bracelets and necklaces.

Since his first day as a jeweler, Chi Huynh has kept bringing new concepts, techniques, and products to the industry. Huynh's wisdom, curiosity, and passion have built Galatea's reputation in the

Figure 27. Winner of a 2022 JCK Jewelers' Choice Award in the Men's category, "Mystic Wolf" from the Muze collection highlights Huynh's talent as a sculptor. Courtesy of Chi Huynh.

jewelry market and garnered several design awards. As consumers seek originality and individuality through innovative, one-of-a-kind jewelry, his techniques and patents will continue to influence the market, opening doors for future generations of gem artists.

ABOUT THE AUTHORS

Dr. Hsu is director of gemology content and professional development, and a technical editor of Gems & Gemology, *at GIA in Carlsbad, California. Ms. Homkrajae is a supervisor of pearl identification, and Mr. Schumacher is photo/video producer of* Gems & Gemology, *at GIA in Carlsbad.*

REFERENCES

Homkrajae A. (2020) Gem News International: A near-field-communication (NFC) technology device embedded in bead cultured pearls. *G&G*, Vol. 56, No. 3, pp. 436–437.

Huynh C. (2004) Carved pearl. World Intellectual Property Organization patent WO2004/054354 A2, issued July 1.

——— (2006) Carved pearl. U.S. patent US7062940B2, issued June 20.

——— (2011) Gemstone setting including a gem faceted to display a plurality of images from an outer focal region. U.S. patent US20110041555A1, issued August 7.

——— (2018a) Jewelry with druzy inset. U.S. patent USD817805S1, issued May 15.

——— (2018b) Jewelry having druzy or geode effect and methods of manufacture. U.S. patent US20180213898A1, issued August 2.

——— (2018c) Jewelry with security bezel for regulating near field communication with an embedded near field communication chip. U.S. patent US10108900B2, issued October 23.

——— (2019) Jewelry that reversibly transitions between two different configurations. World Intellectual Property Organization, patent WO2019/070386 A2, issued November 4.

Lathiya P., Wang J. (2021) Near-field communication (NFC) for wireless power transfer (WPT): An overview. In M. Zellagui, Ed., *Wireless Power Transfer: Recent Development, Applications and New Perspectives.* IntechOpen, London, http://dx.doi.org/10.5772/intechopen.96345

Liddicoat R.T. Jr. (1967) Cultured pearl farming and marketing. *G&G*, Vol. 12, No. 6, pp. 162–172.

Ohkata I. (2011) Medical applications of superelastic nickel-titanium (Ni–Ti) alloys. *In Shape Memory and Superelastic Alloys: Applications and Technologies*, Woodhead Publishing Series in Metals and Surface Engineering, pp. 176–196, https://doi.org/10.1533/9780857092625.3.176

Ortiz C.E. (2008) An introduction to near-field communication and the contactless communication API. www.oracle.com/technical-resources/articles/javame/nfc.html

Zhou C., Ho J.W.Y., Shih S.C., Tsai T.-H., Sun Z., Persaud S., Qi L.-J. (2021) Detection of color treatment and optical brightening in Chinese freshwater "Edison" pearls. *G&G*, Vol. 57, No. 2, pp. 124–134, http://dx.doi.org/10.5741/GEMS.57.2.124

Lab Notes

Editors
Thomas M. Moses | Shane F. McClure

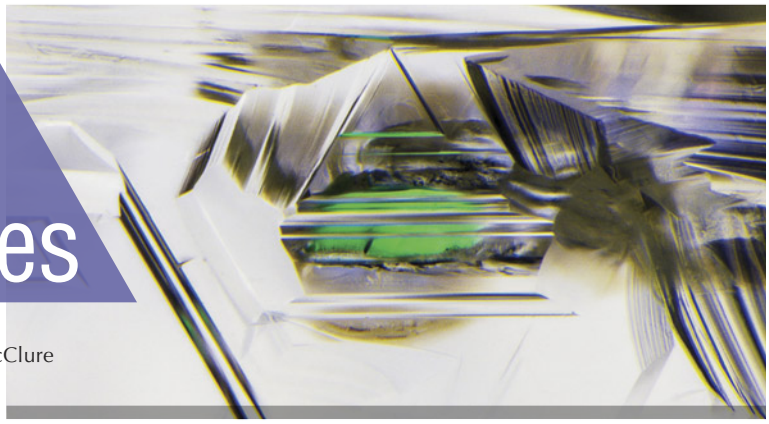

Four-Rayed Star CHRYSOBERYL

GIA's Tokyo laboratory recently received a brownish green cabochon set in a white metal ring with numerous near-colorless marquise brilliants and tapered baguettes (figure 1). The stone measured approximately 12.21 × 9.20 × 8.17 mm. Standard gemological testing showed weak green and yellow pleochroism and a spot refractive index reading of 1.75, as well as a strong diagnostic iron-related 444 nm band observed with a handheld spectroscope. These properties were consistent with chrysoberyl. At first glance the cabochon seemed to display chatoyancy, which would make this a cat's-eye chrysoberyl. However, there was not just a single band of reflected light but two bands intersecting at a 90° angle, so the phenomenon was actually four-rayed asterism.

Chatoyancy is usually created by light reflecting off of parallel needles or tube-like inclusions in a cabochon-cut gemstone. Microscopic observation revealed two sets of inclusions. One consisted of dense minute particles aligned in one direction producing a thick band of reflected light (oriented diagonally in figure 2). The other set was composed of needles oriented along the same direction as the thick band of light. These needles created a second band of reflected light perpendicular to the orientation of the needles. Together, these reflected bands of light resulted in the unique combination of two intersecting cat's-eyes.

Figure 1. Chrysoberyl showing two bands of reflective light displaying four-rayed asterism.

Figure 2. In the star chrysoberyl, short needles and dense minute particles were perpendicular to each other. The particles reflect light and caused the thick band's orientation (seen diagonally here). Field of view 3.7 mm.

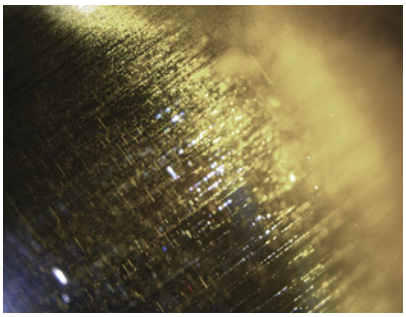

Four-rayed stars are common in diopside, garnet, and spinel. But they are very rare in chrysoberyl, which makes this stone notable.

Yuxiao Li and Yusuke Katsurada

A Closer Look at Internal Etch Channels in DIAMOND

The Carlsbad laboratory recently received a 1.02 ct cushion-cut Fancy Deep brownish yellowish orange diamond (figure 3). The yellowish color of this type Ib/IaA diamond is mainly attributed to single substitutional nitrogen atoms in the diamond lattice. In addition to the presence of multiple pinpoint inclusions, the diamond contained a bundle of internal etch channels extending from a single irregular-shaped opening on the girdle (figures 3 and 4).

Narrow etch channels are rarely observed in gem diamonds. Etch chan-

Figure 3. A 1.02 ct Fancy Deep brownish yellowish orange diamond with subsurface etch channels (upper right).

Editors' note: All items were written by staff members of GIA laboratories.

Gems & Gemology, Vol. 58, No. 4, pp. 474–482.

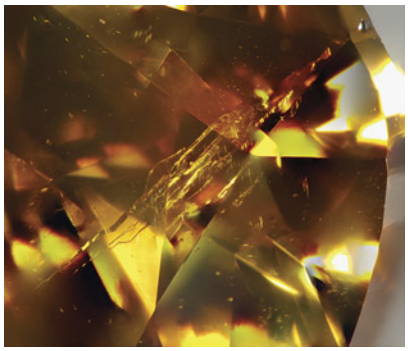

Figure 4. A bundle of internal etch channels extending from a single opening on the girdle. Field of view 2.44 mm.

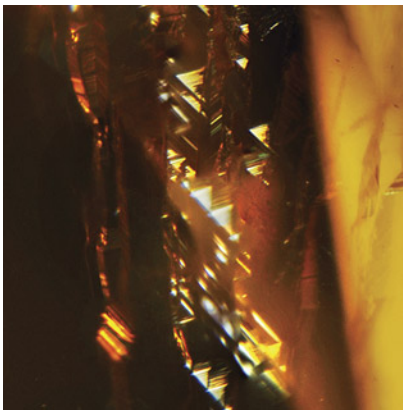

Figure 6. Trigons visible in a subsurface diamond etch channel. Field of view 1.00 mm.

nels can form due to dissolution of the diamond crystal by fluids/melts in the mantle, or during eruption to the surface (T. Lu et al., "Observation of etch channels in several natural diamonds," *Diamond and Related Materials*, Vol. 10, No. 1, 2001, pp. 68–75; J.W. Harris et al., "Morphology of monocrystalline diamond and its inclusions," *Reviews in Mineralogy and Geochemistry*, Vol. 88, No. 1, 2022, pp. 119–166). Defects in the diamond structure such as lattice dislocations are local areas of structural weakness, which are more susceptible to etching. In this diamond, multiple narrow etch channels originate from a single surface opening (figure 5), reflecting selective diamond dissolution as fluids permeated through the stone.

An intriguing feature observed along the walls of the internal etch channels consisted of multiple triangular etch pits known as trigons (figure 6). Trigons are one of the most common features found on the surfaces of rough diamonds, with various sizes, depths, and shapes (e.g., flat- or point-bottomed, attributed to etching by oxidizing fluids/melts; Harris et al., 2022). When present on diamond surfaces, trigons are restricted to the octahedral crystal face and may occasionally form parallel rows that follow the orientation of plastic deformation lines (often called "grain lines" in the trade, caused by dislocation of carbon atoms along octahedral planes). In faceted diamonds, trigons are usually removed by polishing but are occasionally preserved on the girdle. Conversely, trigons reported within internal diamond etch channels are extremely rare (Lu et al., 2001). The occurrence of trigons within a subsurface channel indicates etching along the octahedral crystal face of this diamond.

Mei Yan Lai and Matthew Hardman

Figure 5. An irregular-shaped opening on the girdle where fluids/melts permeated through the diamond and formed the internal etch channels. Field of view 1.26 mm.

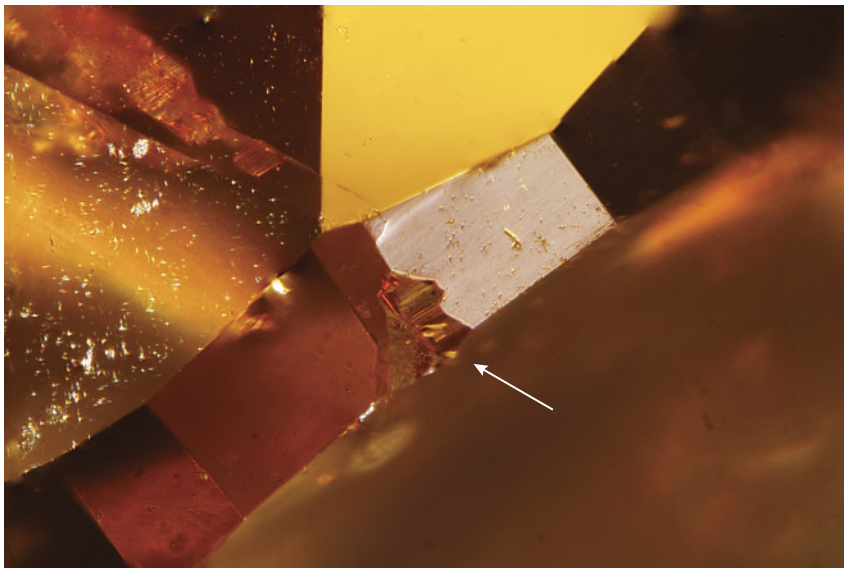

An Extraordinarily Large Cat's-Eye EMERALD

Emerald in cabochon form sometimes displays a chatoyant effect, and comparatively large cat's-eye emeralds are highly sought after. GIA's Tokyo labo-

Figure 7. An unusually large cat's-eye emerald weighing approximately 126 ct.

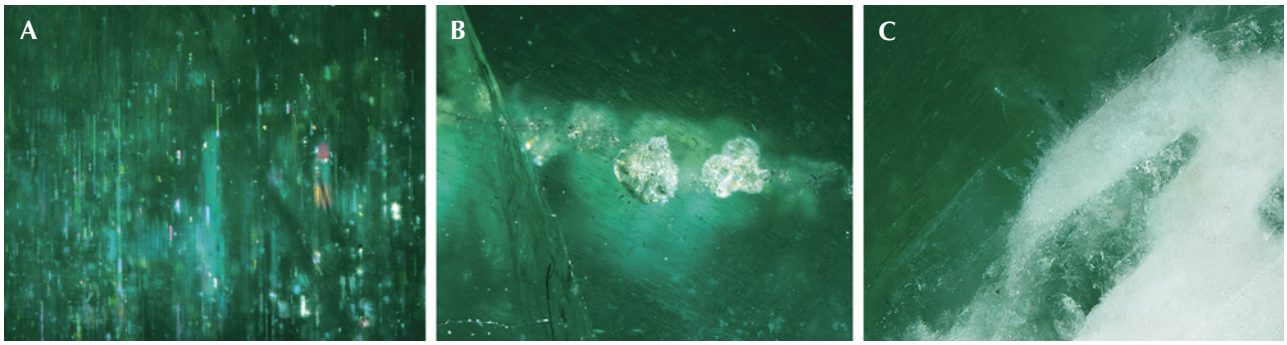

Figure 8. Inclusions observed in the large cat's-eye emerald. A: Rain-like inclusions; field of view 2.18 mm. B: Unknown whitish granular flake-like inclusions; field of view 5.70 mm. C: Aggregates of tiny whitish feldspar crystals confirmed by Raman spectroscopy; field of view 3.60 mm.

ratory recently examined an extraordinarily large semitransparent green cabochon measuring 31.3 × 26.2 × 20.9 mm and weighing approximately 126 ct (figure 7). The stone had a spot refractive index of 1.58 and showed specific chromium absorption lines in the red through a handheld spectroscope, and standard gemological properties identified it as emerald.

The emerald contained numerous reflective rain-like inclusions creating a chatoyant effect (figure 8A), whitish granular flake-like inclusions (figure 8B), and aggregates of tiny whitish crystals which were identified as feldspar by Raman spectroscopic analysis (figure 8C). The ultraviolet/visible/near-infrared absorption spectra showed two broad bands of Cr^{3+} at 430 and 600 nm, with a large Fe^{2+} band at around 850 nm and an Fe^{3+} broad band at 372 nm. Trace element chemical results using laser ablation–inductively coupled plasma–mass spectrometry showed that this emerald had a high iron concentration (2800–2930 ppmw) and medium potassium range (67.8–74.3 ppmw), characteristics similar to the published data of emeralds from the Belmont mine in Minas Gerais, Brazil (e.g., S. Saeseaw et al., "Geographic origin determination of emerald," Winter 2019 *G&G*, pp. 614–646). Inclusions observed in this emerald were also consistent with a Brazilian origin (again, see figure 8).

Brazil is a well-known source of large emerald crystals. One previous report (Summer 2015 Gem News International, pp. 200–201) described a 43 ct Brazilian cat's-eye emerald. The cat's-eye emerald examined here is notable for its size and transparency, and it is one of the largest examined by a GIA laboratory to date.

Makoto Miura

A "Cobalt Blue" GAHNOSPINEL

GIA's Bangkok laboratory recently examined an intense blue 1.01 ct transparent oval mixed cut (figure 9). Standard gemological testing revealed a refractive index of 1.742 and a hydrostatic specific gravity of 3.96. The stone was inert to long-wave and short-wave UV light. Microscopic observation revealed dense intersecting needles, iridescent thin films, particulate clouds, and flaky whitish inclusions. Laser ablation–inductively coupled plasma–mass spectrometry (LA-ICP-MS) was used to obtain oxide weight percentages (wt.% oxides) of aluminum, iron, magnesium, and zinc to calculate the chemical formula of the stone. It was determined to be $(Mg_{0.64}Fe^{2+}_{0.02}Zn_{0.34})Al_2O_4$. All of these properties were consistent with gahnospinel, which is a zinc-rich variety of the spinel group. Its chemical properties result from zinc substituting for magnesium in a solid solution series with end members gahnite ($ZnAl_2O_4$) and spinel ($MgAl_2O_4$).

Figure 9. This 1.01 ct gahnospinel had an intense "cobalt blue" color.

Interestingly, gahnospinel is usually found with a more muted dark blue to dark greenish blue color, but this intense blue specimen contained cobalt as the primary coloring agent, similar to "cobalt blue" gem spinel. Ultraviolet/visible (UV-Vis) spectroscopy showed significant amounts of absorption attributable to cobalt at approximately 550, 593, and 622 nm (figure 10), with additional contribution from iron at approximately 456, 550, and 593 nm (G.B. Andreozzi et al., "Color mechanism in spinel: A multi-analytical investigation of natural crystals with a wide range of coloration," *Physics and Chemistry of Minerals*, Vol. 46, 2019, pp. 343–360; V. D'Ippolito et al., "Color mechanism in spinel: Cobalt and iron interplay for the blue color," *Physics and Chemistry of Minerals*, Vol. 42, 2015, pp. 431–439). The significant amount of cobalt (198–224 ppmw) from LA-ICP-MS data and the reddish Chelsea filter reaction provided strong evidence that the intense blue color was induced by cobalt. While blue cobalt spinel and gahnite have been previously reported (see J.E. Shigley and C.M.

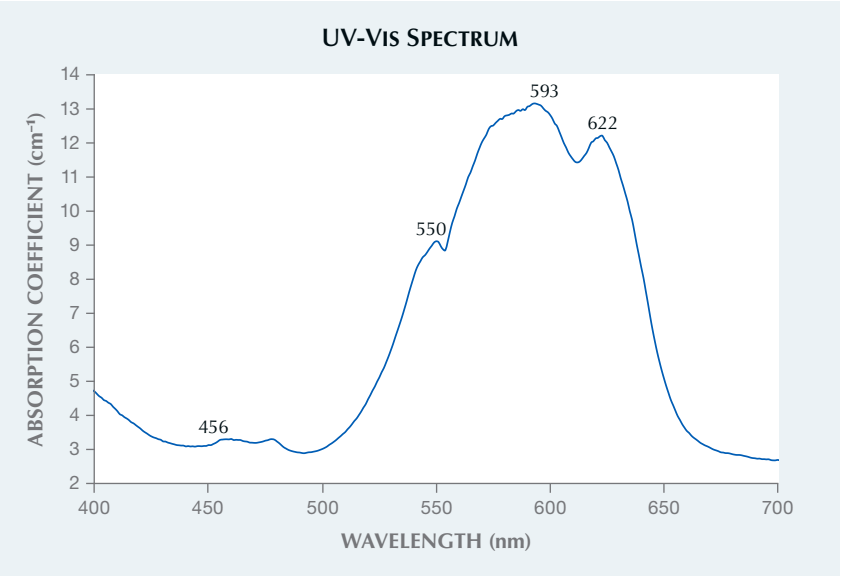

Figure 10. The UV-Vis spectrum of the gahnospinel showed a series of absorption bands at approximately 550, 593, and 622 due largely to Co^{2+} with additional minor contributions from Fe^{2+} and Fe^{3+} absorption bands at approximately 456, 550, and 593 nm.

Stockton, "'Cobalt-blue' gem spinels," Spring 1984 *G&G*, pp. 34–41; T. Stephan et al., "On the colour mechanism of blue gahnite from Nigeria," *Journal of Gems & Gemmology*, Vol. 38, No. 2, 2022, pp. 183–193), to our knowledge this is the first report of blue gahnospinel predominantly colored by cobalt.

Narint Jaisanit

PEARLS

Calcite Found on the Surface of a Saltwater "Nacreous" Pearl

The Hong Kong laboratory recently examined a loose pearl weighing 2.32 ct and measuring 8.45 × 7.27 × 5.36 mm (figure 11). Externally, the cream-colored pearl did not look out of the ordinary and exhibited a soft luster with a relatively clean surface. Examination through a binocular microscope revealed typical overlapping platelets, pits, and scratches. No coating, surface working, or other indications of treatment were observed (figure 12).

Figure 12. The pearl exhibited overlapping surface platelets typically found in nacreous pearls. Field of view 1.10 mm.

Real-time microradiography (RTX) revealed a distinct boundary with twin growth structures consisting of normal growth layers that followed the shape of the pearl (figure 13). No structural characteristics of any known type of cultured pearl were observed, so the pearl was identified as a natural pearl. Energy-dispersive X-ray fluorescence analysis showed high levels of strontium and no traces of

Figure 11. A cream-colored button-shaped loose pearl weighing 2.32 ct, submitted for identification.

Figure 13. RTX examination revealed a clear boundary running across the pearl as well as structures associated with natural formation.

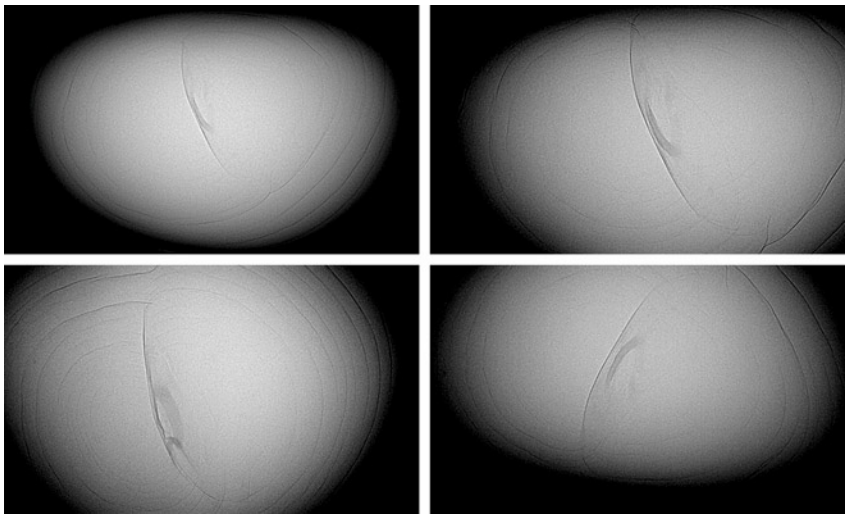

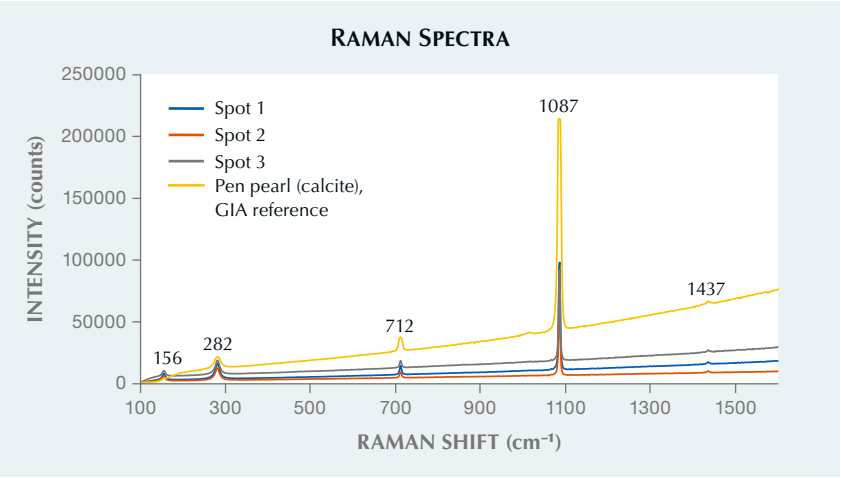

Figure 14. Raman spectra of three spots on the pearl's surface exhibit main peaks at 156, 282, 712, and 1087 cm^{-1} that are diagnostic of calcite.

manganese. This, together with its lack of visible fluorescence to X-ray luminescence, confirmed its saltwater origin.

Despite the typical saltwater nacreous pearl surface appearance, Raman analysis on three random spots with 514 nm laser excitation revealed that the pearl's platelet surface was composed of calcite rather than aragonite, with peaks at 156, 282, 712, 1087, and 1437 cm^{-1} (figure 14) (J. Urmos et al., "Characterization of some biogenic carbonates with Raman spectroscopy," *American Mineralogist*, Vol. 76, 1991, pp. 641–646).

Nacreous pearls are typically composed of small polygonal tablets of aragonite arranged in laminar layers (L. Addadi and S. Weiner, "A pavement of pearl," *Nature*, Vol. 389, 1997, pp. 912–915). Up until the examination of this specimen, Raman analysis on submitted pearls and research samples exhibiting overlapping platelet layers has always shown a mineral composition of aragonite. Calcite is usually found in the form of mosaic or cellular patterns on the surface of some types of pearls, or in the prismatic internal layers. This is the first time GIA has encountered a "nacreous-looking" pearl showing calcite when tested in different positions on its surface, which is unique and certainly worthy of note.

Cheryl Ying Wai Au

Two Black Non-Nacreous Bead Cultured Pearls from *Pinctada margaritifera*

The laboratory in Carlsbad recently received for identification two black pearls, one near-round and one button. The near-round pearl weighed 15.16 ct, while the button weighed 22.19 ct, with dimensions of 13.17 × 13.02 mm and 14.81 × 14.52 mm, respectively. Both displayed a similar vitreous luster and a non-nacreous surface appearance (figure 15). The button-shaped pearl also exhibited a nacreous surface on a small circled area at the base (figure 16). Microscopic examination using fiber-optic illumination revealed that the non-nacreous surface was composed of a mosaic or cellular pattern, resulting from the acicular nature of the individual calcite crystals. Some fine surface lines were also present in random directions across the cellular structures (figure 17). These cellular structures resembled those commonly observed on pen pearls from the Pinnidae family (N. Sturman et al., "Observations on pearls reportedly from the Pinnidae family (pen pearls)," Fall 2014 *G&G*, pp. 202–215).

A Raman spectrometer with 514 nm argon-ion laser excitation was used to examine the surface composition. The non-nacreous surfaces of both pearls showed a calcite spectrum with peaks at 712 and 1085 cm^{-1}, and aragonite peaks at 705 and 1085 cm^{-1} were

Figure 15. Left: Two black pearls, a 15.16 ct near-round and a 22.19 ct button, shown on the nacreous interior surface of a Pinctada margaritifera *shell. Right: The pearls both had a similar vitreous luster and a non-nacreous surface.*

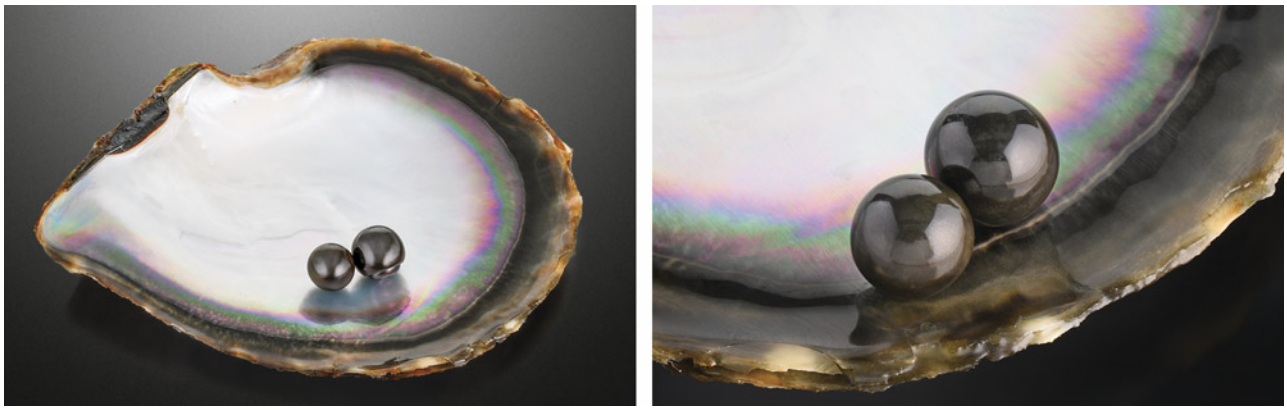

Figure 16. The button-shaped pearl displayed two different surface appearances. The main body was composed of a non-nacreous surface with calcite cellular structure, while the circled area at the base of the pearl had a nacreous surface with an aragonite platelet structure. Field of view 16.24 mm.

Figure 17. The non-nacreous surface of both pearls exhibited a similar cellular structure that could be viewed under high magnification using fiber-optic illumination. Some fine surface lines were present in random directions across the cellular structures. Field of view 1.59 mm.

recorded on the nacreous surface at the circular base of the button-shaped pearl. Energy-dispersive X-ray fluorescence chemical analysis showed low levels of manganese and high strontium content, confirming the pearls formed in a saltwater environment.

The large size, black bodycolor, and cellular structure of the pearls looked similar to the unusual non-nacreous natural pearls reportedly from *Pteria* species (S. Karampelas and H. Abdulla, "Black non-nacreous natural pearls from *Pteria* sp.," *Journal of Gemmology*, Vol. 35, No. 7, 2017, pp. 590–592) and a bead cultured (BC) pen pearl (Winter 2014 GNI, pp. 305–306) previously reported. Under long-wave ultraviolet radiation (365 nm), the pearls exhibited very weak yellow fluorescence that differed from the strong orangy red fluorescence observed in non-nacreous *Pteria* pearls. Real-time microradiography (RTX) revealed a round bead nucleus in the center of both pearls, indicating BC pearl origin (figure 18) similar to the previously reported BC pen pearl. Nevertheless, the ultraviolet/visible reflectance spectrum collected on the button pearl's nacreous surface showed a typical reflectance feature at 700 nm, a key mollusk identification feature attributed to *Pinctada margaritifera* pearls (K. Wada, "Spectral characteristics of pearls," *Gemological Society of Japan*, Vol. 10, No. 4, 1983, pp. 3–11, in Japanese). The reflectance features at 405 and 495 nm normally observed in naturally colored gray to black nacre of *P. margaritifera* shells were also present. Combining the cellular surface structures, BC origin, saltwater environment, and spectroscopic characteristics, we were able to conclude that both were non-nacreous BC pearls from the *P. margaritifera* mollusk.

All pearls are formed from calcium carbonate ($CaCO_3$) polymorphs such as aragonite and calcite together with organic substances as well as water. The most common form of $CaCO_3$ in pearls is a layered structure of aragonite platelets. This structure is the reason pearls display a nacreous surface and pearly luster. A non-nacreous surface indicates a pearl that formed from $CaCO_3$ but not with an aragonite platelet microstructure. Conch and Melo pearls are non-nacreous pearls that possess an aragonite fibrous or lamellar structure that display flame-like surface patterns. Scallop pearls are non-nacreous pearls made of calcite in a honeycomb patchwork of cells. Pen pearls mentioned previously are

Figure 18. RTX imaging revealed a round bead nucleus in the center of each pearl, indicating the pearls were bead cultured.

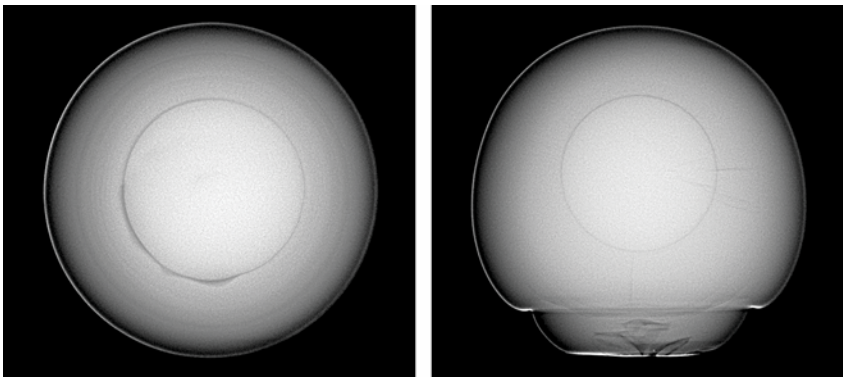

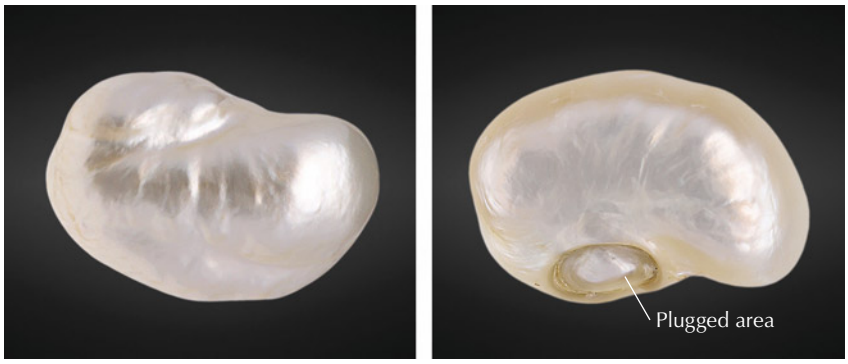

Figure 19. The 169.05 ct filled pearl, viewed from its face (left) and base (right). Note the indented feature on the base through which the filler material was inserted prior to plugging.

another type of calcite pearls with a cellular structure.

These two special occurrences are the first non-nacreous BC pearls from *P. margaritifera* identified by GIA. Cultured pearls from this mollusk, both BC and non-bead cultured, typically display a nacreous surface and are often referred to as "Tahitian" pearls in the market. Genetics is probably the most important factor influencing the biomineralization of a pearl, yet many other factors can be involved such as water environment and health of the mollusk. Organic substances also play an important role in the biomineralization process (C. Jin and J. Li, "The molecular mechanism of pearl biomineralization," *Annals of Aquaculture and Research*, Vol. 4, No. 1, 2017, p. 1032). In nature, many living organisms elaborately control the formation of biominerals for specialized functions such as mechanical support, protection, and mineral storage. Some mollusk species may produce different structures under certain circumstances.

Forozan Zandi, Artitaya Homkrajae, and Stephanie Shaw

A Partially Hollow Natural Blister Pearl Filled with Foreign Materials

Over the centuries, India has maintained its reputation as a natural pearl trading center. Since the launch of GIA's pearl identification service in Mumbai in May 2022, the laboratory has received a variety of interesting items for identification. One that stood out owing to its size and internal structure was a unique partially hollow natural blister pearl with unidentified fillers (figure 19).

The very large baroque white pearl weighed 169.05 ct (33.81 g) and measured 43.12 × 28.83 × 19.26 mm. However, on initial examination, its "heft" (perceived weight compared to its actual weight in comparison to its size) felt heavier than it should have. While the pearl's face-up side exhibited minor surface blemishes and good nacre condition (figure 20A), its base showed a deep oval indentation that looked a bit suspect to the unaided eye and needed further detailed examination. Under 40× magnification, the area revealed a distinct boundary with remnants of a transparent adhesive around it (figure 20B). Evidence of heavy working and polishing on and around the base was also clearly visible (figure 20, C and D).

Many loose nacreous baroque or semi-baroque pearls of this size are hollow to some degree, and most turn out to be blister pearls that were attached to the shell and removed at some point ("An unusual pearl," *GIA Research News*, March 31, 2009) or were shell blisters. In order to ensure the durability of these hollow pearls, and sometimes to add weight and increase their perceived value, they are filled with various materials such as metals, resins, waxes, shell, and other pearls (Fall 2013 Lab Notes, pp. 172–

Figure 20. A: The pearl's face showed minor surface blemishes; field of view 8.00 mm. B: The plugged area (boundary indicated by arrows) on the base with remnants of an adhesive around the oval opening; field of view 1.60 mm. C and D: Smoothed nacre layers provide evidence of heavy working and polishing on the base; field of view 3.00 mm.

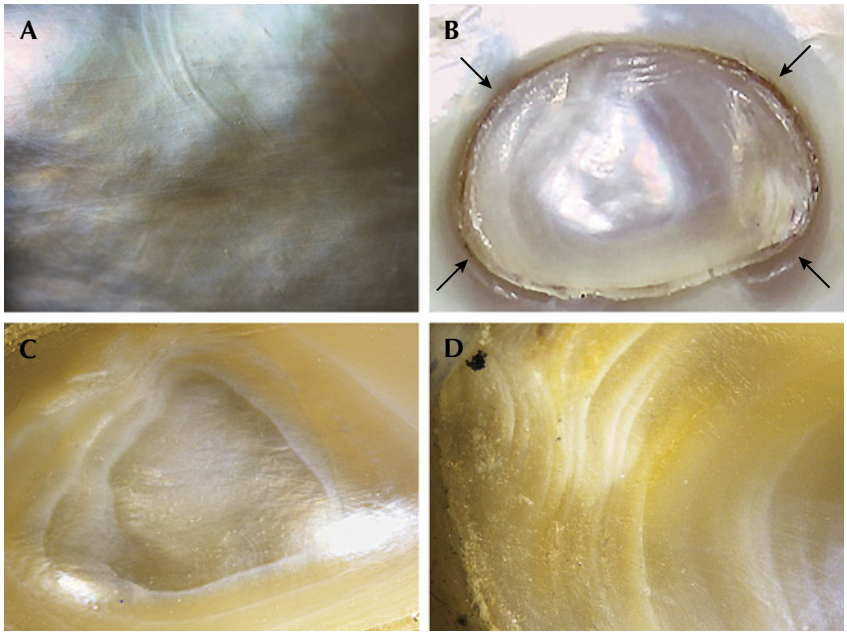

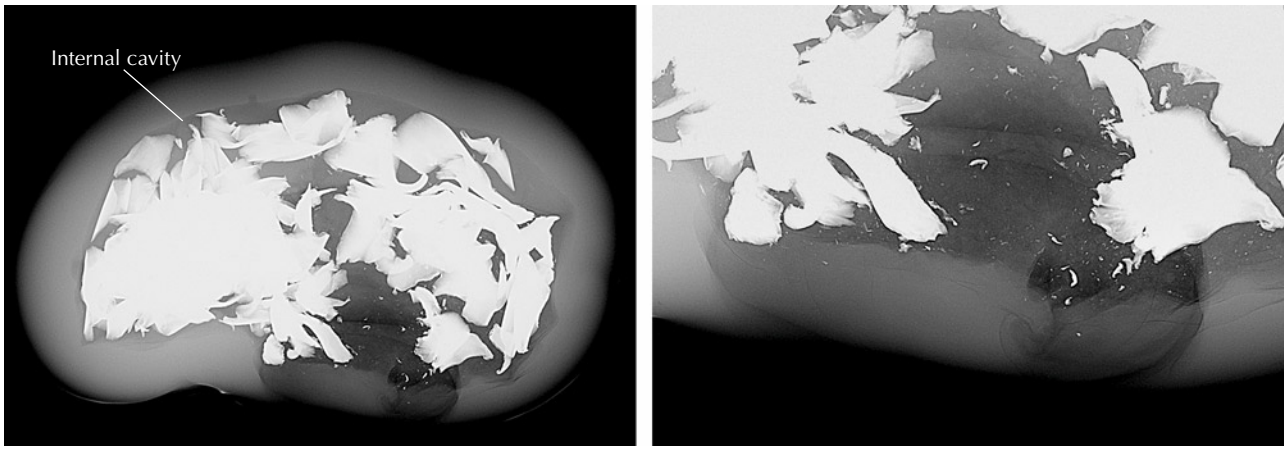

Figure 21. Opaque (white) areas indicate that metal pieces were placed within the pearl's large internal cavity (left). Natural growth arcs and a small darker organic-rich area are visible at the pearl's base (right).

173) and fashioned to improve their external appearance. Although the initial examination indicated that this pearl was likely filled with foreign materials, further analysis was required.

Real-time microradiography revealed a large organic void/cavity filled with a radiopaque white material, probably small metal fragments or metal shavings (figure 21; see also Summer 2019 Lab Notes, pp. 251–254). Areas of greater radio-transparency suggested that some type of bonding or stabilizing material, possibly adhesive, may have been used to hold the foreign pieces in place, and there also appeared to be one other type of radiolucent material within the cavity. The pearl was examined in several directions in order to further analyze the internal structure and fillings. The outline of the void was smooth and blended with the external shape of the pearl. The outer nacre layers revealed fine growth arcs and a small organic-rich area was visible at the base, both of which aligned more with the growth features of a natural pearl. It was clear that this was originally a blister pearl or shell blister that had been cut from a shell, and that the indented area, which was the opening on the base of the pearl, was the point of attachment that was subsequently plugged. X-ray fluorescence proved that the pearl formed in a saltwater environment since most of its surface appeared inert and only a small area at the base displayed a very light greenish yellow reaction uncharacteristic of a freshwater environment.

Energy-dispersive X-ray fluorescence spectrometry on two areas (face and base) showed low or below detection levels of manganese and higher strontium levels, above 1000 ppm, both characteristic of a saltwater environment. The higher strontium levels coupled with the large size indicated that the mollusk from which the pearl originated was *Pinctada maxima*.

Raman analysis using a 514 nm laser excitation on two spots (face and base) of the surface produced high fluorescence due to the pearl's light color and showed a doublet at 702 and 705 cm^{-1} as well as a peak at 1085 cm^{-1} indicative of aragonite. The photoluminescence spectra also displayed high fluorescence together with the aragonite peaks, as observed via Raman, typical of most nacreous pearls. Ultraviolet/visible/near-infrared spectra within the 220–850 nm range collected from the face and base were as expected for white to light cream-colored pearls and showed a predominantly high reflectance. The presence of a prominent 280 nm absorption feature coupled with moderate yellow reaction under long-wave UV excitation indicated that bleaching had most likely not been carried out.

After conducting a full analysis, GIA concluded that this sample most likely formed as a hollow natural blister pearl attached to its shell host. At some point, it was removed and the attachment area left an opening into the pearl. It was eventually worked and filled with foreign fillers (metal shavings/pieces and possibly some other materials) to improve its durability and make it suitable for setting; without the filling, it would not be usable in jewelry. The size, spectral characteristics, and chemistry were also consistent with a *Pinctada maxima* host mollusk.

Roxane Bhot Jain, Abeer Alalawi, Nicholas Sturman, and Chunhui Zhou

Large Faceted Pallasitic PERIDOT

Peridot, the green gem variety of the mineral olivine, is a relatively common gemstone known for forming as irregular nodules in lava flows or as large crystals within pockets of solidified rock throughout many areas of the world. Rarely, this stone can also be sourced from stony iron meteorites that have survived their flaming passage through Earth's atmosphere. These peridot-containing meteorites are known as pallasite, and the gems they contain are known as pallasitic peridot. Due to the extreme conditions endured by extraterrestrial stones, examples of faceted pallasitic peridot usually weigh less than half a carat (A.H. Shen et al., "Identification of extraterrestrial peridot by trace elements," Fall 2011 *G&G*, pp. 208–213). A recent submission to the

TABLE 1. Concentrations of trace elements (in ppmw) in a pallasitic peridot.

Element	Faceted stone	Extraterrestrial range[a]	Terrestrial range[a]
V	12.00	9.18–23.4	0.11–4.46
Li	0.48	0.21–0.96	1.10–14.5
Ni	17.3	8.53–112	1770–4070
Mn	2090	1920–2490	772–1410
Zn	6.59	5.20–9.98	9.04–67.4
Co	6.47	4.37–19.6	84.8–147

[a]*From A.H. Shen et al., "Identification of extraterrestrial peridot by trace elements," Fall 2011 G&G, pp. 208–213.*

Figure 22. The face-up view of a 2.32 ct faceted pallasitic peridot, the largest extraterrestrial peridot seen at GIA to date.

Carlsbad laboratory saw the largest client-submitted example to date at 2.32 ct (figure 22). The gem possessed characteristic inclusions such as thin, stacked red platelets (figure 23, left) and coarse, high-relief fingerprints (figure 23, right).

At GIA, extraterrestrial peridot is distinguished from the terrestrial variety by either energy-dispersive X-ray fluorescence or laser ablation–inductively coupled plasma–mass spectrometry (LA-ICP-MS) analysis of the trace elements vanadium, lithium, nickel, manganese, zinc, and cobalt (Shen et al., 2011). LA-ICP-MS analysis of these elements in the stone was diagnostic of pallasitic peridot when compared to published terrestrial and extraterrestrial data (Shen et al., 2011) (table 1).

Pallasite is named in honor of geologist Peter Simon Pallas, who first documented a stony iron meteorite with "rounded and elongated drops of a very brittle but hard, amber-yellow, transparent glass" discovered in Krasnoyarsk, Siberia, in 1749. At the time, suggestion of an extraterrestrial origin was daring. However, this theory gained support, and by 1794 additional scientific publications accepted the idea (J. Sinkankas et al., "Peridot as an interplanetary gemstone," Spring 1992 *G&G*, pp. 43–51). Today, pallasite is believed to have formed within asteroids containing an iron-nickel core and a silicate mantle (R.T. Dodd, *Meteorites: A Petrologic-Chemical Synthesis*, Cambridge University Press, Cambridge, UK, 1981, 368 pp.).

Britni LeCroy

PHOTO CREDITS
Shunsuke Nagai—1, 7; Yuxiao Li—2; Matthew Hardman—3–5; Mei Yan Lai—6; Makoto Miura—8; Lhapsin Nillapat—9; Tony Leung—11; Nick Chan—12; Cheryl Ying Wai Au—13; Annie Haynes—15; Artitaya Homkrajae—16, 17; Stephanie Shaw—18; Gaurav Bera—19; Nishka Vaz—20; Jayesh Surve—21; Diego Sanchez—22; Britni LeCroy—23

Figure 23. Left: Planar, brownish red thin films are a distinctive inclusion in pallasitic peridot; field of view 1.26 mm. Right: Coarse fingerprints are a common inclusion in both terrestrial and extraterrestrial peridot; field of view 1.99 mm.

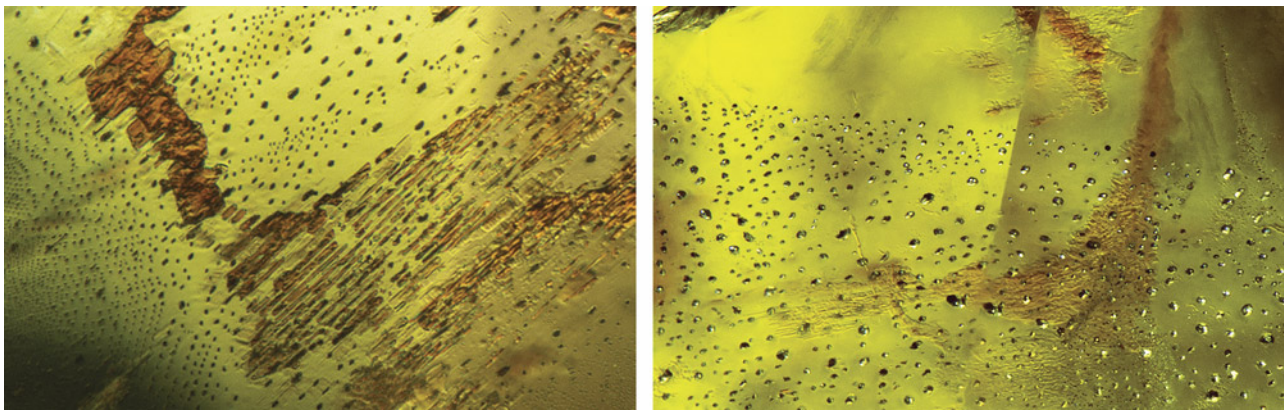

Knowledge and Skills for Today's Hot Topics

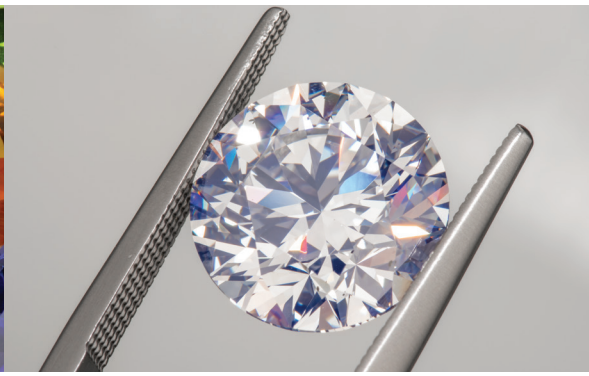

Online and In-Person Seminars Designed for Gem and Jewelry Professionals

- Natural and Laboratory-Grown Diamonds
- Jewelry Design
- Colored Stones
- Pearls
- Bench Skills

Visit **collective.gia.edu/seminars** for schedules and more information.

GIA Alumni receive a 10% discount. Seminars are open to all.

CONTINUING EDUCATION BY GIA Alumni Collective™

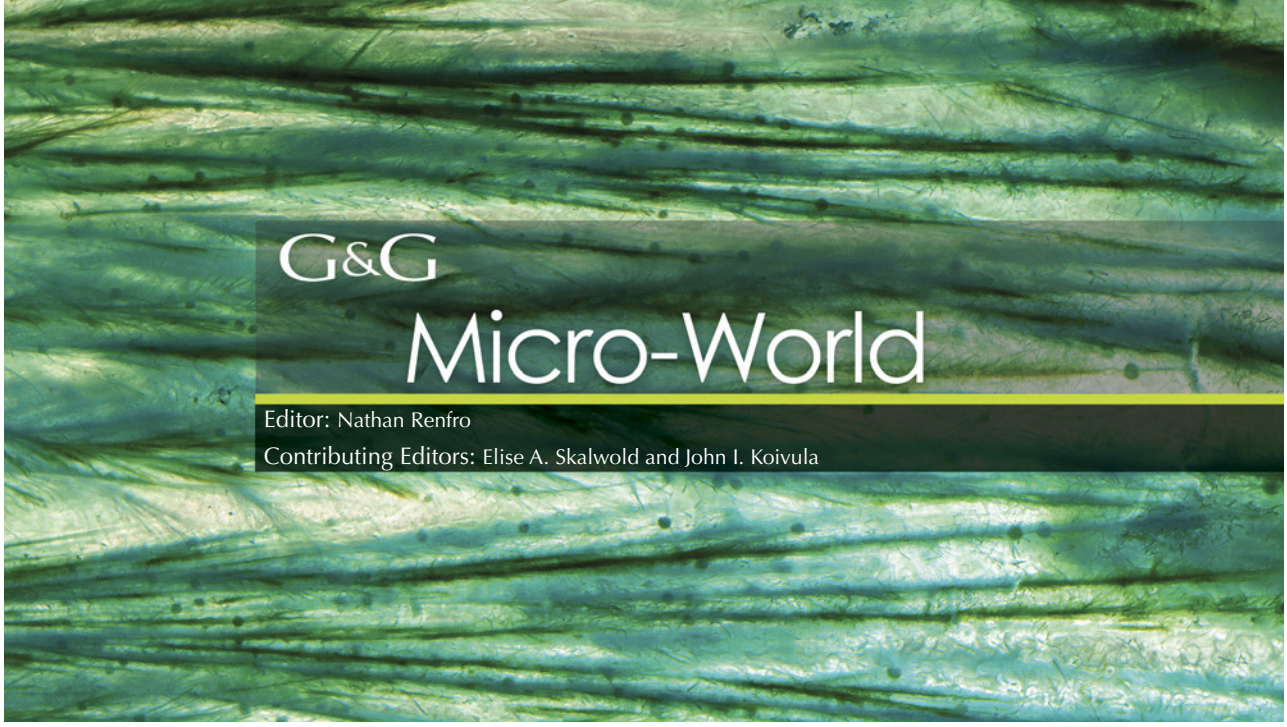

Arsenopyrite in Smoky Quartz

The authors recently examined a smoky quartz gem with interesting bladed inclusions of arsenopyrite (FeAsS), an iron arsenic sulfide mineral. The inclusions generally occurred as thick blades with striated faces in a dark gray color (figure 1). One such inclusion that was exposed to the surface and polished through showed a silvery gray coloration. Energy-dispersive X-ray fluorescence testing revealed significant amounts of iron and arsenic, consistent with the mineral arsenopyrite. The stone was reportedly from the Huanggang mine in Inner Mongolia, China. It was also reported that this stone was cut from a single large crystal that yielded approximately 20 such gems with arsenopyrite inclusions. Also present were numerous fluid inclusions, some of which showed vibrant thin-film interference colors in reflected light (figure 2). These are the first arsenopyrite inclusions the authors have examined in Mongolian quartz.

Nathan Renfro and John I. Koivula
GIA, Carlsbad

Figure 1. Blades of the iron arsenic sulfide mineral arsenopyrite seen in a smoky quartz from the Huanggang mine in Inner Mongolia. Photomicrograph by Nathan Renfro; field of view 4.67 mm.

Unusual "Horsetail" and Columnar Inclusions in Demantoid

Demantoid, a gem variety of andradite garnet, sometimes contains "horsetail" inclusions, a type of fibrous inclusion

About the banner: Stalks of copper minerals and spherical green concretions are seen throughout this rock crystal quartz from the Ray copper mine in Arizona. Photomicrograph by Nathan Renfro; field of view 28.20 mm.

Gems & Gemology, Vol. 58, No. 4, pp. 484–493.

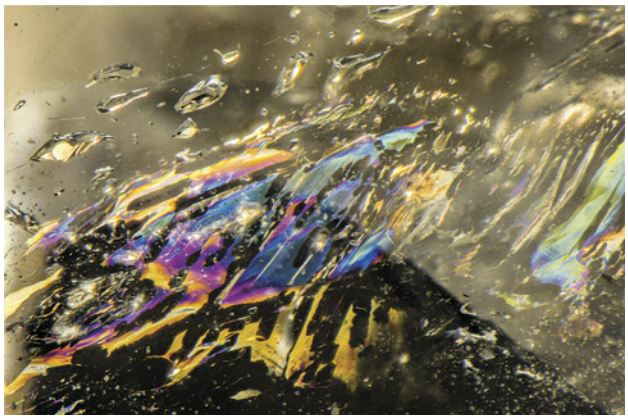

Figure 2. Fluid inclusions that showed vibrant interference colors in reflected light were also observed in the smoky quartz. Photomicrograph by Nathan Renfro; field of view 4.36 mm.

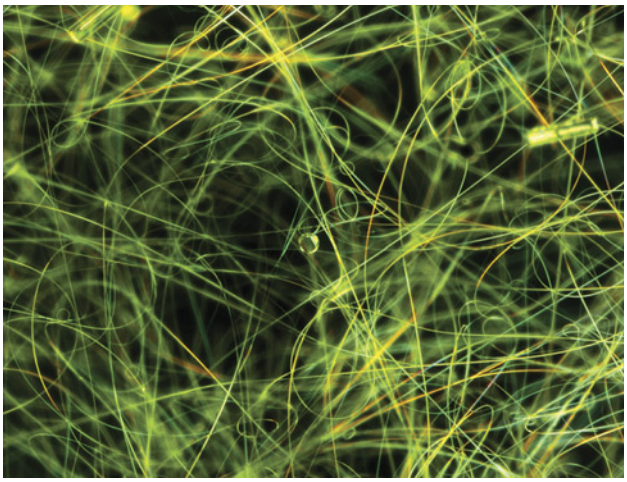

Figure 3. Fibers of serpentine were observed throughout this demantoid garnet in an unusual randomly curved pattern. Photomicrograph by Shunsuke Nagai; field of view 2.00 mm.

commonly seen in demantoid from Russia (e.g., W.R. Phillips and A.S. Talantsev, "Russian demantoid, czar of the garnet family," Summer 1996 *G&G*, pp. 100–111). Recent studies have shown that these horsetail inclusions from Russian demantoid are in fact hollow tubes partially filled with serpentine (e.g., A.Y. Kissin et al., "'Horsetail' inclusions in the Ural demantoids: Growth formations," *Minerals*, Vol. 11, No. 8, 2021, article no. 825).

Recently, the authors had an opportunity to examine a unique yellowish green demantoid weighing 0.73 ct. Horsetail inclusions often occur in a radial form, but these were quite unusual, showing random spiral- or coil-like structures throughout the stone (figure 3). Raman spectroscopic analysis identified these inclusions as serpentine. While their formation remains an open question, horsetail inclusions may suggest complicated geological conditions such as decompression (again, see Kissin et al., 2021).

Also of interest in this stone were two-phase columnar negative crystals containing mobile gas bubbles (figure 4). Based on analysis of the OH stretching region of Raman spectra (e.g., M.C. Caumon et al., "Fused-silica capillary capsules (FSCCs) as reference synthetic aqueous fluid inclusions to determine chlorinity by Raman spectroscopy," *European Journal of Mineralogy*, Vol. 25, No. 5, 2013, pp. 755–763; Winter 2015 Gem News International, pp. 446–448), these inclusions were determined to be mainly composed of saline solutions, possibly a mix of water and small amounts of sodium chloride, although the composition of the gas phase was not detected.

Figure 4. Columnar two-phase negative crystals containing mobile gas bubbles were another unique feature seen in the demantoid garnet. Photomicrographs by Makoto Miura; field of view 1.06 mm.

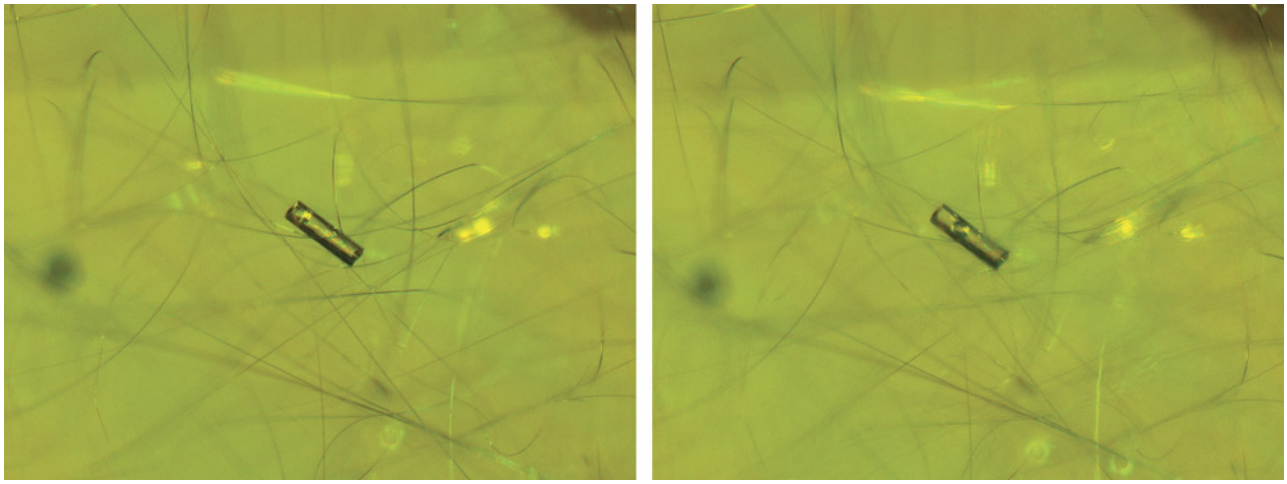

Figure 5. This particle cloud, a typical inclusion in diamond, shows an iridescent appearance and is grouped in a triangular shape viewed in fiber-optic illumination. Photomicrograph by Aprisara Semapongpan; field of view 2.8 mm.

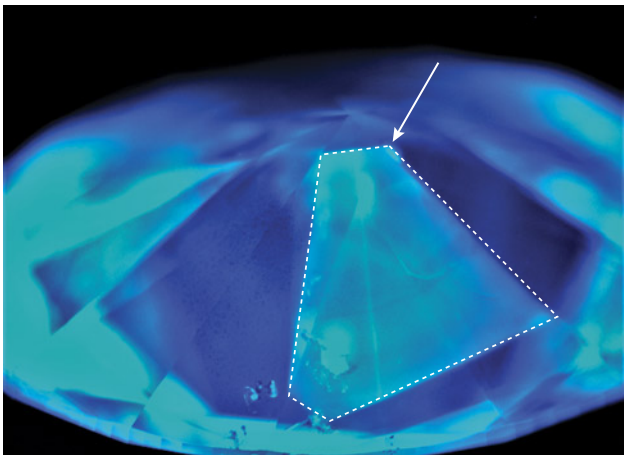

Figure 6. DiamondView imaging of the type IaB diamond reveals a fibrous pattern and a hazy triangular cloud area with blue fluorescence. Image by Aprisara Semapongpan.

Fluid inclusions in demantoid garnet have previously been reported (again, see Winter 2015 GNI, pp. 446–448). However, the columnar shape of the two-phase inclusions seen here is quite unusual considering the cubic crystal system of the host andradite garnet. These two-phase inclusions could be related to the formation of hollow canals within the host demantoid in the presence of water, although we are not yet able to determine how these negative crystals formed in this peculiar shape.

Shunsuke Nagai, Masumi Saito, and Makoto Miura
GIA, Tokyo

A "Galaxy" within a Diamond

The 2.01 ct, D-color, I_1-clarity type IaB diamond in figure 5 reveals an intriguing cloud of particles grouped in a triangular shape. These tiny crystal and particle cloud inclusions resemble a galaxy, as if seeing the Milky Way at night.

The DiamondView image in figure 6 reveals blue fluorescence with a hazy triangular glowing area that matches perfectly with the position of the particle cloud in figure 5. Furthermore, this type IaB natural diamond displays a fibrous pattern in the DiamondView instead of the tree-ring pattern that is typical in type Ia diamond. This fibrous pattern is related to a weak B-aggregated (B-center; 4N+V) signal in Fourier-transform infrared spectroscopy.

Finding and analyzing inclusions in diamonds is fascinating, as you never know where the next diamond will lead you—perhaps you will even discover your own galaxy.

Aprisara Semapongpan
GIA, Bangkok

Omphacite in Pink Diamond

Photomicrography of colored crystal inclusions is a field of seemingly endless possibilities in the realm of colored stones. With regard to diamond, however, the possibilities are far more limited. This is due to the growth origin of diamond within the earth's mantle—an environment few other minerals are able to endure. While colored crystal inclusions in diamond are uncommon, known possibilities include garnet, diopside, corundum, olivine, kyanite, and omphacite, the latter of which was seen in the Fancy brown-pink diamond in figure 7 and identified via Raman spectroscopy.

Figure 7. A bluish green omphacite crystal with surrounding stress fractures seen in a Fancy brown-pink diamond. Photomicrograph by Britni LeCroy; field of view 1.42 mm.

Omphacite is a mineral within the clinopyroxene solid solution series, which also contains the members jadeite, diopside, and aegirine. It typically occurs in eclogite, a high-pressure, high-temperature metamorphic rock also containing garnet. Eclogites form from igneous oceanic crust that has subducted into the mantle. The presence of an omphacite inclusion proves the diamond formed in an eclogitic environment. This is a rare inclusion not often seen at GIA.

Britni LeCroy
GIA, Carlsbad

Aegirine in Poudretteite

Originally discovered in Canada in the 1960s and named for the family that owned the rock quarry where it was found, extremely rare poudretteite was recognized as a new mineral in 1986. In 2000, the first gem-quality stone was discovered in Mogok, Myanmar. Recently, local miners found a new poudretteite deposit near Pein-Pyit village in the northeastern part of Mogok town. Some of these mined poudretteite gemstones contained unusual green crystal inclusions (figure 8).

The author examined two rough gem-quality light pink stones weighing about 1.065 and 1.104 ct. Gemological observation and Raman analysis confirmed that the two samples were poudretteite. The green crystal inclusions were present as both single crystals and sprays of acicular crystals in a radial pattern (figure 9). They had a mostly prismatic crystal shape with a bright yellowish green color. Micro-Raman analysis identified them as aegirine, the first discovery of this mineral in poudretteite from Mogok. Aegirine commonly occurs in alkaline igneous rocks, nepheline syenites, carbonatites, and pegmatites. This mineral inclusion could be an indicator of Mogok origin.

Kyaw Thu
S Gemmological Institute, Yangon, Myanmar

Figure 8. An aegirine crystal inclusion in poudretteite rough from Mogok, viewed with oblique fiber-optic illumination. Photomicrograph by Kyaw Thu; field of view 2.3 mm.

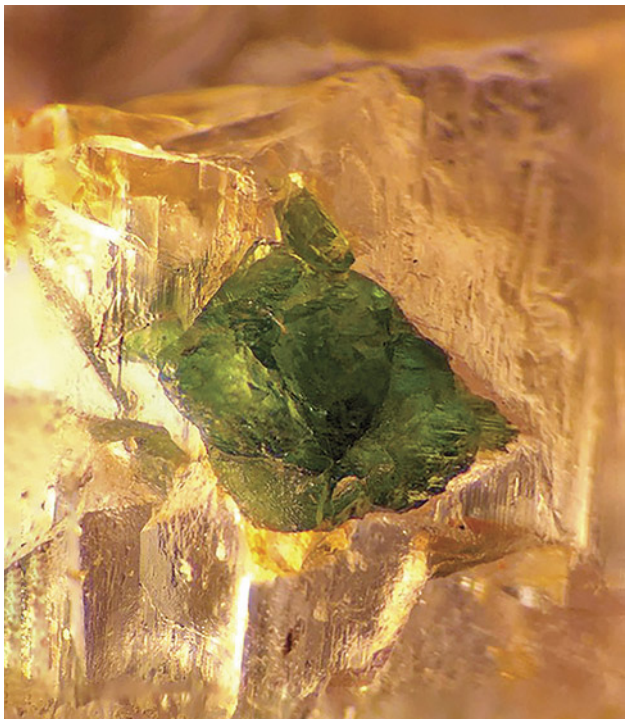

"Electromagnetic Wave" Inclusion in Mong Hsu Ruby

Recently the author examined a vivid red 1.18 ct cushion-cut ruby. This ruby contained several inclusions, such as distinctive hexagonal zoning with a blue core, a cloud of snowflake-like particles, and ladder-like particles. These

Figure 9. Aegirine inclusion showing sprays of acicular crystals in poudretteite rough from Mogok (darkfield and oblique fiber-optic illumination). Photomicrograph by Kyaw Thu; field of view 0.84 mm.

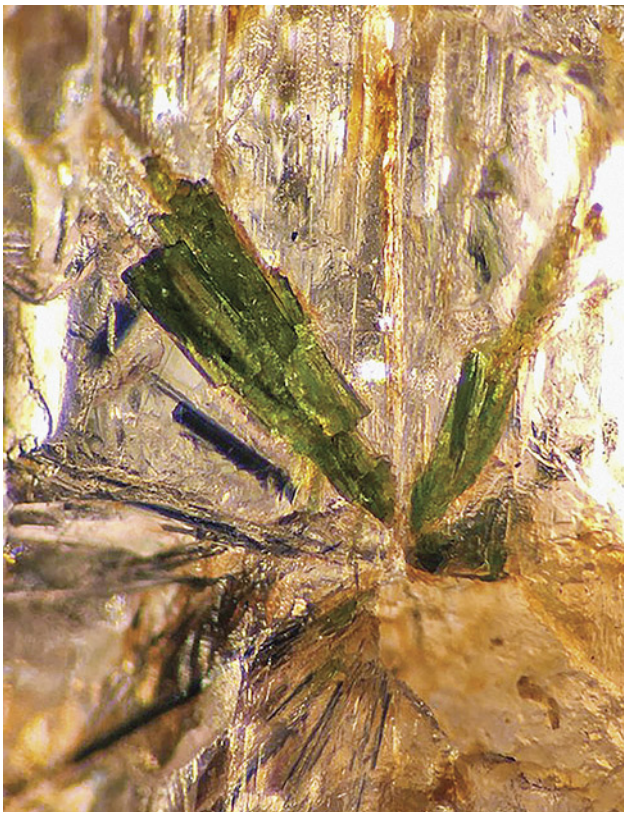

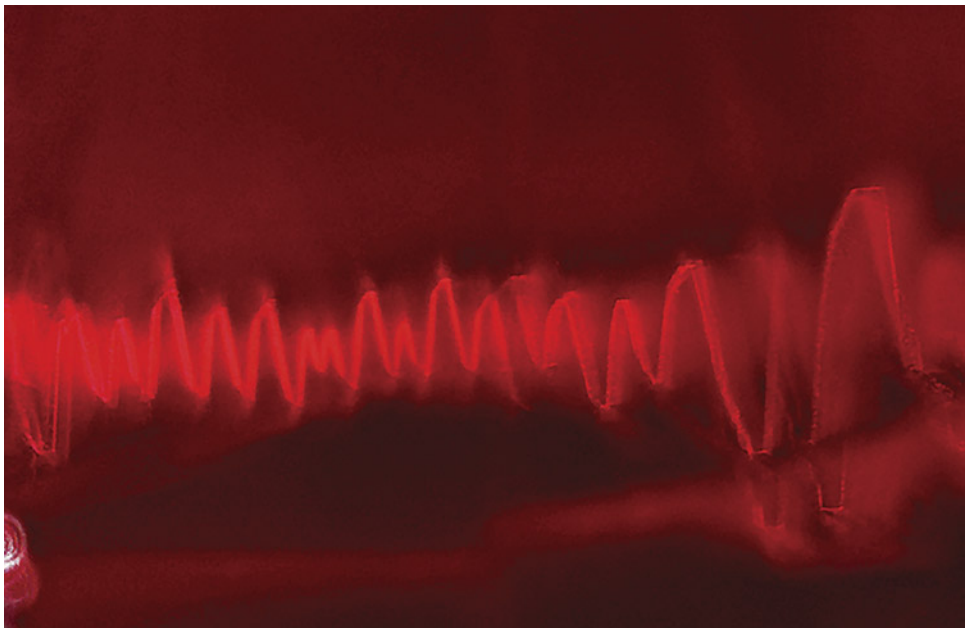

Figure 10. An electromagnetic wave-like pattern of whitish dust in Mong Hsu ruby. Photomicrograph by Narint Jaisanit; field of view 1.70 mm.

inclusions combined with chemical analysis indicated a geographic origin of Mong Hsu, Myanmar. Interestingly, fiber-optic illumination revealed an electromagnetic wave-like pattern of particles (figure 10). Although whitish particles are common in Mong Hsu rubies, this electromagnetic wave pattern is truly unique.

Narint Jaisanit
GIA, Thailand

Volcano-Shaped Internal Feature in Trapiche-Like Sapphire

Trapiche-like sapphires with hexagonal color zoning have been found in the Changle area of Shandong Province, China. Samples examined by the authors possessed a brown-black hexagonal core and a distinct six-rayed pattern (figure 11). The six rays or fibrous arms were oriented perpendicular to the sides of the core and the hexagonal growth structure.

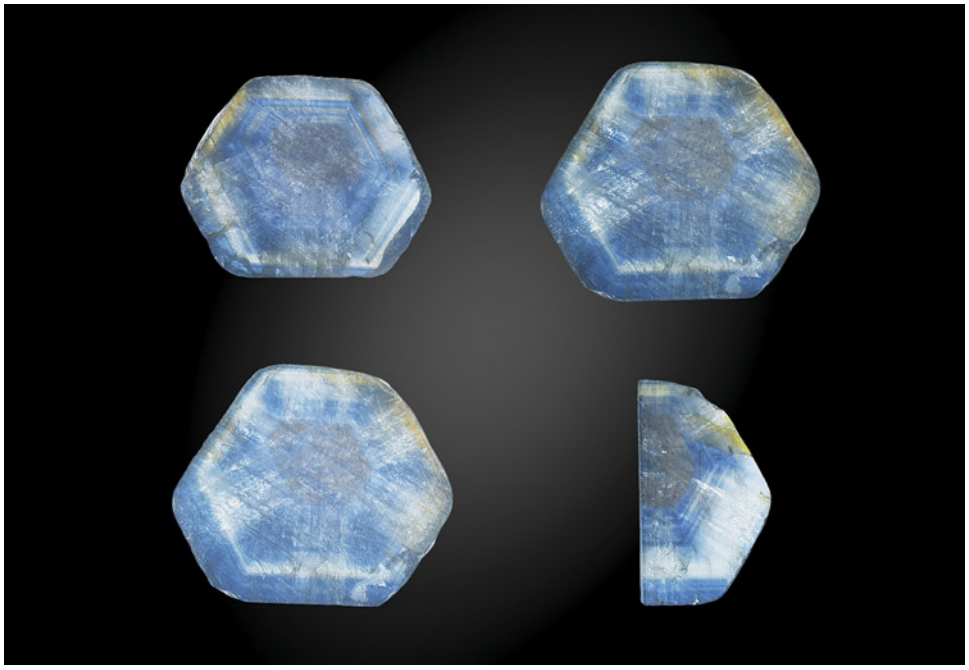

Figure 11. Each of these trapiche-like sapphires from Changle, Shandong Province, has a brown-black hexagonal core in the center and six white radiating arms. Three of the four sample slices weigh ~3.1 ct with a thickness of ~2.1 mm; the sample slice on the bottom right weighs ~0.7 ct with a thickness of ~1 mm. Photos by Suqin Xia.

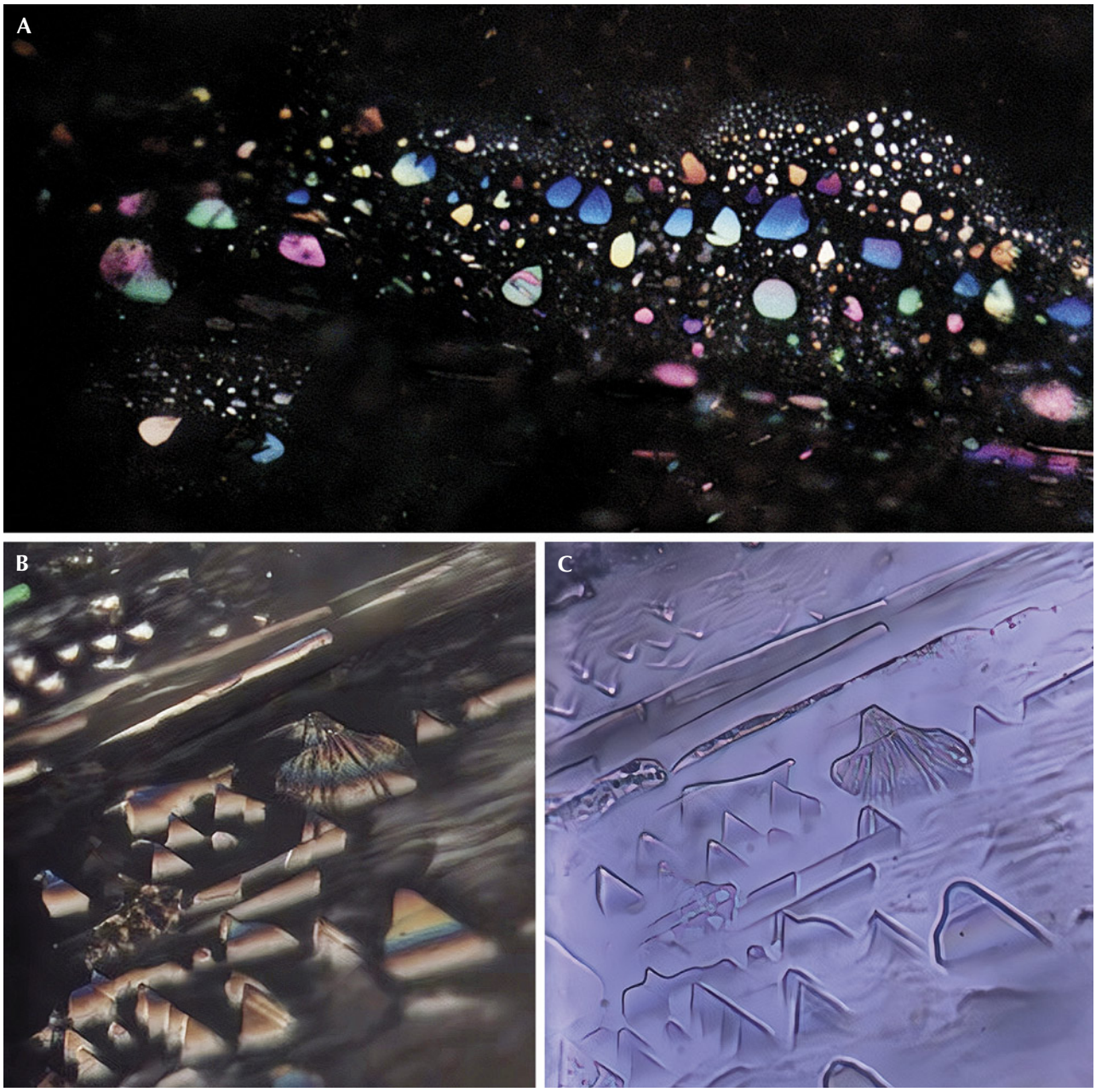

Figure 12. Inclusions along the white arms of trapiche-like sapphire. A: Thin-film inclusions display colorful interference colors under reflected light. B: Triangle-shaped fissures, which are perpendicular to the crystallographic c*-axis, resemble overlapping hills, including a volcano just right of center. These fissures show spectral interference colors under reflected light. C: In transmitted light, the pattern of inclusions resembles a Chinese landscape painting with a volcano in it. Photomicrographs by Xiaojing Lai; fields of view 0.30 mm (A) and 0.15 mm (B and C).*

Graphite was randomly distributed in the dark core region in this sapphire, identified by Raman spectroscopy.

Through further microscopic observation, we found that these fibrous arms were composed of thin-film fluid inclusions and fine fissures generally parallel to their elongation direction (figure 12). Many of these inclusions were two-phase, containing both gas and liquid, and a few were gas-liquid-solid three-phase. Interestingly, the fissures were triangular, scalloped, striped, or irregular in shape and about 10 to 40 µm in size, with spectral interference colors (figure 12A). With overhead lighting, the internal features presented a dramatic scene reminiscent

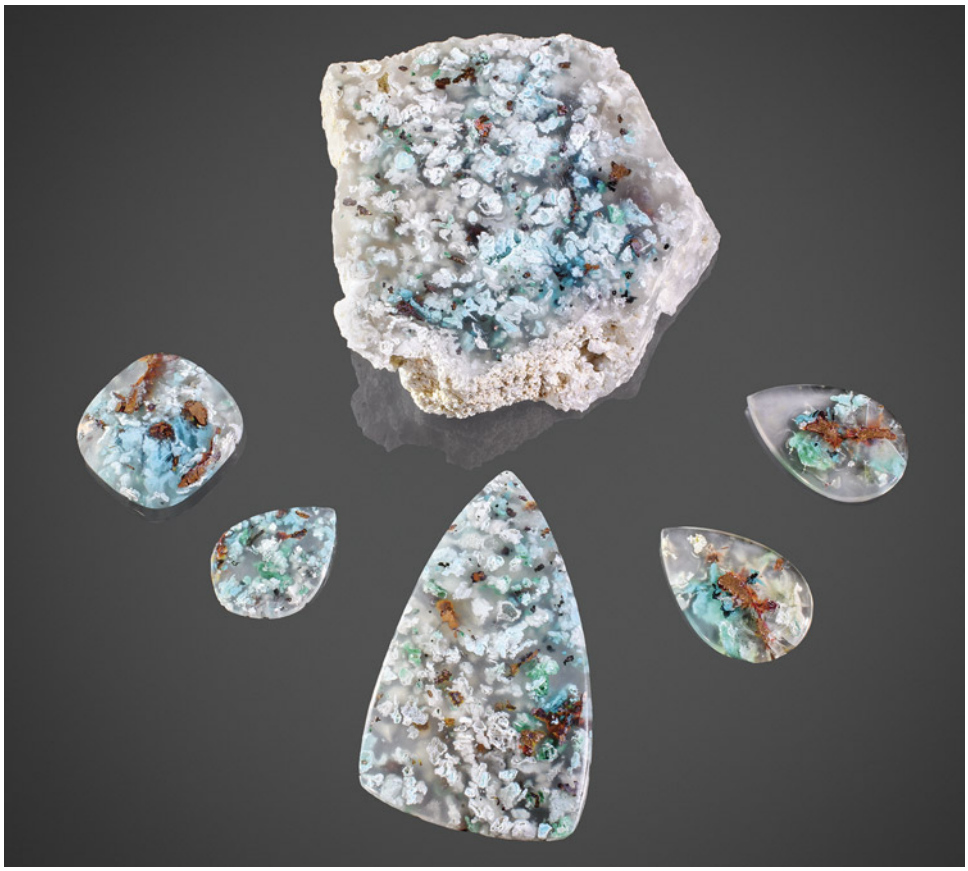

Figure 13. This new chalcedony from Indonesia, which one dealer is marketing under the trade name "Aquadite," contains numerous inclusions composed of copper and copper minerals such as red cuprite, blue chrysocolla, and green malachite. The largest triangular cabochon weighs 78.80 ct. Photo by Annie Haynes; courtesy of Yianni Melas.

of a post-eruption volcano surrounded by overlapping hills and rivers (figure 12B). In transmitted light, however, the same features resembled a Chinese landscape painting, and the previous "rivers" looked more like clouds surrounding the volcano and hills (figure 12C). The internal features found in this sapphire are interesting to gemologists both scientifically and artistically.

Xiaojing Lai and Suqin Xia
Gemmological Institute,
China University of Geosciences, Wuhan

Copper "Confetti" Inclusions in Chalcedony

Recently the author examined an interesting new variety of chalcedony from Indonesia (figure 13). Samples were sourced from Greek dealer Yianni Melas in order to document the new material. Gemologically, the properties are consistent with chalcedony, including a refractive index of 1.54 and a specific gravity of 2.56. However, this material is particularly notable for its mineral inclusions. Much like confetti thrown in the air as a celebration, a multitude of blue, green, and metallic inclusions (figure 14) were scat-

Figure 14. The Indonesian chalcedony contains vibrant inclusions such as greenish blue chrysocolla (A), green malachite, and well-formed crystals of native copper that has in some cases altered to the deep red mineral cuprite (A, B, and C). Photomicrographs by Nathan Renfro; fields of view 10.27 mm (A), 4.17 mm (B), and 4.77 mm (C).

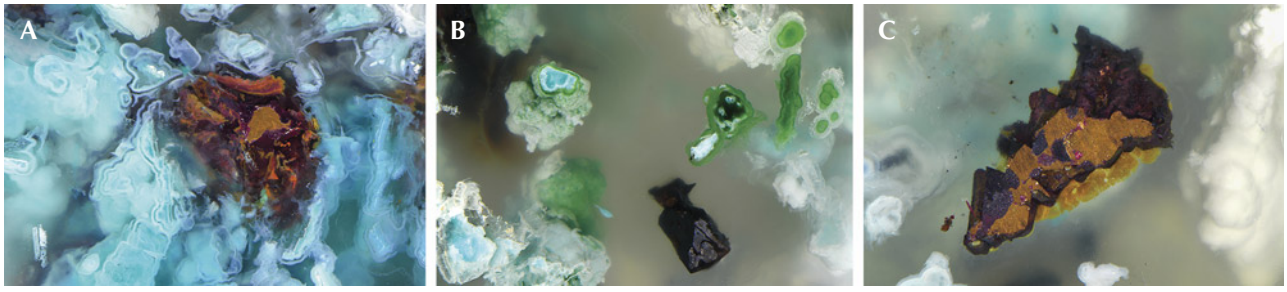

Figure 15. Left: This 3.07 ct purplish pink "dragon" garnet, as seen in daylight-equivalent lighting, displays eye-visible blue apatite inclusions. Right: Red fluorescence in the garnet due to chromium, as seen using long-wave UV. Photos by Jessa Rizzo; courtesy of Ravenstein Gem Co.

tered throughout the chalcedony matrix. Advanced testing, including Raman spectroscopy and energy-dispersive X-ray fluorescence analysis combined with microscopic observation, confirmed the presence of chrysocolla, malachite, native copper, and cuprite.

Melas plans to market this new material under the trade name "Aquadite." This fascinating chalcedony from Indonesia should be a popular gem for any collector who enjoys unique examples of vibrantly colored chalcedony.

Nathan Renfro

Garnet with Apatite Inclusions

The authors recently examined a 3.07 ct garnet sample acquired from Ravenstein Gem Co. by author NR. This gem material, marketed online as "dragon" garnet as an allusion to the mythical creature's changing eye color, was reportedly from a new find at an undisclosed locality in Africa. It is also notable that Lotus Gemology has reported similar material from Tanzania (Summer 2022 *G&G* Micro-World, pp. 226–227). The garnet was a delicate purplish pink color under daylight-equivalent lighting (figure 15, left) and showed a fairly strong red fluorescence when exposed to long-wave ultraviolet light (figure 15, right). Also of note, this sample, as well as many of the other examples showcased online, contained vibrant blue inclusions of apatite (figure 16) as well as typical needle-like silk and minute fluid inclusions.

Gemological testing revealed a refractive index measurement of 1.741 and a hydrostatic specific gravity of 3.81. Further gemological testing with laser ablation–inductively coupled plasma–mass spectrometry revealed the major composition to be pyrope (61.5 mol.%), spessartine

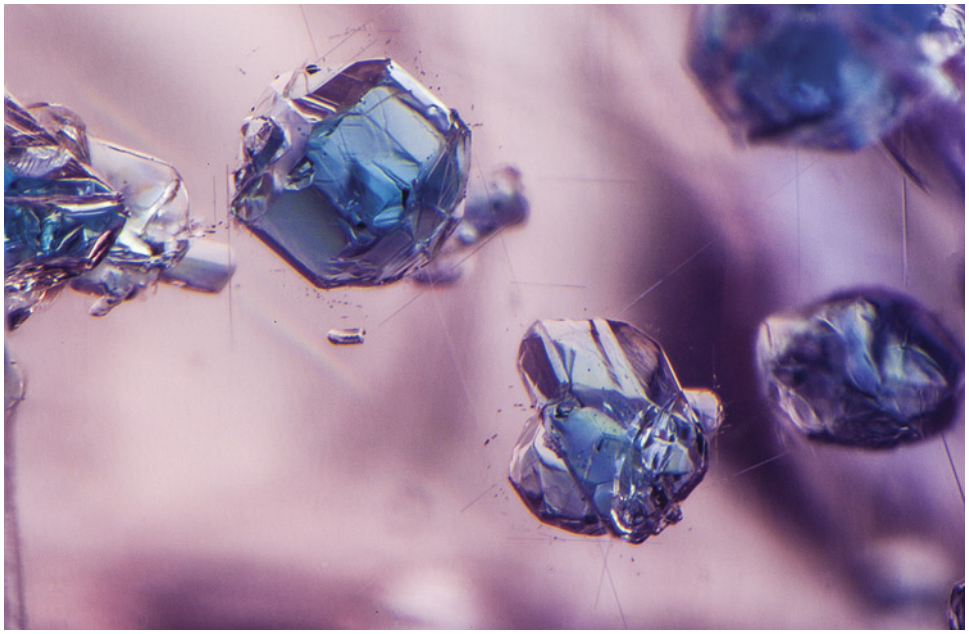

Figure 16. Blue apatite inclusions and rutile needles were prominent throughout the "dragon" garnet reportedly from a new find in Africa. Photomicrograph by Nathan Renfro; field of view 2.40 mm.

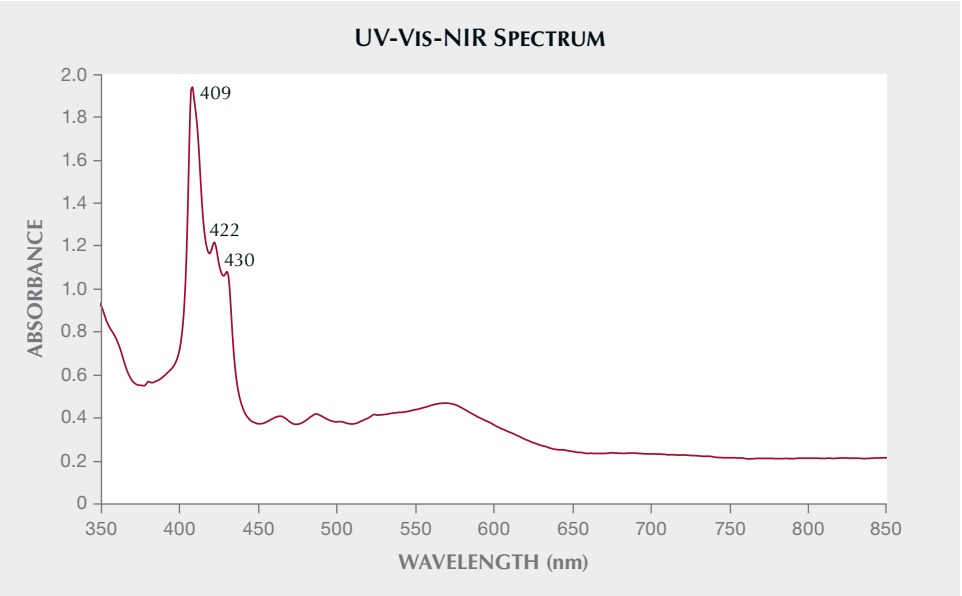

Figure 17. The garnet's UV-Vis-NIR spectrum suggests the color results mainly from manganese, iron, chromium, and vanadium. Narrow bands at 409, 422, and 430 nm are related to manganese in the garnet structure, while absorption bands related to iron are at ~465 and 488 nm (Z. Sun et al., "Quantitative definition of strength of chromophores in gemstones and the impact on color change in pyralspite garnets," Color Research and Application*, Vol. 47, 2022, pp. 1134–1154). A broad band centered at ~572 nm is from vanadium and chromium absorption.*

(29.0 mol.%), grossular (6.5 mol.%), and almandine (2.6 mol.%), a chemistry consistent with pyralspite-series garnets. Notable trace elements in significant quantities were chromium (660 ppmw) and vanadium (343 ppmw) in addition to the rare earth elements yttrium (1206 ppmw), erbium (222 ppmw), and ytterbium (420 ppmw). The ultraviolet/visible/near-infrared (UV-Vis-NIR) spectrum revealed absorption bands that were consistent with the chemical analysis (figure 17), indicating that the color of the garnet results from a mixture of manganese, iron, chromium, and vanadium. Raman analysis confirmed the blue inclusions as apatite. It is also notable that the garnet sample showed a weak color change in daylight compared to various non-standardized, commercially available LED types of lighting, changing from purplish pink to pink-orange. Photoluminescence testing with a 514 nm laser revealed a strong chromium-related emission, consistent with the red fluorescence observed with long-wave UV exposure (figure 18).

The strong red fluorescence, color change under certain LED lights, and presence of significant rare earth elements and vibrant blue apatite inclusions make it quite interesting for any gem collector.

Jessa Rizzo, Nathan Renfro, and Ziyin Sun
GIA, Carlsbad

Quarterly Crystal: Etching on Laurentthomasite

The micro-world of gems and minerals involves the study of not only fluid and solid inclusions but also any significant surface features caused by growth and/or etching. When a rough crystal is fashioned into a gemstone, most

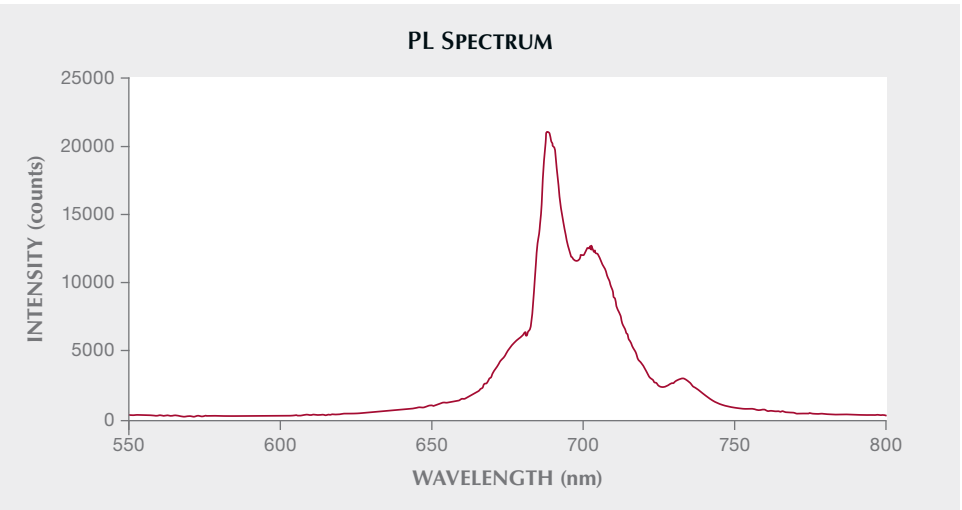

Figure 18. The photoluminescence spectrum collected from the garnet using a 514 nm laser revealed chromium-related emission consistent with the observed red fluorescence under long-wave UV excitation.

Figure 19. This deeply etched 11.24 mm laurentthomasite crystal from Madagascar displayed a rich greenish blue color. The orange color patches are epigenetic limonitic residue. Photo by Annie Haynes; courtesy of Arkfeld Minerals.

if not all surface features of any importance are removed during the lapidary process. So when we encounter an interesting gem crystal, we always take the opportunity to examine the natural surfaces for any interesting evidence of growth or dissolution.

With that in mind, we recently studied a rough-surfaced etched hexagonal crystal of laurentthomasite (figure 19) from Madagascar that measured 11.24 × 9.76 × 4.32 mm and weighed 3.71 ct. Laurentthomasite, with the chemical formula $Mg_2K(Be_2Al)Si_{12}O_{30}$, is a relatively recent mineral approved in 2019 by the International Mineralogical Association (IMA) as a new species in the milarite (osumilite) group. It was named after French mineral dealer Laurent Thomas.

The rough surface of the laurentthomasite prevented the application of standard gemological testing. With magnification, however, we were able to observe a uniaxial optic figure from the crystal in polarized light. As expected, the dichroism displayed was a greenish blue down the optic axis direction and greenish yellow perpendicular to the *c*-axis. Under UV radiation, the crystal's reaction was inert.

Examination of the surface using differential interference contrast microscopy showed an abundance of hexagonal etch features, some with a rather dramatic architecture. Reflecting the hexagonal symmetry of the laurentthomasite, as shown in figure 20, these dissolution features were targeted for photomicrography.

John I. Koivula and Nathan Renfro

Figure 20. Some of the dissolution features observed on the etched surface of the laurentthomasite crystal were reminiscent of decorative hexagonal tiles, as seen using differential interference contrast (left) and diffuse transmitted light (right). Photomicrographs by Nathan Renfro; field of view 1.44 mm.

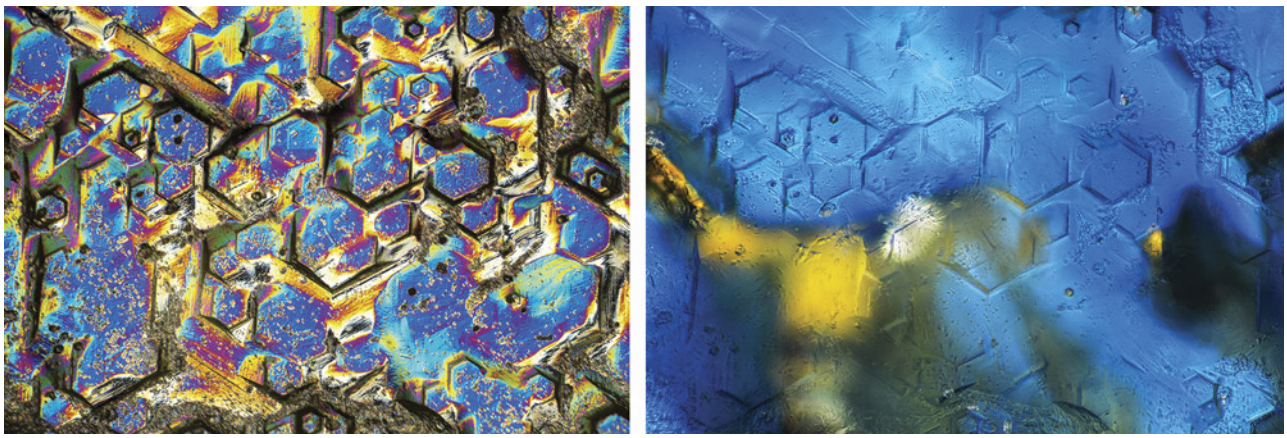

Gems Formed in Magmatic Rocks

The rigid outer layers of the earth (the lithosphere) are composed of minerals and rocks. Minerals are natural chemical compounds that form in certain geological environments and sets of physical and chemical conditions. In the lithosphere, the main mechanisms for mineral formation are cooling and solidification from igneous magmas, crystallization from high-temperature hydrothermal solutions or vapors, crystallization from low-temperature aqueous solutions, and solid-state mineral recrystallization during metamorphism. Gem minerals can be formed by any of these mechanisms.

Minerals have specific chemical compositions and arrangements of constituent atoms (i.e., crystal structure). Approximately 5,800 mineral species are currently recognized by the International Mineralogical Association (IMA), most of them rare and narrowly distributed. Despite the variety of mineral species, almost 97% of the earth's crust is made up of a few elements: oxygen, silicon, aluminum, iron, calcium, sodium, potassium, and magnesium. Hence, the crust is dominated by a small handful of minerals containing these elements (feldspars, quartzes, pyroxenes, amphiboles, and micas). While these minerals are occasionally found as gem-quality pieces, most natural gems are rarer mineral phases that fortunately occur in specific deposits as crystals of a size and quality that can be faceted or polished.

This edition of Colored Stones Unearthed will focus on gem minerals that form in magmatic environments (figure 1). Other environments of gem formation will be discussed in future columns.

Figure 1. These examples of gem minerals that formed in magmatic environments are part of GIA's Eduard Gübelin Collection. From top to bottom and left to right: 29.96 ct sanidine feldspar from Germany, 53.00 ct peridot from Myanmar, 11.58 ct zircon from Thailand, 20.66 ct topaz from Utah, 2.05 ct sapphire from Thailand, 18.36 ct pyrope garnet from the Czech Republic, 19.55 ct black spinel from Thailand, and 2.50 ct ruby from Thailand. Photos by Robert Weldon.

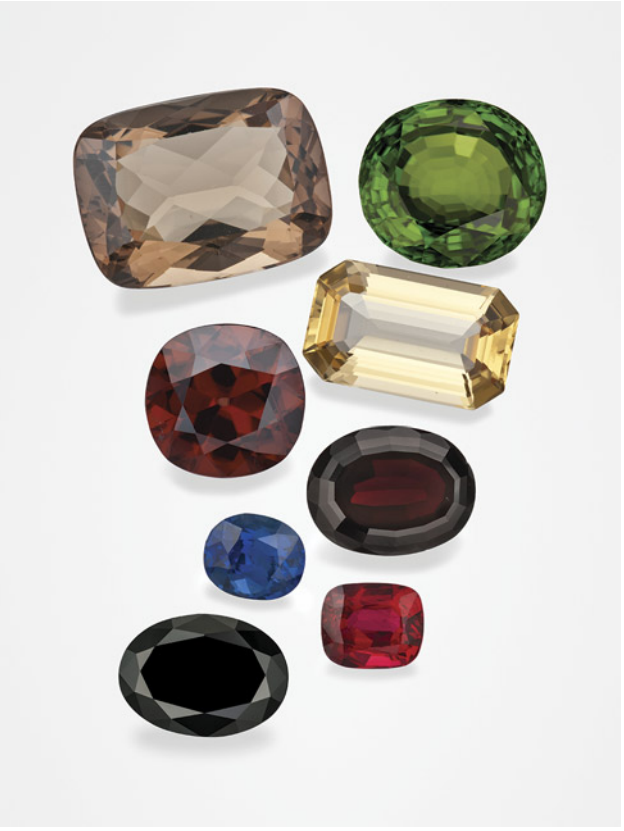

Editors' note: Questions or topics of interest should be directed to Aaron Palke (apalke@gia.edu) or James Shigley (jshigley@gia.edu).

Gems & Gemology, Vol. 58, No. 4, pp. 494–506.

Figure 2. Eruption of the Tungurahua volcano in Ecuador. Various gem minerals can crystallize from molten magmas in the earth's crust or when the magmas erupt at the surface. Magmas also bring up pieces of mantle or crustal rocks called xenoliths *that are of great value for scientific study. Courtesy of Sebastián Crespo Photography/Moment/Getty Images.*

Mineral Formation in Magmas

Magmatic minerals form during the cooling and crystallization of magmas (molten rock) in certain portions of the earth's lithosphere and at the surface (figure 2). These magmas vary in chemical composition, but for most the dominant chemical component is silica (SiO_2). The amount of SiO_2 in a magma dictates many of the properties and eruptive behaviors of volcanic events, and silica concentration can tell researchers a great deal about the geological history of a magma. Basalts, for instance, are silica-poor magmas (typically ~50 wt.%), while rhyolites have high silica contents (typically >70 wt.%). Magmas can form when temperatures rise in the earth and melting of preexisting rocks occurs in the lower crust or upper mantle. Decreases in pressure or the introduction of water or other volatile components can also result in the production of magma deep within the earth. Once formed, magmas can either travel through the crust via fissures, form large magma-filled chambers in other rocks, or be erupted at the earth's surface through volcanic vents (figure 3).

Whatever their origin, the cooling of magmas results in the crystallization of igneous rocks, which are classified according to their texture and mineral composition (table 1). As the magma's temperature decreases and it

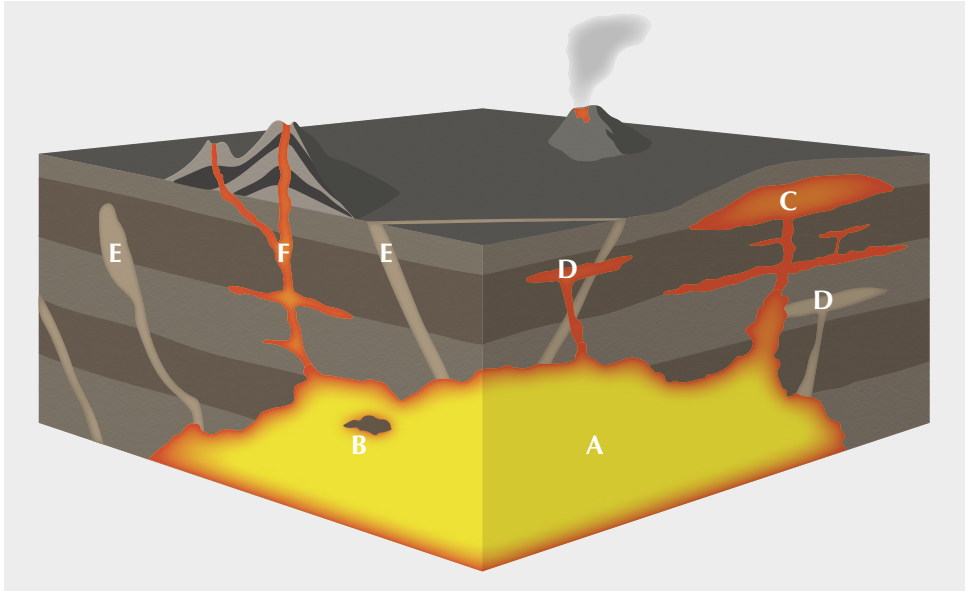

Figure 3. This diagram illustrates various locations where molten magmas can reside in the crust above a large magma chamber, as well as the channels or conduits by which they can reach the surface to form volcanoes: active magma chamber (A), mantle xenolith in chamber (B), laccolith (C), sill (D), dike (E), and volcanic conduit (F). Modified from Johnson et al. (2017).

TABLE 1. Classification of igneous rocks based on mineral composition and texture.

Category	Felsic	Intermediate	Mafic	Ultramafic
Mineral Composition	>10% quartz >50% feldspar <15% mafic minerals	>10% quartz >50% plagioclase >10% orthoclase <15% mafic minerals	20–85% plagioclase 15–50% pyroxene >35% olivine	Olivine and pyroxene
Texture				
Phaneritic (coarse-grained)	Granite, syenite, granodiorite, and tonalite	Diorite	Gabbro	Peridotite and pyroxenite
Aphanitic (fine-grained)	Rhyolite, dacite, and trachyte	Andesite	Basalt	—
Porphyritic (large crystals in fine-grained matrix)	Porphyritic rhyolite	Porphyritic andesite	Porphyritic basalt	—
Vesicular (porous)	Pumice	Pumice	Scoria	—
Glassy (vitreous)	Obsidian	Obsidian	—	—
Pyroclastic (fragmental)	Rhyolitic tuff or breccia	Andesitic tuff or breccia	Basaltic tuff or breccia	—

begins to solidify, mineral formation can occur below the surface (to form intrusive or plutonic or phaneritic rocks with coarser grain size due to slower gradual magma cooling). Alternatively, magma that is erupted at the surface will solidify quickly, often leading to small grain sizes of the constituent minerals (to form extrusive or aphanitic rocks) (figure 4).

Volcanic Eruptions

A volcano forms above an underground magma chamber and is created where the magma is vented or erupted at the earth's surface. Volcanoes occur at specific locations of the crust that are associated with the creation, lateral movement, and then subduction of crustal plates. Most volcanoes are located along boundaries of crustal plates, either at di-

Figure 4. Two examples of important igneous rocks. Rhyolite (left) is an aphanitic extrusive igneous rock, while granite (right) is a phaneritic intrusive igneous rock. They are similar in chemical composition but differ in the size of their constituent mineral grains because they cool and solidify at different rates under different geological conditions. Photos by James St. John/Wikipedia Commons.

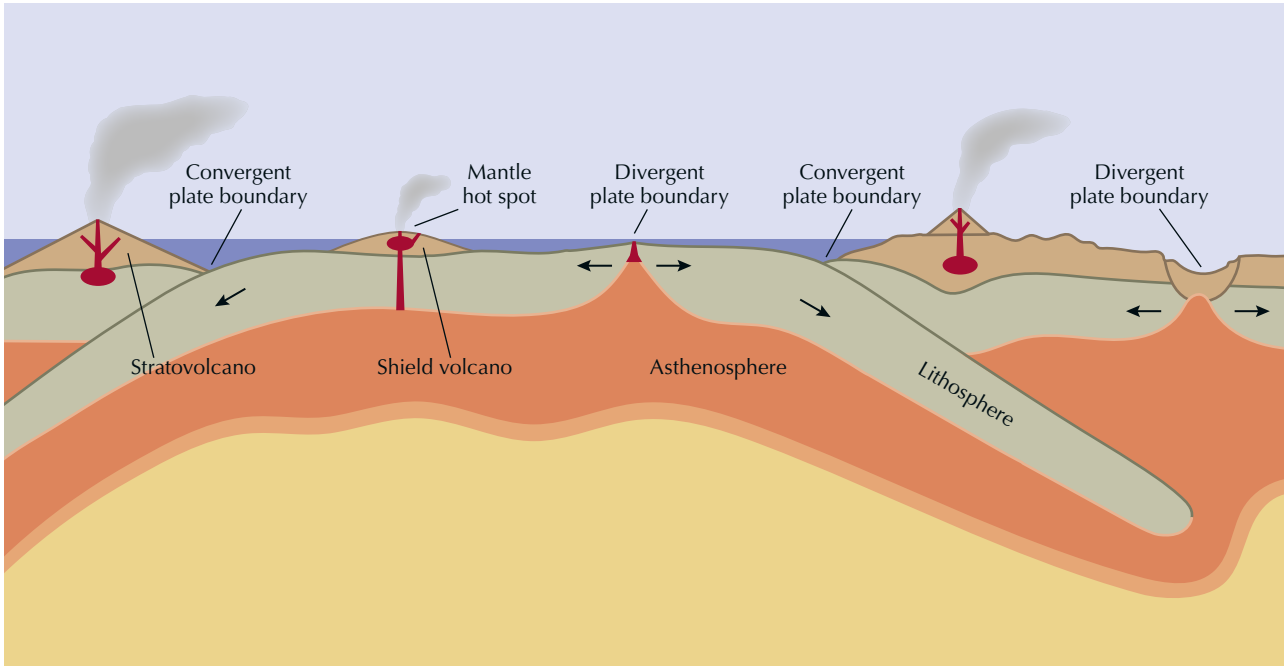

Figure 5. The lithosphere—the solid outer portion of the crust—consists of crustal plates that gradually move laterally over geologic time scales due to convection in the underlying molten asthenosphere. Plates form and then separate along divergent plate boundaries. They come together with one plate colliding or being subducted beneath an adjacent plate along convergent boundaries. Slow movement of crustal plates has resulted in the continents changing position relative to one another in the geologic past. Plate collisions produce uplifted mountain ranges along the collision boundary, as in the Himalayas and the Andes, as well as deep oceanic trenches. Most volcanoes are located along mid-ocean ridges and continental rift zones and along subduction zones. Some also occur within crustal plates, where they form above "hot spots" in the underlying asthenosphere. Plate movement over a hot spot can produce a chain of nearby volcanic islands such as those in Hawaii.

vergent plate boundaries (mid-ocean ridges or continental rift zones where crustal plates separate) or convergent plate boundaries (subduction zones where plates collide). Some volcanoes also occur within crustal plates where they form above "hot spots," anomalously hot areas of the upper mantle. Below Hawaii, for example, successive islands were created as the crustal plate gradually moved over a thermal feature where magmas were generated (figure 5).

Depending on their chemical composition, silica-poor magmas like basalts are very fluid when erupted (and nonexplosive), and they flow down the gentle slopes of volcanoes as molten lava (a shield volcano such as Mauna Kea in Hawaii). Other, more silica-rich magmas like rhyolites are much more viscous and explosive. When erupted, they form higher steep-sided volcanoes that often produce violent ash cloud explosions or pyroclastic debris flows, depositing the particle material along the margins of the volcano or over the surrounding countryside (e.g., a stratovolcano such as Mount Vesuvius in Italy).

Magmas may solidify underground to form various types of intrusive igneous rock bodies. Depending on size and shape, geologists use terms to describe these rock bodies (all of which may be later exposed at the earth's surface by geological processes such as folding, faulting, crustal uplift, and weathering; see again figure 3):

- Dike: a narrow rock body that cuts across other rocks
- Sill: a narrow rock body that runs parallel to sedimentary layers
- Diapir: a domed body of igneous rock that has been forced upward into brittle overlying rocks
- Pluton (or batholith): a large mass of igneous rock
- Laccolith (or lopolith): a body of igneous rock that bulges upward or downward

Magma Crystallization

Minerals in the crust crystallize from magmas over a range of temperatures (~1300° to ~750°C). Most magmas are silica-based compositions and classified according to their silica content, from silica-poor magmas like basalts (~50 wt.% SiO_2) to intermediate magmas like andesites (~60 wt.% SiO_2) to silica-rich magmas like rhyolites (>70 wt.% SiO_2). Silicate magmas are dominated by oxygen and silicon, and they contain lesser amounts of aluminum, calcium, magnesium, iron, sodium, and potassium as well as rarer elements. Non-silica-based magmas such as carbonatites are much less common and can form only under specific geological conditions.

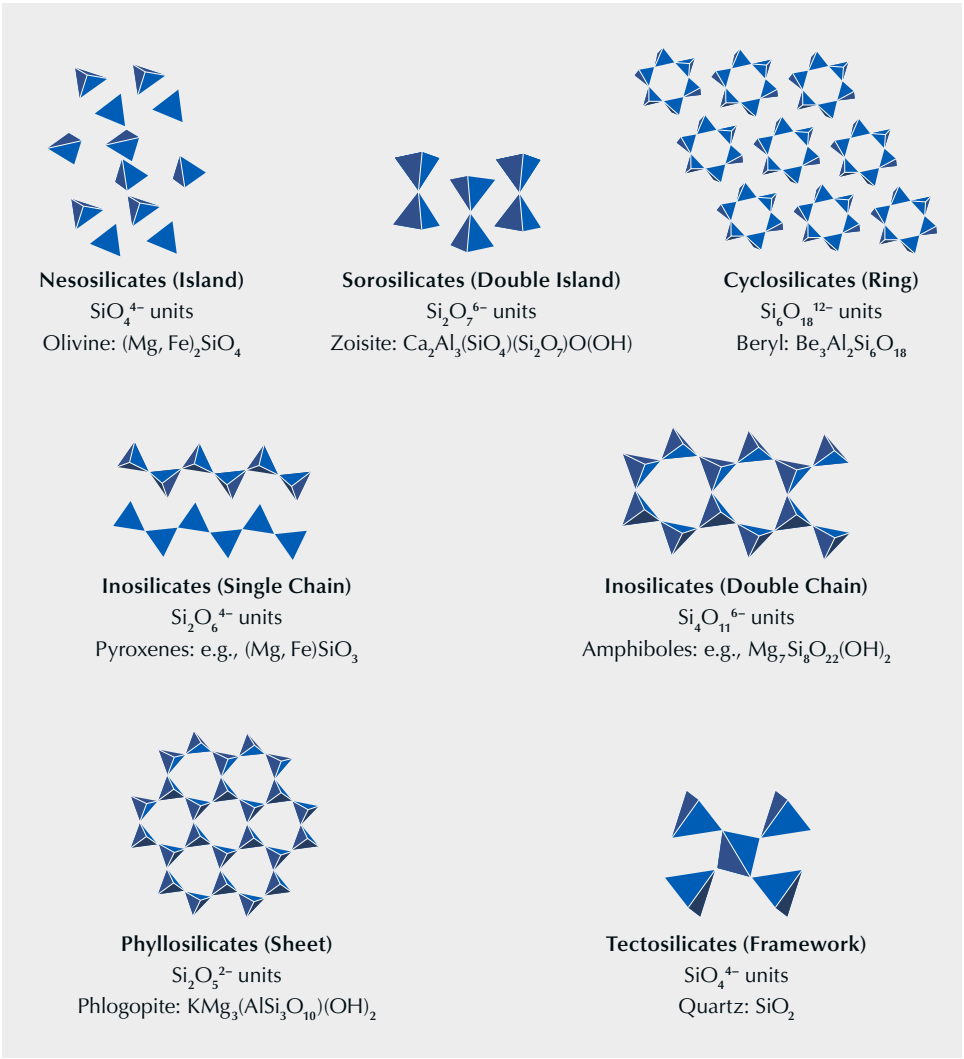

Figure 6. The silica tetrahedron, consisting of four oxygen atoms arranged around a central silicon atom, is the basic structural unit of silicate minerals, which form approximately 90% of the earth's crust. By sharing one or more of the oxygen atoms, these tetrahedra can bond together in various ways (such as pairs, single and double chains, rings, sheets, and frameworks of tetrahedra). Silicate minerals are classified according to the linkage of their silica tetrahedra, or their degree of polymerization, as shown by these illustrations. Illustrations produced using the VESTA software package (Momma and Izumi, 2011).

The silica tetrahedron (SiO_4) is the basic building block of all silicate minerals. It consists of a central silicon atom bonded to four oxygen atoms that form a tetrahedral arrangement. Silica tetrahedra can also bond to one another by sharing one or more of their oxygen atoms to form more complex tetrahedral arrangements (such as pairs, single or double chains, rings, sheets, and frameworks of bonded tetrahedra; see figure 6). These tetrahedra are further connected by atoms of other elements to form the crystal structures of various silicate minerals such as olivine, epidote, pyroxenes, amphiboles, beryl, mica, and feldspars, to name a few.

Several geologic factors influence the evolution of magma composition and crystallization. These include the initial composition of the magma source, the presence of volatiles such as water or elements like fluorine in the magma, partial melting of rocks at the source, interaction with melted or unmelted (restite) minerals, interaction with or assimilation of wall rocks, mixing of magmas, separation of magmas into immiscible melts, loss of volatile phases (degassing), fractional crystallization of minerals, and accumulation of early-formed minerals. As a result of these factors, the overall composition of the magma, and the minerals that crystallize from it, changes over time. Common silicate mineral formation takes place from the magma at progressively cooler temperatures in a specific sequence. This sequence is schematically described by Bowen's reaction series (figure 7). This reaction series illustrates the differences between minerals that typically crystallize from magmas at high temperatures (e.g., olivine, pyroxenes, amphiboles, micas, and calcium-rich feldspar) and those that typically crystallize at lower temperatures (quartz, micas, and potassium-rich feldspar). If early-formed minerals are separated from a magma, the removal of those components changes the composition of the remaining magma, generally leading to more silica-rich compositions (figure 8). Bowen's reaction series can also be considered from the bottom up in that the lower-temperature minerals at the bottom of the diagram are also the first to break down during partial melting. The presence of silica-rich minerals

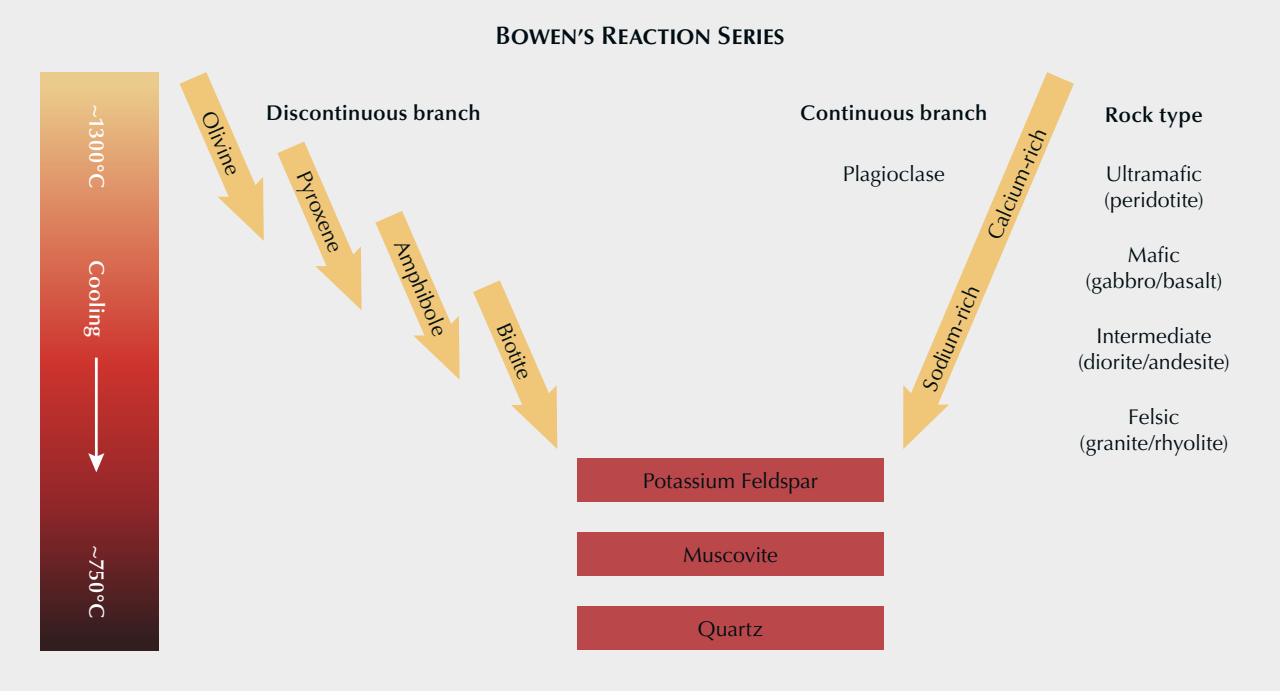

Figure 7. Based on field observations and experimental studies, geologists in the early 1900s began to recognize that the common silicate minerals form at specific temperature ranges from a cooling magma. This sequence of crystallization is known as Bowen's reaction series, named after geologist Norman L. Bowen. Higher and intermediate temperatures are associated with mafic and intermediate magmas, while lower temperatures are associated with felsic (silica-rich) magmas. At higher temperatures, the sequence has two branches. The continuous branch describes the evolution of plagioclase feldspars from calcium-rich to more sodium-rich. The discontinuous branch describes the sequence of formation of different minerals as temperatures decrease. Although geologists now recognize some exceptions, this concept is still accepted as the general model of silicate mineral formation from cooling magmas.

like quartz, micas, and potassium-rich feldspar at the bottom of the diagram demonstrates that the early-formed magmas during partial melting tend to be silica-rich. Removal of such partial melts can produce rhyolitic magmas.

Magmatic rock environments are also important sources for ore deposits—economic and minable concentrations of gold, silver, copper, nickel, platinum, chromium, vanadium, cobalt, and other elements that are not found in large amounts in most silicate minerals.

Hydrothermal and pegmatitic deposits of gems, although related to magmatic activity, will be discussed separately in future editions of this column because of their importance for certain gem deposits.

Gem Mineral Formation from Magmas

Magmatic gems form either by crystallization of the magma at depth or at the earth's surface, and occasionally in rock cavities from a gas phase (a vapor) released during magma cooling. Magma eruptions can also bring up mineral crystals or fragments of deeply formed crystals or rocks (including some gem minerals) derived from other sources—geologists refer to them as *xenocrysts* or *xenoliths*.

When exposed at the surface, igneous rocks often weather and decompose to form smaller particles. Resistant minerals (such as diamond or corundum) can remain in the sedimentary environment and become concentrated in secondary alluvial deposits by the movement of water. Such deposits are sources for several important gem minerals. Over time, long-distance water transport of gem crystals also can winnow out fractured crystals: Those that survive the journey can be waterworn but of higher quality.

Although gem mineral formation from magmas is the subject of this column, some of these same minerals can also form by other geological processes such as metamorphism.

Diamond. Most gem diamonds formed between 1.0 and 3.5 billion years ago and at depths between 150 and 250 km in the lower crust and upper mantle (and in some cases in the lower mantle as deep as 800 km; see Smith et al., 2017). It is now understood that their formation took place from carbon-containing fluids, based on studies of tiny inclusions of minerals and fluids found within diamonds, although the details of this growth process are still the subject of geological study. Once formed, the diamonds were carried to the earth's surface by eruptions of kimber-

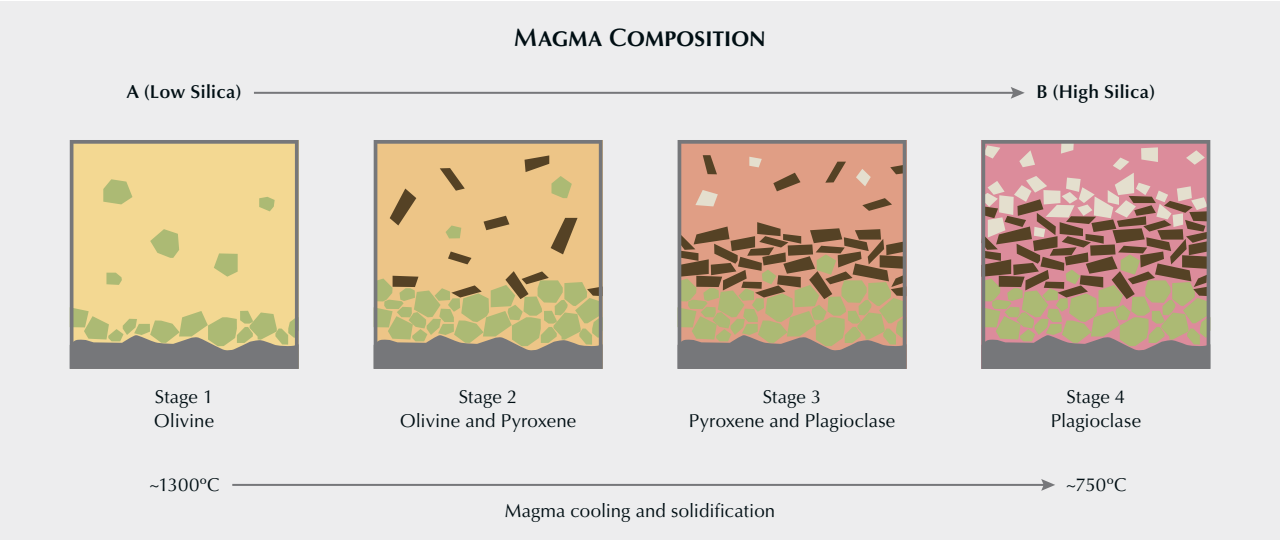

Figure 8. With the cooling and solidification of magmas, mineral formation proceeds in a series of steps illustrated by the discontinuous branch of Bowen's reaction series in figure 7. These simplified diagrams illustrate stages of fractional crystallization of common minerals from a silicate magma. If the starting magma is ultramafic or basaltic in composition (A), during cooling it changes in chemical composition as different minerals form in sequence from the melt. In these diagrams, olivine crystallizes first (stage 1), followed by olivine and pyroxene (stage 2), pyroxene and plagioclase feldspar (stage 3), and finally plagioclase feldspar (stage 4). These crystals are separated from the melt as layers at the bottom of the magma chamber, and the remaining magma (B) gradually becomes more silica-rich (more viscous). The remaining magma becomes depleted in elements that were incorporated in the earlier-formed minerals, and it is enriched in elements that were not easily accommodated in these minerals. Modified from Johnson et al. (2017).

litic or lamproitic magmas (figure 9). Deeply formed diamonds were slowly transported upward by convection in the mantle to a depth where they could be caught up in erupting igneous magmas. Diamond formation was de-

Figure 9. Diamond crystals (1.24–22.32 ct) and samples of diamond-bearing kimberlite. Photo by Orasa Weldon. The loose crystals were donated to GIA by De Beers as part of the Sir Ernest Oppenheimer Student Collection.

Figure 10. Green grains of peridot filling gas cavities in basalt from the San Carlos Apache Indian Reservation in Arizona. Photo by Robert Weldon.

scribed in more detail by Shirey and Shigley (2013) and by Smit and Shirey (2018, 2019). At the surface, diamonds are recovered by mining of primary kimberlite ore and from secondary alluvial deposits. Harris and Staebler (2017) and Smit et al. (2022) provided recent reviews of diamond geology, genesis, and occurrence.

Olivine (Peridot). Olivine is a magnesium-iron silicate mineral with the formula $(Mg,Fe)_2SiO_4$ and a crystal structure consisting of isolated silicate tetrahedra joined by metal cations. It is one of the first minerals to crystallize from silicate magmas, and it occurs in mafic (low SiO_2, high MgO and FeO) and ultramafic (very low SiO_2 at <45 wt.% and high MgO and FeO) igneous rocks that are low in silica such as gabbro and basalt. Magnesium-rich olivines (forsterite) are more common than iron-rich olivines (fayalites) and constitute most gem peridot. Olivines are primary components of the earth's upper mantle (see again figure 8). Much of the peridot on the gem market comes from alkali basalt eruptions that originated in the mantle and carried up large chunks of mantle rocks (including olivine and pyroxene crystals) as xenoliths (Koivula, 1981). These constitute the major deposits in the U.S. state of Arizona (figure 10) and Jilin, China.

Other peridot deposits form as a result of hydrothermal fluid circulation through very magnesium- and iron-rich mantle rocks called *peridotites*, which were brought up to the earth's surface during continental collisional events. These are represented by the deposits in Myanmar, Pakistan, and the classical historical source of gem peridot on Zabargad (Saint John's) Island in the Red Sea of Egypt (figure 11). However the olivine reaches the surface, it quickly weathers and decomposes to form clays.

Rare iron-nickel meteorites that contain crystals of olivine are known as *pallasites* (Sinkankas et al., 1992; Shen et al., 2011). Several recent publications have discussed olivine formation in magmatic igneous rocks as well as gem peridot (Revheim, 2015; Wilson, 2020; Wallace et al., 2021; Seneewong-Na-Ayutthaya et al., 2021).

Quartz. Quartz (SiO_2) and its color varieties (mainly amethyst, citrine, rose quartz, and smoky quartz) have been gem materials since ancient times as crystals, crystal fragments, and cryptocrystalline aggregates (such as chalcedony and agate). It is a principal constituent of granites and other silica-rich igneous rocks where it has crystallized from molten magmas. Amethyst-filled cavities and geodes in basaltic lava flows are an important source of gem crystals. Quartz is resistant to weathering and is commonly found as fragments, sometimes waterworn, in alluvial sediments and soils.

Figure 11. A 69.30 g (346.5 ct) peridot crystal from Zabargad (Saint John's) Island in the Red Sea. Photo by Robert Weldon.

Figure 12. Labradorite feldspar crystals in pieces of weathered basalt from the Ponderosa mine in Harney County, Oregon. Photo by Adriana Gudino.

Feldspar. Feldspars are an important group of potassium-sodium (alkali feldspars: $[K,Na]AlSi_3O_8$) or sodium-calcium minerals (plagioclase feldspars: $NaAlSi_3O_8$–$CaAl_2Si_2O_8$) whose structures are based on a three-dimensional network of silica or alumina tetrahedra. They exhibit extensive chemical solid solutions within the group. Feldspars crystallize from a variety of magma compositions, beginning with more calcium-rich phases to more sodium-rich phases with decreasing magma temperatures (figure 8). Potassium-rich feldspars are among the last minerals to form from a magma. Feldspars are important constituents of both intrusive (granites or diorites) and extrusive (rhyolites or andesites) igneous rocks. As a group, they compose about 60% of the earth's crust. Feldspars weather to form clay minerals and are not usually found in alluvial deposits, as they are not resistant enough. They are commonly opaque but sometimes occur as transparent crystals suitable for faceting (orthoclase, microcline, and oligoclase; see figure 12) or as crystals that exhibit optical phenomena such as aventurescence (sunstone, or rainbow lattice sunstone; Johnston et al., 1991; Pay et al., 2013; Jin et al., 2022), adularescence (moonstone), or iridescence/labradorescence (labradorite) that are cut as faceted stones or cabochons.

Figure 13. Pyrope garnet grains concentrated from an exposed and weathered portion of the Vargem 1 kimberlite seen on the banks of the Santo Inácio River near Coromandel in Minas Gerais, Brazil. These bright red grains are an important indicator mineral in exploring alluvial sediments for diamond-bearing kimberlites. Photo by Robert Weldon.

Garnet. Garnets are an important group of approximately 20 minerals represented by several valuable gemstones such as demantoid, hessonite, rhodolite, and tsavorite. They exhibit a wide variation in chemical composition—the common species are often referred to as "pyralspite" garnets $[(Mg,Fe,Mn)_3Al_2(SiO_4)_3]$ and "ugrandite" garnets $[Ca_3(Cr,Al,Fe)_2(SiO_4)_3]$. Some garnets can display a color change under different lighting conditions, while others exhibit optical phenomena such as asterism because of symmetrically oriented acicular inclusions. Some garnet species are common minerals, while others occur less frequently. Like olivine, the crystal structure of garnet consists of isolated silica tetrahedra linked by a variety of metal cations in several structural sites. They occur widely in metamor-

Figure 14. An almandine garnet in rhyolite from Garnet Hill in White Pine County, Nevada. Photo by Robert Weldon.

Figure 15. A rough multicolored sapphire crystal weighing more than 30 ct from the Changle region of China. Photo by Robert Weldon.

phic rocks, and to a lesser extent as an accessory phase in igneous rocks such as granites, granitic pegmatites, gabbros, and basalts. Pyrope is an important indicator mineral used in the search for diamond-bearing kimberlites (figure 13). The mineral also forms in the crust or upper mantle and is brought up to the surface by ascending magmas or by geologic uplift of deep rocks. While most gem-quality garnet on the market would be considered metamorphic or hydrothermal in origin, on occasion they are found in cavities of erupted igneous rocks like rhyolites, where they were formed by gases released by the cooling magmas (figure 14). Garnets are resistant to abrasion and chemical weathering, so they can remain in sediments and become concentrated in alluvial deposits. A review of garnets and their geological occurrences was provided by Gilg et al. (2008).

Spinel. The magnesium-aluminum oxide spinel ($MgAl_2O_4$) is one species in a group of minerals referred to by the same name that have a similar crystal structure but varied chemical composition. Depending on the minor elements present, it occurs in a variety of colors, with the red variety long being recognized as a gemstone that in earlier times was often referred to as "carbuncle" or "Balas ruby" ("Badakhshan ruby" from Tajikistan) in confusion with ruby. Spinel is a common mineral in metamorphic rocks, but it can also form as an accessory mineral in mafic igneous rocks that are poor in silica and alkali elements. The conditions of formation of a silica-free oxide mineral such as spinel from a silica-containing mafic igneous magma are still a matter of debate among geologists. Spinel is an important constituent of peridotite in the upper mantle and in kimberlites. Because of its hardness, lack of cleavage, high specific gravity, and resistance to weathering, spinel is found concentrated in secondary alluvial sediment deposits.

Corundum. Ruby and the many colors of sapphire of the mineral corundum (Al_2O_3) are among the most important and valuable gemstones because of their occurrence as colored transparent crystals suitable for faceting or polishing. Corundum is colorless when pure, but the potential presence of minor elements (namely chromium, titanium, and iron) can act as coloring agents (Dubinsky et al., 2020). The structure consists of a hexagonal close-packed arrangement of oxygen atoms with aluminum and/or other elements occurring in structural sites. The gem material may display asterism and color-change behaviors. Corundum is found

Figure 16. A topaz crystal on rhyolite matrix from the Thomas Range, Juab County, Utah. Photo by Robert Weldon.

in metamorphic rocks as well as low-silica syenites, pegmatites, and other less common igneous rocks (Simonet et al., 2008; Palke et al., 2019a,b). The mineral also occurs as xenocrysts in igneous alkali basalts; however, rapid weathering of basalt at the earth's surface means that most ruby and sapphire of igneous origin are encountered as loose crystals or fragments in alluvial sediments (figure 15). As with spinel, the conditions of formation of a silica-free oxide mineral such as corundum from a silica-containing mafic igneous magma remain a matter of debate among geologists (Giuliani and Groat, 2019). Nonetheless, sapphire and ruby from the alkali basalt–related deposits have glassy silicate melt inclusions that represent some primordial magma from when the gem corundum was growing. This indicates that although the sapphire and ruby were xenocrysts in the alkali basalts that carried them to the surface, they must have a magmatic origin from deep within the earth. Because of its toughness, hardness, and resistance to weathering, and because the igneous host rocks decompose at the earth's surface, corundum is often found as a detrital mineral in sediments and secondary alluvial deposits.

Zircon. Zirconium is an uncommon element in the earth's crust, so zircon ($ZrSiO_4$) only occurs as small accessory crystals or grains in a wide variety of rocks. Larger transparent crystals are less common, so gem zircon suitable for faceting is rare. The structure is composed of isolated silica tetrahedra bonded together by zirconium atoms. The mineral is normally reddish to yellowish brown, but other colors such as blue and green also occur as a result of trace elements in the crystal structure, radiation exposure, or natural or artificial heating. The mineral's hardness and chemical resistance to weathering mean that it is frequently preserved in sediments and sedimentary rocks. Most of the gem-quality zircon on the market is related to alkali basalt deposits where the zircon are found as xenocrysts. This is similar to the deposits of magmatic gem corundum, and both are often found in the same deposit.

Because they often contain small amounts of radioactive uranium or thorium, zircon crystals provide an important way to date the geologic age of their host minerals or sediments, including some of the oldest minerals dated so far (4.4 billion years for zircon from one locality in Australia). The presence of radioactive minerals causes damage to the crystal structure, so these zircon are described as metamict with an opaque appearance and lower hardness, refractive index, and specific gravity.

Topaz. Topaz, with the formula $Al_2SiO_4(F,OH)_2$, is an aluminosilicate mineral that contains fluorine and/or hydroxyl (OH) ions. The requirement for fluorine limits the range of geological environments for topaz formation. This mineral occurs in open veins or voids forming at low to moderate temperatures in later-stage, silica-rich igneous rocks such as granites, pegmatites, and rhyolites in which a fluorine fluid or vapor appears to have been present (such as the historical topaz occurrence at Schneckenstein, Germany; Zeug et al., 2022). Certain rare granites are so enriched in fluorine that topaz is an essential mineral constituent of the rock. Topaz crystals that grow from late-stage magmatic vapors are also found in cavities in rhyolites (figure 16). Although

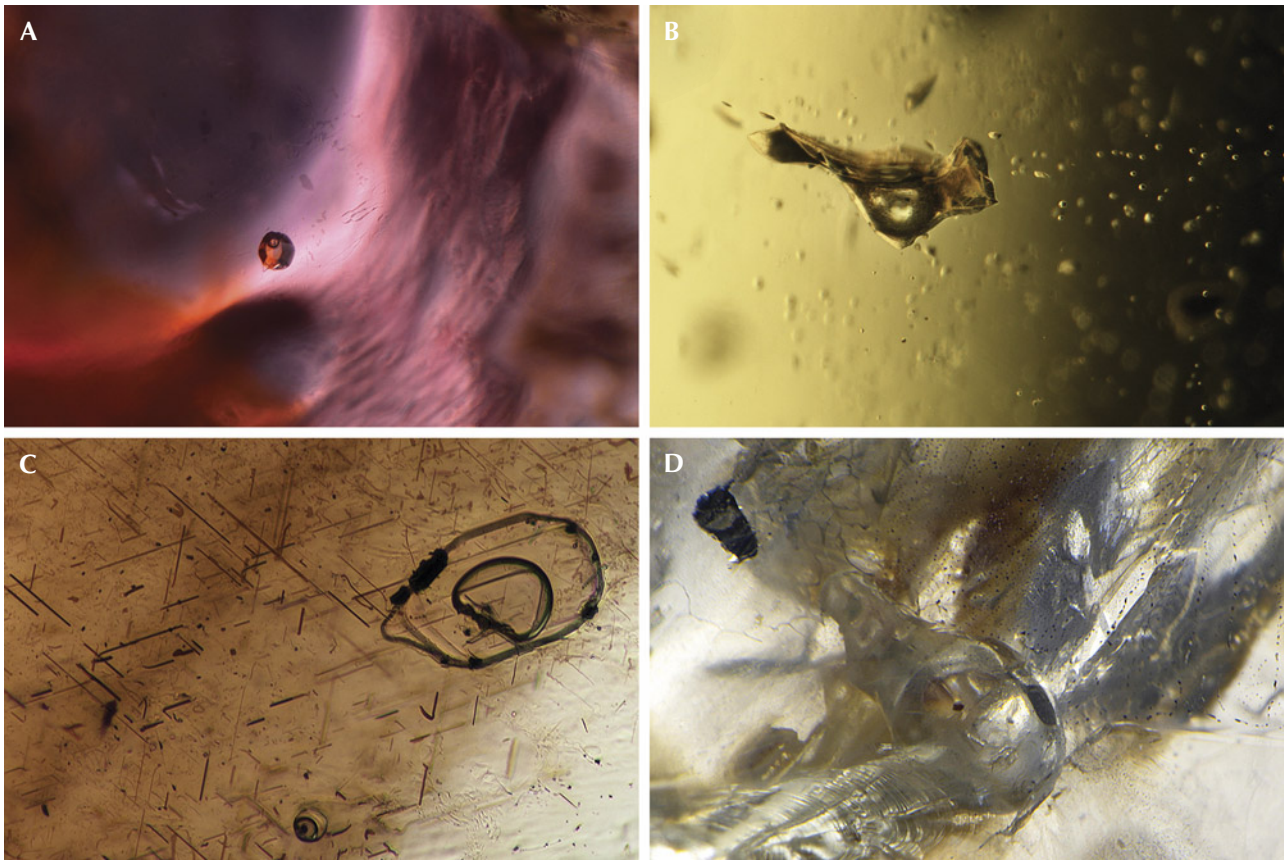

Figure 17. Inclusions observed in magmatic gems that offer evidence of their igneous origin. A: A rounded glassy melt inclusion in a Cambodian ruby; field of view 1.26 mm. B: A glassy melt inclusion with gas bubbles in a peridot from Papakōlea Beach on the island of Hawaii; field of view 1.30 mm. C: A glassy melt inclusion containing a gas bubble along with oriented inclusion needles in a sapphire from Queensland, Australia; field of view 0.71 mm. D: A gas bubble inclusion in a labradorite feldspar from Oregon; field of view 3.59 mm. During the eruption of the host basaltic magma, the release of confining pressure on the feldspar xenocryst allowed the gas bubble to expand to fill a larger volume of space along a fracture. Photomicrographs by Aaron Palke (A and C) and Nathan Renfro (B and D).

it is not as hard as other gem minerals and has a tendency to cleave perpendicular to the long axis of the crystal, topaz is resistant enough to be preserved as waterworn crystals or fragments in alluvial sediments. Often colorless, the mineral can also be blue, yellow, brown, or reddish orange. The crystals are usually transparent and sometimes large. Staebler et al. (2011) reviewed the geological occurrence of this gem mineral.

Inclusions in Magmatic Gems

Gems that crystallize from cooling magmas can exhibit micro-features visible with a gemological microscope. In addition to solid inclusions (such as oriented needles in a magmatic ruby or sapphire), probably the most distinctive micro-feature is a rounded or irregular melt inclusion, which represents a solidified bubble of the silicate magmatic melt present when the host gemstone was crystallizing. Upon cooling, the melt was quenched to a glass, which may contain a gas bubble and perhaps tiny crystals that formed from the glass. Figure 17 presents a compilation of melt inclusions that offer proof of a magmatic geological origin.

Conclusions

From partial melting deep within the earth to post-emplacement processes in volcanic eruptions, many of the world's finest gemstones were derived from magmatic activity. The study of these gemstones can provide geological insights into the generation of magmas within the earth, their transport to the earth's surface, and modes of volcanic processes after eruption. Magmatic gemstones offer many clues to the earth's evolution and the geological processes that shaped our world. The next installment of Colored Stones Unearthed will focus on gemstones formed through metamorphic processes.

REFERENCES

Dubinsky E.V., Stone-Sundberg J., Emmett J.L. (2020) A quantitative description of the causes of color in corundum. *G&G*, Vol. 56, No. 1, pp. 2–28, http://dx.doi.org/10.5741/GEMS.56.1.2

Gilg H.A., Kile D., Liebetrau S., Modreski P., Neumeier G., Staebler G., Eds. (2008) *Garnet – Great Balls of Fire!* Mineral Monograph No. 11, 104 pp., Lithographie Ltd., Arvada, Colorado.

Giuliani G., Groat L.A. (2019) Geology of corundum and emerald gem deposits: A review. *G&G*, Vol. 55, No. 4, pp. 464–48, http://dx.doi.org/10.5741/GEMS.55.4.464

Harris J.W., Staebler G.A., Eds. (2017) *Diamond – The Ultimate Gemstone*. Mineral Monograph No. 19, 152 pp., Lithographie Ltd., Arvada, Colorado.

Jin S.Y., Sun Z.Y., Palke A.C. (2022) Iron oxide inclusions and exsolution textures of rainbow lattice sunstone. *European Journal of Mineralogy*, Vol. 34, No. 2, pp. 183–200, http://dx.doi.org/10.5194/ejm-34-183-2022

Johnson C., Affolter M.D., Inkenbrandt P., Mosher C. (2017) Igneous processes and volcanoes. In *An Introduction to Geology*. Salt Lake Community College Press, Salt Lake City, Utah, https://slcc.pressbooks.pub/introgeology/

Johnston C.L., Gunter M.E., Knowles C.R. (1991) Sunstone labradorite from the Ponderosa mine, Oregon. *G&G*, Vol. 27, No. 4, pp. 220–233, http://dx.doi.org/10.5741/GEMS.27.4.220

Koivula J.I. (1981) San Carlos peridot. *G&G*, Vol. 17, No. 4, pp. 205–214, http://dx.doi.org/10.5741/GEMS.17.4.205

Momma K., Izumi F. (2011) *VESTA 3* for three-dimensional visualization of crystal, volumetric and morphology data. *Journal of Applied Crystallography*, Vol. 44, No. 6, pp. 1272–1276, http://dx.doi.org/10.1107/S0021889811038970

Palke A.C., Saeseaw S., Renfro N.D., Sun Z.Y., McClure S.F. (2019a) Geographic origin determination of blue sapphire. *G&G*, Vol. 55, No. 4, pp. 536–579, http://dx.doi.org/10.5741/GEMS.55.4.536

——— (2019b) Geographic origin determination of ruby. *G&G*, Vol. 55, No. 4, pp. 580–612, http://dx.doi.org/10.5741/GEMS.55.4.580

Pay D., Weldon R., McClure S., Schumacher K. (2013) Three occurrences of Oregon sunstone. *G&G*, Vol. 49, No. 3, pp. 162–171, http://dx.doi.org/10.5741/GEMS.49.3.162

Revheim O. (2015) Peridot from St. John's/Zabargad Island. https://www.mindat.org/article.php/2053/Peridot+from+St.+John%27s+_+Zabargad+Island

Seneewong-Na-Ayutthaya M., Chongraktrakul W., Sripoonjan T. (2021) Gemological characterization of peridot from Pyaung-Gaung in Mogok, Myanmar. *G&G*, Vol. 57, No. 4, pp. 318–337, http://dx.doi.org/10.5741/GEMS.57.4.318

Shen A.H., Koivula J.I., Shigley J.E. (2011) Identification of extraterrestrial peridot by trace elements. *G&G*, Vol. 47, No. 3, pp. 208–213, http://dx.doi.org/10.5741/GEMS.47.3.208

Shirey S.B., Shigley J.E. (2013) Recent advances in understanding the geology of diamonds. *G&G*, Vol. 49, No. 4, pp. 188–222, http://dx.doi.org/10.5741/GEMS.49.4.188

Simonet C., Fritsch E., Lasnier B. (2008) A classification of gem corundum deposits aimed towards gem exploration. *Ore Geology Reviews*, Vol. 34, No. 1-2, pp. 127–133, http://dx.doi.org/10.1016/j.oregeorev.2007.09.002

Sinkankas J., Koivula J.I., Becker G. (1992) Peridot as an interplanetary gemstone. *G&G*, Vol. 28, No. 1, pp. 43–51, http://dx.doi.org/10.5741/GEMS.28.1.43

Smit K.V., Shirey S.B. (2018) Diamonds from the Deep: How do diamonds form in the deep earth? *G&G*, Vol. 54, No. 4, pp. 440–445.

——— (2019) Diamonds from the Deep: Kimberlites: Earth's diamond delivery system. *G&G*, Vol. 55, No. 2, pp. 270–276.

Smit K., Shirey S., Pearson G., Stachel T., Nestola F., Moses T., Eds. (2022) *Diamond: Genesis, Mineralogy and Geochemistry*. Reviews in Mineralogy and Geochemistry, Vol. 88, 875 pp., Mineralogical Society of America, Chantilly, Virginia, and Geochemical Society, Washington DC.

Smith E.M., Shirey S.B., Wang W. (2017) The very deep origin of the world's biggest diamonds. *G&G*, Vol. 53, No. 4, pp. 388–403, http://dx.doi.org/10.5741/GEMS.53.4.388

Staebler G., Hansen S., Liebetrau S., Clifford J., Eds. (2011) *Topaz – Perfect Cleavage*. Mineral Monograph No. 14, 104 pp., Lithographie Ltd., Arvada, Colorado.

Wallace P.J., Plank T., Bodnar R.J., Gaetani G.A., Shea T. (2021) Olivine-hosted melt inclusions: A microscopic perspective on a complex magmatic world. *Annual Review of Earth and Planetary Sciences*, Vol. 49, pp. 465–494, http://dx.doi.org/10.1146/annurev-earth-082420-060506

Wilson W.E. (2020) Sapat Gali, Manshera District, Khyber Pakhtunkhwa Province, Pakistan. *Mineralogical Record*, Vol. 51, No. 6, pp. 785–801.

Zeug M., Nasdala L., Chanmuang-N C., Hauzenberger, C. (2022) Gem topaz from the Schneckenstein Crag, Saxony, Germany: Mineralogical characterization and luminescence. *G&G*, Vol. 58, No. 1, pp. 2–17, http://dx.doi.org/10.5741/GEMS.58.1.2

GIA®

The Report You Trust, Now Fully Digital

More secure and convenient than ever before, the **GIA Diamond Dossier**® is accessible anytime, anywhere with the touch of a finger.

GIA.edu/digital-dossier

GEM NEWS INTERNATIONAL

Contributing Editors
Gagan Choudhary, *IIGJ-Research & Laboratories Centre, Jaipur, India* (gagan.choudhary@iigjrlc.org)
Christopher M. Breeding, *GIA, Carlsbad* (christopher.breeding@gia.edu)
Guanghai Shi, *School of Gemmology, China University of Geosciences, Beijing* (shigh@cugb.edu.cn)

Figure 1. The 9.63 ct pink grossular garnet reportedly from Mogok (A) fluoresced very strong red under long-wave UV (B) and weak chalky red under short-wave UV radiation (C). Photos by Qian Zhang.

COLORED STONES AND ORGANIC MATERIALS

Grossular with strong red fluorescence. The authors recently encountered a pink garnet rough reportedly from Mogok, Myanmar. The garnet was characterized by a light pink color in daylight, and it showed unusual strong red fluorescence under long-wave ultraviolet radiation and a weak chalky red reaction under short-wave UV (figure 1). A previously published report on grossular garnet showed similar fluorescence under long-wave UV, but the short-wave UV reaction was very different (M.S. Krzemnicki, "Pink grossular garnet from Mogok," *Facette*, No. 26, 2020, pp. 26).

Raman spectroscopy identified the garnet as grossular. Electron probe microanalysis determined that the composition was consistent with that of nearly pure grossular with major elements of calcium, aluminum, and silicon ($Ca_{3.114}Al_{2.003}Si_{2.883}O_{11.885}$), and laser ablation–inductively coupled plasma–mass spectrometry (LA-ICP-MS) testing revealed trace elements of titanium, vanadium, manganese, and others (table 1). The pink coloration was due to two weak bands between 470 and 600 nm in the UV/visible absorption spectrum; Geiger et al. (1999) suggested they are related to Mn^{3+} (C.A. Geiger et al., "Raspberry-red grossular from Sierra de Cruces Range, Coahuila, Mexico," *European Journal of Mineralogy*, Vol. 11, No. 6, 1999, pp. 1109–1113).

A photoluminescence spectrum recorded with 325 nm laser excitation displayed a strong narrow band at 604 nm accompanied by some weaker bands at 583, 595, 617, 631, 645, and 660 nm (figure 2). Gaft et al. (2013, 2022) pub-

Editors' note: Interested contributors should send information and illustrations to Stuart Overlin at soverlin@gia.edu.

Gems & Gemology, Vol. 58, No. 4, pp. 508–526.

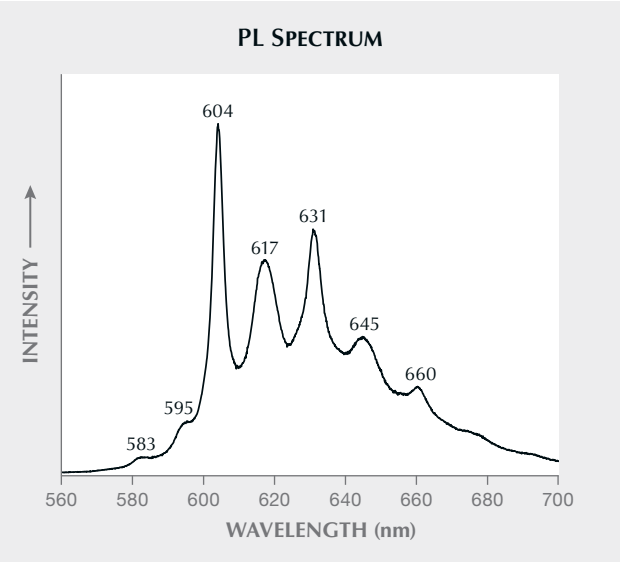

Figure 2. The photoluminescence spectrum collected on the grossular using 325 nm excitation at 300 K.

lished two papers about the luminescence of grossular (M. Gaft et al., "Laser-induced time resolved luminescence of natural grossular $Ca_3Al_2(SiO_4)_3$," *Journal of Luminescence*, Vol. 137, 2013, pp. 43–53; M. Gaft et al., "Zero-phonon Mn^{2+} luminescence in natural grossular $Ca_3Al_2(SiO_4)_3$," *Journal of Luminescence*, Vol. 248, 2022, article no. 119001). Our result is consistent with their 2022 result. They proposed that such luminescence emission may be related to the presence of Mn^{2+}.

In order to describe the pink grossular fluorescence features in detail, 3D fluorescence spectral data (i.e., excitation-emission mapping or EEM) was collected at room temperature using a Jasco FP-8500 fluorescence spectrometer (figure 3). The excitation wavelengths varied from 350 to 630 nm, with a step size of 1 nm and an excitation bandwidth of 5 nm. The emission spectra were collected from 400 to 680 nm, with the bandwidth set to 2.5 nm and a data interval of 0.1 nm, showing five obvious emission wavelengths at 604, 617, 631, 645, and 660 nm and their corresponding optimal excitation wavelength at 388 nm.

To our knowledge, this is the first time a detailed fluorescence analysis of pink grossular has been documented.

Qian Zhang and Andy H. Shen
Gemmological Institute,
China University of Geosciences, Wuhan

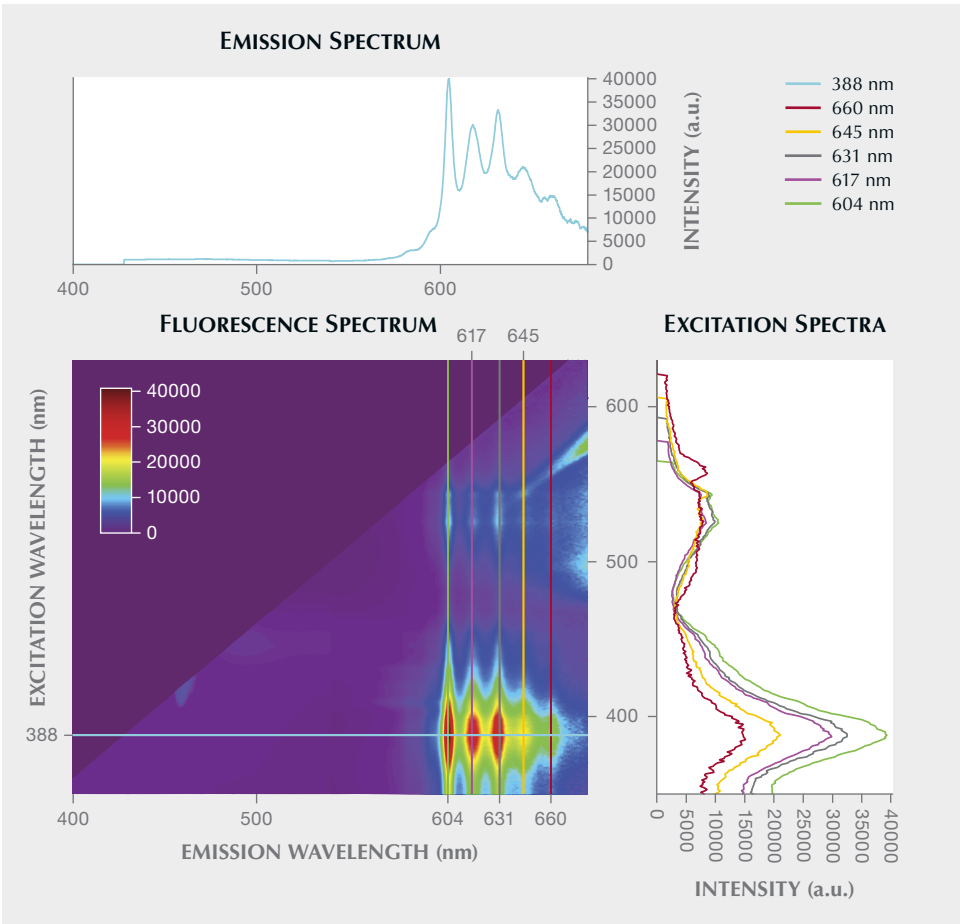

Figure 3. The 3D contour map of the pink grossular's fluorescence spectrum. The stacked excitation spectra are not scaled or shifted for clarity.

TABLE 1. LA-ICP-MS trace element chemistry (in ppmw) of the pink grossular.

	Ti	V	Cr	Mn	Fe	Nb	Sn	Nd
Spot 1	272	10.8	8.50	66.4	30.9	85.2	16.7	0.21
Spot 2	226	12.4	8.09	61.8	48.9	96.1	10.5	0.71
Spot 3	219	12.8	bdl[a]	59.4	bdl	97.1	10.3	0.39
Spot 4	265	9.05	bdl	66.0	35.3	83.4	16.5	0.19
Spot 5	280	9.06	6.31	67.5	bdl	75.9	21.2	0.34
Detection limits	1.58	0.15	4.21	1.68	23.70	0.07	1.31	0.16

[a]*bdl: below detection limit*

Extremely rare hellandite inclusion found in a Mogok ruby. Recently, Guild Gem Laboratories (Shenzhen) received a 0.45 ct ruby (figure 4) for origin determination. Standard gemological testing, including a refractive index of 1.762–1.770 and specific gravity of approximately 4.00, and Fourier-transform infrared spectroscopy confirmed its identity as corundum. Additionally, energy-dispersive X-ray fluorescence revealed extremely low iron (247 ppmw) and relatively high chromium (3819 ppmw) and vanadium (448 ppmw) concentrations, consistent with those in marble-hosted samples.

Microscopic observation showed a typical inclusion scene for Burmese ruby from Mogok, including nested concentrations of fine, long to short rutile needles (figure 5) and irregular calcite crystals (figure 6). To our surprise, two transparent brownish crystals (figure 7) were observed. Their slightly corroded state indicated these crystal inclusions' protogenetic origin. Micro-Raman spectroscopy using 473 nm laser excitation produced some interesting results. Raman analysis showed several distinct peaks at 207, 238, 298, 317, 349, 423, 475, 574, 793, 868, 987, and 1018 cm^{-1}, consistent with those of hellandite according to the RRUFF database (figure 8; see B. Lafuente et al., 2015, https://rruff.info/about/downloads/HMC1-30.pdf). These hellandite inclusions are rarely observed in ruby from any origin.

Hellandite, a rare borosilicate mineral with the proposed ideal formula of $(Ca, REE)_4(Y, Ce)_2Al_2(B_4Si_4O_{22})(OH)_2$, comes in various colors, including colorless, brown, brownish red, gray, green, and yellow. First found in granitic pegmatite in Norway, hellandite belongs to the

Figure 4. This 0.45 ct oval-shaped ruby, measuring 4.25 × 3.65 × 3.24 mm, exhibited a highly saturated red color. Photo by Huixin Zhao.

Figure 5. Dense, nested concentrations of silk in the ruby suggest an origin of Mogok, Myanmar. Photomicrograph by Huixin Zhao; field of view 1.13 mm.

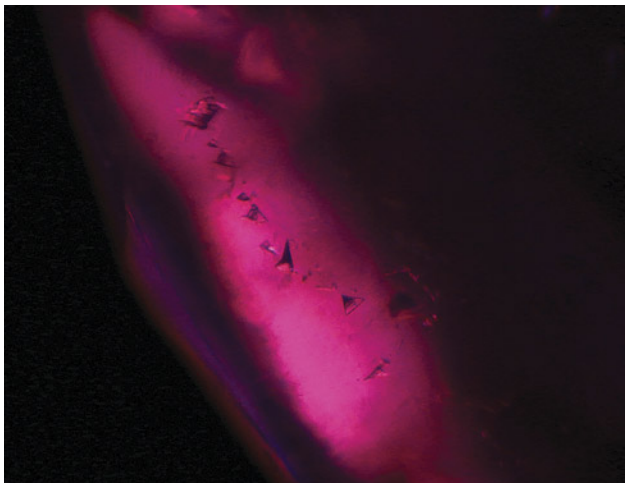

Figure 6. A series of irregular calcite crystals in the ruby from Mogok. Photomicrograph by Huixin Zhao; field of view 1.84 mm.

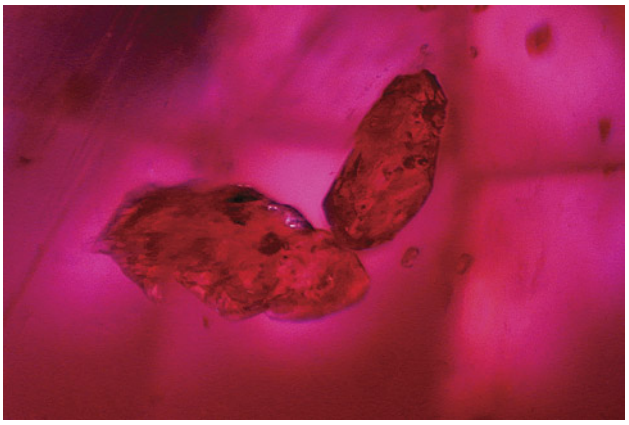

Figure 7. These two transparent brownish hellandite crystals found in a Mogok ruby possibly represent a new ruby inclusion. Photomicrograph by Huixin Zhao; field of view 1.70 mm.

monoclinic crystal system. Its crystal structure was determined on a specimen from Predazzo, Italy, and described as $B_4Si_4O_{22}$ chains parallel to the *c*-axis (M. Mellini and S. Mellini, "Hellandite: A new type of silicoborate chain," *American Mineralogist*, Vol. 62, No. 1-2, 1977, pp. 89–99).

Myanmar's ruby deposits occur in marbles intercalated with gneisses that are sometimes intruded by granitoids (G. Giuliani and L.A. Groat, "Geology of corundum and emerald gem deposits: A review," Winter 2019 *G&G*, pp. 464–489). Therefore, we speculate that hellandite crystals

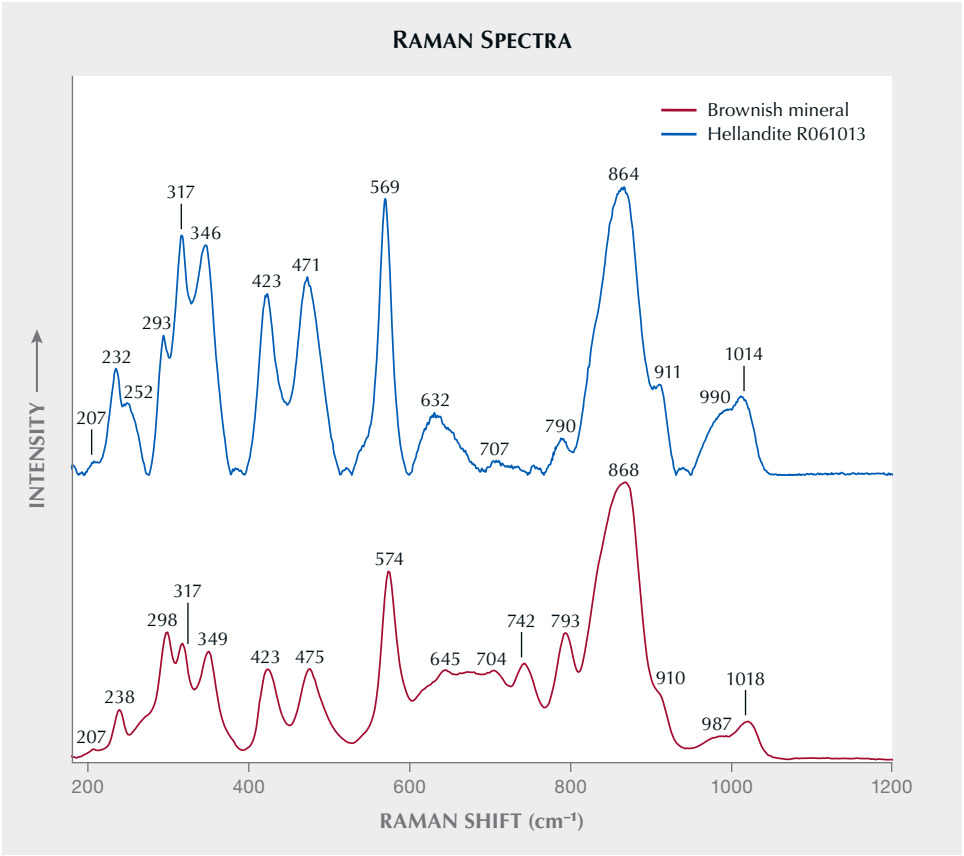

Figure 8. Raman analysis identified the two transparent brownish crystals shown in figure 7 as hellandite. Spectra are offset for clarity.

Figure 9. This bangle, weighing 40.10 g, was identified as quartzite. Photo by Su Xu.

in the granitoids intruding gneiss were captured by ruby when the ruby formed.

To our knowledge, this is the first time hellandite has been observed in ruby. This finding allows for a better understanding of included minerals in the ruby from the geological setting of the Mogok mine.

Xueying Sun, Yujie Gao (peter.gao@guildgemlab.com), and Qi Han
Guild Gem Laboratories, Shenzhen

Quartzite bangle with fuchsite inclusions. Jadeite jade bangles are always popular in the Chinese market. With high prices and rising demand for these products, a bangle with an appearance similar to jadeite was encountered recently.

The bangle was submitted to the National Gold-Silver Gem & Jewelry Quality Inspection Center (Sichuan) for identification. It was semitransparent with a white and green bodycolor resembling that of jadeite (figure 9). However, standard gemological testing showed a refractive index of 1.54 and a specific gravity of 2.67, values that were both significantly below those of jadeite and more in line with quartz. It showed no reaction under Chelsea filter. Using a polariscope, the material was found to be composed of polycrystalline aggregates. Microscopic examination revealed a granular aggregate structure and different microcrystalline mineral inclusions.

The identity was further confirmed by analytical testing. Fourier-transform infrared (FTIR) reflectance spectroscopy showed peaks at 489, 537, 691, 778, 798, 1105, and 1178 cm^{-1} that were consistent with the characteristic spectrum of quartzite (sometimes referred to as "quartzose") (figure 10) (X. Jin et al., "Gemmological and vibrational spectrum characteristics of micaceous quartzose jade 'strawberry crystal'," *Journal of Gems & Gemmology*, Vol. 23, No. 3, 2021, pp. 20–28). Energy-dispersive X-ray fluorescence (EDXRF) analysis revealed trace amounts of iron throughout and chromium exclusive to the green inclusions.

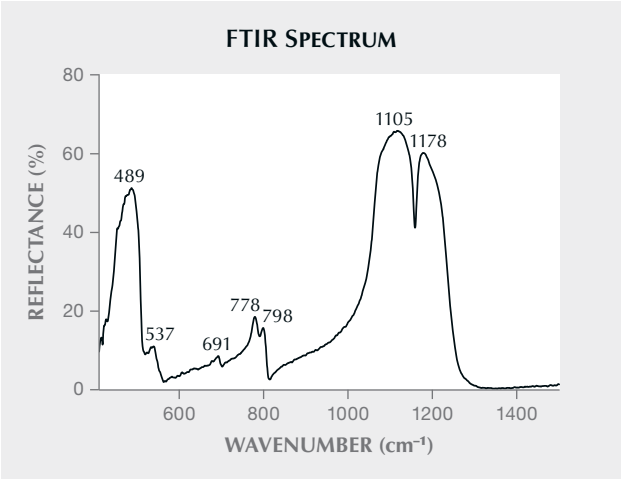

Figure 10. The bangle's infrared reflectance spectrum exhibited characteristic peaks at 489, 537, 691, 778, 798, 1105, and 1178 cm^{-1} that are typical for quartzite.

These green flaky inclusions were slightly oriented. Raman combined with EDXRF analysis identified them as fuchsite ($K(Al,Cr)_2(AlSi_3O_{10})(OH)_2$), a green chromium-colored variety of muscovite (figure 11A) (Fall 2013 GNI, pp. 183–184). Additionally, brassy yellow inclusions in a range

Figure 12. The UV-Vis spectrum of the green area showed two broad absorption bands centered at 423 and 600 nm in addition to a weak peak at 684 nm, indicating the presence of chromium.

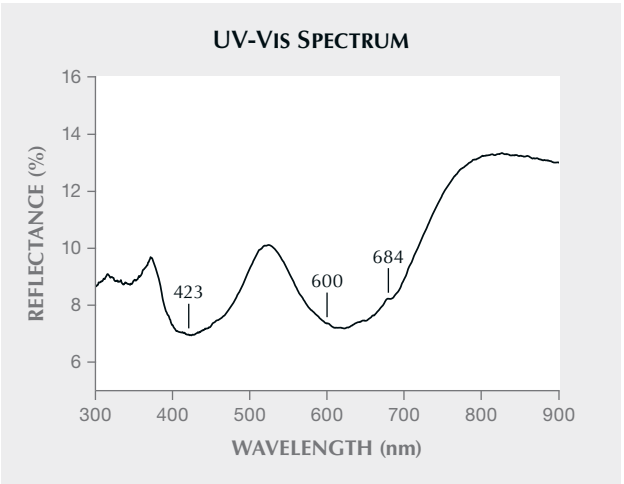

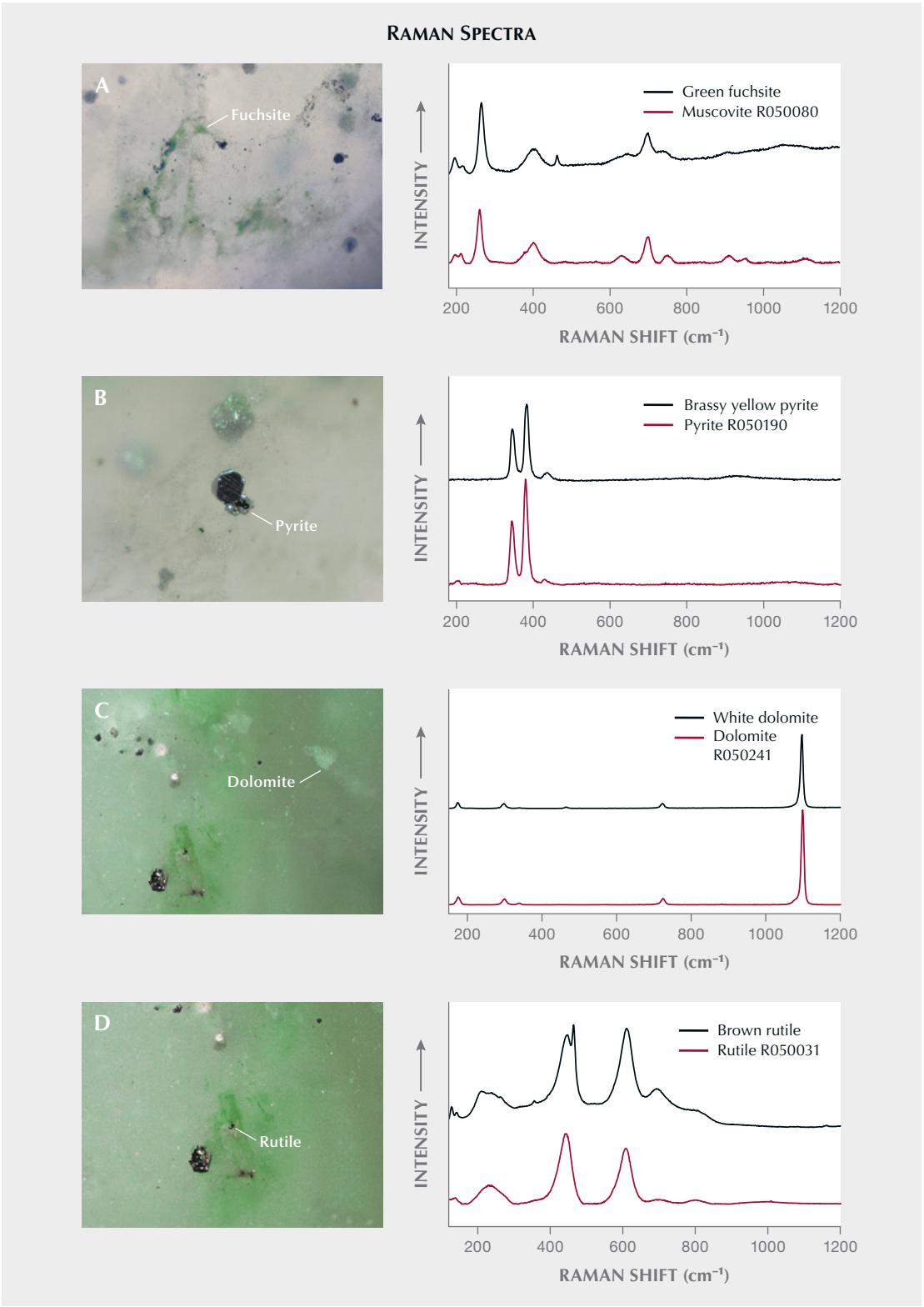

Figure 11. Photomicrographs and Raman spectra of inclusions in the bangle (black) and the reference spectrum in the RRUFF database (red): flaky fuchsite (A), brassy yellow pyrite (B), white dolomite (C), and brown rutile (D), shown in darkfield illumination (A) and reflected light (B–D). Photomicrographs by Su Xu; fields of view 0.2 mm (A), 1 mm (B), 0.8 mm (C), and 0.05 mm (D). See B. Lafuente et al. (2015), https://rruff.info/about/downloads/HMC1-30.pdf. Spectra are offset vertically for clarity.

Figure 13. Left to right: Reconstructed root amber (assembled from small fragments and from powders), natural Burmese root amber, and plastic imitation. Photos by Yilei Feng.

of sizes were confirmed as pyrite (figure 11B) using Raman spectroscopy. Raman also identified some white blocky inclusions in a nearby area as dolomite (figure 11C), as well as some tiny brown rutile inclusions found as irregular, randomly scattered grains (figure 11D).

Ultraviolet/visible spectroscopy corresponding to the green areas showed two broad absorption bands at about 423 and 620 nm, with a weak peak at 684 nm (figure 12). These features have been assigned to Cr^{3+} in fuchsite.

To our knowledge, fuchsite contained in quartzite is usually uniformly scattered in the form of tiny flakes. The uneven distribution of green fuchsite that resulted in patches of green in this bangle is noteworthy. The patchy green spots resemble the color concentrations often observed in jadeite. Despite the bangle's resemblance to jadeite, gemological tests such as refractive index, microscopic observation, and infrared and Raman spectroscopy readily identify it.

Su Xu
National Gold-Silver Gem & Jewelry Quality Inspection Center, Sichuan
Xiaoping Shi
Sichuan Provincial Coal Design & Research Institute

SYNTHETICS AND SIMULANTS

Identification of natural, reconstructed, and imitation root amber. Natural root amber is a variety of Burmese amber with a distinct appearance, good luster, and deep color (Y. Wang, *Amber Gemology*, China University of Geosciences Press, Beijing, 2018, p. 145). Root amber was named for its similarity in color and structure to tree roots. Root amber beads are popular in the Chinese market, and the Guangzhou Gemstone Testing Center receives many of them for identification. Recently we have noticed three different types submitted for identification (figures 13 and 14): natural root amber, reconstructed root amber (assembled from either pressed powders or small fragments), and plastic imitations.

Specific gravity (SG) was measured for three natural Burmese root amber samples (N-1 through N-3), three samples reconstructed from pressed powders (M-1 through M-3), three samples reconstructed from pressed fragments (M-4 through M-6), and three plastic imitations (P-1 through P-3). The SG of most varieties of regular Burmese amber samples is within 1.020–1.050, except for root amber and reddish amber (1.060–1.110). Overall, the natural root amber had higher SG (1.044–1.107) than that of regular Burmese amber and much lower SG than that of the reconstructed root amber from pressed amber powders (1.133–1.137) and plastic imitations (1.161–1.167). The root amber reconstructed from pressed fragments, meanwhile, had an SG of 1.075–1.077. The variations in SG of the reconstructed amber were due to differences in internal structure and/or gas porosity.

Most importantly, the internal features of the samples were quite different. There were some cellular or porous structures in the natural Burmese root amber (figure 15A). The typical red-brown dots of Burmese amber could be detected in both transparent and opaque zones (figure 15B). The flow-like pattern of natural Burmese root amber can be lamellar, annular, or flocculent, and there are natural tran-

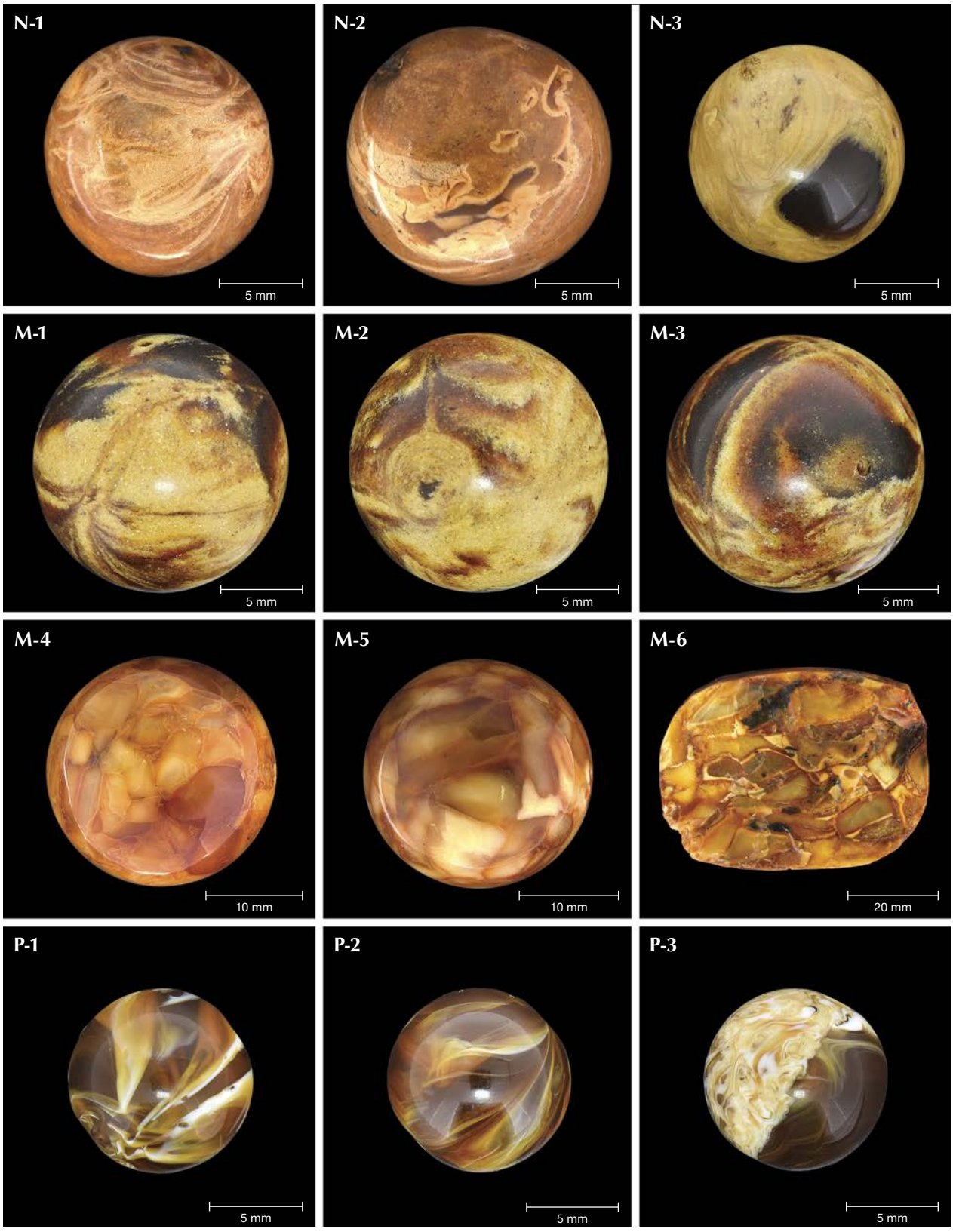

Figure 14. Natural Burmese root amber beads (N-1 through N-3), root amber beads reconstructed from pressed amber powders (M-1 through M-3) and small fragments (M-4 through M-6), and plastic root amber imitations (P-1 through P-3). Photos by Yilei Feng and Zhaoyi Li.

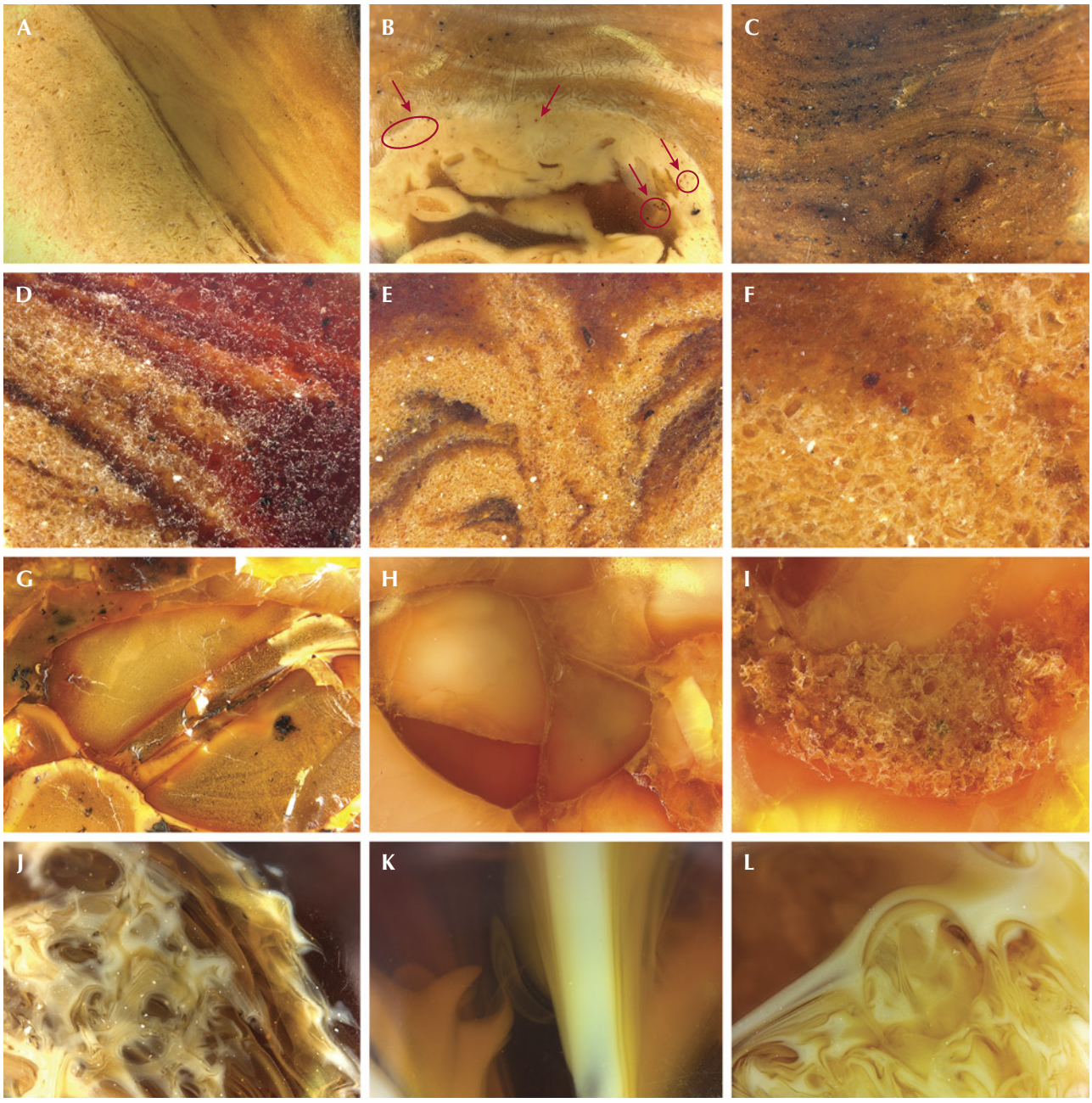

Figure 15. Row 1: Internal features of natural Burmese root amber beads: cellular or porous structures (A), red-brown dots in both transparent and opaque zones (B), and the lamellar flow-like pattern with a natural color transition (C). Row 2: Root amber beads reconstructed from pressed amber powders: a flow-like pattern formed by an accumulation of powders (D and E) and a granular texture (F). Row 3: Root amber beads reconstructed from small fragments of pressed amber: clear and rigid borders of the fragments (G and H) and a small granular texture seen in a larger patch structure (I). Row 4: Plastic root amber imitations showing ribbon-, string-, or ring-like patterns (J–L, respectively). Photomicrographs by Yilei Feng and Zhaoyi Li. Fields of view: 10.6 mm (A), 9.0 mm (B), 5.6 mm (C), 2.80 mm (D), 10.4 mm (E), 7.7 mm (F), 11.3 mm (G), 10.7 mm (H), 9.3 mm (I), 5.6 mm (J), 5.0 mm (K), and 4.9 mm (L).

sitions between varying colors (figure 15C). The internal features of the root amber reconstructed from pressed powders displayed an unnatural flow-like pattern similar to the veins of a leaf (figure 15, D–E). Under higher magnification, these

samples displayed a granular texture (a sugar- or sand-like pattern with apparent broken particles), confirming that small amber micro-particles had been pressed (figure 15F). There were very clear and rigid borders in the root amber reconstructed from fragments (figure 15, G and H). Some granular texture could still be found in these samples (figure 15I). The flow-like pattern of plastic imitation is mostly ribbon-, string-, or ring-like, with a sense of separation between the brown matrix and the obvious boundaries (figure 15, J–L).

Using Fourier-transform infrared (FTIR) spectroscopy, the plastic imitations were quickly identified in the mid-infrared range (3500–500 cm^{-1}). The extremely strong peak at 1731 cm^{-1}, three peaks of increasing intensity (1240, 1192, and 1148 cm^{-1}), and other peaks suggest that the material is an amino resin (figure 16, blue line). The vibration peaks of functional groups of natural root amber mainly appear at 2928, 2860, 1720, 1458, 1375, 1227, 1141, 1028, and 974 cm^{-1}, consistent with the main FTIR peaks of Burmese amber (figure 16, green line). The obvious "Baltic shoulder" (Y. Wang et al., "Characteristics of hydrothermally treated beeswax amber," Fall 2019 *G&G*, pp. 370–387), composed of a broad and weak absorption shoulder at 1265 cm^{-1} and a sharp peak at 1158 cm^{-1} as well as an absorption peak near 887 cm^{-1}, appeared in two reconstructed root amber specimens (figure 16, pink and purple lines). It can be inferred that these two reconstructed samples were pressed from rough Baltic amber.

Yan Li, Yilei Feng, and Zhaoyi Li
Gemmological Institute,
China University of Geosciences, Wuhan

Yamei Wang
Gemmological Institute,
China University of Geosciences, Wuhan
Guangzhou Gemstone Testing Center,
China University of Geosciences, Wuhan

Synthetic rock crystal quartz cluster with natural-looking inclusions. A client recently submitted for identification the piece shown in figure 17, assuming it to be a natural mineral specimen. It weighed 1114 g, measured 119 × 126 mm, and contained colorless transparent to semitransparent crystals. Eye-visible inclusions as well as numerous tiny crystals and some minute powdered material were seen around the cluster's base.

Standard gemological testing yielded a refractive index of 1.542–1.555, a specific gravity of 2.65, and inert reactions under long- and short-wave UV radiation, properties consistent with quartz. Microscopic examination revealed obvious fluid and two-phase inclusions (figure 18). Examination by

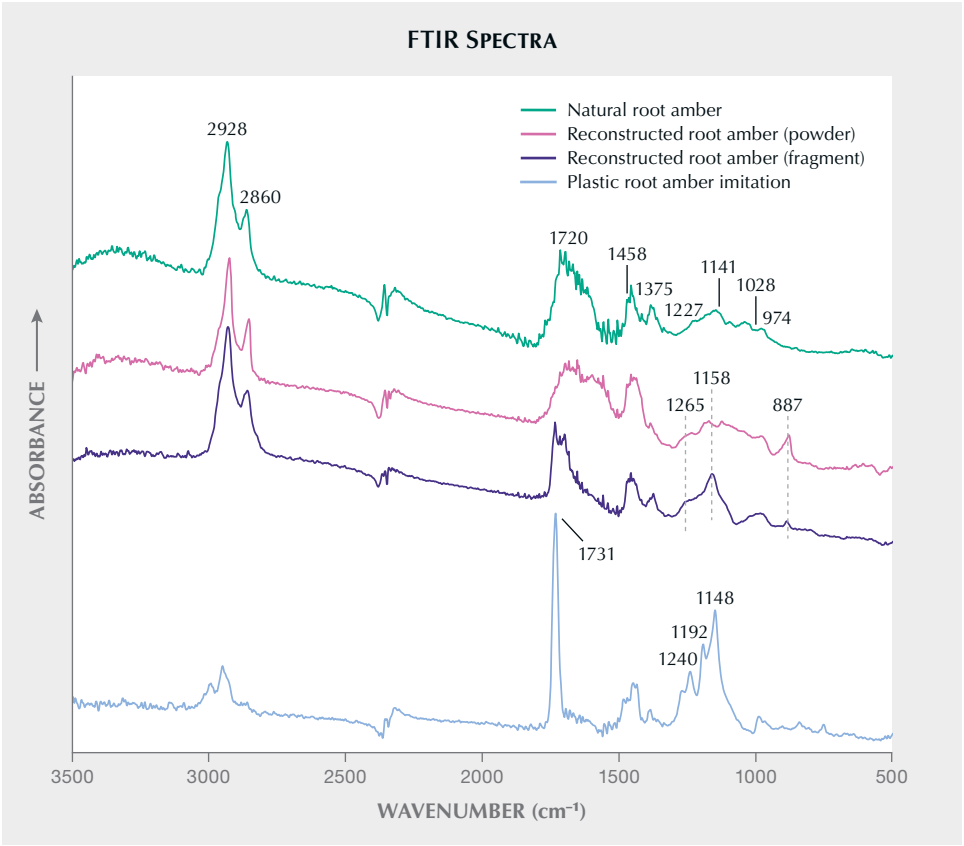

Figure 16. FTIR spectra of natural, reconstructed, and imitation root amber in the mid-infrared range (3500–500 cm^{-1}). Spectra are offset vertically for clarity.

Figure 17. The cluster specimen weighing 1114 g and measuring 119 × 126 mm. Photo by Lai Tai-An Gem Lab.

Fourier-transform infrared (FTIR) spectroscopy showed an absorbance region in the 400–1600 cm^{-1} range, also consistent with quartz, and Raman spectroscopy confirmed the identification. However, the most important data came from the FTIR analysis in transmission mode in the 1000–6000 cm^{-1} range. A characteristic peak of synthetic quartz at 3584 cm^{-1} (figure 19) was observed, while peaks consistent with natural quartz (3378, 3482, and 3595 cm^{-1}) were not detected. Similar spectra were collected from the other crystals in the group, confirming a synthetic origin (S. Karampelas et al., "Infrared spectroscopy of natural vs. synthetic amethyst: An update," Fall 2011 *G&G*, pp. 196–201; Winter 2015 Lab Notes, pp. 439–440).

Figure 18. Magnification revealed obvious fluid and two-phase inclusions within the crystals. Photomicrograph by Lai Tai-An Gem Lab; field of view 4.60 mm.

Synthetic quartz crystal clusters are not new to the market, but as the use of synthetic quartz has increased, such crystal specimens have become available on numerous online shopping platforms. Surprisingly, most of them are sold as "natural quartz clusters." One of the common trade methods for separating natural and synthetic quartz clusters is to observe the striations on the prism faces. In natural quartz, the striations form horizontally (perpendicular to the *c*-axis), while synthetic quartz typically displays diagonal or triangular striations (figure 20) (Winter 2016

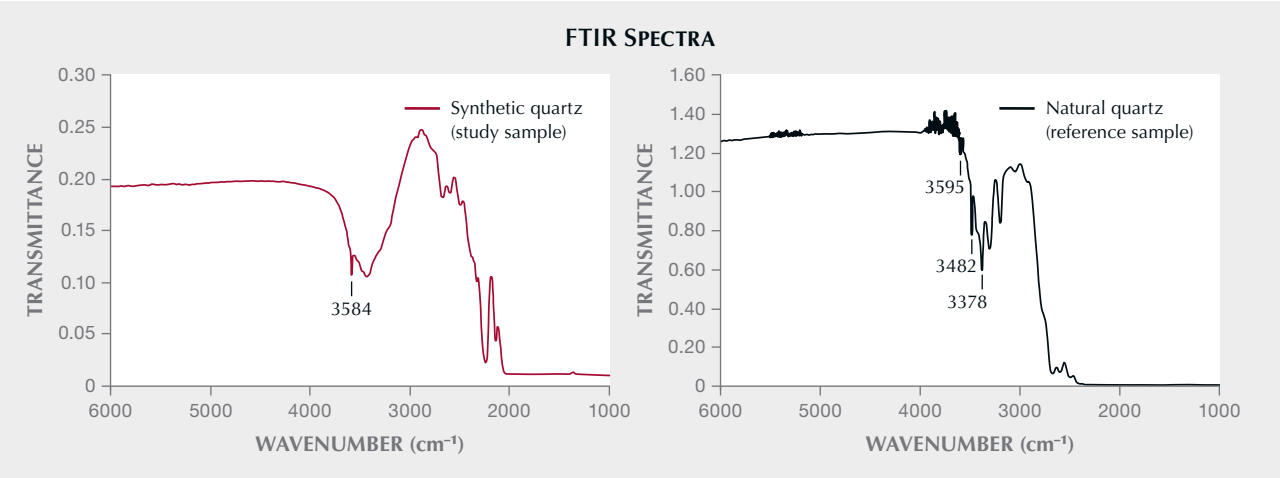

Figure 19. A peak at 3584 cm^{-1} in the FTIR spectrum proved the rock crystal quartz specimen was synthetic (red). In contrast, a natural quartz reference sample analyzed by our lab exhibits peaks at 3378, 3482, and 3595 cm^{-1} (black) that were absent in the sample.

G&G Micro-World, pp. 425–426). This method may aid in identification but should not be considered diagnostic, since the striations can be faked.

When synthetic quartz clusters are fashioned into polished products, the potential of misidentifying them as "natural quartz" increases significantly, especially with inexperienced consumers and small-scale labs lacking analytical equipment. In such cases, the inclusion scene is almost identical to that observed in natural quartz, and the helpful prismatic face growth lines disappear. Therefore, members of the trade should be cautious when handling synthetic quartz, although the crystal clusters may be somewhat easier to identify.

Larry Tai-An Lai (laitaiangemlab@gmail.com)
Lai Tai-An Gem Laboratory, Taipei

Red-dyed spodumene imitating ruby. A semitranslucent deep red oval faceted gem, measuring 13.88 × 9.08 × 5.88 mm and weighing 5.72 ct (figure 21), was recently submit-

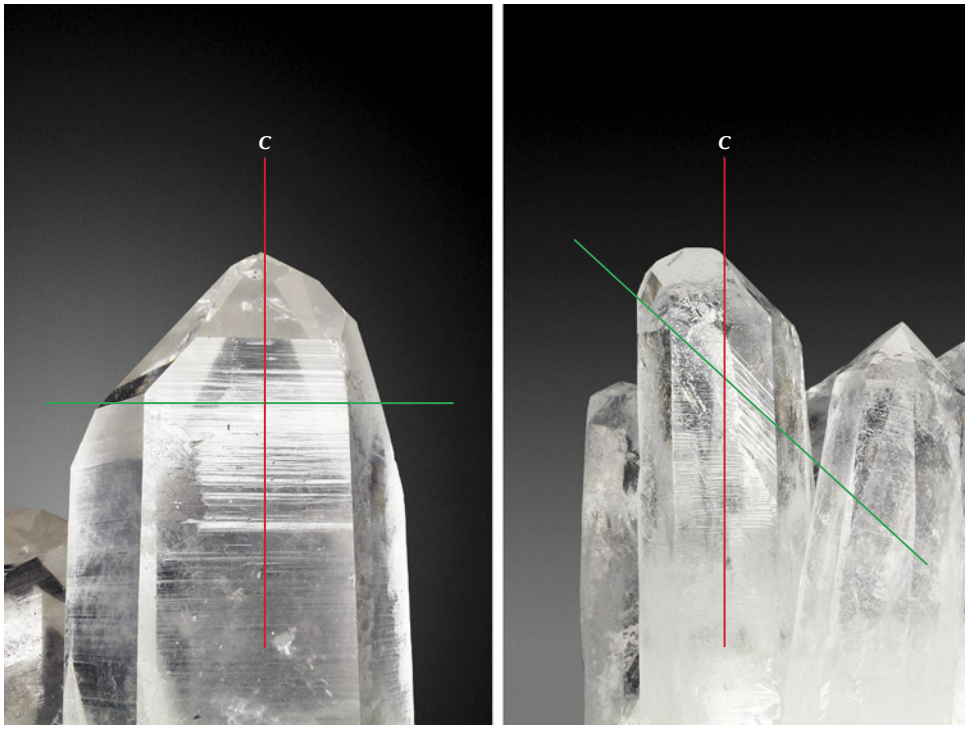

Figure 20. Natural quartz's horizontal prismatic striations, relative to the c*-axis (left, reference sample), were instead diagonal in the synthetic quartz cluster studied (right). Because striations can be faked, they should not be considered diagnostic. Photos by Lai Tai-An Gem Lab.*

Figure 21. A semitranslucent 5.72 ct red-dyed spodumene, presented as "red corundum." Photo by Guy Borenstein.

ted to Stuller Inc. by a client for a custom design. The stone was presented as "red corundum." But initial quality control testing showed a biaxial refractive index of 1.659–1.678 with a birefringence of 0.019, which did not correspond with corundum.

Due to the incorrect identity, the stone was sent to Stuller's gemological laboratory for further analysis. Standard gemological testing revealed a specific gravity of 3.237, with a moderate orange reaction to long-wave UV and a very weak reaction, along the fractures, to short-wave UV, typical of spodumene species. Further analysis, using a 532 nm Raman laser, also provided well-matched results for spodumene ($LiAl(SiO_3)_2$). Although the collected results clearly pointed to spodumene, the deep red color it displayed was questionable and required further investigation.

Unpolarized ultraviolet/visible/near-infrared (UV-Vis-NIR) spectroscopy showed two merging broad bands centered at 530 and 561 nm (figure 22). The former is probably associated with the Mn^{3+} chromophore (H.U. Rehman et al., "An X-ray absorption near-edge structure (XANES) study on the oxidation state of chromophores in natural kunzite samples from Nuristan, Afghanistan," *Minerals*, Vol. 10, No. 5, 2020, article no. 463), while the latter was previously reported as associated with red dyeing (K. Schmetzer et al., "Dyed natural corundum as a ruby imitation," Summer 1992 *G&G*, pp. 112–115). A possibly iron- and manganese-related shoulder at 430 nm (R. Lu, "Color origin of lavender jadeite: An alternative approach," Winter 2012 *G&G*, pp. 273–283) was also observed.

Fourier-transform infrared (FTIR) spectroscopy revealed peaks at 2954, 2924, 2872, and 2854 cm^{-1} (figure 23), typical of a universal paraffin oil filler (M.L. Johnson et al., "On the identification of various emerald filling substances," Summer 1999 *G&G*, pp. 82–107; L. Kiefert et al., "Identification of filler substances in emeralds by infrared and Raman spectroscopy," *Journal of Gemmology*, Vol. 26, No. 8, 1999, pp. 501–520). Under deep UV illumination (<225 nm), the foreign filler in the surface-reaching fractures fluoresced strongly pink while the spodumene host rock was inert. The effect was especially prominent in a cavity near the girdle (figure 24).

Microscopic examination verified the FTIR, UV-Vis-NIR, and deep UV findings and revealed surface-reaching cleavages and fractures filled with a red foreign substance (figure 25), as well as natural inclusions.

The recorded results confirmed the gem as a red-dyed spodumene. Although spectroscopy identified some manganese, the lack of pink/red reaction under deep UV suggests a low concentration (Lu, 2012). Therefore, the authors assume that the starting material was either colorless or very pale pink spodumene.

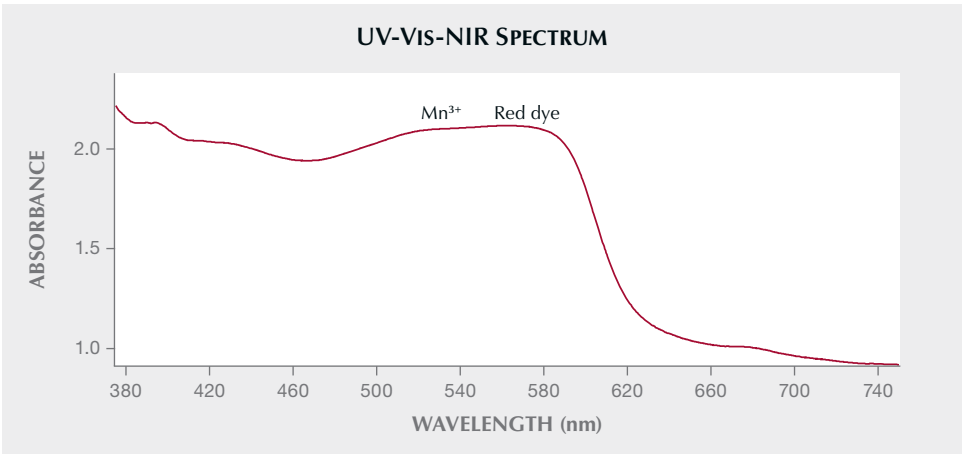

Figure 22. The unpolarized UV-Vis-NIR spectrum of the dyed spodumene shows a broad band centered at 561 nm due to the red dye. The band centered at 430 nm may be related to an intervalence charge transfer species between neighboring iron and manganese, while the band at 530 nm may be related to Mn^{3+}.

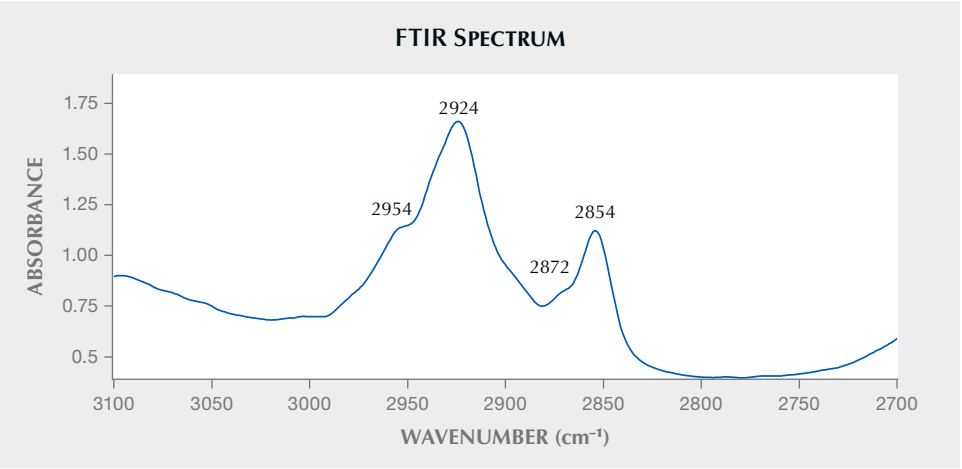

Figure 23. The FTIR spectrum of the dyed spodumene shows a series of peaks at 2954, 2924, 2872, and 2854 cm^{-1}, associated with a typical universal paraffin oil.

Introducing red dye to intensify the color of corundum is a longstanding practice (Schmetzer et al., 1992). To the best of our knowledge, however, this is the first time a spodumene has been treated with a colored oil to imitate ruby. The result masks the true identity of the gem, and without gemological testing, an uneducated trader could misidentify it as a color-enhanced ruby.

Guy Borenstein and Sean O'Neal
Stuller Inc.
Lafayette, Louisiana

CONFERENCE REPORT

GSA 2022 annual meeting. The Geological Society of America (GSA) held its annual meeting October 9–12 in Denver, Colorado. GIA's tenth technical session, entitled "Gemological Research in the Twenty-First Century—Gem Materials and Localities," featured twelve oral presentations and five posters (figure 26), covering broad topics including diamond, sapphire, tourmaline, sunstone, nephrite, and other gem materials.

Colored Gemstones and Other Subjects. The session started with recent research on colored gemstones. **Dr. Peter Heaney** (Pennsylvania State University, State College) opened with a keynote presentation addressing the structural coloration in colored gemstones that is produced by micro- or nano-structures. This structural coloration results from the interference of nanoparticle inclusions with light waves, including film interference, diffraction grating, scattering, and photonic crystals. Nanoparticles were characterized by a variety of techniques, including scanning electron microscopy (SEM), focused ion beam (FIB), transmission electron microscopy (TEM), and atomic force microscopy (AFM). Dr. Heaney summarized his group's state-of-the-art

Figure 24. Deep UV imaging of the spodumene's surface showed strong luminescence of the dye within a cavity as well as surface-reaching fractures. Image by Guy Borenstein; field of view 6.25 mm.

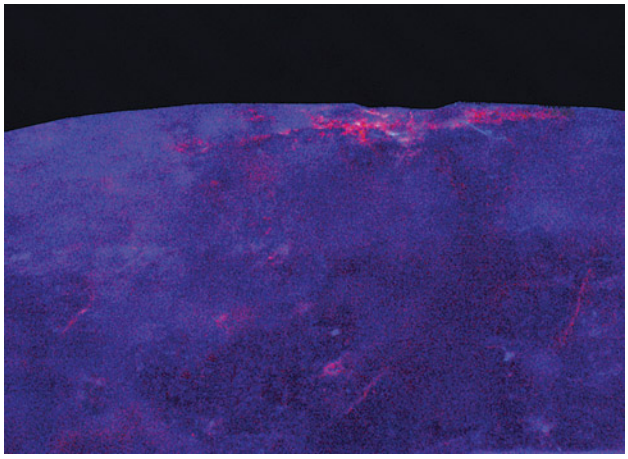

Figure 25. Color concentration within surface-reaching fractures confirmed dye treatment in the spodumene. Photomicrograph by Guy Borenstein; field of view 2.66 mm.

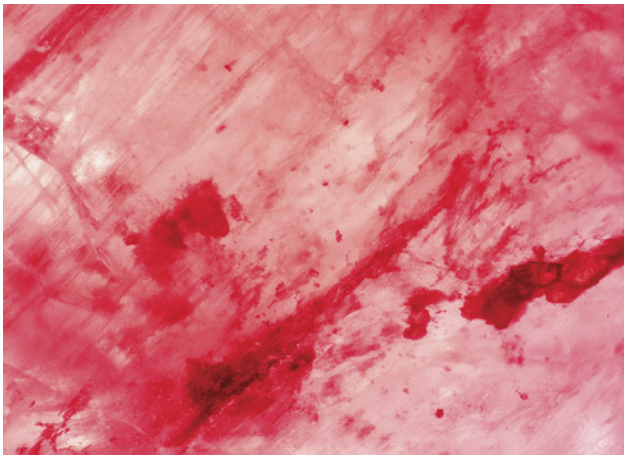

Figure 26. GSA 2022 oral and poster presenters. Left to right: Elina Myagkaya, Shiyun Jin, Che Shen, Stephanie Persaud, Roy Bassoo, Rhiana Henry, Alexander Goodsuhm, Rachelle Turnier, Yusuke Katsurada, Mei Yan Lai, Matthew Hardman, Christopher Breeding, Evan Smith, and Peter Heaney. Photo by Robert Weldon.

research on iridescent gemstones, including three-dimensional photonic arrays of hematite (Fe_2O_3) nanoneedles, quasi-periodic void layers in goethite (FeOOH), blazed gratings of Brazil twinning in iridescent quartz, and hierarchical oscillation layers in iris agate. Continuing with the topic of structural colorization, **Dr. Shiyun Jin** (GIA, Carlsbad) investigated the cause of special colors (green, red, and watermelon) and the optical effects of pleochroism in Oregon sunstone. The absorption and scattering power of copper nanoparticles in sunstone was tested with experimental absorption/scattering spectra and modeling based on Maxwell's equations. By comparing his experimental results and simulations, Dr. Jin concluded that the metallic copper nanoparticles in Oregon sunstone absorb and scatter incident light differently with respect to light polarization, thus yielding various color effects. **Che Shen** (Munsell Color Science Laboratory, Rochester Institute of Technology) studied the color change in sapphire caused by varying the amounts of six major chromophores (V^{3+}, Cr^{3+}, Fe^{3+}, Fe^{2+}-Ti^{4+}, h-Cr^{3+}, and h-Fe^{3+}). Using chromatic adaptation transformation (CAT), the color of sapphire under daylight and incandescent light were modeled by combining various chromophores. Shen concluded that blue/purple sapphire is caused by Fe^{2+}-Ti^{4+} and Cr^{3+}, green/reddish brown sapphire by Fe^{2+}-Ti^{4+} and Fe^{3+}, and pink/purplish brown sapphire by Fe^{2+}-Ti^{4+}, Cr^{3+}, and Fe^{3+}.

Figure 27. Aaron Palke presented the various types of melt inclusions in Montana's secondary sapphire. James Shigley (seated) moderated the session. Photo by Robert Weldon.

Other oral presentations focused on sapphire formation. **Dr. Aaron Palke** (GIA, Carlsbad) investigated the multiple types of melt inclusions in Montana's secondary sapphire, especially silica-rich felsic, sulfide, and polycrystalline melts (figure 27). The presence of multiple types of melt inclusions indicates that these sapphires are of magmatic origin. Further research on Montana sapphire by **Alexander Goodsuhm** (GIA, Carlsbad) constrained the formation conditions for Montana sapphire using zircon concentrations in rutile inclusions. Zircon concentrations in rutile inclusions ranged from 194 to 1340 ppm using inductively coupled

plasma–mass spectrometry. Missouri River sapphire was suggested to form at a higher temperature (~750°C) than Rock Creek sapphire (~660°C). **Dr. Rachelle Turnier** (GIA, Carlsbad) studied sapphire from Myanmar, Madagascar, and Sri Lanka, pairing photoluminescence (PL) spectra and trace element contents. Dr. Turnier observed that Cr^{3+} in sapphire is an efficient luminophore with intense red luminescence emission. Chromium in the corundum lattice can overcome high iron concentration and still cause intense luminescence. For example, 3 ppmw Cr^{3+} and 2500 ppmw Fe^{3+} can still yield luminescence of 1,000,000 counts/s/mW.

Other colored gemstone studies included beryl (oral), tourmaline (oral), and nephrite (poster). **Dr. Rhiana Henry** (Earth, Ocean and Atmospheric Sciences Department, University of British Columbia, Vancouver) investigated structural changes in response to chemical composition variation in beryl ($Be_3Al_2Si_6O_{18}$). Beryl's crystal structure was analyzed using single-crystal X-ray diffraction (XRD), and chemical composition was acquired via electron microprobe analysis (EPMA). She concluded that beryl's crystal structure could be calculated using the average ionic radii of the measured cations at the aluminum site (octahedron site) and the beryllium site (one of the tetrahedron sites). **Dr. Yusuke Katsurada** (GIA, Tokyo) investigated the dominant chromophores (Fe^{2+} and Cu^{2+}) in cuprian Paraíba tourmaline. Oriented wafers were prepared to collect both o-ray and e-ray ultraviolet/visible/near-infrared (UV-Vis-NIR) absorption spectra. Copper and iron concentrations were measured with laser ablation–inductively coupled plasma–mass spectrometry. This study contributes to the simulation of unpolarized UV-Vis-NIR spectrum and the approximation of copper and iron concentrations in cuprian tourmaline. **Ping Li** (Tongji University, Shanghai) demonstrated nephrite's microstructure as an indicator of origin. Nephrite microstructure, including grain size and mineral aggregation, were observed under the petrographic microscope. Nephrites from Xiaomeiling, Maxianshan, and Longxi in China underwent different extents of tectonism and metasomatism.

In recent years, GIA's Research and Development department has broadened its areas of interest, which was demonstrated in two other presentations. **Dr. Matthew Hardman** (GIA, Carlsbad) investigated the capability of machine learning to classify treated/untreated and synthetic/natural gemstones. More than 3,000 PL spectra of diamonds and 500 sets of trace element data of pearls were studied using the Boruta statistical algorithm. This approach identified PL peaks at 67.6, 503.2, 524.3, and 575.0 nm as important in identifying the treatment of CVD lab-grown diamond. Using machine learning, Dr. Hardman confirmed that manganese concentration is significant in identifying seawater or freshwater origin in pearls. **Dr. Sona Taijiryan** (GIA, Carlsbad) presented a poster on the main gem trading routes of the early modern period, from 1500 to 1800 CE. By translating an eighteenth-century manuscript from an Armenian gem merchant in India, Dr. Tajiryan demonstrated the East-West trade routes for the most popular gems in the first half of that century, including Indian diamonds, Southeast Asian rubies and spinels, Colombian emeralds, Sri Lankan pearls, and Mediterranean corals.

Diamonds. **Dr. Evan Smith** (GIA, New York) investigated a 910 ct type IIa diamond from Lesotho to indicate its formation in the mantle. This type of large and highly pure diamond is commonly known as CLIPPIR (Cullinan-like, large, inclusion-poor, pure, irregular) diamond. Inclusions such as cohenite (Fe_3C), troilite (FeS), and metallic Fe-Ni-C-S melt were identified using synchrotron X-ray diffraction at Argonne National Laboratory. The geochemistry of these inclusions confirmed a sublithospheric origin of the host diamond and provided evidence that during the diamond's formation, subduction of basaltic ocean crust to the lower mantle was occurring. **Dr. Mei Yan Lai** (GIA, Carlsbad) shared her recent doctoral research completed at the University of Alberta, which investigated lithospheric mantle composition and volatile recycling in the West African Craton. Inclusion mineralogy, major/trace elemental composition, and carbon/nitrogen host isotopic analyses for 105 diamonds from the Koidu mine in Sierra Leone were systematically analyzed. Dr. Lai indicated two significant and distinct episodes of eclogitic diamond formation in Koidu diamonds: cores precipitated from crustal melts and rims formed from mantle-derived melts.

Other presentations examined diamond in sedimentary systems. In alluvial environments, alpha radiation can cause a green or brown surface color. **Dr. Christopher M. Breeding** (GIA, Carlsbad) reported on his recent study of a rare pink stain in a natural type Ib Fancy brownish yellow diamond, a feature also caused by radiation damage. PL spectroscopy suggested that high concentrations of nitrogen-vacancy (NV^-) defects caused the pink color. It was suspected to have originated as a green diamond that turned pink as a result of higher temperature burial. Also, **Dr. Roy Bassoo** (GIA, Carlsbad) reported on various thermal annealing experiments on natural colorless diamonds to imitate diamond residence in a natural sedimentary system. Nitrogen content and aggregation, defect concentration, and luminescence color response upon heating were studied using Fourier-transform infrared (FTIR) spectroscopy, PL spectroscopy, and optical UV luminescence, respectively. Dr. Bassoo concluded that diamonds in a sedimentary system do not change their bodycolor, but such a system can influence defect-related luminescence.

GIA poster sessions highlighted three interesting colored diamond projects. First, **Sarah Arden**, **Abadie Ludlam**, and **Elina Myagkaya** (GIA, New York) presented their study on etch channels in a 3.17 ct pink type IIa diamond. A profusion of meandering ("worming") channels of various lengths embedded in this pink diamond were observed with micro X-ray computed tomography (CT). High strain was observed under the polariscope, and GR1 defects were mapped as clusters around etch channels using PL. The authors hypothesized two possible formation mechanisms

Figure 28. The GIA booth attracted GSA attendees from all over the world. In the foreground, Nathan Renfro speaks with a visitor. Photo by Cathy Jonathan.

for the etch channels' formation: (1) a type of line defect causing localized strain that is more vulnerable to dissolution and/or (2) Rose channels caused by micro-twinning and subsequently etched by mantle fluids. **Skyelar Caplan** (GIA, New York) reported a new color center (525 nm) as the cause of type Ia Fancy pink diamond. The 525 nm band together with an H-related 835 nm broad band caused a transmission for yellow and green light (610–660 nm) and resulted in a pink color. The 525 nm band observed in the UV-Vis absorption spectrum was related to high nickel content. **Stephanie Persaud** (GIA, New York) investigated two types of color-changing diamonds, chameleon and cryogenic, using spectroscopic analysis. Chameleon diamond changes from grayish green to orangy yellow upon heating, while cryogenic diamond changes from dark gray to light yellow when cooled to freezing temperatures. The cause of color change upon heating/cooling was attributed to changes in energy within the electron band gap.

In addition to the research talks and posters, GIA's booth in the exhibition hall also attracted many visitors. **Robert Weldon** (GIA, Carlsbad) hosted a demonstration of the use of light and camera settings for gemstone photography. He shared the stories and knowledge behind his photographs of the Hope diamond, the Dom Pedro aquamarine, and other notable gems. **Nathan Renfro** (GIA, Carlsbad) demonstrated techniques for inclusion photomicrography (figure 28) using different types of light sources.

An evening reception jointly hosted by GIA and the Mineralogical Society of America was held on October 11. The event provided gemologists and mineralogists with a great opportunity to exchange ideas and facilitate collaboration. In another GSA technical session, **Dr. James Shigley** shared GIA research opportunities with early-career mineralogists and crystallographers. Overall, the 2022 GSA meeting attracted strong attendance and notable interest in the gemology technical sessions and exhibits. We look forward to the 2023 GSA meeting, scheduled for October 15–18 in Pittsburgh, Pennsylvania.

Si Athena Chen, Tao Hsu, and James E. Shigley
GIA, Carlsbad

AUCTION REPORTS

Fall 2022 auction highlights. The astounding results of colored diamond sales in the spring auction season (Summer 2022 GNI, pp. 260–263) left expectations high for fall. Pink diamonds set the scene for the beginning of the season, starting with a bang at a Sotheby's stand-alone sale in Hong Kong in October. Selling for $57.7 million, almost three times its estimate, the 11.15 ct Williamson Pink Star (figure 29) became the second most valuable jewel ever sold at auction. After 20 minutes and 50 bids, the GIA-graded natural Fancy Vivid pink internally flawless cushion-shaped diamond broke the record price per carat for any diamond or gemstone sold at auction, at $5.2 million a carat.

The colored diamond trend headed downward the following month with the Fortune Pink (figure 30) at Christie's Magnificent Jewels sale in Geneva, selling below expectations at the lower end of its estimate. Fetching $28.9

Figure 29. The 11.15 ct Williamson Pink Star is set in an 18K pink and white gold ring, along with 1.41 carats of trapeze-cut diamonds and 0.14 carats of brilliant-cut pink diamonds. Courtesy of Sotheby's.

million, the GIA-graded 18.18 ct stone is the largest pear-shaped Fancy Vivid pink diamond ever sold at auction.

Figure 30. The 18.18 ct Fortune Pink sold in Geneva for $28.9 million. Courtesy of Christie's.

Figure 31. Surrounded by pink diamonds, this 31.62 ct Fancy blue diamond pendant sold within its estimate at $11.8 million. Courtesy of Christie's.

Another pink diamond, a 13.15 ct emerald cut, was slated to lead Christie's December Magnificent Jewels sale in New York before it was withdrawn weeks before the auction and later revealed as alleged stolen property. A 31.62 ct Fancy blue diamond pendant (figure 31) was then placed as the top lot of the auction. The GIA-graded pear modified brilliant cut, noted by Christie's as the largest of its kind to appear at auction, garnered $11.8 million, toward the lower end of the estimate. Three other blue diamonds offered by Sotheby's from the De Beers Exceptional Blue collection drew lackluster results throughout the season. Two were left unsold, and one was withdrawn prior to auction.

In an unexpected conclusion to the season, the Golden Canary (figure 32) sold below its estimate at $12 million. Without a reserve, Sotheby's anticipated the 303.10 ct pear-shaped Fancy Deep brownish yellow diamond to secure more than $15 million in the New York auction. Still, the diamond became the third most valuable diamond ever sold at auction, Sotheby's noted. As the largest flawless or internally flawless and largest pear-shaped diamond graded by GIA to date, the Golden Canary can be traced back to a young girl's discovery of an 890 ct rough near her uncle's house in the Democratic Republic of the Congo in the early 1980s. The 407.48 ct Incomparable, the largest of the 15 finished stones from the rough diamond, was recently transformed into the Golden Canary to improve its color and shape.

The real surprise of Sotheby's New York auction—and perhaps the season—was the sale of a ring featuring a 6.25 ct emerald recovered from the legendary 1622 shipwreck of the *Nuestra Señora de Atocha*. The ring sold in just five minutes for $1.2 million, more than 17 times its estimate. All proceeds were donated to humanitarian efforts in Ukraine.

Erica Zaidman
GIA, Carlsbad

IN MEMORIAM

Peter Keller. *Gems & Gemology* mourns the passing of Dr. Peter Keller (figure 33) on November 8, 2022. Keller dedicated 50 years of his life to the gemological community and made countless contributions to GIA and *G&G*.

Born in 1947 in Allentown, Pennsylvania, Keller became interested in rocks and minerals at an early age. After obtaining his undergraduate degree in geology from George Washington University, Keller earned a master's degree and a PhD in geology and earth science from the University of Texas. Keller began his career as curator of the Gem and Mineral Hall at the Natural History Museum of Los Angeles County before joining GIA as director of education in 1980.

Figure 33. Dr. Peter Keller during his time as director of education at GIA. Photo by GIA.

For more than a decade, Keller was instrumental to *G&G* as an author and as associate editor. In the first half of the 1980s, he wrote several landmark articles documenting his visits to gem deposits worldwide. "Emeralds of Colombia" (Summer 1981) received third place in *G&G*'s annual Most Valuable Article awards. He was a key contributor to *G&G*'s Spring 1986 special issue on China, reporting on the emerging gem resources in various Chinese provinces.

In addition to writing for *G&G*, Keller wrote and published two influential books, *Gemstones and Their Origins* (1990) and *Gemstones of East Africa* (1992). He even ventured into filmmaking earlier in his career, serving as associate producer on a documentary film titled *Gems of the Americas*, which was coproduced by the Natural History Museum of Los Angeles County and GIA.

Keller spent much of his career as president and CEO of the Bowers Museum in Santa Ana, California. He is survived by his wife, children, stepchildren, and grandchildren. We extend our deepest condolences to his family, friends, and colleagues.

Figure 32. The 303.10 ct Golden Canary, recently recut from the Incomparable, became the third most valuable diamond sold at auction. Courtesy of Sotheby's.

ERRATUM

In the Fall 2022 article "Gems on Canvas: Pigments Historically Sourced from Gem Materials," the photos in figures 13, 15, and 20 were credited to the National Gallery of Art in Washington, DC, in error. The photos are courtesy of the National Gallery in London.